
The Velocity Ellipsoid of Elliptical Galaxies

Isabella Söldner-Rembold



München 2018

The Velocity Ellipsoid of Elliptical Galaxies

Isabella Söldner-Rembold

Dissertation
an der Fakultät für Physik
der Ludwig-Maximilians-Universität
München

vorgelegt von
Isabella Söldner-Rembold
aus München

München, den 11. September 2018

Erstgutachter: Priv.-Doz. Dr. Ortwin Gerhard
Zweitgutachter: Priv.-Doz. Dr. Roberto Saglia
Tag der mündlichen Prüfung: 25. Oktober 2018

Contents

1	Introduction	1
1.1	Dark Matter	1
1.2	Elliptical Galaxies	2
1.3	Collisionless Galaxy Dynamics	5
1.3.1	Jeans Modelling	7
1.3.2	N-body modelling	9
1.3.3	Schwarzschild Modelling	13
1.4	Velocity Ellipsoids of Elliptical Galaxies	13
1.4.1	Results from Schwarzschild Modelling	13
1.4.2	Velocity Ellipsoid in the Milky Way	14
1.4.3	The JAM method	15
1.4.4	Applications of JAM	16
1.4.5	Tests of the JAM method	16
2	Velocity Ellipsoids in Elliptical Galaxies	19
2.1	Introduction	20
2.2	Data	24
2.2.1	Choice of Target Galaxies	24

2.2.2	Photometry	25
2.2.3	Kinematic Data	26
2.3	NMAGIC Models	30
2.3.1	Fitting the Observables	30
2.3.2	Fitting the velocity ellipsoid	31
2.3.3	Pseudo-SAURON velocity fields	32
2.3.4	Initial Models	33
2.4	NGC 4660: a well-constrained galaxy	38
2.4.1	JAM models for NGC 4660 via Jeans equation	38
2.4.2	NMAGIC dynamical model fits to the kinematic data	38
2.4.3	The only physical JAMs are nearly meridionally isotropic	39
2.4.4	The tension between the data and the JAM structure	40
2.4.5	Inclination	41
2.4.6	Mass-to-Light Ratio	41
2.5	NGC 4697: Models in different dark matter halos	42
2.5.1	Models for NGC 4697 without dark matter halo	42
2.5.2	Models with dark matter halo	51
2.5.3	Total Density Slopes	57
2.6	Negative Weights	58
2.6.1	Method	59
2.6.2	The effect of using negative weights on JAM assumptions	60
2.7	Summary and Discussion	61
2.8	Conclusions	66

Appendices	71
2.A Photometry Appendix	71
2.A.1 MGE Data	71
2.A.2 Sérsic Fit	73
2.A.3 Comparison to other Photometry	74
2.A.4 Composite Image	74
2.A.5 MGE Fitting Routine	76
2.A.6 Photometry used in NMAGIC	77
2.A.7 Spherical Harmonics	77
2.B Kinematics Appendix	80
2.B.1 4-fold symmetrising ATLAS ^{3D} data of NGC 4697	80
2.B.2 The SLUGGS data	81
2.B.3 Comparison of the different kinematic data sets	84
2.B.4 Scaling the SLUGGS data	87
2.B.5 Estimating errors for the 2D SLUGGS Kinematics	93
2.B.6 Resolution and NMAGIC Calibration	93
2.C NMAGIC Method Details	93
2.C.1 Pseudo-SAURON velocity fields	93
2.D JAM models of different dark matter halos	94
2.D.1 Adapting Observables to the JAM method	94
2.D.2 Model without dark matter	95
2.D.3 JAM Model Dark Matter Halos	97
2.E Modelling Appendix	97
2.E.1 NGC 4660	97

2.E.2	NGC 4697	97
3	Triaxial Models	111
3.1	Triaxial N-Body Models using Made-to-Measure Method	112
3.2	Applications of Triaxial Modelling	115
3.2.1	Testing a Schwarzschild Model	115
3.3	Modelling M87	117
3.3.1	Photometry	117
3.3.2	Potential	119
3.3.3	M87 NMAGIC Models	123
3.4	Conclusions	123
4	Spherical Jeans models of stars and gas kinematics in NGC 4278	125
4.1	Data	126
4.2	Data for use in JAM modelling	129
4.2.1	Photometry	129
4.2.2	Root-mean-square velocity (v_{rms})	129
4.2.3	HI Data	131
4.3	Jeans Modelling	131
4.3.1	v_{rms} predictions from spherically symmetric Jeans models	134
4.4	The galaxy NGC 4283: a satellite being disrupted while orbiting in the NGC 4278 halo	140
4.4.1	Conclusion	147
5	Summary and Conclusions	149
	Acknowledgements	161

List of Figures

2.1	Velocity Ellipsoid Diagram.	22
2.2	Extended photometry of NGC 4660.	23
2.3	Original and four-fold symmetrised ATLAS ^{3D} kinematic data.	28
2.4	ATLAS ^{3D} and 2D SLUGGS kinematic data.	29
2.5	NGC 4660 internal Kinematics of initial models for NMAGIC.	34
2.6	NGC 4660 internal kinematics of initial models for NMAGIC ($c_{(R,z)}$ and β_z)	35
2.7	JAM method models of NGC 4660.	42
2.8	NGC 4660 projected kinematics of NMAGIC data-driven models	43
2.9	NGC 4660 internal kinematics of NMAGIC data-driven models	44
2.10	NGC 4660 projected kinematics of NMAGIC cross-driven models.	45
2.11	Comparison of NGC 4660 v_{rms} data and models.	45
2.12	NGC 4660 internal kinematics of models with global β_z as an observable.	46
2.13	NGC 4660 internal kinematics of NMAGIC models with different RDS.	46
2.14	NGC 4660 χ^2 and cross parameter c_{30} for models with diferent RDS.	47
2.15	NGC 4697 JAM velocity field models.	47
2.16	Comparison of NGC 4697 v_{rms} data and models.	48
2.17	NGC 4697 internal kinematics of NMAGIC data-driven models.	48

2.18	The normalized cross term $c_{R,z}$ and z -anisotropy of NGC 4697.	49
2.19	NGC 4697 χ^2 and cross parameter c_{30} for different RDS.	51
2.20	Dark matter JAM models of NGC 4697 reduced χ^2	52
2.21	Dark matter JAM models of NGC 4697 $\Delta\chi^2$	53
2.22	The median anisotropy β_z with dark matter halo	53
2.23	The Mass-to-Light Ratio with dark matter halo.	54
2.24	The total density slopes of the different stellar and dark halo models A-K.	58
2.25	The entropy S and the change of entropy with time $\delta S/\delta w_i$	60
2.26	Characteristics of negative particle models.	62
2.27	Histogram of the negative weights in models where the JAM condition is enforced.	63
2.28	Internal Kinematics of models with global target $\beta_z = 0.29$	64
2.A.1	The MGE photometric data of NGC 4660 from Scott et al. (2013).	72
2.A.2	The major axis surface brightness profile of NGC 4660.	72
2.A.3	Contours of the Photometry of NGC 4660.	73
2.A.4	The major axis surface brightness profile of NGC 4660 in the transition region.	75
2.A.5	The original composite image of NGC 4660, MGE fit and residual between the two.	76
2.A.6	The major axis surface brightness profile of NGC 4660.	78
2.A.7	Normalisation of the Sérsic profile of NGC 4660.	79
2.B.1	Velocity of the NGC 4697 ATLAS ^{3D} data in kms^{-1} vs radius.	81
2.B.2	Diagram of a kinematic field where the major axis is aligned with the y -axis.	82
2.B.3	Original ATLAS ^{3D} Data.	83
2.B.4	Shifted and Recentered ATLAS ^{3D} Data.	83
2.B.5	Four-fold symmetrised ATLAS ^{3D} data.	84
2.B.6	SLUGGS Kinemetry Profiles.	85

2.B.7	The 2D SLUGGS kinematic data, velocity, σ , h_3 and h_4	86
2.B.8	Velocity Ratio of SLUGGS and ATLAS ^{3D}	88
2.B.9	The 2D SLUGGS kinematic data, velocity, velocity dispersion, h_3 and h_4	89
2.B.10	Transition between ATLAS ^{3D} and SLUGGS.	90
2.B.11	Transition between ATLAS ^{3D} and SLUGGS.	91
2.B.12	Gaussian Noise for velocity, σ , h_3 , and h_4	92
2.D.1	NGC 4697 MGE Photometry	96
2.D.2	The 2D probability of the parameters M/L and z - anisotropy in JAM Jeans Models.	98
2.E.1	Kinematics of different data-driven halo models.	99
2.E.2	Kinematics of different cross-driven halo models.	100
2.E.3	Comparison of ATLAS ^{3D} kinematic data of NGC 4660.	101
2.E.4	The circular velocity of NGC 4697	102
2.E.5	Internal Kinematics of NGC 4697.	103
2.E.6	Internal Kinematics of NGC 4697 (JAM assumption and photometry)	104
2.E.7	NGC 4697 Internal Kinematics Tension.	105
2.E.8	NGC 4697 Internal Kinematics Tension (differently weighted γ)	106
2.E.9	Comparison to 1D SLUGGS data (Kinematics Only).	107
2.E.10	Comparison to 1D SLUGGS data (Cross Only).	108
2.E.11	Comparison to 1D SLUGGS data (Kinematics + Cross).	109
1	The x , z , and y -views of a triaxial particle model in NMAGIC.	113
2	Internal kinematics of a triaxial NMAGIC model.	114
3	Surface brightness in V -band of M87.	117
4	Circular velocity profile of M87 from different literature.	118

5	Surface density projection of M87.	120
6	Velocity dispersion of M87 NMAGIC models.	121
7	Anisotropy of M87 NMAGIC models.	122
1	Surface brightness profile of NGC 4278.	127
2	Velocity distribution of NGC 4278 PNe.	128
3	Line-of-sight velocities of PNe of NGC 4278 and NGC 4283.	128
4	Azimuthally averaged v_{rms} data of NGC 4278.	130
5	HI circular velocity data from Morganti et al. (2006).	138
6	Jeans model to v_{rms} of NGC 4278 with different r_{vir}	141
7	Jeans model to v_{rms} of NGC 4278 with different concentrations.	142
8	Jeans model to v_{rms} of NGC 4278 with different β_2	143
9	Phase space diagram of GCs and PNe around NGC 4278.	144
10	Spatial distribution of PNe and GCs around NGC 4278.	145
11	The PNe and GCs associated to the substructure of NGC 4278	146

List of Tables

2.1	Characteristics of initial models into NMAGIC for NGC 4660 and NGC 4697.	39
2.2	Properties of the dark matter halo models.	59
2.3	Characteristic parameters of the models of NGC 4660.	67
2.4	JAM fit parameters to the ATLAS ^{3D} data of NGC 4660 and NGC 4697. . .	68
2.5	Characteristic parameters of the models of NGC 4697.	69
2.A.1	Sérsic parameters of NGC 4660.	79
2.A.2	MGE fit parameters.	80
1	Properties of NGC 4278 and NGC 4283.	131
2	Dark matter fraction of NGC 4278 for different models.	139
3	Jeans models parameters for NGC 4278.	139
4	Dark matter fraction f_{DM} of NGC 4278.	140

Zusammenfassung

In der vorliegenden Arbeit wurde die Ausrichtung der Geschwindigkeitsellipse der elliptischen Galaxien NGC 4660 und NGC 4697 mit Hilfe des NMAGIC “Made-to-Measure” Modells untersucht. Als Daten wurden ATLAS^{3D} and SLUGGS kinematische Daten verwendet. Die häufig verwendeten anisotropischen Jeans-Modelle (JAM) machen die Annahme $\langle v_R v_z \rangle = 0$. Es wurde daher untersucht, ob zylindrisch ausgerichtete Geschwindigkeitsellipse ($\langle v_R v_z \rangle = 0$) in elliptischen Galaxien mit realen Verteilungsfunktionen vorhanden sein können. Wir finden, dass es keine physikalischen Modelle von NGC 4660 und NGC 4697 mit gleichzeitiger globaler Anisotropie und zylindrisch ausgerichteten Geschwindigkeitsellipsoiden gibt. Modelle, für die die Orientierung des Geschwindigkeitsellipsoids keine Rolle spielen, sind die einzigen Modelle mit realen Verteilungsfunktionen und zylindrisch ausgerichteten Geschwindigkeitsellipsoiden. Die Qualität von Modellen mit $\langle v_R v_z \rangle = 0$ hängt daher davon ab, wie isotrop die interne Struktur der zu modellierenden Galaxie ist. Wir untersuchen den Einfluss dieser Einschränkung auf das Masse-Licht-Verhältnis und den damit verbundenen Anteil dunkler Materie. Eine Untersuchung verschiedener Verteilungen von dunkler Materie in NGC 4697 zeigt, daß ein Halo von dunkler Materie im intermediären Massenbereich die kinematischen Daten bis zu einem effektiven Radius von $1.5 R_e$ gut reproduziert, wenn die Ausrichtung der Geschwindigkeitsellipse nicht eingeschränkt wird. Mit der Bedingung zylindrischer Ausrichtung dagegen läßt sich kein gutes Modell für die Kinematik konstruieren. Die Qualität der Modelle nimmt dabei mit ansteigender Dunkler-Materie-Halo ab.

Wir untersuchen die Verteilungen der dunklen Materie und der Orbitale für die intermediäre Galaxie NGC 4278 mit dem sphärischen Jeans-Modell unter Benutzung von HI-Rotationsdaten. Wir benutzen planetarische Nebel (PNe) als Indikatoren in den Regionen, in denen das Sternenlicht für die Absorptionslinien-Spektroskopie zu schwach ist. Durch Kombination der v_{rms} -Geschwindigkeiten der extragalaktischen PNe mit denen der SAURON-IFU-Daten berechnen wir ein Profil, an das die Jeans-Modelle angepasst werden. Die HI-Rotationskurve ermöglicht eine Beschränkung des totalen Potentials der Galaxie. NGC 4278 ist von besonderem Interesse wegen ihres flachen quadratischen Geschwindigkeitsmittels, welches typisch für eine elliptische Galaxie hoher Masse ist. Mit Hilfe unserer Modelle zerlegen wir das Potential in die Terme für stellare und dunkle Materie und finden, daß NGC 4278 mit Modellen mit grossem Anteil dunkler Materie konsistent ist. Außerdem

ergibt sich, dass die Gesamtmasse gut durch eine Dichteverteilung der Form $\rho \approx r^\gamma$ mit einem Faktor $\gamma = -2.1$ beschrieben wird.

Um die kinematische Struktur der Galaxie NGC 4283 in der Nachbarschaft von NGC 4278 zu untersuchen, benutzen wir ebenfalls PNe. Die PNe der Galaxien sind klar getrennt aufgrund der verschiedenen mittleren Geschwindigkeiten von $(622 \pm 21) \text{ km s}^{-1}$ für NGC 4278 and $(1050 \pm 21) \text{ km s}^{-1}$ für NGC 4283. Im PNe-Phasenraum finden wir mehrere PNe mit Geschwindigkeiten innerhalb weniger Standardabweichungen von der mittleren Geschwindigkeit der Galaxie NGC 4283, die aber räumlich einem über NGC 4279 ausgedehnten Gezeitenstrom zugeordnet werden können. Es handelt sich dabei wahrscheinlich um abgestreifte Materie von NGC 4283. Dieselbe Analyse wurde mit Kugelsternhaufen wiederholt, die nur zwei Objekte enthalten, die mit NGC 4278 assoziiert sind und, ungewöhnlicherweise, kein einziges mit NGC 4283. Dabei wird dieselbe Abstreifung von Materie beobachtet. Die Existenz dieser Substruktur mit einem $\gamma = -2.1$ Dichteprofil, in Verbindung mit der kinematischen Achsenverschiebung der Sterne und des Gases dieser Galaxie, lassen darauf schließen, dass in dieser Galaxie mehrere unabhängige Akkretionsereignisse stattfinden. Ein solcher Verlauf ist typisch für massive elliptische Galaxien.

Abstract

We present an investigation into the alignment of velocity ellipsoids in the elliptical galaxies NGC 4660 and NGC 4697 using the NMAGIC Made-to-Measure Dynamical Modelling approach, with ATLAS^{3D} and SLUGGS kinematic data. We test whether cylindrically aligned velocity ellipsoids ($\langle v_R v_z \rangle = 0$), assumed by the widely used Jeans Anisotropic Models (JAM), can be present in elliptical galaxies with real distribution functions. We find that there are no physical models of NGC 4660 and NGC 4697 with both global anisotropy and cylindrically aligned velocity ellipsoids. The only models with real distribution functions and $\langle v_R v_z \rangle = 0$ are found to be isotropic models, where velocity ellipsoid orientation is irrelevant. The quality of models with $\langle v_R v_z \rangle = 0$ is therefore dependent on the similarity of their internal structure to isotropy. We probe the effect of this limitation on Mass-to-Light Ratio and dark matter content. A study of several dark matter distributions of NGC 4697 finds that an intermediate dark matter halo reproduces kinematic data well to $1.5 R_e$ when the alignment of velocity ellipses is left unconstrained. Whilst constrained to have cylindrical alignment, no good quality models to the kinematics are found, with quality of models decreasing with increasing dark matter halo.

We investigate the dark matter distribution and orbit distribution of the intermediate elliptical galaxy NGC 4278 using spherical Jeans modelling and HI rotation data. We use planetary nebulae as tracers beyond the point that stellar light becomes too faint for absorption line spectroscopy. Combining the v_{rms} of the PNe with that of SAURON IFU data, we compute a profile to which the Jeans models are made. The HI rotation curve provides a constraint on the total potential of the galaxy. NGC 4278 is an interesting target as it has a flat root-mean-square velocity which is more characteristic of a large mass elliptical galaxy. Using our models to decompose the potential into stellar and dark matter, we find that NGC 4278 is consistent with the models with a considerable amount of dark matter. Additionally the total mass is well reproduced by a total power law density $\rho \approx r^\gamma$, with $\gamma = -2.1$, which points to an accretion history.

The PNe additionally trace a galaxy nearby to NGC 4278 named NGC 4283. The planetary nebulae of the galaxies are well separated using the mean velocities at (622 ± 21) kms^{-1} for NGC 4278 and (1050 ± 21) kms^{-1} for NGC 4283. Using the phase space of the PNe, several PNe were found with velocity within a few σ of the mean velocity of NGC 4283 but spatially associated to a stream across NGC 4278. This is thought to be a substructure of stripped matter from NGC 4283. The same analysis was repeated on globular clusters (which have only has objects associated to NGC 4278 and unusually none to NGC 4283) and have found the same stripping effect. The presence of this substructure, the $\gamma = -2.1$ density profile, along with other kinematic misalignment of the stars and gas in this galaxy all points to several independent accretion events occurring to this galaxy. This type of accretion history is more typical of massive ellipticals.

Chapter 1

Introduction

1.1 Dark Matter

The visible matter in the Universe is made of gas, stars, and dust. The amount of visible matter is not sufficient, however, to explain the gravitational forces present in the Universe. One type of models that can explain the presence of excess matter postulates the existence of dark matter, which interacts only gravitationally but is invisible to the electromagnetic force.

There are several different types of astronomical evidence for the existence of dark matter. Historically, the earliest evidence was the observation by Oort (1932) that the velocities of nearby stars are too high given their mass. Zwicky (1933) measured the velocity dispersion of a galaxy cluster and concluded that the dispersions imply a factor of 10 to 100 more mass than the visible matter contained in the galaxy. Zwicky (1933) concluded that this could be explained by some form of invisible matter (Trimble, 1987).

Subsequent work by Babcock (1939) on the M31 galaxy, Ostriker et al. (1974) and Rubin et al. (1978) on spiral galaxies, and Einasto et al. (1974) on galaxy clusters showed through the analysis of rotation curves that galaxy mass increases in the region beyond radii that the visible matter would indicate. Further astronomical evidence for dark matter has been found using gravitational lensing (e.g Wu et al., 1998; Natarajan et al., 2017) and the measurement of the Cosmic Microwave Background (CMB, Ade et al., 2016).

While there is indirect evidence for the existence of dark matter, experiments have so far failed to directly detect dark matter interactions, theorised, among others, to be weakly interacting massive particles (WIMPs, Liu et al., 2017).

To understand how matter, dark or visible, forms structures requires to go back to the

beginning of the Universe. The Universe evolved from an extremely hot and dense state according to the current standard model, suitable for the emergence of subatomic particles and their subsequent fusion into nuclei. As Hubble (1929) first discovered, the Universe is expanding, cooling as it expands. The discovery of Cosmic Microwave Background supports this view, first detected by Penzias & Wilson (1965). The CMB is a low temperature black body radiation, first measured using NASA’s Cosmic Background Explorer (COBE), with a temperature of ~ 2.73 K (Smoot et al., 1992). It originates from the epoch of recombination, at the time in the evolution of the Universe where ionised electron-proton plasma recombined to form hydrogen.

Following the COBE map, there have been more measurements of the CMB performed by the Degree Angular Scale Interferometer (DASI Kovac et al., 2002), by BOOMERanG (Masi, 2002), and the WMAP (Bennett et al., 2013) and Planck Collaborations (Ade et al., 2016). The temperature fluctuations in the CMB have been found to be very small and Gaussian on all scales (Komatsu, 2003; Ade et al., 2016).

Small anisotropies in density and temperature existed at the beginning, where the small perturbations in density later form the observed structures of the Universe, such as large scale structures, galaxies and clusters. This occurs during the inflationary epoch, where the Universe expands rapidly (Guth, 1981; Peacock, 1999). Numerical simulations such as the Millennium Simulation (Springel et al., 2005) give a picture of how dark matter structures formed from the density perturbations. The development of structures is hierarchical, with smaller structures merging into larger structures. These simulations are used to find relationships between the density and halo radius, such as the NFW profile (Navarro et al., 1996):

$$\rho_{\text{NFW}}(r) = \frac{\rho_s}{(r/r_s)(1+r/r_s)^2}, \quad (1.1)$$

where r_s is a scale length, and ρ_s is a characteristic density.

1.2 Elliptical Galaxies

Galaxies are classified by their morphology. Elliptical galaxies (E0-E7) generally appear smooth on the sky, with no features and with their light ellipsoidal in shape. They have a bright centre, and their ellipticity varies from almost round (E0) to very flattened (E7). Lenticular galaxies (S0) share the feature of a bright centre, and in addition have a disk. Together, lenticular and elliptical galaxies are known by the historical name of “early-type galaxies” (ETGs). In addition, there are spiral galaxies (Sa-Sb), which have a flat disk and a central bulge or pseudo-bulge. Spiral arms can be present in the disk, and some spiral galaxies additionally have a bar (SB). Spiral galaxies are historically referred to as late-type galaxies. Irregular galaxies are galaxies that do not morphologically fit into any of the above mentioned categories. Central densities in elliptical galaxies are high compared

to for example the Milky Way disk.

We primarily deal with ETGs in this thesis, as we probe a dynamical modelling method (Cappellari, 2008) which has been applied to large samples of ETGs in, for example, ATLAS^{3D} (Cappellari et al., 2011) and SAMI (Scott et al., 2015). It has also been applied to samples with both ETGs and spirals in MaNGA (Li et al., 2018). Since the less complicated potential structure of ETGs is easier to model dynamically, we have chosen elliptical galaxies as our test cases. Due to the large number of stars typically present in an elliptical galaxy, approximately 10^9 to 10^{11} , spread over a large area of the order of tens of kiloparsecs (kpc), the density of such galaxies is low.

Surface Brightness

Elliptical galaxies generally have a bright central nucleus, with surface brightness decreasing rapidly with increasing radius. There are several methods to characterise the surface brightness profiles of elliptical galaxies. One example is the profile from Sérsic (1968):

$$I(R) = I_e \exp \left(-b_n \left[\left(\frac{R}{R_e} \right)^{1/n} - 1 \right] \right), \quad (1.2)$$

where n is the Sérsic index, I_e is the intensity at the effective radius R_e that encloses half the light of the galaxy, and b_n is a factor dependent on n . A double-component Sérsic profile parametrisation from Hopkins et al. (2009), allowing more complex photometry, is given by:

$$I_{\text{tot}} = I' \exp \left(-b'_n \left(\frac{r}{R_{\text{inner}}} \right)^{\frac{1}{n'_s}} \right) + I_0 \exp \left(b_n \left(\frac{r}{R_{\text{outer}}} \right)^{\frac{1}{n_s}} \right), \quad (1.3)$$

where R_{inner} and R_{outer} are the effective radii of the inner and outer profile, n'_s and n_s are their Sérsic indices, and I' and I_0 are the normalisations. The parameters n'_s and n_s are fixed to $n'_s = 1.0$ and $n_s = 1.88$, given by Hopkins et al. (2009), while the effective radii and normalisation are fitted. The parameter b_n is computed using the equation from Ciotti (1991):

$$\Gamma(2n) = 2\gamma(2n, b_n), \quad (1.4)$$

where Γ and γ are the complete and incomplete Gamma functions, respectively.

Kinematics

The line-of-sight velocities of a galaxy can be found using the broadened absorption line spectrum from the atmospheres of stars in the galaxy. In nearby galaxies, individual stars can be resolved, but in distant galaxies only the cumulative spectrum of the stars

along the line-of-sight is observed. These lines are Doppler-shifted according to the line-of-sight velocities (Binney & Merrifield, 1997). The velocity profiles gathered from these measurements can be fit by a Gaussian function, which gives the mean velocity and velocity dispersion, and the Gauss-Hermite moments that describe the velocity profiles as a polynomial function defined as:

$$u_n(w) = (2^{n+1}\pi n!)^{-\frac{1}{2}} H_n(w) e^{-w^2/2}, \quad (1.5)$$

where $w = (v - \hat{v})/\hat{\sigma}$ and $H_n(w)$ are the Hermite (Hermite, 1864) polynomials.

The Gauss-Hermite moments allow deviations from a pure Gaussian function. Since stellar velocity profiles often deviate from Gaussian functions, this feature can be an advantage. The fitted velocity \hat{v} and velocity dispersion $\hat{\sigma}$ are different and can also differ from the mean v and σ (Bender et al., 1994). The commonly used third and fourth moments, h_3 and h_4 , represent the skew and kurtosis of the velocity profile, respectively.

Gauss-Hermite velocity profiles have been used effectively to break the mass-anisotropy degeneracy. The mass-anisotropy degeneracy appears because the information on the line-of-sight velocity and dispersion is consistent with multiple combinations of potentials and anisotropy profiles for a galaxy. For example, outside the centre of a galaxy a radial anisotropy decreases the velocity dispersion profile of the galaxy. Adding more mass to the gravitational potential, by either increasing the mass-to-light ratio or increasing the amount of dark matter, increases the velocity dispersion profile. The galaxy is therefore consistent with a higher potential and anisotropy, or with a lower potential and lower anisotropy. Both scenarios match the same data (e.g. Gerhard, 1993; Merritt, 1993; Saglia et al., 1997).

Gerhard (1993) concludes that the shape of the velocity profiles, quantifiable by the Gauss-Hermite moments, depends strongly on the anisotropy of the system and less on the stellar density and potential. The shape of the velocity profiles therefore constrains the anisotropy. Using this anisotropy and the velocity dispersion profile then constrains the other possible variables such as the potential.

Planetary Nebulae as Kinematic Tracers

As a star ages it goes through different stages, depending on its mass. Planetary Nebulae are one of the stages for stars that lie in the range between 1 and 8 solar masses, occurring just before they become a white dwarf. The stars that undergo the planetary nebulae phase are at the end of the asymptotic giant branch of the Hertzsprung - Russell diagram. Planetary Nebulae have a strong [OIII] emission line at $\lambda = 5007$ Angstrom (\AA), and therefore can be detected out to distances far away from the galaxy centre where the surface brightness of the galaxy is low. From these planetary nebulae the line-of-sight velocity can be measured out to several R_e .

Galactic matter and potentials

The gravitational potential of a galaxy combines all the different components of matter that are present, which are stellar and gas. In addition, it is theorised that dark matter represents a third component contributing to the potential. The amount of stellar matter present in the galaxy is derived from the luminosity of the galaxy, with a conversion factor known as the mass-to-light ratio (M/L), which determines how much of the light seen is due to matter. The mass-to-light ratio can be obtained using different methods, one using dynamical modelling of the velocity dispersion to find the best fitting potential. Another method is stellar population modelling (e.g. Binney & Merrifield, 1997).

1.3 Collisionless Galaxy Dynamics

Elliptical galaxies can be approximated as gravitationally bound systems of stars that move in a potential created by the gravitational attraction between all stars. The following description of the dynamics of elliptical galaxies is based on Binney & Tremaine (2008) and Gerhard (1994).

From this assumption and the law of gravitational attraction, the virial theorem can be derived. If the assumption of virial equilibrium is made, the virial theorem can be used to define relevant quantities such as the dynamical time, which is defined as the time scale over which the galaxy responds to alterations to the gravitational potential.

The gravitational force of each star acting on every other star can be calculated. However, the system is approximated to be continuous, assuming each star is under the influence of the collective potential of all other stars. This continuous gravitational potential can therefore be related to the density, ρ , of the stars using Poisson's equation:

$$\nabla^2\Phi = 4\pi G\rho \quad (1.6)$$

where Φ is the gravitational potential and G is the gravitational constant.

In order to demonstrate that the galaxy can be described as a continuous system, the velocity perturbation of individual stars on a test star is derived. This yields the relaxation time, which is the time taken for the velocity perturbations on the star to have resulted in the star forgetting its original velocity and orbit. The level of perturbation for one relaxation time is given by the condition that the velocity perturbations equal the original velocity. The velocity perturbations, and therefore relaxation time, are shown to depend on the density of the galaxy.

The density of a galaxy is generally low. Since it varies with radius, a characteristic relaxation time for the whole galaxy is defined using its dynamical time. The dynamical

time depends on the mean velocity and virial radius of a system. The dynamical time is always smaller than the relaxation time, which has several implications. Since very long dynamical times of the order $\sim 10^7$ to 10^8 years are characteristic of elliptical galaxies, typical relaxation times are 10^{15} years, which is longer than the age of the Universe. This implies that current galaxies have not completely forgotten the initial orbits and velocities of the system, thereby allowing us to study the dynamics of a galaxy today to learn about its history. Phase-mixing has erased most of the detailed history while parameters like global shape and anisotropies/rotation still relate to the original state.

Furthermore, as the relaxation time is long, individual star perturbations are small, and the galaxy can be approximated as a phase-space fluid in a mean gravitational field.

Using the fluid assumption, a phase-space distribution function for the galaxy is defined. It can be represented as the quantity $f(\mathbf{x}, \mathbf{v}, t)$, with $f(\mathbf{x}, \mathbf{v}, t) d^3\mathbf{x} d^3\mathbf{v}$ the number of stars with spatial coordinates in the volume $d^3\mathbf{x}$, with velocity $d^3\mathbf{v}$. Projecting the distribution function in phase space we obtain all galaxy observables such as density or kinematics.

The third consequence of being the dynamical time being smaller than the bulk of stellar evolution lifetimes that the number of stars can be taken as being constant with time. The stellar evolution time scale depends on the luminosity of the star, with higher mass stars having a shorter stellar evolution time scale. The assumption of mass conservation leads the collisionless Boltzmann equation (CBE) given by:

$$\frac{df}{dt} = \frac{df}{dt} + \mathbf{v} \cdot \frac{df}{d\mathbf{x}} - \frac{d\Phi}{d\mathbf{x}} \cdot \frac{df}{d\mathbf{v}} = 0, \quad (1.7)$$

where t is time. The CBE gives how the distribution function, f , changes with time, and with position \mathbf{x} and velocity \mathbf{v} , showing that the distribution function does not change along orbits. This condition leads directly into the concept of integrals of motion. The distribution function f is also an integral of motion because it is constant along orbits. Hence f can be written as function of integrals of motion which is called Jeans's theorem.

From Binney & Tremaine (2008) an integral of motion is any function of phase-space coordinates (\mathbf{x}, \mathbf{v}) that is constant along any orbit. There is always six constants of motion in 6-dimensional phase space. If the system is integrable, there are three isolating and three phase integrals. Energy is an integral of motion if the potential is time-independent, and the angular momentum in different directions is an integral of motion depending on the shape of the potential. In a spherical potential all three components of the angular momentum are an integral of motion, while in a system that is only axisymmetric about the z -axis, only the z -component of the angular momentum vector is an integral of motion. This principle of energy and angular momentum as integrals of motion in spherical and axisymmetric system is later used in this thesis to find the distribution functions of the initial particle models, using the method of De Lorenzi et al. (2007).

Stäckel potentials are a specific form of potential in which the Hamiltonian-Jacobi equa-

tion is separable in ellipsoidal coordinates. de Zeeuw et al. (1986) investigates triaxial models with Stäckel potentials, taking advantage of their analytical form to make mass models. The three methods of dynamical modelling that are commonly used are Jeans equations, the Schwarzschild orbit-superposition method, and made-to-measure N-body modelling.

1.3.1 Jeans Modelling

The stellar hydrodynamic equations can be found from the CBE given in Equation 1.7 by taking the velocity moment of the CBE. The Jeans equations result from solving these equations for the velocity moments of different orders, rather than solving for the distribution function f . The moments are defined as:

$$\rho \equiv \int f d^3\mathbf{v}; \quad \bar{v}_i \equiv \int f v_i d^3\mathbf{v}; \quad \overline{v_i v_j} \equiv \int f v_i v_j d^3\mathbf{v}, \quad (1.8)$$

where the density ρ is the zeroth order moment, the first order moment is the streaming velocity \bar{v}_i with i being the Cartesian component of the velocity, and $\overline{v_i v_j}$ is the second moment of the velocity. The zeroth order equation, also known as the continuity equation therefore is:

$$\frac{\partial \rho}{\partial t} + \frac{\partial(\rho \bar{v}_i)}{\partial x_i} = 0 \quad (1.9)$$

and the first moment, also known as the momentum equation:

$$\frac{\partial(\rho \bar{v}_j)}{\partial t} + \frac{\partial(\rho \overline{v_i v_j})}{\partial x_i} + \rho \frac{\partial \Phi}{\partial x_j} = 0. \quad (1.10)$$

The zeroth order equation depends on the first order moment \bar{v}_i , and the first order equation depends on the second moment $\overline{v_i v_j}$. This is true for all moment orders, each moment depending on the moment one order higher. This set of equations can therefore not be closed unless assumptions are made. These assumptions can be illustrated by rewriting the momentum equation using the velocity dispersion tensor:

$$\sigma_{ij}^2 = \overline{(v_i - \bar{v}_i)(v_j - \bar{v}_j)} = \overline{v_i v_j} - \bar{v}_i \bar{v}_j \quad (1.11)$$

with the velocity vector \bar{v}_j and with the continuity equation subtracted to give:

$$\rho \frac{\partial \bar{v}_j}{\partial t} + \rho \bar{v}_i \frac{\partial \bar{v}_j}{\partial x_i} = -\rho \frac{\partial \Phi}{\partial x_j} - \frac{\partial(\rho \sigma_{ij}^2)}{\partial x_i} \quad (1.12)$$

There are several forms of this equation, depending on the assumptions. One type is the spherically symmetric Jeans equation, which assumes that the potential and kinematic properties of the galaxy are spherical. For illustration we take on a spherical geometry,

where the index $i = (r, \theta, \phi)$. In the case of spherical symmetry, streaming motions are assumed to vanish. This results in the first order, as well as all second moments with non-identical indexes, also known as the cross moments, $\overline{v_r v_\theta}$, $\overline{v_r v_\phi}$, and $\overline{v_\theta v_\phi}$, vanishing. This results in the equations:

$$\frac{d\rho\sigma_{rr}^2}{dr} + \frac{\rho}{r}(2\sigma_{rr}^2 - \sigma_{\theta\theta}^2 - \sigma_{\phi\phi}^2) + \rho\frac{d\Phi}{dr} = 0; \quad \sigma_{\theta\theta}^2 = \sigma_{\phi\phi}^2 \quad (1.13)$$

Defining a spherical anisotropy parameter $\beta = 1 - \sigma_{\theta\theta}^2/\sigma_{rr}^2$ and given the density, potential, and anisotropy parameter of a galaxy, the radial velocity dispersion $\sigma_{rr}(r)$ can be estimated. A combination of σ_{rr} and $\sigma_{\theta\theta}$ is integrated along the line-of-sight to obtain the line-of-sight velocity dispersion $\sigma_{\text{LOS}}(r)$, which is the quantity commonly observed for real-galaxies in the sky. This method is applied in Chapter 4 to probe the elliptical galaxy NGC 4278.

Cylindrically symmetric Jeans equations are another form of the Jeans equations, with a different set of assumptions in order to close the set of equations. Here, we use cylindrical geometry, with the index $i = (R, z, \phi)$. The assumption of axial symmetry, $\partial\Phi/\partial\phi = \partial f/\partial\phi = 0$, yields a set of three second-moment Jeans equation in cylindrical notation:

$$\frac{\partial(\rho\overline{v_R^2})}{\partial R} + \frac{\partial(\rho\overline{v_R v_z})}{\partial z} + \rho\left(\frac{\overline{v_R^2} - \overline{v_\phi^2}}{R} + \frac{\partial\phi}{\partial R}\right) = 0 \quad (1.14)$$

$$\frac{\partial(\rho\overline{v_R v_\phi})}{\partial R} + \frac{\partial(\rho\overline{v_\phi v_z})}{dz} + \frac{2\rho\overline{v_R v_\phi}}{R} = 0 \quad (1.15)$$

$$\frac{\partial(\rho\overline{v_R v_\phi})}{\partial R} + \frac{\partial(\rho\overline{v_z^2})}{\partial z} + \frac{\rho\overline{v_R v_z}}{R} + \rho\frac{\partial\Phi}{\partial z} = 0. \quad (1.16)$$

In order to close these six-moment equations, we assume that the only possible streaming motion is in the azimuthal direction ϕ , with $\overline{v_R} = \overline{v_z} = 0$. For the classically used cylindrical Jeans equations, the velocity dispersion tensor is assumed to be meridionally isotropic, with $\sigma_{RR}^2 = \sigma_{zz}^2$. This results in all of the cross moments becoming zero.

Instead of assuming semi-anisotropy, Cappellari (2008) constructs the Jeans Anisotropic Models. Here, the assumption of semi-isotropy is made, with $\overline{v_R^2} = b\overline{v_z^2}$, when b represents a constant anisotropy. In addition, they set $\overline{v_R v_z} = 0$. With these assumptions the Jeans equations take the form:

$$\frac{b\rho\overline{v_z^2} - \rho\overline{v_\phi^2}}{R} + \frac{\partial(b\rho\overline{v_z^2})}{\partial R} + \rho\frac{\partial\Phi}{\partial R} = 0 \quad (1.17)$$

$$\frac{d(\rho\overline{v_z^2})}{dz} + \rho\frac{d\Phi}{dz} = 0. \quad (1.18)$$

These equations determine $\overline{v_\phi^2}$. In order to separate this relation into $\sigma_{\phi\phi}$ and $\overline{v_\phi}$, additional

steps and assumptions need to be applied. Cappellari (2008) uses the equation

$$[\overline{v_\phi}]_k = \kappa_k \left([\overline{v_\phi^2}]_k - [\overline{v_R^2}]_k \right)^{1/2}, \quad (1.19)$$

where the index k represents summation over Gaussian functions on which the moments are calculated. The constant κ defines how similar the system is to an isotropic rotator with $\kappa = 1$. When the anisotropy parameter $b = 1$ then κ is identical to the parameterisation of Satoh (1980).

The use of the Jeans equations comes with some caveats. The Jeans equations are moments of the CBE. Therefore, if a distribution function is valid for a stellar system, it must satisfy the Jeans equations. In this regard, the Jeans equations could be used to discard distribution functions that do not describe the stellar system. However, as the Jeans equations are an open system, which is closed using different assumptions on the form of the velocity dispersion tensor and the symmetry of the stellar system, the moments resulting from equations such as the spherical, cylindrical, or semi-isotropic Jeans equations do not necessarily correspond to a real physical distribution function. In addition, the solution is not unique, and several distribution functions may fit a set of moments.

Further effects of these assumptions can be more easily illustrated using the concept of the velocity dispersion tensor ellipsoid. This ellipsoid has its principal axis defined by diagonalising the velocity dispersion tensor σ_{ii}^2 . Its shape and alignment are described by the components of the tensor, σ_R^2 , σ_z^2 , $\overline{v_R v_z}$, and by σ_r^2 , σ_θ^2 , $\overline{v_r v_\theta}$ in spherical coordinates. The general equation of the orientation of the velocity ellipsoid is:

$$\tan 2\alpha_c = \frac{2\overline{v_i v_j}}{v_{ii}^2 - v_{jj}^2} \quad (1.20)$$

and the axis ratio is given by:

$$q_c^2 = \frac{\overline{v_{ii}^2} + \overline{v_{jj}^2} - \sqrt{(\overline{v_{ii}^2} - \overline{v_{jj}^2})^2 + 4\overline{v_i v_j}^2}}{\overline{v_{ii}^2} + \overline{v_{ii}^2} + \sqrt{(\overline{v_{ii}^2} - \overline{v_{jj}^2})^2 + 4\overline{v_i v_j}^2}}, \quad (1.21)$$

where in cylindrical coordinates $i = R$ and $j = z$, while in spherical coordinates i, j refer to r and θ . These equations show that the assumption $\overline{v_R v_z} = 0$ on the cross term alters the axis ratio of the ellipses and the alignment of the ellipses to always have a value of $\alpha_c = 0^\circ$ in the cylindrical regime.

1.3.2 N-body modelling

NMAGIC is an N-body made-to-measure code fully described in De Lorenzi et al. (2007). It is based on the made-to-measure method of Syer & Tremaine (1996), incorporating

observational errors in order to match the photometric and kinematic data of the modelled galaxies. N-body modelling uses a set of particles, each with their own mass, to sample the phase-space of the galaxy and thereby model the galaxy.

NMAGIC has been applied to a variety of galaxies and problems, such as modelling of the intermediate-luminosity elliptical galaxies NGC 3379, NGC 4697 and NGC 4494 as performed in De Lorenzi et al. (2009), De Lorenzi et al. (2008) and Morganti et al. (2013) respectively. In Das et al. (2011) the massive elliptical galaxy NGC 4649 is modelled, and the Milky Way is modelled in Portail et al. (2015a), Portail et al. (2015b), and Portail et al. (2017a). The Hercules stream of the Milky Way is analysed through NMAGIC modelling in Pérez-Villegas et al. (2017). NMAGIC was extended to allow chemodynamical modelling of the Milky Way in Portail et al. (2017b). Furthermore, Blaña Díaz et al. (2018) uses NMAGIC to model M31 using stellar kinematics from Opitsch (2016) and Opitsch et al. (2017). In this thesis we use it to investigate JAM models in elliptical galaxies in Chapter 2 and make triaxial elliptical galaxy models in Chapter 3.

The N-body models are approximate solutions to the CBE, as with each change of the particles the gravitational field also changes. However, since it is possible to make the time increments small and therefore any change in the gravitational field very small, this represents a good approximation. The distribution function in a N-body model can be approximated using particles of weight w_i where i are the individual particles. The distribution function is then modelled as:

$$f \approx \sum_{i=1}^N w_i f_i, \quad (1.22)$$

where w_i are the weights of the particles, N the number of particles, and f_i is the distribution function of the particle,

$$f_i(\mathbf{x}, \mathbf{v}, t) = \partial(\mathbf{x} - \mathbf{x}_i(t)) \times \partial(\mathbf{v} - \mathbf{v}_i(t)) \quad (1.23)$$

with \mathbf{x}_i being the position of the particle i at time t and \mathbf{v}_i its velocity. For each particle the position coordinates \mathbf{x}_i and the velocities \mathbf{v}_i are known in all three dimensions. The gravitational field generated by these particles can be calculated using a potential solver directly from the particles. This is referred to as the self-consistent potential. The particles can also be placed in an externally parameterised gravitational potential. The model is propagated in time by integrating the second law of motion for a small time step dt . In order to fit the observables, the weights of the particles can also be changed slowly over time. This is done by maximising a profit function F , which is obtained by changing particle weights w_i over time:

$$\frac{dw_i}{dt} = \epsilon w_i \frac{\partial F}{\partial w_i} \quad (1.24)$$

where ϵ is a parameter setting the typical time-scale of the weight evolution. For observables

the profit function is given generally by:

$$F = -\frac{1}{2} \sum_{jk} (\Delta_j^k)^2 = -\frac{1}{2} \sum_{jk} \left(\frac{y_j^k - Y_j^k}{\sigma(Y_j^k)} \right)^2, \quad (1.25)$$

where y_j^k is the j th observable from the model of data set k , Y_j^k represents the observed data of data set k , and $\sigma(Y_j^k)$ are the uncertainties associated to the data of data set k . The model is evolved such that the difference between the model and the data is minimised relative to the uncertainties on the data.

Any observable of a distribution function can be written as:

$$y_j = \int K_j(\mathbf{x}, \mathbf{v}) f(\mathbf{x}, \mathbf{v}) d^3\mathbf{x} d^3\mathbf{v}, \quad (1.26)$$

where K_j is the kernel of the observable. Rewriting this for a particle model:

$$y_i(t) = \sum_{i=1}^N w_i K_j(\mathbf{x}_i(t), \mathbf{v}_i(t)), \quad (1.27)$$

where N is the number of particles. The total weight of the particles $w_{tot} = 1$. Within NMAGIC an additional entropy term is used for the profit function. The entropy term ensures that the particle weights do not deviate too much from a set of pre-defined priors \hat{w}_i , preventing issues such as very large particles or particles becoming 0 if this is desired. The entropy term S is added into the profit function as:

$$F = \mu S - \frac{1}{2} \sum_{jk} (\Delta_j^k)^2, \quad (1.28)$$

where μ governs the relative strength of the entropy term S in the equation. When μ is large, then the model will stay close to the priors \hat{w}_i , with a smooth distribution function. If the μ term is too small, the model will be very noisy, with very large particles, while if μ is too large the particle weights cannot change sufficiently to model the data. The entropy can be defined in several different ways, but the standard parameterisation is as follows:

$$S = - \sum_i w_i \ln(w_i / \hat{w}_i). \quad (1.29)$$

The derivative of the entropy term in the profit function is therefore:

$$\mu \frac{dS}{dw_i} = -\mu(\ln(w_i / \hat{w}_i) + 1), \quad (1.30)$$

from which it can be seen that this is a curve peaking at \hat{w}_i/e , with a positive gradient if the particle weight is $w_i < \hat{w}_i/e$ and a negative gradient when $w_i > \hat{w}_i/e$, with the curve having an asymptotic limit at 0. This definition of the observable $y_i(t)$ and profit function

F with entropy can be used to rewrite Equation 1.24 in order to obtain the force-of-change equation (FOC) for a particle model:

$$\frac{dw_i(t)}{dt} = \epsilon w_i(t) \left(\mu \frac{\partial S}{\partial w_i}(t) - \sum_{jk} \frac{K_j(\mathbf{x}_i(t), \mathbf{v}_i(t))}{\sigma(Y_j^k)} \Delta_j^k(t) \right). \quad (1.31)$$

The assumption in the transition between Equations 1.24 and 1.31 is that the kernel K_j does not depend on the weight of the particles. This force-of-change equation has the particle weights converge when F is maximised with respect to all particle weights w_i .

When dealing with multiple data sets it can have some advantages to weight their contributions to the force-of-change equation differently. Although the force-of-change already takes into account the observational errors, there are instances where the observational errors between data sets vary widely. In practice, this results in one data set being matched well by the model and the other not at all. One cause of this issue, occurring Portail (2016)'s Milky Way model is a large difference in number of constraints, in this particular case having 26880 density data constraints and 164 kinematic data points. Another reason for this that arose particularly in the course of this work, discussed in more detail in Section 2.3, is when tension exists between two different observables. By varying the contribution to the force-of-change equation from each observable different models can be achieved. This is done by altering the force-of-change equation:

$$\frac{dw_i(t)}{dt} = \epsilon w_i(t) \left(\mu \frac{dS}{dw_i}(t) - \sum_k \gamma_k \sum_j \frac{K_j(\mathbf{x}_i(t), \mathbf{v}_i(t))}{\sigma(Y_j^k)} \Delta_j^k(t) \right) \quad (1.32)$$

such that γ_k represents a numerical weight on different data sets, based on the method of Long & Mao (2010).

Spherical Harmonics

Spherical harmonics are used in two places in this thesis. One is in the potential solver, which is the spherical harmonics solver from De Lorenzi et al. (2007). The second place is in the density observable. In order to fit the density observable for different galaxies the photometry is deprojected into the 3D density and then expanded upon spherical harmonics which are fit inside NMAGIC. We have chosen to model a spherical harmonics expansion of the deprojected luminosity density. The spherical harmonics has expansion coefficients A_{lm} , with a 1D radial grid r_k , with all of the expansion coefficients together describing the shape of the galaxy. The spherical harmonics are given by:

$$a_{lm,k} = L \sum_i \gamma_{ki}^{CIC} Y_l^m(\theta_i, \phi_i) w_i, \quad (1.33)$$

where L is the luminosity of the galaxy, Y_l^m the spherical harmonics functions, and γ_{ki}^{CIC} a cloud-in-cell selection function as in De Lorenzi et al. (2007). When expressing a 3D

density in spherical harmonic form, the number of radial bins, n_r , as well as l and m has to be chosen.

1.3.3 Schwarzschild Modelling

The Schwarzschild method superimposes orbits in order to find self-consistent solutions to the CBE (Schwarzschild, 1979, 1982). The Schwarzschild technique has the distribution defined as in N-body modelling by Equation 1.22, except that instead of w_i and f_i representing each particle, they represent the orbits instead. Following from this equation, and the orbital phase-space projection of any observable, such as in Equation 1.8, any observable can be written as a linear superposition of orbits.

Schwarzschild modelling uses a density and gravitational potential to integrate a library of orbits. The orbits are superimposed and the observables of the resulting distribution function are compared to the data observables. The procedure is repeated with different densities and potentials to minimise the value of χ^2 .

There are different ways to choose the initial conditions of the orbits used, known as orbit sampling techniques. As with previous methods, a Schwarzschild model must fulfil the conditions that it is collisionless and in equilibrium. Additionally, in order to ease implementation, spherical symmetry or axisymmetry may be assumed.

1.4 Velocity Ellipsoids of Elliptical Galaxies

1.4.1 Results from Schwarzschild Modelling

Levison & Richstone (1985a) construct Schwarzschild models of flattened oblate galaxies. Their analysis breaks their models into two different types of galaxies, those whose oblate structure are supported primarily by anisotropy of the velocity dispersions and those whose structure are supported by rotation. The models that are supported primarily by anisotropy, with very low L_z , have cylindrically aligned velocity ellipsoids. The models that are supported primarily by rotation, with maximal L_z , have the minor axis of the velocity ellipsoid aligned spherically.

The models with intermediate L_z are further divided into two classes, models with maximal \bar{v}_Φ and models with minimal \bar{v}_Φ . Maximal \bar{v}_Φ models are aligned in the same way as maximal L_z models except for the region close to the major axis, where they are spherically aligned. Minimal \bar{v}_Φ models are aligned almost cylindrically along the minor axis, and in the rest of the model close to spherically. Levison & Richstone (1985a) also

show that the tilt of the velocity ellipsoid is independent of the M/L ratio being constant or changing with radius.

Levison & Richstone (1985b) expand on the study in Levison & Richstone (1985a) by constructing models which have the velocity moments of real galaxies. The models have velocity ellipsoid alignments similar to either of the intermediate L_z models in the previously discussed papers.

1.4.2 Velocity Ellipsoid in the Milky Way

There have been several studies of probing the velocity ellipsoid of the Milky Way and its connection to the shape of the potential. In a theoretical approach, Smith et al. (2009) states that spherical alignment of the velocity dispersion tensor has been known since Eddington (1915) and Chandrasekhar (1939), and applied first by Lynden-Bell (1962). Lynden-Bell (1962) states the theorem that a triaxial velocity dispersion tensor, which is spherically aligned everywhere, implies that the potential must be spherically symmetric. Smith et al. (2009) modifies this theorem, stating that if the potential is non-singular, only one of the non-degenerate eigenvectors of the velocity dispersion tensor must be aligned radially everywhere in order to have a spherically symmetric potential. Several of these studies measure the deviation of the velocity ellipsoid from a spherical alignment. One such study is Bond et al. (2010), using SDSS, which finds that the velocity ellipsoid is aligned in spherical coordinates with little variations, ranging between 1 and 5° and the shape invariant. Evans et al. (2016) reanalyses the data set from Bond et al. (2010), ruling out a cylindrical alignment of the velocity ellipsoid in the Milky Way, and showing a general alignment with spherical coordinates. Building on the work in Smith et al. (2009), they show that a spherically aligned system would lead to a separable or Stäckel potential. Solving the Hamiltonian in the case of cylindrical alignment, they find that triaxial velocity ellipsoids are only possible when the potential is non-separable, and giving a density profile which is stratified in layers of z . Evans et al. (2016) states that if the velocity ellipsoid is aligned in cylindrical polar coordinates, then the potential must be separable in cylindrical polar coordinates, which is generally not the case in elliptical galaxies. This could be possible if higher-moments of the distribution function are non-zero. They also test the alignment of the velocity ellipsoid in the Milky Way using an N-body Syer Method. They find that outside the stellar halo the misalignments from spherical alignment are $\lesssim 6^\circ$. Inside the stellar halo this is also generally true, with a few regions of larger misalignment.

The result of the spherical alignment of the Milky Way velocity ellipsoids is found by several different methods. In Smith et al. (2009) the tilt of the velocity ellipsoid in a sample of 1800 halo subdwarfs in a $\sim 250 \text{ deg}^2$ field is used to probe the shape of the Milky Way's potential. The subdwarfs used are at a distance where the halo dominates the potential. They find only a small deviation from the spherical alignment, with a tilt

angle $\alpha_{r\theta} = 3.4^\circ \pm 1.3^\circ$. Since in a perfectly spherical potential, the spherical tilt angle and spherical cross term would become zero, this implies a deviation from a spherical halo. This deviation can be explained by the presence of the bulge and the disk, with the dominant difference coming from the disk.

Büdenbender et al. (2015) calculates the tilt angle of the velocity ellipsoid in the Milky Way from G-type dwarf stars in the solar neighbourhood and finds some deviation from the spherical alignment, which increases with galaxy height. This is done for several metallicity bins, and the tilt angle found is found to be consistent within the error bars between the bins. From this they construct a relation of tilt angle with height, which remains close to, but slightly deviates from spherical alignment. Büdenbender et al. (2015) goes on to construct vertical Jeans models, with the assumption that there is no tilt to the velocity ellipsoid, and that the radial and vertical motions can be decoupled.

The Jeans models are made for two different metallicity sub-samples in the galaxy. Although these are different populations, in equilibrium they should both trace the same potential. However, Büdenbender et al. (2015) find a discrepancy between the best fitting local matter density found by the Jeans models of the two populations. This discrepancy can be explained by the assumption that the velocity ellipsoid is perfectly spherically aligned. In reality this assumption is false and there is some correlation between the radial and vertical motions in the galaxy. Binney et al. (2014) analyse a sample of stars within ~ 2 kpc of the Sun, and fit velocity ellipsoids to four different classes of stars within that sample. Comparing the fitted velocity ellipsoids to Jeans-based dynamical models used for predicting axisymmetric potentials (Binney, 2012) leads them to conclude that a maximal disk gravitational potential describes the Milky Way well.

1.4.3 The JAM method

Jeans Anisotropic Modelling (JAM) solves the axisymmetric Jeans equations using the assumption of a cylindrically aligned velocity ellipsoid with $\sigma_R \neq \sigma_z \neq \sigma_\phi$. The JAM equations first calculate the second velocity moment, $v_{rms} = \sqrt{v^2 + \sigma^2}$, and then separate random motion, or rotation v and ordered motion, or velocity dispersion, σ .

The multi-Gaussian expansion (MGE) is a way of parameterising the surface brightness of the galaxy using the sum of two-dimensional Gaussians, in the case of a two dimensional surface brightness profile. The MGE formalism can be used to deproject the projected surface brightness found from fitting a galaxy image into the 3-D intrinsic density profile, assuming the inclination of the galaxy. The JAM equations are written using the MGE formalism for the density and other density derived quantities. The MGE formalism can be used for both real and simulated data. Li et al. (2016) found by using data from cosmological simulation that the resolution of the MGE greatly affects their results. They find an increase from 5% to 19% error in recovering stellar mass when changing their

resolution from 0.5 to 2 kpc h^{-1} .

1.4.4 Applications of JAM

The Jeans Anisotropic Modelling method has been applied to a wide variety of scientific problems. Cappellari et al. (2015) use the method to investigate the mass profiles of early-type galaxies, using both ATLAS^{3D} Integral Field Unit kinematic data and SLUGGS globular cluster data out to up to $4R_e$ for a sample of 14 galaxies. Their sample is selected to be axisymmetric fast rotators. It is the first paper that studies the mass profiles of elliptical galaxies as part of a larger, homogeneously analysed, sample, and concludes that the total density profiles of the entire sample are isothermal with $\rho_{\text{total}} \propto r^{-2}$ where r is galactic radius. They find that the stellar-only density profiles fall off more steeply with radius, with a slope of $\rho_{\text{stars}} \propto r^{-3}$ at 4 effective radii. Constraining the shape of the total density is a significant result, and can provide constraints on cosmological models.

Another major result which used the JAM method is from Cappellari et al. (2012), which found by analysing the ATLAS^{3D} sample of 260 early-type galaxies that there is a systematic variation of the initial mass function with mass-to-light ratio. Several other important applications are shown in Cappellari et al. (2009) which uses the technique to find the black hole mass of Centaurus A, which is in good agreement with the previous results of the black hole mass using gas kinematics in Neumayer et al. (2007). They also find the orbital anisotropy of Centaurus A using the spherical Jeans method.

1.4.5 Tests of the JAM method

The JAM method makes several assumptions, therefore it is useful to know how well it represents the galaxies it models and the galaxy characteristics it is used to recover. One study done on the recovery of galaxy characteristics is done using Illustris in Li et al. (2016). They take 1413 galaxies from the Illustris simulation and perform JAM fits on them, with the aim of recovering matter composition, anisotropy and galaxy shape. They test both their own simulations and the JAM method. For example, some of the difficulties in recovering M/L are said to be down to insufficient resolution of the density of the simulated galaxies.

On the other hand, their findings regarding the JAM method are that within $2.5 R_e$ the JAM model finds the total mass distribution for galaxies with 10% accuracy and for prolate galaxies with 18%. This is compared to the Schwarzschild method of Thomas et al. (2007) which recovers oblate galaxies total masses at 3% and 20% for oblate and prolate respectively. Both Thomas et al. (2007) and Li et al. (2016) are unable to accurately separate their total mass estimate into a dark matter and stellar matter component, with

Thomas et al. (2007) underestimating stellar mass and Li et al. (2016) both over and underestimating stellar masses for different galaxies and shapes. The oblate shape does not display a trend, but both prolate and triaxial galaxies do. Stellar mass is overestimated by an average of 18%, while dark matter masses are underestimated by an average of 22%. Li et al. (2016) find that the accuracy of parameter recovery depends on the inclination, with galaxies with inclinations lower than 60° having high errors in the inclination and anisotropy recovery. For galaxies the inclination accuracy is 5° , with 2° bias, and the error in the z -anisotropy is 0.11 with a bias of -0.02 . El-Badry et al. (2017) investigates the accuracy of Jeans modelling in low mass galaxies, with stellar masses less than $10^{9.5}M_\odot$. They find that stellar feedback effects can cause short-term fluctuations in the potential of the low mass galaxies, which can lead to dynamical masses having errors of $\sim 20\%$.

Lablanche et al. (2012) test applying the axisymmetric JAM to barred galaxies, which are not axisymmetric. They do not include dark matter in their study. Similarly to Cappellari (2008) they find an anisotropy offset. The z -anisotropy recovered is found to have a systematically lower anisotropy of $\beta_z = 0.05$.

These studies motivate a more thorough study of the velocity ellipsoid alignment and the effect of assuming it is cylindrical. These previous studies have focused on the how well the JAM models recover galaxy characteristics such as M/L and anisotropy. While we do also investigate this in this thesis, we also study the JAMs by directly constructing JAM-like orbit distributions. This investigation is presented in Chapter 2. In Chapter 3 we construct triaxial elliptical galaxy models using NMAGIC and model the galaxy M87. In Chapter 4 we use planetary nebulae kinematics and the spherical Jeans equation in order to analyse the distinct kinematic components and dark matter in elliptical galaxy NGC 4278.

Chapter 2

Velocity Ellipsoids in Elliptical Galaxies

This chapter is based on Söldner-Rembold & Gerhard (2018), in prep.

Abstract Context: Jeans Anisotropic Models (JAMs) are widely used to study the dynamical structure of early-type galaxies (ETGs). Aims: We study here whether JAMs have physical orbits distribution functions, and whether they correctly recover ETG properties. Method: We use the NMAGIC Made-to-Measure Modelling approach and ATLAS^{3D} and SLUGGS kinematic data to construct dynamical models for two fast rotator ETGs, NGC 4660 and NGC 4697. We compare these with models that instead, or additionally, enforce cylindrically aligned Velocity Ellipsoids (caVEs, $\langle v_R v_z \rangle = 0$) as assumed in JAMs. Results: Dynamical models are found which provide excellent fits to the kinematic data for both galaxies. However, these models do not have caVEs over the majority of the meridional plane. No solutions are found with constant z-anisotropy and caVEs; such models may not be physical. The only models with real orbit distribution functions and $\langle v_R v_z \rangle = 0$ are found to be isotropic (so the VE orientation is irrelevant) apart from small regions around the major axis. How well models with $\langle v_R v_z \rangle = 0$ fit a galaxy is therefore dependent on its similarity to an isotropic dynamical structure. We also look for models that fit the kinematic data approximately and are not far from caVEs. These models and near-isotropic $\langle v_R v_z \rangle = 0$ models have mass-to-light ratios (M/L) that are higher by only 5% and 10%, respectively, than for kinematics-driven models. We also apply the different classes of models to a sequence of dark matter halos for NGC 4697. We find that an intermediate dark matter halo reproduces the kinematic data well to the limit of the SLUGGS data at $1.5 R_e$ when the alignment of VEs is left unconstrained. Whilst JAM-constrained models all fit the data best for no dark matter halo in the galaxy. Conclusions: Our results suggest that the only JAM models with physical distribution functions are nearly merid-

ionally isotropic, and that JAM models with constant $\beta_z \neq 0$ are unphysical. JAMs are nonetheless useful to estimate approximate M/L ratios for ETGs. However, relative best-fit comparisons between JAM models in different potentials to infer dark matter profiles or IMF variations may be unreliable and need to be verified by dynamical models with unconstrained VEs.

2.1 Introduction

Dynamical modelling is an important tool to understand the structure of galaxies and their properties, such as mass and kinematic structure, assuming dynamical equilibrium. Models finding the orbit distributions of stars, implicitly making use of Jeans theorem, include distribution functions over integrals or actions, Schwarzschild orbit superposition models, and made-to-measure particle models (Binney & Tremaine, 2008). These methods are quite involved and therefore often make assumptions about the structure of the galaxies, such as spherical or axial symmetry, but Schwarzschild and M2M models can handle triaxial systems and even rotating bars, even if at considerable computational cost (Dehnen, 2009; van den Bosch & de Zeeuw, 2010; Portail et al., 2015a).

Models based on solving the Jeans moment equations are generally much faster and therefore well-suited to model large samples of galaxies. Jeans equation models always make assumptions about the structure of the galaxies, their spatial symmetry as well as their kinematic structure. Frequently used are the Jeans Anisotropic (JAM) Models, which assume the alignment of the velocity ellipsoids in cylindrical coordinates (Cappellari, 2008). In recent galaxy surveys the method has been used to show that the velocity and velocity dispersion of the galaxies are well represented by the JAM models, and indicating that total density profiles are tightly constrained and close to isothermal (Cappellari et al., 2015). Using JAM models on two-dimensional stellar kinematics data, such as ATLAS^{3D}, also allow us to constrain the dark matter halo profiles or even the systematic variation of the stellar initial mass function (IMF) (See Cappellari, 2016, for a review).. JAM models are also used to interpret the SAMI (Scott et al., 2015), and MaNGA (Li et al., 2018) surveys.

The main advantage of JAM models is that they are simple to solve, due to assumption that the velocity ellipsoids of the JAM models are aligned cylindrically in the meridional plane, illustrated On Figure 2.1. The alignment of the velocity ellipsoid is governed by the cross term $\langle v_R v_z \rangle$, and for a cylindrically aligned system $\langle v_R v_z \rangle = 0$. The anisotropy in the meridional plane is parametrised in terms of the velocity dispersion in (R, z, Φ) cylindrical coordinates, $\beta_z = 1 - \sigma_z^2 / \sigma_R^2$.

However, it remains to be verified that JAM models are physical, i.e., they have underlying physical and positive orbit distribution functions. An example that illustrates that this

is not guaranteed are the Stäckel potentials which have a fixed velocity ellipsoid (Eddington, 1915). In general, the shape of the velocity ellipsoid can be influenced by the distribution function but only in a limited way (Dehnen & Gerhard, 1993; Dejonghe & de Zeeuw, 1988).

This suggests that under certain circumstances the cylindrically aligned velocity ellipsoid is unphysical (see also Binney, 2014). The theorem by Evans et al. (2016) states that if the velocity ellipsoid is aligned in cylindrical polar coordinates, then the potential must be separable in cylindrical polars. Such potentials are unlike those in elliptical galaxies. This makes it unlikely that JAM models are physical, unless the odd higher-order moments of the distribution function do not all vanish. In this Chapter, we address with direct reconstruction of the orbit distribution whether cylindrically aligned velocity ellipsoids are physical for the potentials of real early-type galaxies.

There have been previous studies focusing on the effectiveness of the JAM technique in recovering galaxy characteristics. The original JAM paper by Cappellari (2008) finds that Schwarzschild models of near-edge-on galaxies obtain anisotropies $\Delta\beta_z = 0.05$ larger than the JAM models fitted to the same data, thought to be due to the constant z-anisotropy assumed by the JAM models at intermediate latitudes. $\delta\beta_z$ is the difference between the β_z of the JAM models and β_z of the Schwarzschild models. Lablanche et al. (2012) probe the accuracy with which the JAM technique recovers mass-to-light ratios and anisotropies of simulated barred galaxies. Li et al. (2016) fit JAM models to 1413 galaxies from the Illustris simulation to test how well the mass-to-light ratio, dark matter decomposition, and anisotropy are recovered. They find that the total galaxy mass within $2.5 R_e$ is constrained with 10% accuracy but the decomposition into dark matter and stellar matter has errors of $\sim 30 - 40\%$. Mass-to-light ratios for oblate galaxies are on average unbiased but are overestimated for prolate galaxies by 18%.

Here we study the orbit distribution functions of JAM models for the two fast-rotator galaxies, NGC 4660 and NGC 4697. We use galaxy potentials rather than simple model potentials because of the apparent similarity of Schwarzschild models for some galaxies to the dynamical structure of JAM models, and also to test some results on ETG dark matter halos found with JAMs. We concentrate on fast rotating galaxies because their inner parts are believed to be axisymmetric (Cappellari, 2016; Pulsoni et al., 2017), while slow rotating galaxies are triaxial and therefore not consistent with the JAM assumptions. For analysing both galaxies we use the NMAGIC M2M particle methods to fit orbit distribution to the combined photometric and kinematic constraints (De Lorenzi et al., 2007, 2008, 2009). With this method it is easy to enforce JAM model constraints for the velocity ellipsoids, which allows us to test the consistency of the observed velocity fields with the JAM assumptions. We use the ATLAS^{3D} kinematic data, and for NGC 4697 also the SLUGGS data, as constraints on our NMAGIC particle models. This has the advantage that Gauss-Hermite moments of the data are known so that the model of the data will have no assumed parametrisations which might bias the outcome. With the NMAGIC particle method we can additionally enforce the JAM model constraint on the velocity ellipsoids.

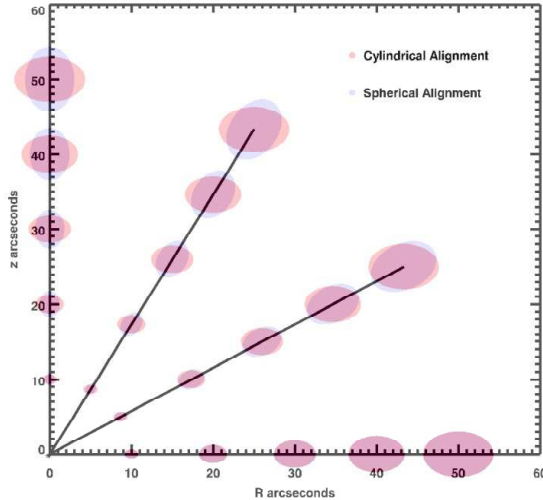


Figure 2.1: A diagram illustrating cylindrically (red) and spherically (blue) aligned velocity ellipsoids in the meridional plane. This diagram shows that along the major axis the cylindrical and spherically aligned ellipsoids are identical. On the intermediate and minor axis they are however misaligned.

This Chapter is organised as follows: Section 2.2 details the sample selection, and photometric and kinematic data used, Section 2.3 determines the NMAGIC modelling process, and Sections 2.4 and 2.5 presents our results, Section 2.6 discusses the attempt of NMAGIC models using negative particle weights. Finally, Section 2.8 gives a summary of results and our conclusions.

Elliptical galaxies can be approximated as systems of stars in which each star is under the influence of the collective potential of all other stars, the dark matter, and a small amount of gas. The dynamics of the stars is described by the collisionless Boltzmann equation (CBE) which states that the distribution function does not change along orbits. In dynamical equilibrium, f can be written as a function of the integrals of motion, or more generally, of the stellar orbits, and can be recovered from the measured stellar density and kinematics, e.g., by Schwarzschild’s method. A simpler method is to use Jeans equation to relate the stellar density and gravitational potential to the velocity moments of f .

To solve these moment equations requires making assumptions by which the system of equations can be closed at low order. In the cylindrically symmetric case, the only possible streaming motion is in the azimuthal direction, ϕ , with $\overline{v_R} = \overline{v_z} = 0$. For the classical semi-isotropic solution of the cylindrical Jeans equations, the velocity dispersion tensor is assumed to be meridionally isotropic, $\sigma_{RR}^2 = \sigma_{zz}^2$. Cappellari (2008) generalize this approach with the so-called Jeans Anisotropic Models (JAMS), for which it is assumed

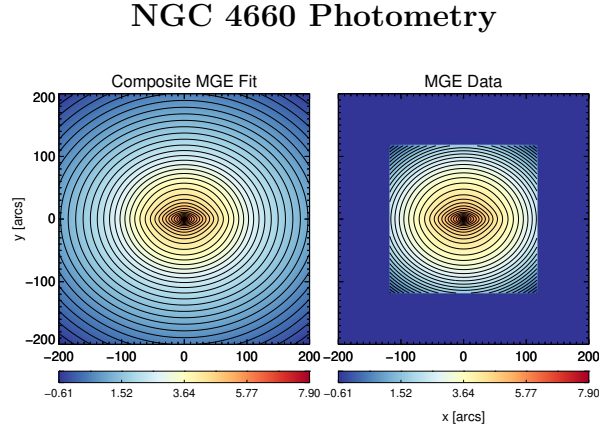


Figure 2.2: Left: The MGE fit to the Composite image. The Composite image consists of the Scott et al. (2013) MGE data in the centre, and an extension using a double-component Sérsic profile with inner index $n'_s = 1.0$ and outer index $n_s = 1.88$. The MGE fit to Composite image plotted here has a $\chi^2 = 1.71$. Right: The original MGE data from Scott et al. (2013). The colour scale is in units $\text{Log}_{10} L_{\odot,r}$ in each pixel. The contours are in steps of 0.5 mag/arcsec^2 . The largest Gaussian of this data has a dispersion of $39''$.

that the cross term $\overline{v_R v_z} = 0$ and $\overline{v_R^2} = b \overline{v_z^2}$, where b is a constant anisotropy. With these assumptions the Jeans equations take the form:

$$\frac{b \overline{\rho v_z^2} - \overline{\rho v_\phi^2}}{R} + \frac{\partial(b \overline{\rho v_z^2})}{\partial R} + \rho \frac{\partial \Phi}{\partial R} = 0 \quad (2.1)$$

$$\frac{\partial(\overline{\rho v_z^2})}{\partial z} + \rho \frac{\partial \Phi}{\partial z} = 0. \quad (2.2)$$

The above equations determine $\overline{v_\phi^2}$, but in order to separate this into $\sigma_{\phi\phi}$ and v_ϕ , additional steps and assumptions need to be applied. Cappellari (2008) uses the equation

$$[\overline{v_\phi}] = \kappa_k \left([\overline{v_\phi^2}] - [\overline{v_R^2}] \right)^{1/2}, \quad (2.3)$$

where κ is a constant, κ and b define how similar the system is to an isotropic rotator, for which the anisotropy parameter $b = 1$. Then, κ is identical to the parameterisation of Satoh (1980).

These assumptions on the velocity dispersion tensor made for JAMS can be illustrated by the concept of the velocity ellipsoid, whose shape and alignment are described by the components of the tensor $\langle \sigma_R^2 \rangle$, $\langle \sigma_z^2 \rangle$, $\langle v_R v_z \rangle$, or by $\langle \sigma_r^2 \rangle$, $\langle \sigma_\theta^2 \rangle$, $\langle v_r v_\theta \rangle$ in spherical coordinates. The general equation for the orientation of the velocity ellipsoid is:

$$\tan 2\alpha_c = \frac{2 \langle v_i v_j \rangle}{\langle v_{ii}^2 \rangle - \langle v_{jj}^2 \rangle} \quad (2.4)$$

and the axis ratio is given by:

$$q_c^2 = \frac{\langle v_{ii}^2 \rangle + \langle v_{jj}^2 \rangle - \sqrt{(\langle v_{ii}^2 \rangle - \langle v_{jj}^2 \rangle)^2 + 4\langle v_i v_j \rangle^2}}{\langle v_{ii}^2 \rangle + \langle v_{jj}^2 \rangle + \sqrt{(\langle v_{ii}^2 \rangle - \langle v_{jj}^2 \rangle)^2 + 4\langle v_i v_j \rangle^2}} \quad (2.5)$$

where in cylindrical coordinates i is R and j is z , while in spherical coordinates i, j refer to r and θ . In the case of the JAMS, the two assumptions made in order to close the equations are a cylindrically aligned velocity ellipsoid $\langle v_{Rv_z} \rangle = 0$ and a z anisotropy parametrised as $\beta_z = 1 - \sigma_z^2/\sigma_R^2$. Figure 2.1 illustrates cylindrically and spherically aligned velocity ellipsoids in the meridional plane. From this it can be seen that on the major axis the cylindrical and spherical anisotropies are identical.

However, on the minor axis, positive anisotropy in cylindrical alignment corresponds to negative anisotropy ($\beta_r < 0$, where $\beta_r = 1 - \sigma_\theta^2/\sigma_\theta^2$) in spherical alignment, while on intermediate axes changing the value of the anisotropy cannot align the velocity ellipsoids. For spherical models, deviation from cylindrical alignment is therefore seen most prominently close to the $\theta = 45^\circ$ angle in the meridional plane. In this paper, rather than giving the $\langle v_{Rv_z} \rangle$ term for our models, we use the more physically meaningful normalized cross term $c_{R,z}$ defined as:

$$c_{R,z} = \frac{\langle v_{Rv_z} \rangle}{\sigma_R \sigma_z}. \quad (2.6)$$

2.2 Data

2.2.1 Choice of Target Galaxies

Fast rotators comprise the majority of the ATLAS^{3D} sample, so we therefore chose NGC 4660 and NGC 4697 which are both fast rotators in that sample. The two galaxies chosen are quite different in their dynamical structure and in the extent to which they are constrained by the IFU data, therefore our results will be more widely applicable because not due to particular features of a single galaxy. NGC 4660 is chosen because it is a small galaxy (effective radius of $R_e = 12.1''$) so a large part of the model is constrained by the ATLAS^{3D} velocity field, around $3 R_e$. This is an advantage in comparison to galaxies where only the central part of the galaxy is covered, as particles on orbits with a large radial range can be constrained with kinematic data for the entire orbit. NGC 4697 is chosen as a contrast, a galaxy with effective radius $R_e = 96.4''$, where only $1/3 R_e$ is kinematically constrained, and the orbits should have relative freedom.

Both galaxies are nearly edge on and flattened. Li et al. (2016) have found the accuracy of parameter recovery in their JAM model tests depends on the inclination, with galaxies

with inclinations lower than 60° having high errors in the inclination and anisotropy recovery. For NGC 4660 the inclination is 67° given by the JAM fit from Cappellari (2008) and for NGC 4697 the inclination is 80° and defined by the nuclear dust lane along the major axis (Dejonghe et al., 1996; De Lorenzi et al., 2008). The inclinations being well-known minimises the degeneracy associated with the modelling.

NGC 4697 is a galaxy of luminosity $2.31 \times 10^{10} L_{\odot,r}$ (Cappellari et al., 2013a), with an effective radius $R_e = 96.4''$ and a Sérsic index n of 4.6 for a single-component Sérsic fit (Krajnović et al., 2013). NGC 4660 is a galaxy of luminosity $6.47 \times 10^9 L_{\odot,r}$ (Cappellari et al., 2013a), with $R_e = 12.1''$, and $n = 3.5$ for a single-component Sérsic fit (Krajnović et al., 2013). The SAURON IFU therefore reaches approximately $3 R_e$ for NGC 4660 and $1/3 R_e$ for NGC 4697.

The orbital structure for NGC 4660 is well constrained by ATLAS^{3D} data, since the majority of the mass is kinematically constrained. Since for NGC 4697 only $1/3 R_e$ is kinematically covered, the orbital structure is much less constrained than for NGC 4660. More freedom in the internal kinematic structure could be possible, as the outer orbits are not constrained. In Section 2.5.2 we will investigate how the JAM assumptions affect the dark matter halo results from the modelling. For this, we improve the radial coverage of the data using SLUGGS data from Foster et al. (2016) ranging to $1.6 R_e$ are used for NGC 4697 in addition to the ATLAS^{3D} data.

2.2.2 Photometry

The photometry used for NGC 4697 is presented in De Lorenzi et al. (2008), deprojected in De Lorenzi et al. (2008) using the method from Magorrian (1999).

The photometry used for NGC 4660 is the Multi-Gaussian-Expansion (MGE) parametrisation, developed by Cappellari (2002), from Scott et al. (2013). The MGE fitting method combines Gaussians with different axis ratios, dispersions, and amplitudes to fit 2D photometric data. The Gaussian with the largest dispersion of the NGC 4660 parametrisation by Scott et al. (2013) is $39''$, as shown on Figure 2.2. The photometric profile is accurate until $\sim 100''$.

The kinematic data extends to $30''$, and the density deprojected from the photometry needs to extend to radii several times larger than the kinematic data, as some orbits which affect the kinematics at the centre can extend to large radii. The photometric profile is therefore extended beyond the limit of the Scott et al. (2013) data to $180''$. This is done by fitting a double-component Sérsic profile to the major axis photometry and then using an axis ratio to extend the photometry in two-dimensions. The double-component Sérsic

profile parametrisation from Hopkins et al. (2009) allows for a more complex profile:

$$I_{\text{tot}} = I' \exp \left(-\kappa' \left(\frac{r}{R_{\text{extra}}} \right)^{n'_s} \right) + I_0 \exp \left(\kappa \left(\frac{r}{R_{\text{outer}}} \right)^{n_s} \right), \quad (2.7)$$

where R_{extra} and R_{outer} are the effective radii of the inner and outer profiles, n'_s and n_s are their Sérsic indices, and I' and I_0 are the normalisations. The parameters n'_s and n_s are fixed to $n'_s = 1.0$ and $n_s = 1.88$, given by Hopkins et al. (2009), while the effective radii and normalisation are fitted. The parameter κ is computed using the equation from Ciotti (1991) $\Gamma(2n) = 2\gamma(2n, \kappa)$. The 1D double-component Sérsic fit to the major axis is then converted to a 2D-profile, taking into account the axis ratio of the galaxy. The axis ratio of the Gaussian with the largest dispersion of the MGE fit, $q = 0.85$, is used to extend the profile.

An MGE fit is then performed to the data with a $\chi^2 = 1.17$, shown on Figure 2.2. An MGE is fitted to the extended image. It follows the MGE profile from Scott et al. (2013) in the region of overlap. The new extended MGE deprojection is therefore used to calculate the density of the galaxy.

2.2.3 Kinematic Data

ATLAS^{3D} Data

The ATLAS^{3D} kinematic data used are the fitted velocity v , velocity dispersion σ , and the h_3 and h_4 moments in Voronoi bins from Cappellari et al. (2011). The unsymmetrised data are used for NGC 4660, because the galaxy is off-centre in the Integral Field Unit (IFU) for NGC 4660, while for NGC 4697 the data are symmetrised.

The data of NGC 4697 from Cappellari et al. (2011) is also used. To check the symmetry of the velocity field, residuals are taken between the halves of the velocity field with negative rotation and positive rotation. These residuals of the NGC 4697 ATLAS^{3D} data revealed an offset between the anti-symmetric velocities along the negative and positive major axis of 10 km s^{-1} . To achieve a symmetrically rotating velocity field, we subtract a global value of 5 km s^{-1} . All the kinematic fields are recentered by $x'_c = x_c + 0.2''$ due to an offset between $v - v_{\text{sys}}=0$ and the central coordinate of the field. Subsequently, we four-fold symmetrise the v , σ , h_3 and h_4 fields using the method from Cappellari (2008), shown on Figure 2.3. For NGC 4697, however, the kinematic coverage is limited ranging to $1/3 R_e$. We therefore use additional data to extend the kinematic coverage of NGC 4697.

SLUGGS 2D Kinematics NGC 4697

Foster et al. (2016) provide a radial kinematic profile of fitted v , σ , h_3 and h_4 ranging to $150''$, or $1.6 R_e$, from the SLUGGS slit data. The SLUGGS data has a sparse spatial coverage, and Foster et al. (2016) use kinemetry to make a “physically meaningful fit” to the data. From these data we can generate approximate kinematic fields to provide good spatial coverage of NGC 4697. This would be sufficient to our purposes to make dynamical models that are a good representation to the galaxy including the halo, with a focus on the general structure rather than small deviations.

The analytic 2D kinematic equations allow anti-symmetric quantities to azimuthally vary within ellipses. We fit a linear least-squares regression to the radial data, and then construct a 2D kinematic field from these in ellipses with ellipticity $\epsilon = 0.32$.

Once we have generated a 2D kinematic field, we can compare it to other 2D kinematics such as ATLAS^{3D} and the VIMOS data from Spiniello et al. (2015), ranging to $\approx 60''$ along the major axis, as well as long-slit data along the major ($\approx 100''$) and minor axis ($\approx 50''$) from De Lorenzi et al. (2008), as well as the long-slit data from Binney et al. (1990). We find that the VIMOS, ATLAS^{3D}, and long-slit data are consistent with one another. The velocity v is lower in the SLUGGS data set than in ATLAS^{3D} and VIMOS. There is also an offset present in h_3 .

These offsets have been discussed in previous publications (e.g. Foster et al., 2016; Cappellari et al., 2015; Spiniello et al., 2015). In Cappellari et al. (2015), JAM models are fitted to the combined SLUGGS and ATLAS^{3D} data sets, and the offset between the two is compensated by scaling up the v_{rms} of the SLUGGS data using a single scaling factor to match the v_{rms} of the ATLAS^{3D} data. As ATLAS^{3D} data is consistent with both VIMOS and the long-slit data, we scale the SLUGGS data to match the ATLAS^{3D} kinematics in the regions of overlap. Binney et al. (1990) and De Lorenzi et al. (2008) retain a constant rotation of 100 km s^{-1} ranging out to $100''$ on the major axis. This is probably caused by the small number of slitlets near the major axis in SLUGGS, which leads to significant spatial smoothing in the kinemetry fit.

Scaling the SLUGGS data

The offset between the two 2D velocity and h_3 ATLAS^{3D} and SLUGGS fields varies between the major, minor and intermediate axes of the field. Therefore scaling the SLUGGS data by a single global factor for the global field will not be sufficient. Hence, we use a symmetric cosine expansion to the ratio between the two data sets for v and h_3 separately to scale the SLUGGS data. This scaling results in the SLUGGS and ATLAS^{3D} data being consistent

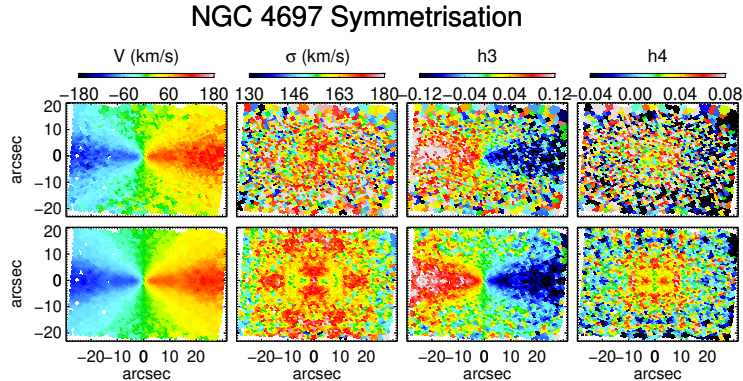


Figure 2.3: The original, unsymmetrised (top) ATLAS^{3D} kinematic data (v , σ , h_3 and h_4), and the four-fold symmetrised data (bottom) using the method from Cappellari (2008).

within measurement uncertainties.

The symmetrised velocity fields of ATLAS^{3D} and the scaled SLUGGS field are shown on Figure 2.4.

Use as an NMAGIC observable

Since the SLUGGS 2D kinematics are produced using analytic functions, the measurement errors and the grid on which they are evaluated must be chosen. As measurement uncertainties we chose the average measurement error of the radial profiles from Foster et al. (2016), which we calculate to be for the velocity field $\Delta_v = 14\text{kms}^{-1}$, for the dispersion $\Delta_\sigma = 7.2\text{kms}^{-1}$, and for h_3 , $\Delta_{h_3} = 0.029$, and h_4 , $\Delta_{h_4} = 0.015$. The resolution of the grid chosen seeks to maximise the resolution of the data given the particle resolution of the model. Producing several different NMAGIC models at different resolution, grids of 50×50 and 100×100 pixels, yields no significant difference. We therefore chose a resolution of 100×100 pixels for the field, beyond which the particle noise would become too high at large radii.

We added randomly sampled Gaussian noise to the SLUGGS 2D kinematics with σ corresponding to Δ_v , Δ_σ , Δ_{h_3} , and Δ_{h_4} . To evaluate the best fitting models an adaptation of Zhu et al. (2018) method was used. We evaluated the χ^2 of all the models and then subtracted the minimum χ^2 of the models. Then calculating the $\sqrt{2 * N_{\text{kin}}}$ where N_{kin} is the number of kinematic bins provides the 1σ confidence interval.

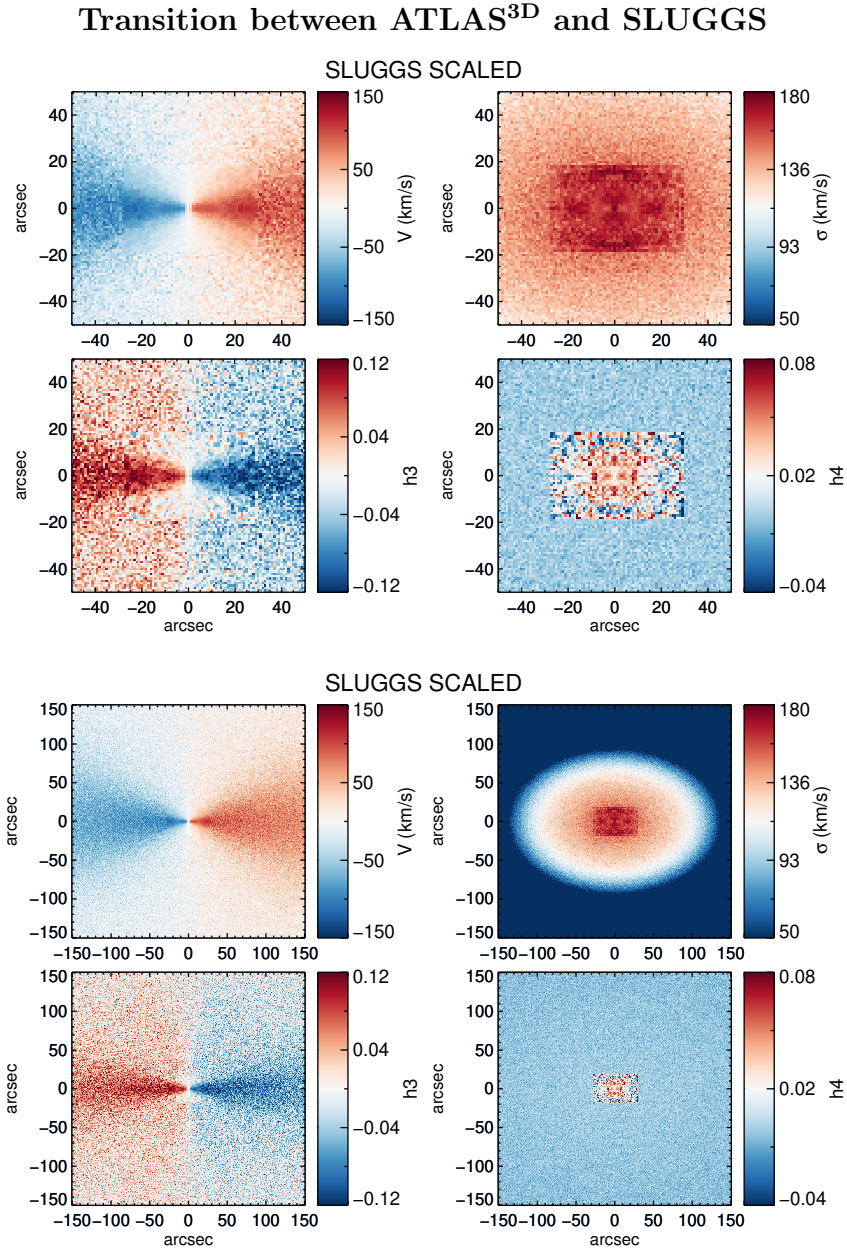


Figure 2.4: The four-fold symmetrised ATLAS^{3D} measurement data inside Voronoi bins of NGC 4697 in the centre, and around it the 2D SLUGGS data calculated analytically from 1D kinemetry profiles to 50'' (top) and the full field to 150'' (bottom) with v and h_3 scaled to the ATLAS^{3D} data using a symmetric cosine expansion.

2.3 NMAGIC Models

In the sections below, we use the made-to-measure particle method to construct dynamical model for the two galaxies. These models are either based only on the observed photometry and kinematics, or they are additionally constrained to minimize the cross term $\langle v_R v_z \rangle$ in order to generate models with JAM kinematics. For this we modify the NMAGIC made-to-measure code implemented in De Lorenzi et al. (2007).

2.3.1 Fitting the Observables

The M2M method gradually changes the particle weights w_i of an N-body model over time in order to reproduce the observables by maximising a profit function F :

$$\frac{dw_i}{dt} = \epsilon w_i \frac{\delta F}{\delta w_i}, \quad (2.8)$$

where ϵ is a parameter setting the typical time-scale of the weight evolution. For observables, the profit function is given by:

$$F = -\frac{1}{2} \sum_j \left(\frac{y_j - Y_j}{\Delta_{Y_j}} \right)^2, \quad (2.9)$$

where y_j is the observable from the model, Y_j represents the observed data, and Δ_{Y_j} are the uncertainties associated with the data. The model is evolved such that the difference between the model and the data is minimised relative to the uncertainties on the data.

The observables fitted in this paper are the density, the kinematics, M/L , $\langle v_R v_z \rangle$ term, and z-anisotropy in the meridonal plane. The axisymmetric density represented by spherical harmonics as in Equation 25 in De Lorenzi et al. (2007). The SAURON IFU kinematics and SLUGGS 2D kinematics fields are fitted according to Equation 6 in De Lorenzi et al. (2008), and the M/L adjusted using Equation 25 in De Lorenzi et al. (2008). In addition we adjust the cylindrical cross term of the velocity ellipsoid and the z-anisotropy as described in Section 2.3.2

In such a case, where there are multiple observables with widely different numbers of observational constraints in each observable, their contributions to the force of change equation can be varied:

$$\frac{dw_i(t)}{dt} = \epsilon w_i(t) \left(\mu \frac{dS}{dw_i}(t) - \sum_k \gamma_k \sum_j \frac{K_j(\mathbf{x}_i(t), \mathbf{v}_i(t))}{\sigma(Y_j^k)} \Delta_j^k(t) \right) \quad (2.10)$$

such that γ_k represents a numerical weight on different data sets, following the method of gitet2010MNRAS.405..301L. The γ_i are often adjusted such that then the evolution of the

model is influenced similarly by all observables. In this paper its been set that the total $\gamma_{\text{tot}} = 1$, where γ_{tot} is the sum of all γ parameters of all the observables (e.g., cross term, kinematics).

Temporal smoothing (Syer & Tremaine, 1996; De Lorenzi et al., 2007) is used in order reduce shot noise of the particle model. It is applied in the calculation of the observables and increases the effective number of particles by substituting $y_j(t)$ with:

$$\tilde{y}_j(t) = \int y_j(t - \tau) e^{-\alpha\tau} d\tau \quad (2.11)$$

where τ is an integral of time and $1/\alpha$ is the smoothing time.

2.3.2 Fitting the velocity ellipsoid

JAM models assume that the velocity ellipsoid is aligned cylindrically ($\langle v_R v_z \rangle = 0$). In typical uses of NMAGIC, the $\langle v_R v_z \rangle$ term is not altered and any physical alignment of the velocity ellipsoids is allowed. Here we wish to steer the particle models towards the cylindrical velocity ellipsoids assumed by the JAM models. To this purpose we introduce a module to evolves the NMAGIC model towards cylindrically aligned velocity ellipsoids, i.e. a target $\langle v_R v_z \rangle = 0$.

The method is similar to fitting measurement data, but adjusts the internal kinematics of the model, similar as the density in Dehnen (2009). To calculate the $\langle v_R v_z \rangle$ term, the particles are binned, and the $\langle v_R v_z \rangle$ term is calculated directly from their known velocity vector, weighted by the mass of the individual particles. The models are axisymmetric, within an error due to the particle noise, therefore, do not vary significantly in ϕ . The meridional plane (R, z) is averaged over the ϕ direction. This increases the signal-to-noise of the cross term. This binning regime we employ is shown on Figures 2.5 and 2.6.

The observable (y_j) used is the $\langle v_R v_z \rangle$. This is calculated in bins of (R, z, ϕ), as in the binning scheme above. For each bin the target (Y_j) is therefore $\langle v_R v_z \rangle = 0$ within each (R, z, ϕ) bin. Therefore in Equation 2.9, $\langle v_R v_z \rangle = Y_j = 0$. In order to allow comparison between models we use the cross term correlation $c_{(R,z)}$, with typical values of the cross term correlation $c_{(R,z)}$ lying between -0.5 and 0.5 .

The orientation of the velocity ellipsoid is a quantity internal to the galaxy, and therefore does not have traditional measurement errors associated to it. Nevertheless NMAGIC uses a χ^2 minimisation method in order to evolve the model towards an observable. We therefore we need to associate a physical meaningful error $\Delta(Y_j)$ to the fitted $\langle v_R v_z \rangle = Y_j = 0$. We therefore scale it using the models internal values. Hence, in order to calculate $\Delta(Y_j)$, the initial model is temporally smoothed before fitting. A fraction of the temporally smoothed value of the mass-weighted $\langle v_R v_z \rangle$ term in each bin is taken as $\Delta(Y_j)$ at the start of the

fit. This fiducial error, $\Delta(Y_j)$ in combination with a suitably set γ parameter is therefore set to evolve the model towards $\langle v_R v_z \rangle = 0$. There are different possibilities for setting the error than this. We have tested different methods, such as setting the error to be constant for each bin, and a variation on the binning scheme and have found convergence to the same model within the noise of the cross term.

For the purposes of using the $\langle v_R v_z \rangle$ term as an observable equation 2.9 therefore becomes:

$$F = -\frac{1}{2} \sum_j \left(\frac{v_{Rz,j}}{\Delta_v} \right)^2. \quad (2.12)$$

In a similar way, the anisotropy β_z of the model can also be evolved towards a target value. This method is used later both for the creation of the initial models with a specific anisotropy structure. It can also be used to probe the concept introduced and used in the JAM models of Cappellari (2008) of a constant β_z for the whole galaxy. However, it a different target β_z can be set for each bin.

The observable used for equation 2.9 is therefore given by:

$$Y_j = (\beta_{z,\text{target}} - 1) * v_{RR,j} + v_{zz,j}. \quad (2.13)$$

where $v_{RR,j}$ and $v_{zz,j}$ are the cylindrical R and z second moments of the galaxy. An example value for $\beta_{z,\text{target}}$ would be 0 for a meridionally isotropic model for every bin in the galaxy. When we present the internal kinematics of the galaxy, we discuss the regions close the major axis, minor axis, and the region close to the $\theta = 45^\circ$ angle. These regions are defined in terms of their θ values in spherical coordinates. As shown on Figure 2.1, the strongest deviation between the cylindrical and spherical coordinate systems occur close to $\theta = 45^\circ$, covering approximately 30% of the meridional plane. If there is deviations from the JAM this is where we expect them to most strongly occur. To quantify the deviation of the JAM in a single parameter we therefore use the highest 30 % absolute values of the cross correlation $c_{(R,z)}$, named the cross parameter c_{30} . Similarly, we name the highest 30 % absolute values of the z-anisotropy β_z the beta parameter β_{30} .

2.3.3 Pseudo-SAURON velocity fields

In Sections 2.4 and 2.5 below, we will investigate models of the two galaxies that are based only on the photometry and on putting JAM-constraints on the velocity ellipsoids, and wish to compare their kinematic observables with the observed kinematics. For this we need to kinematically “observe” these models without reference to the observed data. In the more common dynamical modelling, the v and σ of the galaxy kinematic data are used to calculate the Gauss-Hermite moments of the model kinematics, and the model

fitting for this case is done by requiring the model $h_1 = h_2 = 0$ and h_3, h_4 to match the observed values in each spatial element (De Lorenzi et al., 2008). Once the best-fitting model is determined, the residual values of h_1, h_2 are used to compute the best model v, σ iteratively from the data values while h_3, h_4 are simultaneously updated. For the case of observing the kinematics of the JAM NMAGIC models, the only differences are that the iterations start from the first and second moment v, σ in the spatial element, until $h_1 = h_2 = 0$ when the final (v, σ, h_3, h_4) are determined, and that we scale the internal kinematics by a mass-to-light ratio that allows comparison to the ATLAS^{3D} velocity field. For this we use the average values obtained in the kinematic fits, i.e., $M/L = 4.75$ for NGC 4660, and $M/L = 5.0$ for NGC 4697.

Scaling the dark matter halo

The scaling of internal units using M/L has further implications when a dark matter halo is employed using a parameterisation scaled using kms^{-1} , as in Section 2.5.2. In Section 2.5.2, we use a series of dark matter halos that are scaled using v_0 in kms^{-1} and therefore employ the internal units to kms^{-1} scaling used for the previous ‘‘Kin Only’’ final models. Tests were done varying this internal scaling, with no significant effect on the conclusions drawn from the models.

2.3.4 Initial Models

The NMAGIC M2M method requires initial particle models. These are subsequently evolved in NMAGIC to take on galaxy characteristics such as kinematics. We use initial models which have the same density as our galaxy, but with four different anisotropy structures, in order to ensure that the final modelling results are independent of the initial particle model. The four initial models, shown in Figure 2.5 and 2.6 are:

- **‘‘Isotropic’’ model ICA** In spherical anisotropy β_r this model has mild radial anisotropy, and in cylindrical β_z anisotropy is meridionally nearly isotropic, with some scatter to $\beta_z \sim 0.1$ beyond $150''$ for both NGC 4660 and NGC 4697.
- **‘‘Mildly Anisotropic’’ model ICB** This model has strong radial spherical anisotropy β_r along the major axis, becoming mildly spherically tangentially anisotropic on the minor axis. The cylindrical anisotropy is radial along the major axis, and close to isotropic on the minor and intermediate axis. For NGC 4660 this model has a β_z ranging between ~ 0.4 and 0.6 close to the major axis (between $\theta = 60^\circ$ to 120°), and a $\beta_z \sim 0$ on the intermediate (between $\theta = 25^\circ$ to 60° and $\theta = 120^\circ$ to 155°) and minor axis (between $\theta = 0^\circ$ to 25° and $\theta = 155^\circ$ to 180°). NGC 4697 has a β_z close

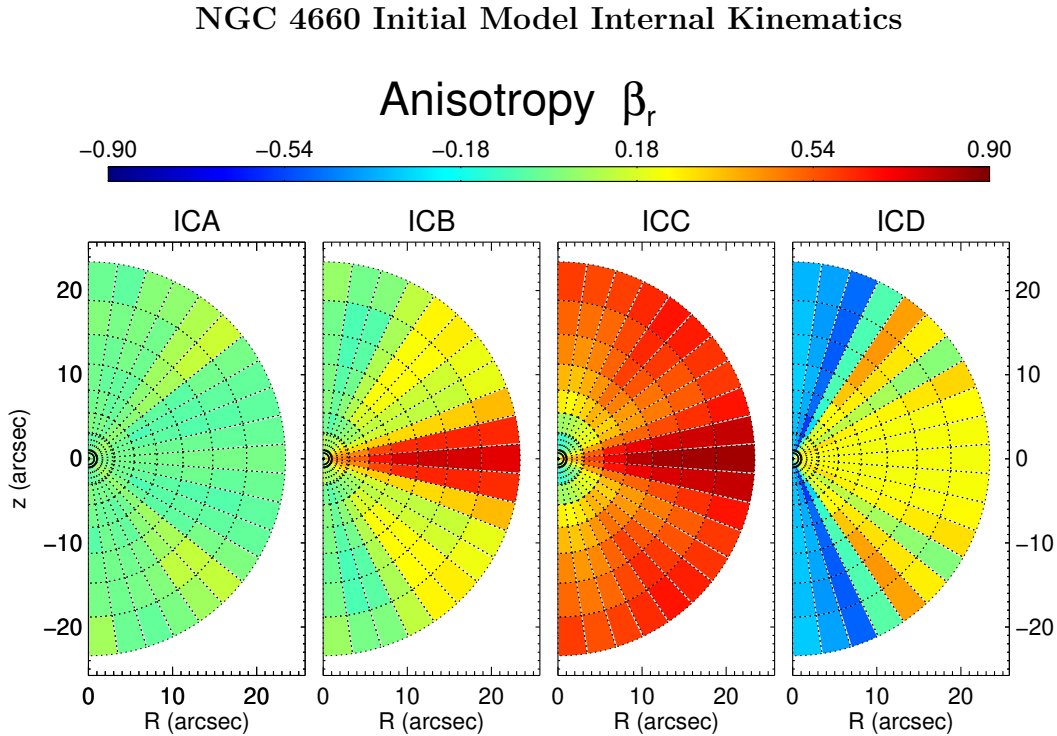


Figure 2.5: Internal kinematics (β_r anisotropy) in the meridional plane (R, z) plane of particle models of the galaxy NGC 4660, summed over the ϕ direction of the galaxy. The velocity moments are calculated directly from the particles in every bin. The figure shows the r -anisotropy $\beta_r = 1 - \sigma_\theta^2/\sigma_r^2$. The models represented here are different initial models used for NGC 4660, which are characterised by their different internal anisotropy structures. Left to right these are labelled: the isotropic model (ICA), the mildly anisotropic initial model (ICB), the strongly anisotropic initial model (ICC), and the JAM-like initial model (ICD). Each of the models has a non-zero cross term.

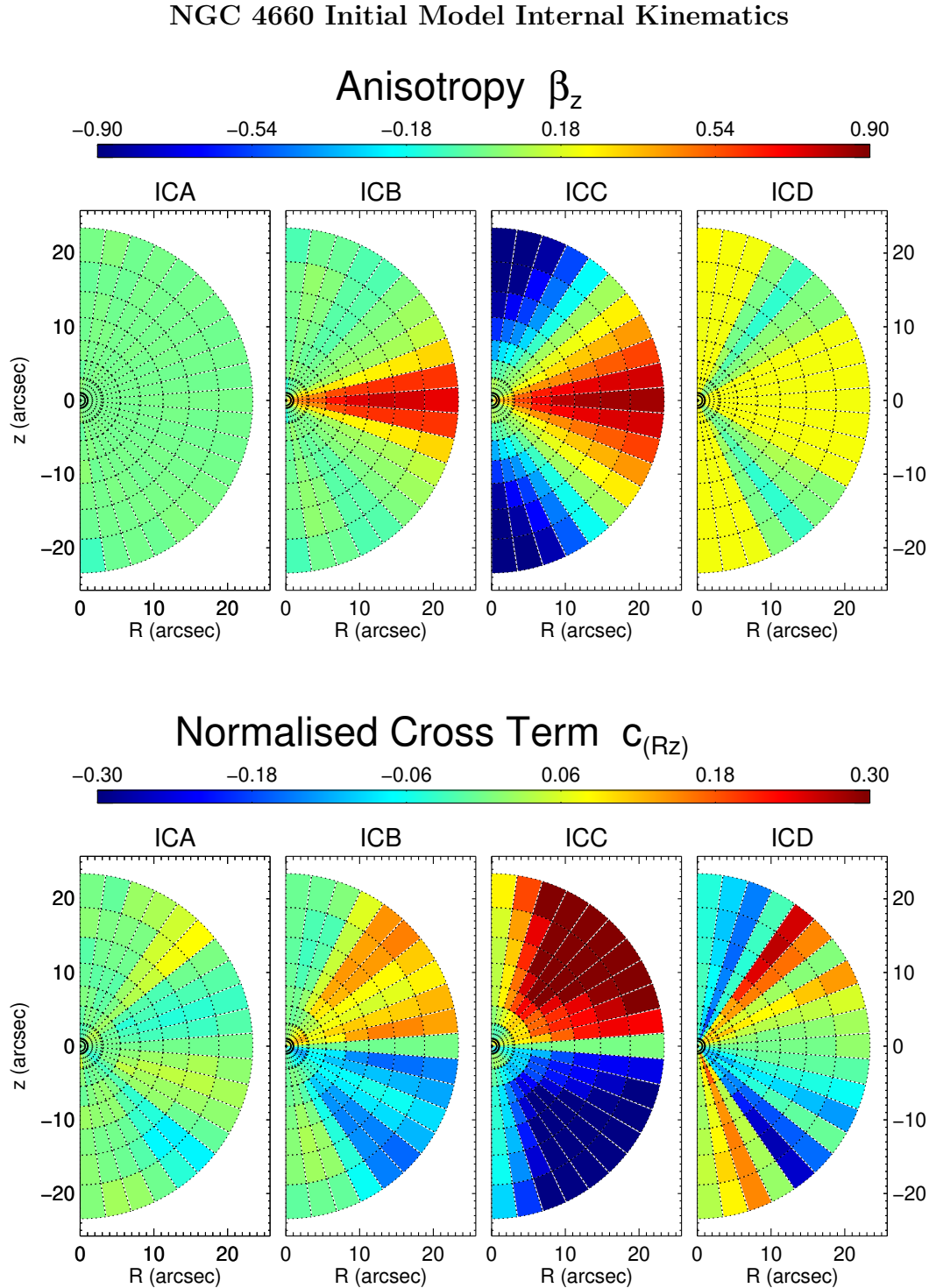


Figure 2.6: Same as previous figure. The top row shows the β_z anisotropy, the bottom row the cross term correlation $c_{(R,z)}$. The initial models C and D, which have significant z -anisotropy on the intermediate (between $\theta = 25^\circ$ to 60° and $\theta = 120^\circ$ to 155°) and minor axis (between $\theta = 0^\circ$ to 25° and $\theta = 155^\circ$ to 180°) have a much higher cross term than models A and B which are more isotropic on the intermediate and minor axis.

to 0.4 on the major axis, with a gradual change to a β_z of 0.2 along the intermediate axis. It has an isotropic $\beta_z \sim 0$ along the minor axis.

- **“Strongly Anisotropic” model ICC** The β_r of the ICC model is strongly radial. In terms of cylindrical anisotropy it is strongly radial close the major axis, and strongly tangential close to the minor axis. NGC 4660 has a β_z ranging between ~ 0.4 and 0.8 close to the major axis, and a $\beta_z \sim -0.3$ to 0.6 close to the minor axis, and a $\beta_z \sim 0$ on the intermediate axis. For NGC 4697 there is a strong radial β_z of 0.8 along the major axis, and a tangential β_z of -0.8 along the minor axis. The intermediate axis is close to isotropic.
- **“JAM-like” model ICD** The “JAM-like” model has radial β_r in the major and intermediate axis area, with a fast transition to tangential anisotropy along the minor axis. The β_z anisotropy is radial along the major and minor axis, with isotropy along the intermediate axis. It is known as the “JAM-like” model as radial anisotropy along the minor axis means the velocity ellipsoid is cylindrically aligned, as can be seen in the illustration of Figure 2.1. This model is characterised for both NGC 4660 and NGC 4697 for having $\beta_z \sim 0.23$ close to the minor and major axis, and $\beta_z \sim 0$ on the intermediate axis.

In order to create an initial particle model, first a spherical particle model is made using the method from De Lorenzi (2007) adapted from Debattista & Sellwood (2000). This first derives a spherical stellar potential from a spherical luminosity density, in the case of NGC 4660 using the major axis of the deprojected photometry.

The spherical density is given in terms of the energy E and the angular momentum L by:

$$\mathcal{N}(E, L) = 8\pi^2 L f(E, L) \tau(E, L) \quad (2.14)$$

where f is the distribution function and τ is the radial period of one oscillation of a particle with (E, L) . The particle distribution $\mathcal{N}(E, L)$ is integrated over to find the mass in the (E, L) space. It is subdivided into sections of n_E in energy and n_L in angular momentum, such that the area $j = n_E n_L$, covers a fraction of M/j of the active mass, where M is the total mass of the galaxy in the range. The resulting orbits are then populated by n_{EL} particles of the same number, and the total number of particles in the model is $N = n_E n_L n_{EL}$. For NGC 4660, the parameters chosen were, $n_E = 150$, $n_L = 250$, and $n_{EL} = 20$, giving a total particle number $N = 750000$, which was determined in previous work by De Lorenzi (2007) to have sufficient resolution for elliptical galaxies. In combination with the above we use the circularity equation from Gerhard (1991) for the distribution function, which allows us to add some anisotropy to our particle model.

In the next step, using NMAGIC, the spherical particle model is evolved with the oblate photometry of NGC 4660 as an observable, resulting in an oblate particle model with the three-dimensional density deprojected from the photometry. This oblate particle model is

a good representation of the density of NGC 4660, however, has no rotation. The kinematic data of NGC 4660, however, suggest that some rotation is present in the galaxy. When rotation is desired in a final NMAGIC model the use of an initial NMAGIC which already has some rotation present aids convergence. Therefore rotation is added to the oblate initial model by reversing the particle orbits. Retrograde particles are switched with a probability p given by De Lorenzi et al. (2008):

$$p(L_z) = p_0 \frac{L_z^2}{L_z^2 + L_{crit}^2} \quad (2.15)$$

where $L_{crit} = 0.001$ and is used to prevent a discontinuity at $L_z = 0$, as shown in Kalnajs (1977), which could affect the stability of the particle model. The parameter p_0 governs how many particles are switched, the larger this parameter the larger the rotation of the model. We used four different values of p_0 , 0.4, 0.6, 0.8 and 1.0 and compared the v/σ of the resulting rotating model to the v/σ of the ATLAS^{3D} data, and therefore a value of $p_0 = 0.6$ chosen as the most suitable.

Two of NGC 4660's initial models were made using this method, the mildly radially anisotropic model ICB and the strongly radially anisotropic model ICC. The other two initial models, the isotropic (ICA) and JAM-like (ICD) models, were evolved in NMAGIC to have a specific β_z structure. For NGC 4697 we use the initial model from De Lorenzi et al. (2008) to make four initial models with different phase space structures, just as for NGC 4660. For the models to the SLUGGS data presented in Section 2.5.2, we modify the mildly anisotropic model ICB to have more rotation at large radii (ICB2) using the particle switching method to have an initial model which includes sufficient rotation in the outer parts of the galaxy to converge on the SLUGGS v more easily.

In Table 2.1 the photometric χ^2 , c_{30} and β_{30} of the initial models are given. The table is for NGC 4660 and NGC 4697 with a potential of stars only (no dark matter). Without using the $\langle v_R v_z \rangle$ term as an observable, c_{30} ranges between the lowest value of 0.0391 for the isotropic model and highest value of 0.331 for the strongly anisotropic initial model. Considering the isotropic, and mildly and strongly anisotropic model the larger the anisotropy the larger the $\langle v_R v_z \rangle$ term. It is interesting to note that the JAM-like model has a lower β_{30} of 0.233 than the mildly isotropic model which has 0.399, but a higher c_{30} of 0.156 in comparison to the mildly anisotropic model's value of 0.123. Not only does the JAM-like initial model have a non-zero c_{30} , it has a larger c_{30} than the mildly anisotropic model. On Figure 2.6 it can be seen that this is because of large deviations from $c_{30} = 0$ in the regions where the cylindrical and spherical regimes most deviate, at 45° and 135° .

2.4 NGC 4660: a well-constrained galaxy

2.4.1 JAM models for NGC 4660 via Jeans equation

We start our modelling of NGC 4660 with JAM models calculated using the analytic Jeans approach of Cappellari (2008). This allows easy variation of parameters, i.e. inclination, anisotropy β_z , M/L , rotational parameter κ and dark matter halo. Previous JAM modelling by Cappellari (2008); Cappellari et al. (2013a) has given best values for the (inclination i , anisotropy β_z) = (68°, 0.23) and (74°, 0.14) of NGC 4660, for the case without dark matter halo. Using the MGE and JAM IDL codes from Cappellari (2008) we reproduce the (68°, 0.23) model on Figure 2.7 and also show some models with different β_z (0, 0.4) to illustrate the sensitivity of the model kinematics to this parameter. Figure 2.7 shows the v_{rms} , v and sigma fields obtained for $i = 68^\circ$ and these β_z with the best-fitting M/L and κ parameters. Clearly the best JAM model fits the kinematics of the galaxy very well. The model for $i = 74^\circ$, $\beta_z = 0.14$ fits achieves a similarly good, but different fit (e.g., M/L increase of 6%) as the JAM method is quite sensitive to inclination.

2.4.2 NMAGIC dynamical model fits to the kinematic data

In this section we determine best NMAGIC dynamical models from the kinematics and photometry. This allows us to understand what the data on their own tell us about the dynamical structure of the galaxy, as well as to have a basis for the comparison with models including the JAM constraint. The NMAGIC models do not make any assumption on the dynamical structure. However, if the data did not uniquely constrain the model, then these models would depend on the initial dynamical model used by NMAGIC. Therefore we here present dynamical models obtained from different initial models whose kinematic structure is shown on Figure 2.5 (in Section 2.3.4). We find that the final dynamical model is insensitive to the initial model, as shown on Figure 2.8. This is because NGC 4660 is a small galaxy with $R_e = 12.1''$ so a large part of the model ($\sim R_e$) is constrained by the ATLAS^{3D} velocity field.

The internal dynamical structure of all these data-driven models is very similar, as shown in the meridional plane diagrams on Figure 2.9. The spherical anisotropy β_r shows strong radial anisotropy near the major axis becoming tangentially anisotropic at intermediate angles (between $\theta = 25^\circ$ to 60° and $\theta = 120^\circ$ to 155°) and strongly tangentially anisotropic on the minor axis. This is similar to the models that initially motivated JAMs (Cappellari et al., 2006a; Thomas et al., 2009). However, the normalized cross term of the particle models is ± 0.3 in a cone away from the R and z axes, and the z -anisotropy is of order 0.7 on the z and R axes, reaching small values at intermediate meridional angles. Therefore, the dynamical models determined only from the data are quite different from

JAM models at intermediate angles.

We conclude that data-only driven models for NGC 4660 are more or less unique, and have a dynamical structure for the assumed inclination which at intermediate angles is very different from JAMs fitted to the data.

Table 2.1: Table of the different characteristic parameters of the initial models of NGC 4660 and NGC 4697. Column 1 is the galaxy name, Column 2 is the name of the initial model type, Column 3 is the photometric χ^2 of the model to the A_{lm} , Column 4 is the Cross Parameter, and Column 5 is the z -anisotropy β_z parameter of the model.

Galaxy ID	Initial Model	Photometry χ^2	Cross Parameter	β_z Parameter
NGC4660	Isotropic ICA	0.1234921	0.0391	0.0169
NGC4660	Mildly Anisotropic ICB	0.0183696	0.123	0.399
NGC4660	Strongly Anisotropic ICC	0.0272577	0.331	0.712
NGC4660	JAM-like ICD	0.4394227	0.156	0.233
NGC4697	Isotropic ICA	0.1472216	0.0500	0.0282
NGC4697	Mildly Anisotropic ICB	0.0164404	0.0686	0.277
NGC4697	Strongly Anisotropic ICC	0.0218442	0.293	0.512
NGC4697	JAM-like ICD	0.0066763	0.129	0.311

2.4.3 The only physical JAMs are nearly meridionally isotropic

To study the effect of cylindrically aligned velocity ellipsoids on the model, we describe a set of different models which use the $\langle v_R v_z \rangle$ term as an observable. In these models, we use both the photometry and the $\langle v_R v_z \rangle$ term as an observable. It is important for the models to match the deprojected density well, to allow comparisons between distribution functions fitting to the same density. In the cases throughout this paper where there is tension between the photometry and any other observable, the photometry is always weighted to produce a reduced $\chi^2 < 1$. The models in this section match the photometry very well. Figures 2.10 and 2.13 show models with only the JAM constraint fitted in addition to the photometry.

Figure 2.13 shows that the cross term in these models indeed becomes nearly zero, but also that the anisotropy vanishes in most of the meridional plane except near the major

(R -) axis where it is radially anisotropic ($\beta_z \sim 0.7$). On the R -axis this radial anisotropy is consistent with spherical radial anisotropy. Note that the result is independent of the initial model, see Figure 2.10.

Models with these dynamical properties fit the observed rotation velocity field fairly well, but they are a poor fit to the velocity dispersion field and to h_4 (Figure 2.10). The main conclusions are that excepting on the major axis the only JAM for this galaxy is meridionally isotropic, and contrary to the fitted JAM, this model is not a good fit to the data.

The strongly radially anisotropic initial condition (ICD) model has difficulty converging towards the JAM-like model as it is very different from an isotropic model. We therefore do not continue with this particular initial model from now on.

Figure 2.12 shows models in which additionally $\beta_z = 0.23$ (Cappellari, 2008) was added as constraint. These models end up with a significant cross term at intermediate angles, and significant anisotropy variations across the meridional plane. The conclusion is that a constant z -anisotropy does not appear to be dynamically viable.

2.4.4 The tension between the data and the JAM structure

Finally, we investigate models driven by the data and the JAM assumptions. The idea here is that perhaps a reasonable fit to the data could be achieved by only small departures from the JAM condition. Comparing Figures 2.8 and 2.10, the differences in v , σ , h_3 and h_4 are apparent. Same as in Sections 2.4.2 and 2.4.3, we use the four initial models described in Section 2.3.4 as input models for one model. We determine that just as in 2.4.2 the choice of input model does not affect the result. We therefore proceed with only one input model for the rest of this section “ICB”.

The resulting models, however, do not fit the JAM condition and ATLAS^{3D} kinematics, they are therefore named “tension” models. In order to explore this “tension” we do series of models which weight the $\langle v_{RVz} \rangle$ term (γ_{cross}) and the kinematics (γ_{kin}) differently with respect to each other by using the γ parameter in Equation 2.10.

A series of models with different γ_{cross} and γ_{kin} is shown, where $\gamma_{\text{total}} = \gamma_{\text{cross}} + \gamma_{\text{kin}}$. Their kinematic χ^2 decreases with increasing γ_{cross} , while the cross parameters goes close to 0 with increasing γ_{cross} . Therefore, if the $\langle v_{RVz} \rangle$ term is used as an observable and the model tries to fulfill the JAM conditions, a compromise is made in the kinematic fits of the ATLAS^{3D} data. The reduced χ^2 of the kinematics of the “Tension” models is larger than for the kinematic observable only fits described in Section 2.4.2, shown as $\gamma_{\text{cross}}/\gamma_{\text{total}} = 0$. This increase in χ^2 is global, but also particularly driven by the σ .

As well as a decrease in accuracy in the kinematics, the “tension” models also have a higher $\langle v_R v_z \rangle$ correlation term than the models which only use the $\langle v_R v_z \rangle$ term as an observable, shown as $\gamma_{\text{cross}}/\gamma_{\text{total}} = 1$ on Figure 2.10, described in Section 2.4.3.

The internal kinematics of the “tension” model $\langle v_R v_z \rangle$ term show that while the $\langle v_R v_z \rangle$ term only models only deviate from 0 strictly along the major axis, the “tension” models vary from 0 in the entire range between 45° and 135° . This is reflected in the cross term parameter, which is larger in these models than in the cross term only models. No model is found where the data are fitted well and the cross term is nearly zero. If such a model existed, the NMAGIC method should have found it because no other constraints were imposed. Therefore this suggests that no dynamically self-consistent such model exists, i.e., that the JAM models fitted to the (v, σ) maps have no underlying physical orbit distribution (distribution function).

There is an increase in anisotropy in the “tension” models, suggesting that while anisotropy is needed to fit the ATLAS^{3D} kinematics, it is incompatible with a $\langle v_R v_z \rangle$ term of 0. In conjunction with the findings in Section 2.4.3, this leads to the overall conclusion that that anisotropy is inconsistent with $\langle v_R v_z \rangle = 0$ for NGC 4660.

2.4.5 Inclination

We repeated the analysis of Section 2.4.4 for the inclination $i = 74^\circ$ found in Cappellari et al. (2013a), shown on Figure 2.14 as the dashed lines. The same trend in χ^2 and cross parameter with γ are found for this inclination. We find that $i = 74^\circ$ has lower values for both the χ^2 and cross term, we therefore agree more with the Cappellari et al. (2013a) value of the inclination, not the Cappellari (2008) value of $i = 68^\circ$. For models unconstrained by the JAM condition we find a 1% difference in M/L , as NGC 4660 is very well constrained by the kinematics.

2.4.6 Mass-to-Light Ratio

Even though the JAM models fitted to the velocity and sigma maps appear to have no underlying physical distribution function, the $M/L = 4.93$ obtained from the best JAM fit at inclination $i = 68^\circ$ differs from that obtained from the NMAGIC models for the data, 4.75 ± 0.01 , only by 3%. For $i = 75^\circ$ our best JAM fit value of $M/L = 5.21$ is different by 9% from the NMAGIC model value of $M/L = 4.8$. It can be seen in Table 2.4, which shows the parameters of the JAM fits, that different global β_z values give different values of M/L and therefore mass as their best fit.

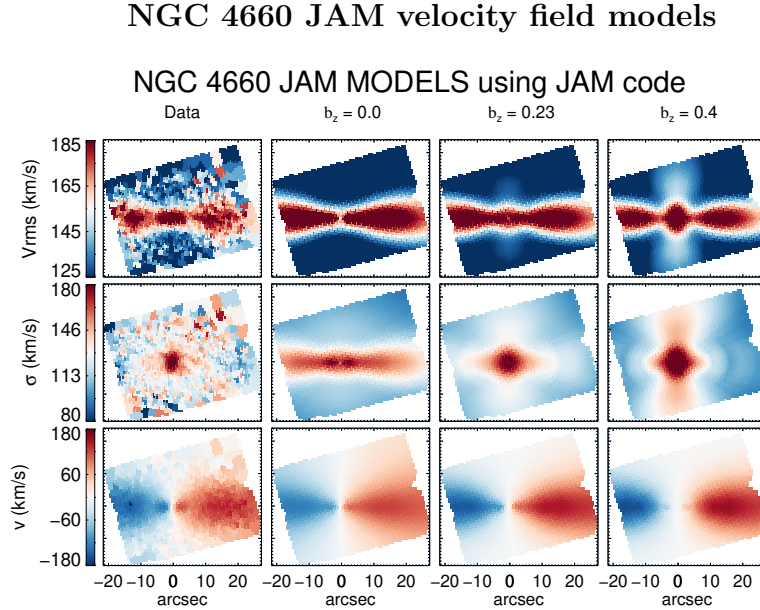


Figure 2.7: Models of NGC 4660 made using the JAM method. The top row is the ATLAS^{3D} v_{rms} data compared to the v_{rms} of stellar matter only JAM models with different values of β_z . The middle row gives the velocity and the bottom dispersion of those models.

2.5 NGC 4697: Models in different dark matter halos

In this section we describe similar dynamical models for NGC 4697, thereby investigating a galaxy with different dynamical structure and for which the dark matter halo is more important. We first discuss the case when the galaxy is constrained only by the SAURON data, leaving considerable freedom to the model, and then proceed to models with a sequence of dark matter halos that are constrained additionally by the SLUGGS data as described in Section 2.2.3.

xf

2.5.1 Models for NGC 4697 without dark matter halo

JAM models for NGC 4697 via Jeans equation

As in Section 2.4.1 we first compare JAM models made of NGC 4697 to the v_{rms} , mean velocity and dispersion of the ATLAS^{3D} data. For the density we deproject an MGE fit to the photometry of NGC 4697. We take an inclination of $i = 70^\circ$ and $i = 80^\circ$, as in

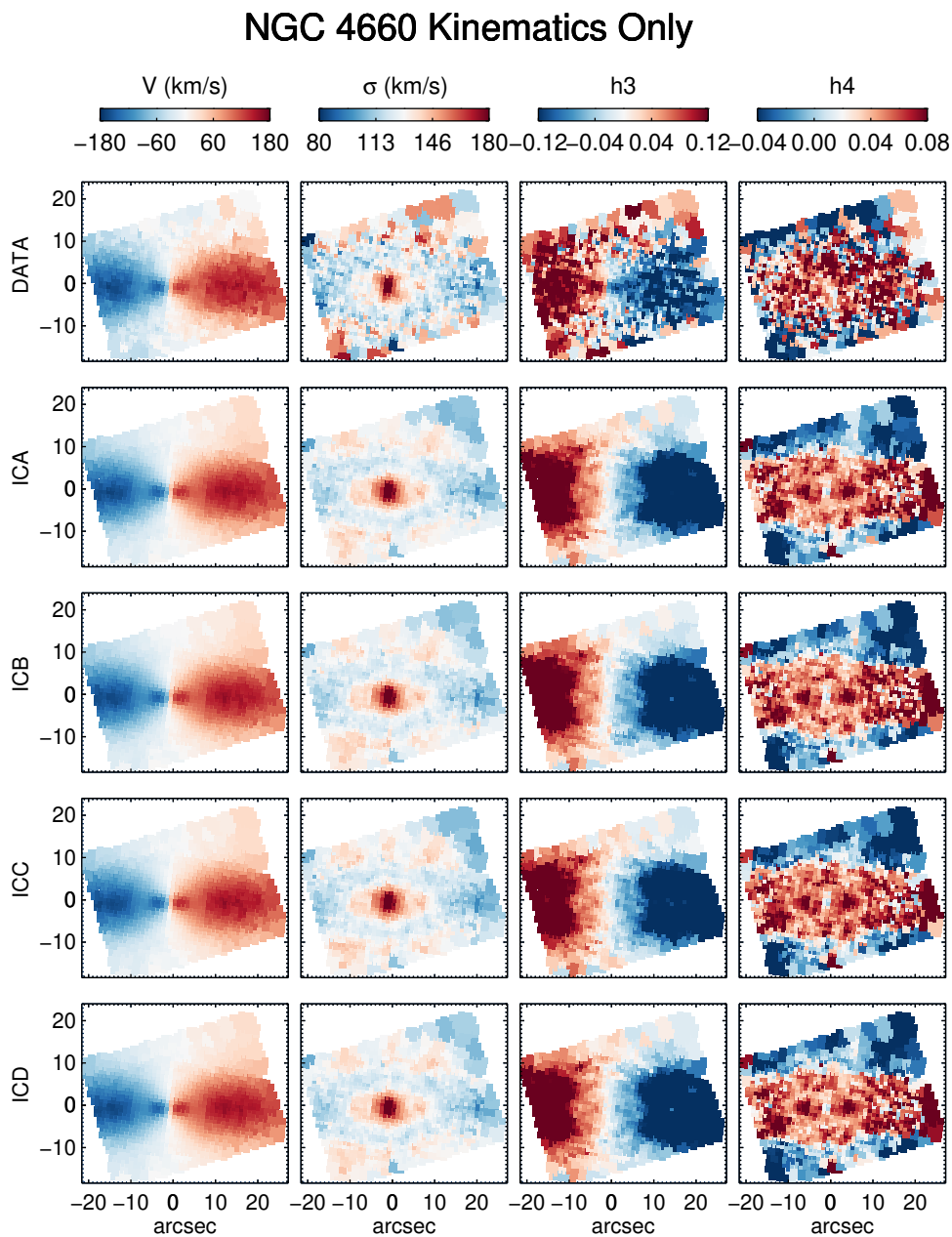


Figure 2.8: The first row shows the ATLAS^{3D} kinematic data, v , σ , and the h_3 and h_4 moments of NGC 4660. Subsequent rows show the projected kinematics of NMAGIC models which use the photometry and kinematics as an observable with no JAM assumption. The models differ which initial model is used, from top to bottom: Isotropic ICA, Mildly Anisotropic ICB, Strongly Anisotropic ICC, and “JAM-like” ICD. The resulting projected kinematics are very similar, showing the kinematic data is reproduced independently of initial conditions.

NGC 4660 Internal Kinematics for Kinematics Only Models

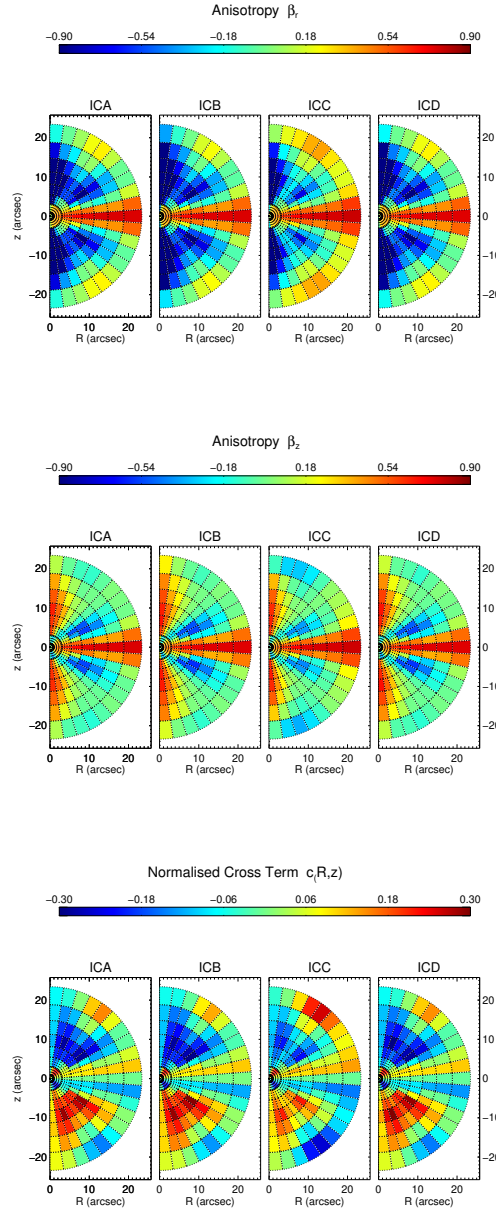


Figure 2.9: The top row shows the r -anisotropy $\beta_r = 1 - \sigma_\theta^2/\sigma_r^2$, the middle row the β_z anisotropy, and the bottom row the cross term correlation $c_{R,z}$ of models that fit the ATLAS^{3D} kinematics and photometry. in the meridional plane of NGC 4660 within 30'' with initial models from left to right: the “isotropic” model ICA, the “mildly-anisotropic” model ICB, “the strongly anisotropic” model ICC, and the “JAM-like” model ICD.

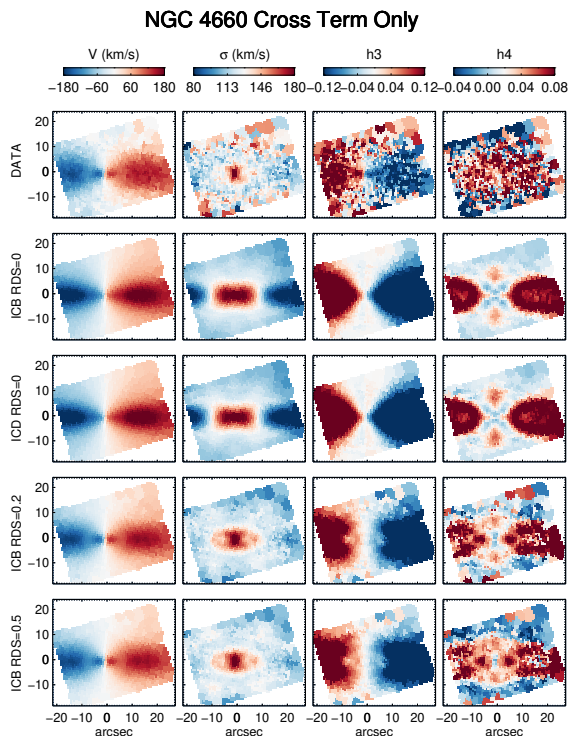


Figure 2.10: The first row shows the ATLAS^{3D} kinematic data, v , σ , and the h_3 and h_4 moments of NGC 4660. The second and third row show models which only use the JAM condition as an observable, with two different initial models ICB and ICD. The fourth and fifth rows show models which both use the JAM condition and the kinematics as observables with different relative data strengths (RDS) of $\gamma_{\text{Kin}}/\gamma_{\text{Total}} = 0.2$ for row four and 0.5 for row five.

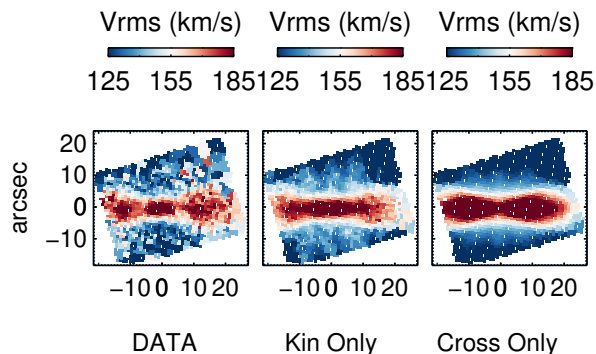


Figure 2.11: NGC 4660 v_{rms} ATLAS^{3D} data (right), compared with the v_{rms} of a data-driven NMAGIC model (“Kin Only”) and a JAM condition NMAGIC model (“Cross Only”) for NGC 4660. The Gauss-Hermite moments of the same models (both ICB) are shown on Figure 2.8 for the “Kin Only” and Figure 2.10 for the “Cross Only” model.

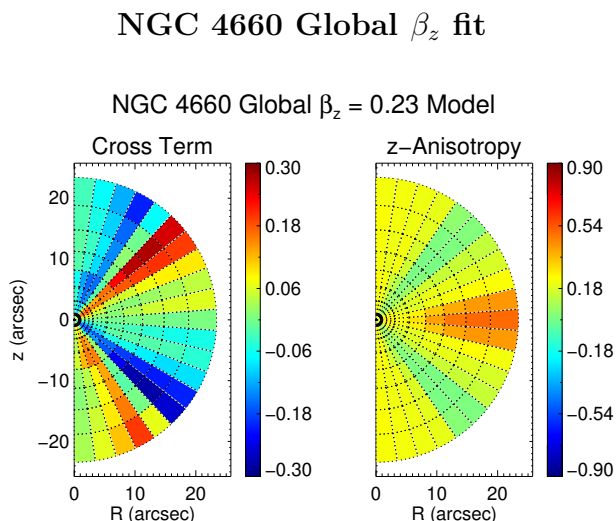


Figure 2.12: Left to Right: The cross term correlation $c_{(R,z)}$ and the z -anisotropy in the meridional plane of NGC 4660 within $30''$ of a model which fits a global β_z of 0.23 over the whole galaxy. The photometry is well fitted with a χ^2 of 0.0760, with the compromise being made on the β_z fit on the intermediate axis. Forcing a whole galaxy of $\beta_z = 0.23$ more rigidly causes a breakdown of the density fit.

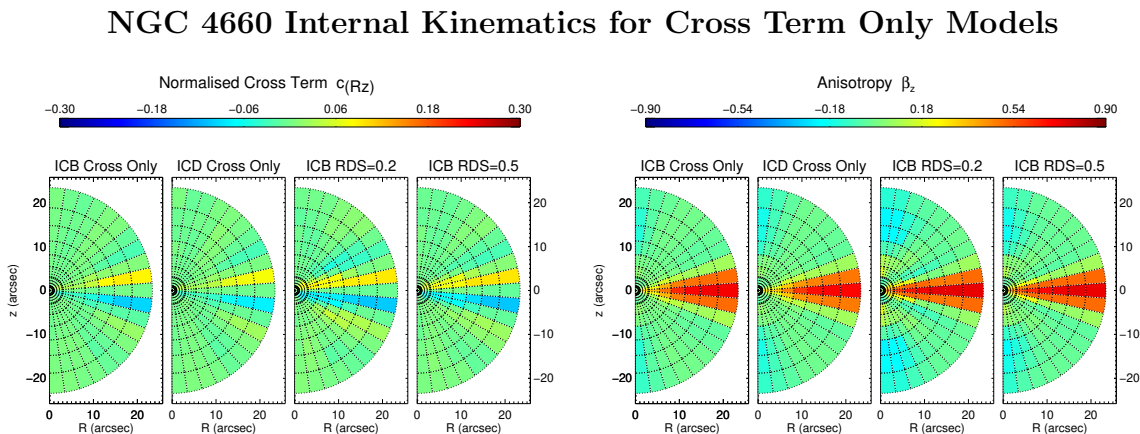


Figure 2.13: Same as Figure 2.9 with the models left to right: model which only uses JAM assumption and photometry with initial model ICB, model which only uses JAM assumption and photometry with initial model ICD, model which uses kinematics, JAM assumption, and photometry as observables with relative data strength $RDS = 0.2$, model which uses kinematics, JAM assumption and photometry with $RDS = 0.5$.

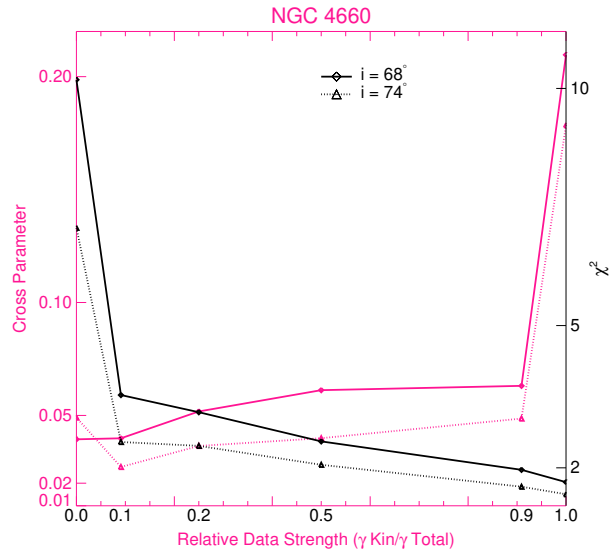


Figure 2.14: The total kinematic χ^2 (black, right y -axis) and the cross parameter c_{30} (pink, left y -axis) vs the relative data strength. The larger the relative data strength (γ Kin/ γ Total), the stronger the kinematics are fitted with respect to the cross term. The maximum is 1, where only the kinematics are fitted without cross term, and the minimum is 0, where only the cross term is fitted without kinematics.

NGC 4697 JAM velocity field models

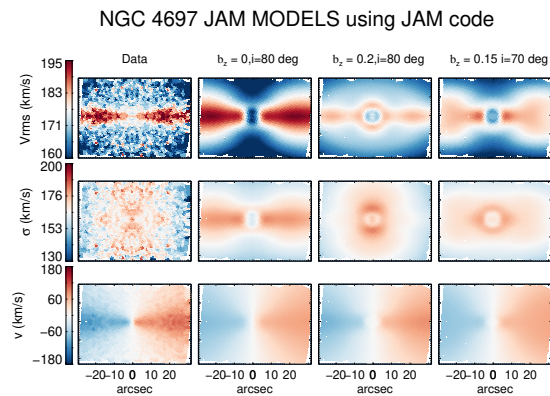


Figure 2.15: The v_{rms} (top row), mean dispersion (middle row), and mean velocity (bottom row) of JAM models for NGC 4697. The first column shows the ATLAS^{3D} kinematic data, column 2 a JAM model with $\beta = 0$, $i = 80^\circ$, column 3 a JAM model with $\beta = 0.2$, $i = 80^\circ$, column 4 a JAM model with $\beta = 0.15$, $i = 70^\circ$.

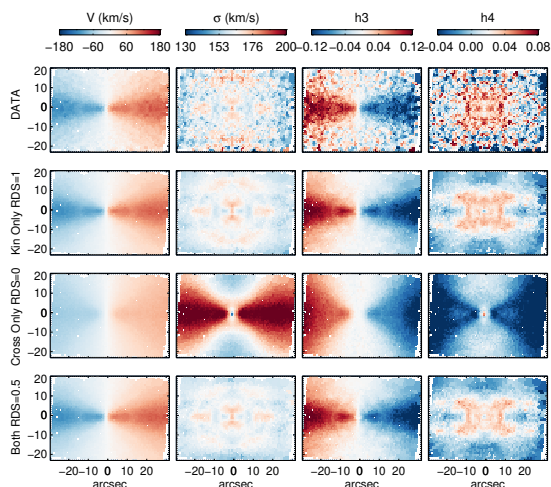


Figure 2.16: The first row shows the ATLAS^{3D} kinematic data, v , σ , and the h_3 and h_4 moments of NGC 4697. The subsequent rows show NMAGIC models of NGC 4697: the kinematics-driven model (second), the JAM constraint only model (third), and a model that uses both the kinematics and JAM constraint with relative data strength $\gamma_{\text{Kin}}/\gamma_{\text{Total}} = 0.5$ (fourth row).

NGC 4697 Internal Kinematics

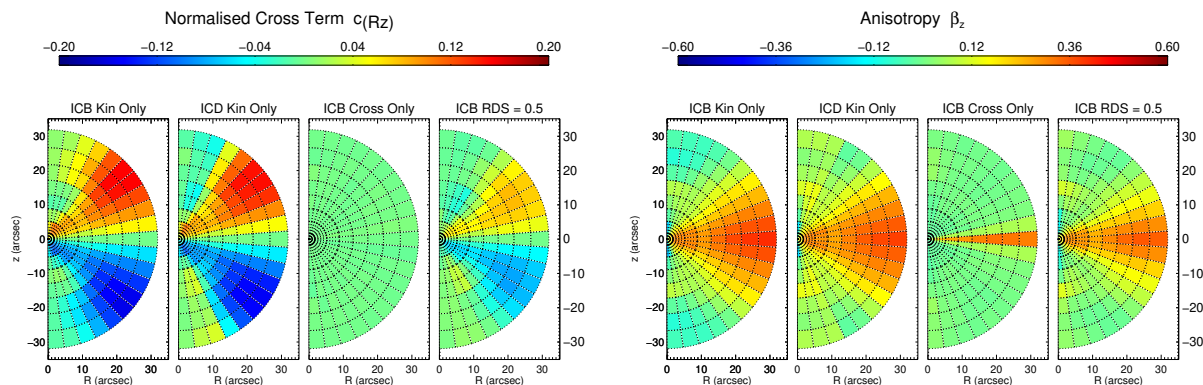


Figure 2.17: The normalised cross term $c_{R,z}$ (left) and the z -anisotropy (right) of NMAGIC models that fit the ATLAS^{3D} kinematics and photometry (left two panels), photometry and JAM constraint (middle panel), and a tension model with $\text{RDS} = 0.5$ (fourth panel in both plots).

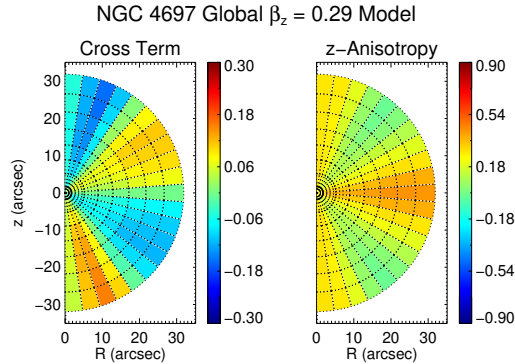
NGC 4697 Global β_z fit

Figure 2.18: Left to Right: The normalized cross term $c_{R,z}$ and z -anisotropy in the meridional plane of NGC 4697 within $30''$ of a model which attempts to fit a global β_z of 0.29 over the whole galaxy. The photometry is well fitted with a χ^2 of 0.00136, with the compromise being made on the β_z fit on the intermediate axes. Forcing a whole galaxy of $\beta_z = 0.29$ more rigidly causes a breakdown of the density fit.

De Lorenzi et al. (2008) and we sample several different β_z , shown in Table 2.4. A JAM model of NGC 4697 was previously made in Cappellari et al. (2013a), with inclination $i = 70^\circ$ and global $\beta_z = 0.29$. On Figure 2.15 we show the best two models we found at each inclination respectively, $i = 80^\circ$ with a global β_z of 0.2 and $i = 70^\circ$ with a global β_z of 0.15. The choice of inclination is shown to have a significant impact on the models kinematics. We also show an isotropic model β_z at $i = 80^\circ$.

NMAGIC dynamical model fits to the kinematic data

Next we make stellar matter only models of the galaxy to the ATLAS^{3D} kinematics in order to understand its dynamical structure without any restrictions on velocity ellipsoid orientation. Similarly to NGC 4660, all four models ICA - ICD reproduce NGC 4697's photometry well. The projected ATLAS^{3D} kinematics are modelled very well for each of the models, shown on Figure 2.16. The internal kinematics, shown on Figure 2.17, are less similar than those for the models of NGC 4660. This is due to the fact that only $1/3 R_e$ is covered by the ATLAS^{3D} kinematic field, in comparison to NGC 4660's $3 R_e$. The freedom this gives the NMAGIC models in terms of orbits is demonstrated by the different internal kinematic structures, while fitting the projected kinematics similarly well.

For all four kinematics-driven models, however, the $\langle v_R v_z \rangle$ term is much larger than 0, meaning that despite the increased level of freedom by the model, none conforms to the JAM assumption.

The only physical JAMs are nearly meridionally isotropic

In order to see how well NGC 4697 can be reconstructed when only the JAM assumption is applied we make a series of models, just as in Section 2.4.3 for NGC 4660, which use only the photometry as an observable, with the JAM assumption as additional constrain we find that when the $\langle v_{Rv_z} \rangle$ term is used as an observable only one internal structure is arrived at, a meridionally isotropic one (Figure 2.17). This model is a very bad fit to the σ -data (see Figure 2.16) of NGC 4697.

A model is also made fitting the photometry and a constant anisotropy of $\beta_z = 0.29$ for NGC 4697. The fit does not succeed, with the model being isotropic near $\theta = 45^\circ$. This further supports the conclusion that on the intermediate axis, where the spherical and cylindrical alignment regimes differ the most, a constant anisotropy of β_z is not possible, see Figure 2.18.

The tension between the data and the JAM structure

The previous results show a structural difference between the velocity dispersion map of the data and that of the model fitting the cross term. As the cross term model is isotropic, it has many near-circular orbits (e.g. Dehnen & Gerhard, 1993), resulting in the distinctive dispersion shape in the model. This shape is not present in the data, therefore all the models which attempt to fit both quantities display tension most prominently in the velocity dispersion. We investigate this with models which fit both the cross term and the kinematics, parametrised by the relative data strength parameter (RDS) defined in Section 2.4, $\gamma_{\text{Kin}}/\gamma_{\text{Total}} = 0.2$. Models with $\text{RDS} \leq 0.2$ show a prominent “x-shape” in the σ -map, models with $\text{RDS} \geq 0.8$ fit the data well at the price of significant c_{Rz} and β_z variations. The compromise model with $\text{RDS} = 0.5$ is shown in Figures 2.17 and 2.16. It provides a reasonable fit to the data, with total reduced χ^2 of the ATLAS^{3D} kinematics of 0.422, and a cross parameter of 0.0469 which is about half that in the JAM constrained only model. These quantities are shown on Figure 2.19.

Inclination

We repeat the previous analysis for an inclination of 70° , as used in Cappellari et al. (2013a). Results are shown as the dashed line on Figure 2.19. The models with inclination 70° display the same trend of kinematic χ^2 and cross parameter with relative data strength (RDS). They generally have a higher χ^2 and higher cross parameter than for 80° , so in contrast to the JAM models of Cappellari et al. (2013a) our models prefer 80° . This is different than for NGC 4660, where we agree with Cappellari et al. (2013a) for the inclination.

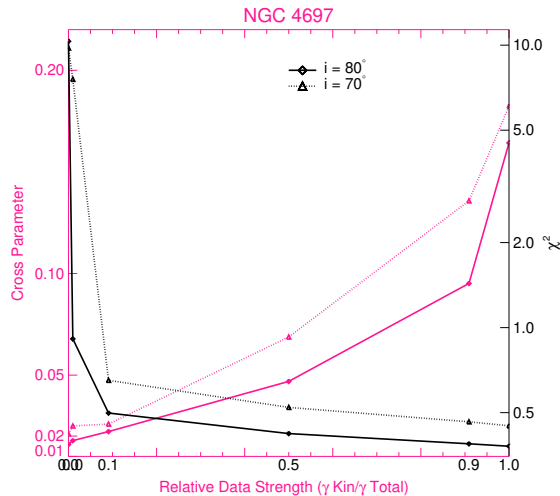


Figure 2.19: The total kinematic χ^2 (black, right y -axis) and the cross parameter c_{30} (pink, left y -axis) versus the relative data strength for NGC 4697. The larger the relative data strength ($\gamma_{\text{Kin}}/\gamma_{\text{Total}}$), the stronger the kinematics are fitted with respect to the cross term. The maximum is 1, where only the kinematics are fitted without cross term, and the minimum is 0, where only the cross term is fitted without kinematics.

In summary, the models for NGC 4697 are qualitatively similar to those for NGC 4660, and all the conclusions from Section 5 are confirmed.

2.5.2 Models with dark matter halo

Having shown that NGC 4660 and NGC 4697 show the same velocity ellipsoid alignment behaviour using models without dark matter, we now investigate the effect of the velocity ellipsoid alignment on models with dark matter halos in NGC 4697. We use parametric dark matter halos as in De Lorenzi et al. (2008) with a logarithmic potential (Binney & Tremaine, 2008):

$$\phi_{\text{D}}(R', z') = \frac{v_0^2}{2} \ln(r_0^2 + R'^2 + \frac{z'^2}{q_\phi^2}), \quad (2.16)$$

where v_0 and r_0 are constants that determine the mass and shape of the potential, q_ϕ is the axis-ratio of the potential, and R' and z' are cylindrical coordinates with respect to the halo equatorial plane. In Table 2.2 the parameters used to generate a selection of dark matter halos from low to high dark matter content are given, labelled A–K.

In this section, we use both SLUGGS (see Section 2.2.3 for details) and ALTAS^{3D} kinematics to constrain the models, using the more extended range to probe the dark matter

Dark Matter Models

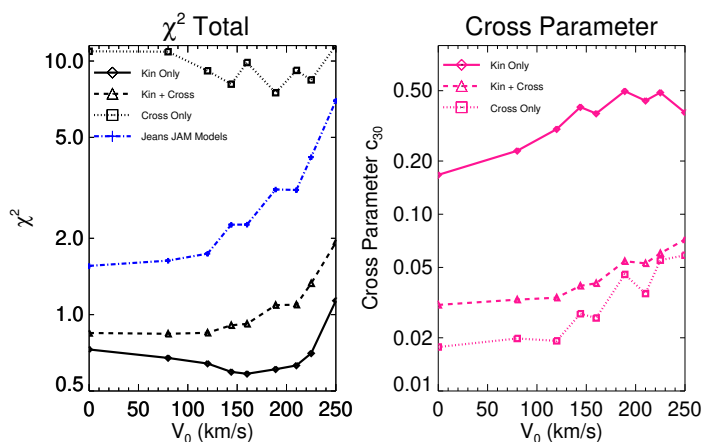


Figure 2.20: Left: Total reduced χ^2 (combining Photometry, ATLAS^{3D} and SLUGGS kinematics) of three different model types of NGC 4697 against dark halo velocity parameter v_0 . In the case of halos D with $q = 0.9$ and F with $q = 0.9$, v_0 is given by v_0q . The different model types are indicated on the graph. Right: The cross parameter with dark matter matter halo parameter v_0 for the same models of NGC 4697. The JAM condition is perfectly enforced when the cross term parameter is 0. This shows that the χ^2 of the models which do not enforce the JAM condition is better than those that enforce it, and that the more the JAM condition is enforced, the worse the fit to the kinematics.

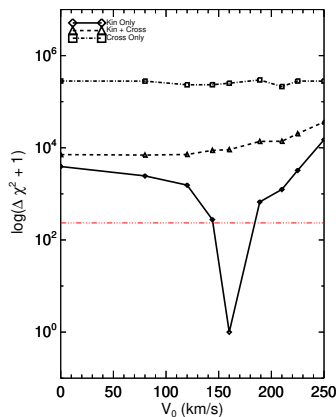


Figure 2.21: The $\Delta\chi^2 = \chi^2 - \chi_{\min}^2$ (ATLAS^{3D} and SLUGGS kinematics) of different model types of NGC 4697 against dark halo velocity parameter v_0 . The models shown are those which only use SLUGGS and ATLAS^{3D} kinematics as an observable (bold line) and the model which fits SLUGGS, ATLAS^{3D} and the JAM condition (dashed line), as well as the models which only enforce the JAM condition (dotted-dashed line). Note the large difference in scale. In the case of halos D with $q = 0.9$ and F with $q = 0.9$, v_0 is given by $v_0 q$. The red line indicates the 1σ confidence level for the best fitting model.

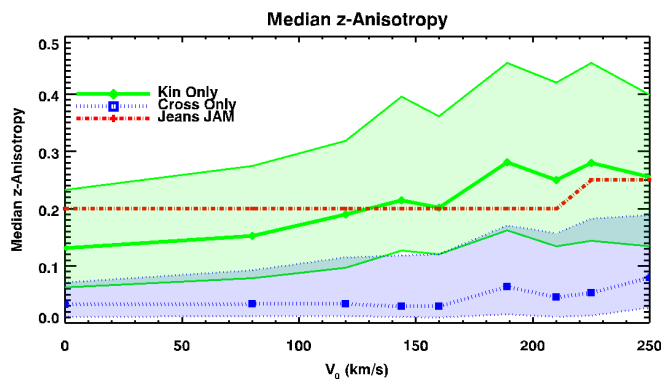


Figure 2.22: The median (50% percentile) anisotropy β_z of NMAGIC models of NGC 4697 against dark halo parameter v_0 . The bold line gives β_z of the models which use only the SLUGGS and ATLAS^{3D} kinematics as an observable. The dotted line gives the β_z of models which use only the JAM assumption. The shaded regions give the 30% and 70% percentiles.

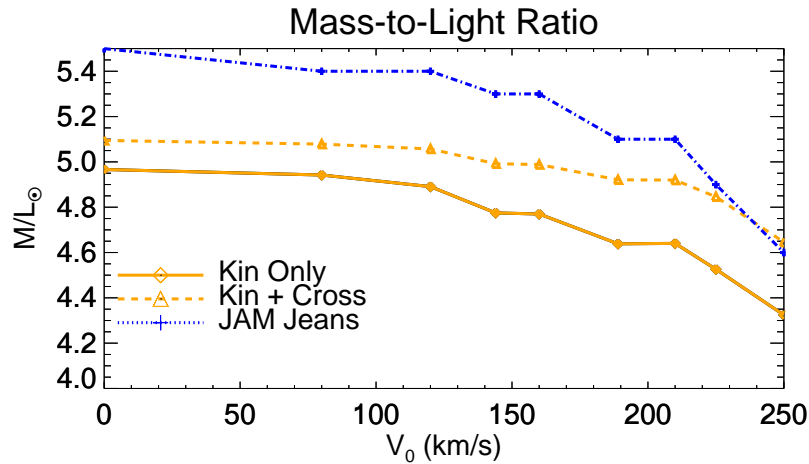


Figure 2.23: The Mass-to-Light Ratio of NMAGIC models of NGC 4697 against dark halo parameter v_0 . The bold line gives M/L of the models which use only the SLUGGS and ATLAS^{3D} kinematics as an observable. The dashed line gives the M/L of models which use the kinematics and the JAM assumption as a constraint, which is higher for every dark halo. The blue line shows the M/L of JAM Jeans models, which are even higher.

in NGC 4697. We again construct three different types of models:

- Models which use the photometry and kinematics as fitted observables without JAM assumption (“Kin Only”)
- Models which use only the photometric an JAM assumption with no fitted kinematic observables (“Cross Only”)
- Models which use the photometry, kinematics as fitted observables as well as the JAM assumption (“Kin + Cross”)

The third type of model demonstrates the “compromise” model between fitting the kinematics well and the JAM assumption well. We compare these models to the 2D kinematic field of ATLAS^{3D}, as in other sections. We also compare to the 2D SLUGGS velocity field, in order to assess the projected kinematics at large radii. As the SLUGGS kinematic fields are partially analytically extended we also compare our models to the original SLUGGS data, presented on 1D elliptical radii, by Foster et al. (2016).

Kinematics-driven dark matter halo models

We find models with several different dark matter halos which fit both the ATLAS^{3D} and SLUGGS kinematics well. The intermediate dark matter potentials D and F reproduce

the kinematics best, with lower mass dark matter potentials A-C, and higher mass potentials J09 and K having a higher χ^2 for the combined ATLAS^{3D} and SLUGGS kinematics (Figure 2.20). The velocity dispersion is the biggest discriminator between the models, with v , h_3 and h_4 being similarly well fitted between the models, due to the large errors on those quantities. Figure 2.20 shows that several models are fitted well, but due to the large number of data points the best fitting model is quite well determined statistically. Figure 2.20 has a total reduced χ^2 of about a minimum of 0.6 rising lightly to 0.7 (A) and 1.05 (K). Even though many of these points have a reduced $\chi^2 < 1$, they may not all work as models due to the sheer number of points.

A modified $\Delta\chi^2$ method from Zhu et al. (2018) is used to demonstrate this, shown on Figure 2.21. The reason why we use this and not the more common $\Delta\chi^2$ method is because the model prediction for each fitted model at a given data point has noise of order the observable error. Different from, e.g., an analytic model which predicts one and only one value for each data point for both the right model and any wrong model. In Zhu et al. (2018) they show that the models fluctuate depending on small perturbations to the data, and verify that the model errors are of order $\sqrt{2N_{\text{kin}}}$. We therefore calculate the 1σ confidence level as $\sqrt{2N_{\text{kin}}} = 233$, shown as a red line on Figure 2.21. Halo D09, with an axis ratio of $q = 0.9$, fits the kinematics best, provided the χ_{min}^2 subtracted from all the χ^2 values. The 1σ confidence interval is derived from the number of SLUGGS observables (17600) and number of SAURON observables (9400), where $N_{\text{obskin}} = 4N_{\text{binkin}}$.

In all of our fits we place primary importance in reproducing the photometry of the galaxy very well, which is achieved in all our model fits, so it is not a good discriminating quality between models. All models in this section achieve a photometric χ^2 of 0.0035 or below.

We thus obtain a good model to the data using only the kinematics as constraints, with halos D and D09 being preferred above F and F09 and with halos A and K excluded as viable for this galaxy. We stress that all the models have significant non-zero cross terms, shown on Figure 2.20, ranging from A with the lowest value of 0.17 for the cross parameter, to halo K with the highest value of 0.38, and a trend present of increasing cross term with increasing dark matter halo v_0 . Halos D and F with a spherical halo have larger cross terms than their counterparts D09 and F09 which are slightly flattened.

Both models with no dark matter content (A) and the high dark matter models (K) are far above the 1σ confidence interval. The 2D SLUGGS data is modelled data designed to demonstrate that using data with these properties can be used to discriminate between different dark matter halo models using NMAGIC. The confidence level following Zhu et al. (2018) rules out models with no dark matter content and high data content for these amount of modelled data points and corresponding error.

We also compare our models to the original 1D kinematic data from Foster et al. (2016),

coming to the same conclusions regarding preferred and worst fitting halos.

Cross Term Only Dark Matter Models

We next use the JAM constraint fitting the $\langle v_R v_z \rangle$ term to be 0 for dark matter halos A to K. These models fit the photometry data well, with all χ^2 remaining below 0.041.

Figure 2.20 shows that the lowest value of the cross parameter is achieved by the stellar-only model, labelled A, of 0.017. A clear trend can be observed, with larger dark matter halos having higher cross term values. Previously we discussed larger anisotropies lead to larger cross terms, which is also confirmed here, on Figure 2.20, where larger dark matter halos, which lead to larger anisotropies for all model types and therefore larger cross terms. The z -anisotropies of the cross term only models, although varying slightly with dark matter halo, are all close to isotropy, just as the models for NGC 4660. On Figure 2.22 we show the median z -anisotropy with the 30% and 70% percentile, comparing the cross term only and the data driven models. It shows that while the data driven models have an internally varying non-zero anisotropy, with a strong trend with dark matter, the cross term only models remain nearly meridionally isotropic.

These models were not evolved to minimise the χ^2 of either the SLUGGS or ATLAS^{3D} kinematic data. Therefore there are significant deviations for velocity, dispersion, h_3 and h_4 to the data. Comparing the full 2D kinematic field to the data and successful fit to the kinematics for halo D, in particular the distinct “X”-shape in the velocity dispersion can be noted, in clear morphological contrast to the kinematic data (see Figure 2.E.2). This “X”-shape is thought to be caused by the circular orbits required for isotropy, and therefore the $\langle v_R v_z \rangle = 0$. We can therefore conclude these models are very different from the kinematic data in several respects.

Kinematics and Cross Term Dark Matter Models

Our last “Kin + Cross” sequence of models explores whether models can be found in the sequence of dark matter halos that strike a useful compromise between matching the Atlas3D and SLUGGS data and having the dynamical structure of the JAMS. Figure 2.20 compares such models with $RDS = 0.1$ to the previous “Kin Only” and “Cross Only” model sequences in their $\Delta\chi^2 = \chi^2 - \chi_{\min}^2$ values and c_{30} parameters. From these values is clear that using both the kinematics and the JAM parameters has not resulted in a model which fits both the JAM condition and the kinematics as well as the respective previous model sequences, but compromises by conforming to both constrains less well. This compromise is further apparent in the velocity dispersion maps of the models which show it is a slightly more rounded X-shape, an average between the elliptically shaped kinematic data and the

X-shape required by the isotropic orbits needed to produce a $\langle v_R v_z \rangle$ term close to 0. In terms of internal kinematics this tension is shown on Figure 2.22, where the z -anisotropy of the “Kin + Cross” Model is considerably lower than for the “Kin Only” models, but higher than the “Cross Only” models.

It is important to note that, due to the restrictions on anisotropy, these models fit less well with increasing dark matter halo mass (v_0). The best model in terms of total χ^2 and c_{30} parameter is halo A. This leads to the conclusion that, if the JAM condition were enforced both strongly (“Cross”) or partially (“Kin + Cross”), that halo A would be preferred by the data (i.e., without dark matter). Whereas halo D with a moderate dark matter halo is preferred when only the data are fitted. Thus using JAM-like models to measure properties such as the dark matter fraction in galaxies may induce biases in the results.

Jeans JAM models

Jeans JAM models were made to the ATLAS^{3D} and SLUGGS 2D kinematics as in Sections 2.4.1 and 2.5.1 with the same dark matter halos as used in the previous sections. On Figure 2.20 the reduced χ^2 of the JAM is shown, with the lowest reduced χ^2 being that of the model with no dark matter (A). Furthermore, a χ^2 trend is displayed with halos with dark matter content. Models with less dark matter have a lower reduced χ^2 . This same trend is displayed by the NMAGIC models compromising between the JAM condition and kinematics, but not by the NMAGIC kinematics models which produce the best model. The NMAGIC models for the modelled SLUGGS 2D data prefer a region around model D90, the Kin+Cross models and the (Jeans) JAM models would prefer model A, not the best model D90. Using the modelled SLUGGS 2D data we therefore demonstrate that for 2D data with these properties the Jeans JAM method results in a different dark matter halo than the NMAGIC method. Therefore this is an example where JAM modelling does not get the best dark halo model from the data.

2.5.3 Total Density Slopes

Finally, we investigate the density slopes of the combined stellar and dark matter components for each of the halos of the kinematics-driven models, shown in Figure 2.24. The purple shades the area between our best two halo models D and F, i.e. the region of density which fits the data best, with grey power laws shown for reference. The SLUGGS data extent is to $\sim 1.5R_e$ ($\log(r/R_e) = 0.4$).

The entire density profile is not well represented by a single power law $\rho \propto r^{-\alpha}$, so to describe its slope we fit three: One for between $0.1R_e - 0.5R_e$ (central fit), one for

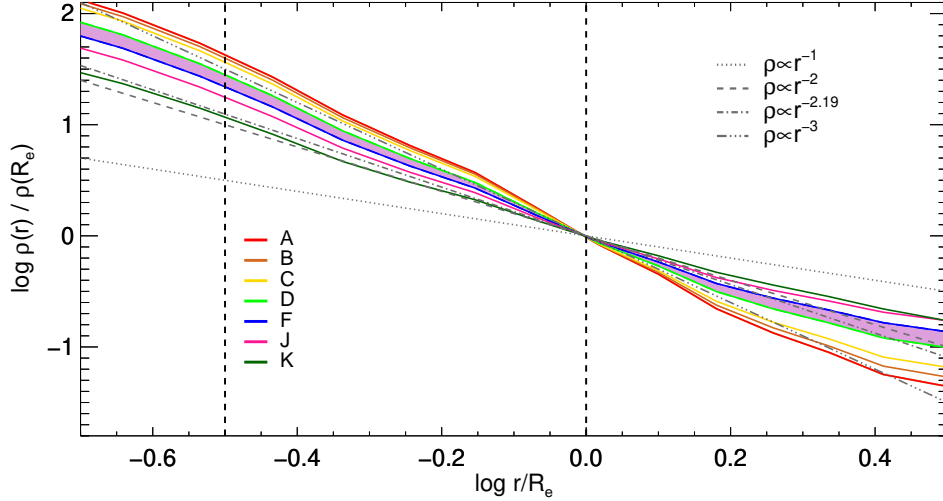


Figure 2.24: The total density slopes of the different stellar and dark halo models A-K. The purple-shaded region connects models D and F for which the combined photometry and SLUGGS and ATLAS3D kinematics are fitted best, with similarly good χ^2 . Various single power-law slopes are plotted for reference. The vertical dashed lines separate the regions for which separate power-law slopes are given in the text.

$0.5R_e - 1R_e$ (inner fit) and one for between $1R_e - 1.5R_e$ (outer fit). The central fit is quite similar for all halos, being dominated by stellar matter with a best slope of $\alpha_C = 2.08$ for halo D and $\alpha_C = 2.04$ for halo F. The inner fit gives $\alpha_I = 2.82$ for halo D and $\alpha_I = 2.58$ for halo F. For the outer fit, we find $\alpha_O = 2.05$ for halo D and $\alpha_O = 1.74$ for halo F. This indicates a strong baryonic concentration within a flattened dark matter halo, but the details may depend on our choice of models.

2.6 Negative Weights

Having found no physical (positive) distribution functions with cylindrically aligned velocity ellipsoids, we test whether allowing negative weighted particles in NMAGIC, and therefore an unphysical distribution function, allows this. We modified NMAGIC to allow

Halo Name	r_0/R_e	v_0 (kms ⁻¹)	q_ϕ
A	0	0	1.0
B	3.88	80	1.0
C	3.88	120	1.0
D	2.96	160	1.0
D ($q = 0.9$)	2.96	160	0.9
F	2.96	210	1.0
F ($q = 0.9$)	2.96	210	0.9
J ($q = 0.9$)	2.96	250	0.9
K	1.97	250	0.8

Table 2.2: The dark matter halo code is given in Column 1, with the parameters r_0, v_0 , and q_ϕ used to parametrise the dark matter halo in Equation 2.16. The effective radius $R_e = 96.4''$ of NGC 4697 is used here.

negative weights. This is done by altering the entropy term to allow negative weights.

2.6.1 Method

The purpose of the entropy term in the force-of-change equation is to keep the weights of the particles close to the prior, preventing effects such as very massive particles. The larger the μ term in the force-of-change equation, the smoother the distribution function of the model. If the μ term is too small, the model will be very noisy, with very large particles, while if the entropy is too large, the particle weights cannot change sufficiently to model the data. For conventional NMAGIC fits, the entropy equation is set such that the weight of the particles cannot become zero or negative.

The typical entropy equation used is:

$$S = - \sum_i w_i \ln(w_i / \hat{w}_i), \quad (2.17)$$

where \hat{w}_i are the prior, and w_i the current weights of the model. In order to allow the particles to have negative weights, the entropy equation and the force-of-change equations have been modified. The new entropy equation used is:

$$S = \sum_i \frac{1.0 - \left(\frac{w_i - \hat{w}_i}{\hat{w}_i}\right)^2}{q^2} \hat{w}_i \quad (2.18)$$

which yields

$$\frac{\delta S}{\delta w_i} = \frac{-2(w_i - \hat{w}_i)}{\hat{w}_i q^2} \quad (2.19)$$

Entropy Plots

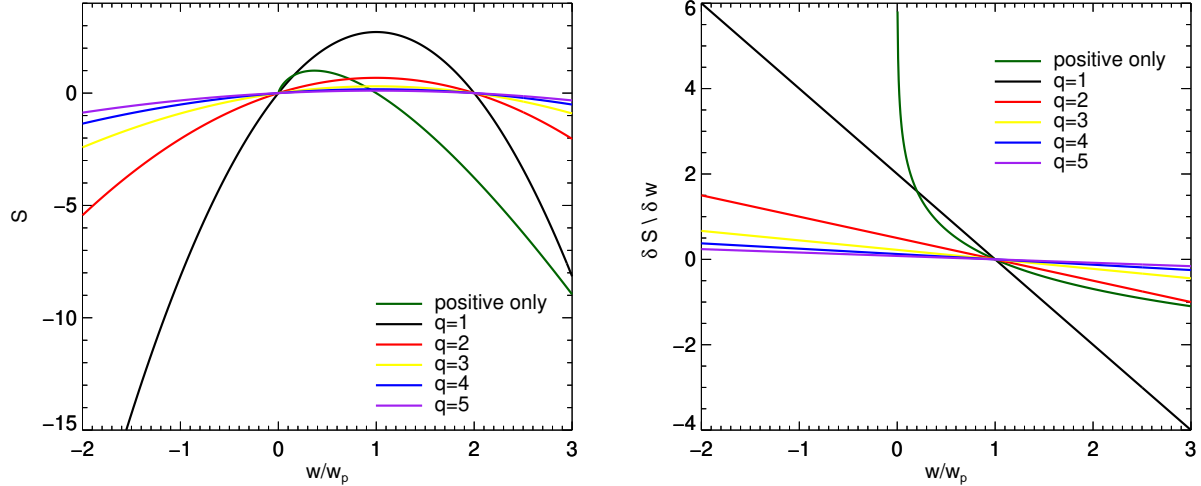


Figure 2.25: The entropy S in arbitrary units (left) and the change of entropy with time (right) $\delta S / \delta w_i$, where the dark green is the ‘standard’ entropy curve, and the other curves show the entropy with different values of q allowing negative weights, on the y -axis, and on the x -axis a range of weights normalised by a constant prior weight.

The equation to change the weights of the particles (force-of-change) usually contains a factor of w_i , which is replaced by \hat{w}_i , where \hat{w}_i are all positive:

$$\frac{dw_i}{dt} = \epsilon \hat{w}_i \left[\mu \frac{\delta S}{\delta w_i}(t) - \sum_j \frac{K_j[z_i(t)]}{Y_j} \Delta_j(t) \right] \quad (2.20)$$

The parameter q used in Equation 2.18 to control the slope of the entropy term, a smaller term being less permissive to negative weights, shown on Figure 2.25. On Figure 2.25 equations 2.18 and 2.19 for several different values of $q = 1, 2, 3, 4, 5$ are compared to the original entropy Equation 2.17.

2.6.2 The effect of using negative weights on JAM assumptions

Having shown that the only JAM condition conforming model with a real distribution function found is a nearly isotropic model, we test whether allowing negative particles allows the model more freedom to conform to the JAM condition. We therefore make a series of models to NGC 4697, fitting the JAM condition using entropy which allows negative particles. By altering the slope of the entropy through altering the q parameter, with examples shown on Figure 2.25, we allow the models to have more or less negative particles. We use $q = 1, 2, 3, 4$ and 5 .

We find that, despite allowing the model to have the freedom to have negative particles, the cross parameter $c_{(R,z)}$ is still lowest for the positive distribution model presented in Section 2.5. A possible explanation for this effect is that the orbits allowed in a distribution function are still fixed despite allowing negative particles. Adding some negative particles does not allow deviation from these fixed orbits, and therefore a similar behaviour in the alignment of the velocity ellipsoid. Instead the negative particles are treated by the model as a means of weighting some orbits more strongly than others, in the same way that in a positive model the weights of the particles are changed from high to low for certain orbits. This is supported by the distribution of the weight of the particles in a negative model, the majority of negative particles are of a low weight, with the amount of negative particles increasing with increasing q as expected.

In addition to the $\langle v_R v_z \rangle$ term models we also tested the concept of a single global β_z using negative particles, with the β_z for several different q values for a $\beta_z = 0.29$. The same issue non-conformity to a total β_Z along the intermediate axis of the galaxy is shown for the models which include negative particles, with no change shown with respect to the positive only model of Section 2.5, also shown on the Figure.

2.7 Summary and Discussion

In this article we study the distribution function of two galaxies, NGC 4660 and NGC 4697. For NGC 4660, the ATLAS^{3D} IFU covers $3 R_e$, meaning the galaxy is very well constrained. In Section 2.4 we construct a series of stellar-only models in NMAGIC. For the four different initial models tested (ICA-ICD), the kinematic without JAM constraint models resulted in models with very similar projected and internal kinematics, with anisotropy throughout the galaxy. When the JAM constraint is applied, the resulting models equally all have very similar properties, with the projected kinematics representing the ATLAS^{3D} data less accurately than when no constraint is applied.

The internal kinematics of the NGC 4660 models with the JAM constraint applied show a cross term close to zero in all areas except close to the major axis. The z -anisotropy vanishes in the areas where the cross term is zero, and is radial in the major axis areas where the cross term is non-zero. For this galaxy, we are thus unable to find a model that fits the photometry with a global zero cross term. We conclude that, in order to have a zero cross term in a physical model, the z -anisotropy has to also be zero, making orientation of the velocity ellipsoid irrelevant. Since NGC 4660 has a strong disk, total isotropy cannot be reached along the major axis, leading to deviations of the cross term close to the major axis.

In contrast, the NGC 4697 galaxy has only $1/3$ of R_e covered by the ATLAS^{3D} IFU. In addition, it is more massive than NGC 4660 with a less strong disk. Performing the

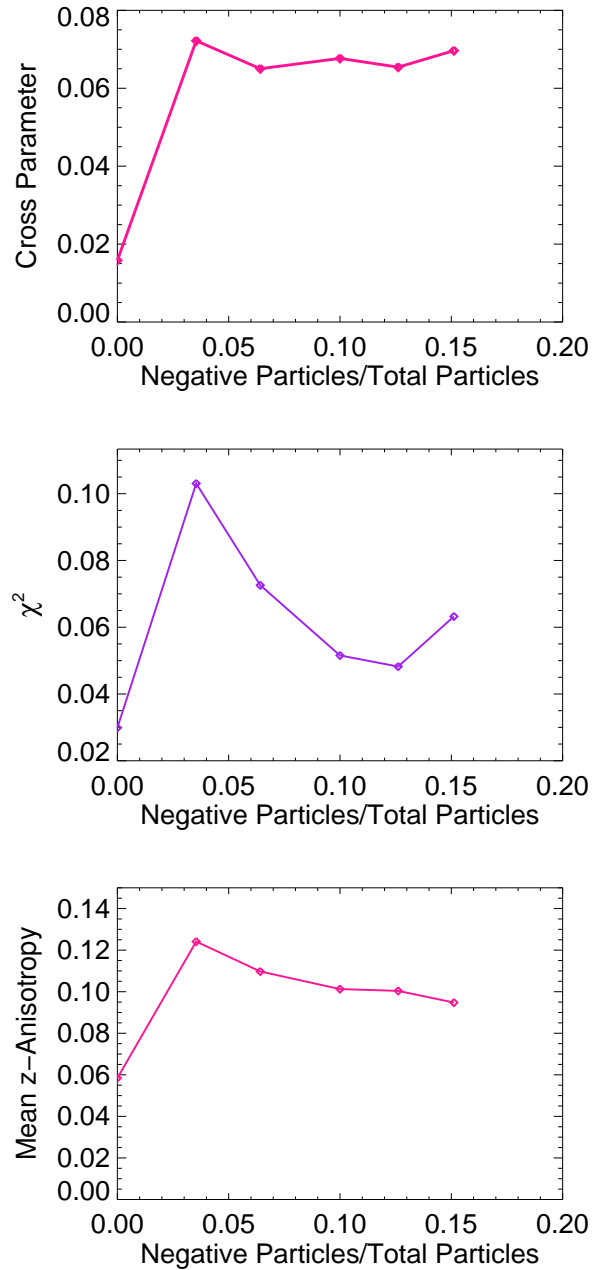


Figure 2.26: The cross term parameter, photometric χ^2 , and mean β_z of models compared to negative particle fraction in the entire model. The different negative particle fractions are achieved by changing the q parameters from the entropy equation 2.18. The higher the q parameter, the more negative particles present in the model.

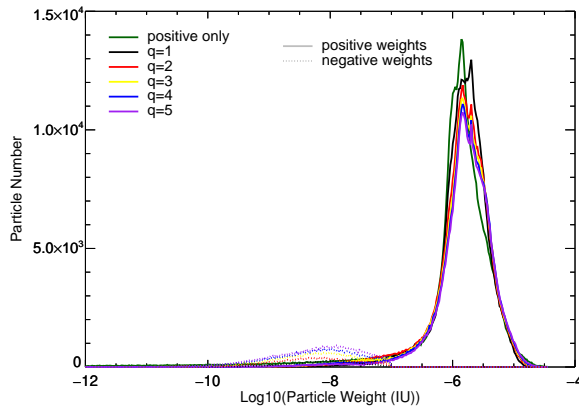


Figure 2.27: Histogram of the negative weights in models where the JAM condition is enforced.

same analysis as for NGC 4660, we construct a series of models with stellar matter only for NGC 4697 with four different initial models as described in Section 2.5. For the models to the kinematics and without a JAM constraint the projected ATLAS^{3D} kinematics and density are similarly well fit for all initial models. The internal kinematics, however, vary depending on which initial model is used. A coverage of $1/3$ of R_e is not sufficient to discriminate between different internal anisotropy structures. When the JAM condition is enforced on the NGC 4697 models, the cross term is well fitted to be zero globally. However, the resulting models both do not match the ATLAS^{3D} kinematics well, and have similar internal structures, independent of the initial model. This similar internal structure, just as with NGC 4660, is consistent with isotropy when the cross term is zero. There is not sufficient coverage to discriminate between different internal structures when the JAM condition is not applied. However, when the JAM condition is applied, the same internal structure of isotropy always results.

We test two inclinations for both galaxies. For NGC 4660 these are 68° (Cappellari, 2008) and 74° (Cappellari et al., 2013a). We find that an inclination of 74° is a better match to the data both when unconstrained and constrained by the JAM condition. For models unconstrained by the JAM condition we find a 1% difference in M/L , as NGC 4660 is very well constrained by the kinematics. The difference in M/L between models that enforce the JAM condition and do not use NMAGIC is $\approx 1 - 2\%$ for the tested inclinations of 68° and 74° . This difference increases for models made using the JAM modelling technique. It lies in the range of $7 - 12\%$ for 74° and $2 - 7\%$ for 68° . For both M/L values the difference increases with increasing JAM model anisotropy. Comparing to the value for the mass-follows-light models from Cappellari et al. (2013a), we find a 3% lower M/L .

The two inclinations tested for NGC 4697 are 70° (Cappellari et al., 2013a) and 80° (Dejonghe et al., 1996; De Lorenzi et al., 2008). Applying the stellar-matter-only mod-

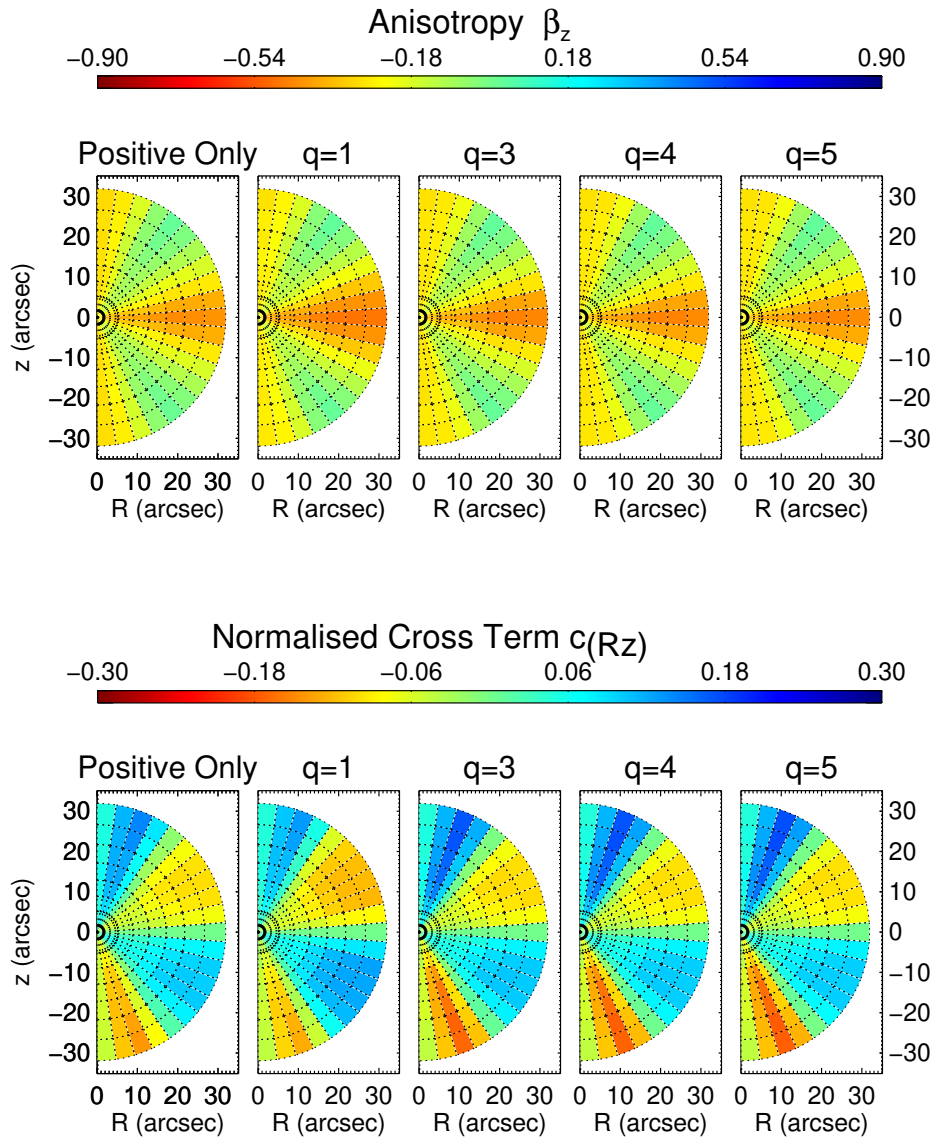


Figure 2.28: The z -anisotropy (top) and the cross term (bottom) of NGC 4697 models with global targets $\beta_z = 0.29$. For left to right: a model with only positive weight particles, and four models with negative weight particles with increasing parameter $q = 1, 3, 4, 5$, and therefore increasing negative particle fraction.

els to the ATLAS^{3D} kinematics only, leaving the JAM condition unconstrained, we find that the M/L differ between these inclinations by 0.4%. When the unconstrained models are compared to the NMAGIC models constrained by both the kinematics and the JAM condition, their M/L differ in the range (4–7)% depending on the relative weighting of kinematics and cross term constraint. The JAM models made using the JAM modelling technique for 80° give values between 9% and 18% for the stellar-only model with varying anisotropies. The conclusion is therefore that the M/L derived from JAM techniques are to be interpreted with care, as they can vary from those found using a physical model by amounts between 2% and 18% depending on the chosen galaxy.

Li et al. (2016) performed JAM fits on Illustris simulation galaxies, calculating their recovery of total mass, and stellar and dark matter, as well as inclination and anisotropy. Their error of recovery of galaxy characteristics depends on the JAM models and the limitations of simulated galaxies. In their tests on two individual galaxies they find an M/L discrepancy of 2% for one case and 140% for another. The second much larger discrepancy is, however, caused by a low-resolution MGE fit resulting in an underestimation of the stellar density in the inner part of the galaxy. They find their error on the M/L for the total sample to be (30 – 40)%, degenerate with dark matter recovery. They conclude that with improved simulation resolution this error might be improved. In addition, they find that their error in recovering stellar mass depends on galaxy shape. For prolate and triaxial galaxies the recovered stellar masses are 18% higher and the dark matter masses are 22% lower. The total mass, however, is recovered within 10%. Given the different analysis and approach, comparing these results to Li et al. (2016) is not straightforward, but the general finding that output properties from JAM should be treated with care depending on the galaxy characteristics stands.

In order to constrain the models at more extended radii, we use the SLUGGS kinematic data out to $2.5 R_e$. The extended kinematics constraining the orbits at large radii, where the dark matter most affects the orbits, allows us to investigate how the JAM constraint relates to dark matter in Section 2.5.2. A series of five models constrained by both the ATLAS^{3D} and SLUGGS kinematics found that a moderate dark matter halo, D , with $v_0 = 160 \text{ km s}^{-1}$, is the best representation of the data. When the JAM constraint is applied to the models, we find great shape differences in kinematics to the data, especially the velocity dispersion. No good model representation of the data is found. The internal structure, just as found in NGC 4660 and in the NGC 4697 ATLAS^{3D} JAM condition models, is isotropic where the cross term is zero, which applies globally in this case.

In addition, the potential which is the closest to the kinematic data of the models is A, which contains no dark matter. The galaxy models that have more dark matter also have increased anisotropy. As we have shown, isotropy is required for the JAM condition to be enforced, which could explain the reason why, contrary to expectation for this galaxy, the stellar-only model is favoured by (Jeans) JAM condition models. This is in contrast to the kinematics-driven NMAGIC models which do not favour a particular dark matter

configuration. Therefore using JAM models to differentiate between different dark matter distributions is not reliable.

Using cosmological simulations and strong lensing data, Remus et al. (2013) find that elliptical galaxies move towards a total density slope of $\alpha = 2$, converging to this eventual slope with each merger. In the analysis of Cappellari et al. (2015), a sample of 14 galaxies using JAM modelling to the v_{rms} data of ATLAS^{3D} and SLUGGS is combined. They find that the total density slope, containing both dark and baryonic matter, is tightly constrained with $\alpha = 2.19 \pm 0.03$. For NGC 4697 they find a slope of $\alpha = 2.23 \pm 0.023$ for the total slope for the whole radial range. For the region within one R_e , they find a slope of $\alpha_I = 2.16$ and for R_e in the range 1–4 they find $\alpha_O = 2.34$. Comparing the inner value of the slope of $\alpha_I = 2.16$ to the inner range value of $\alpha_I = 2.58 - 2.82$ for our best models, we find a steeper slope than Cappellari et al. (2015). The outer range of our best models, $\alpha_I = 1.74 - 2.05$, compared to their outer value of $\alpha_O = 2.34$, is more shallow. We demonstrate that for this galaxy the model which best represents the ATLAS^{3D} and SLUGGS kinematics is not a single power law.

2.8 Conclusions

The results described in this chapter suggest that the only JAM models with physical distribution functions are nearly meridionally isotropic, and that JAM models with constant $\beta_z \neq 0$ are unphysical. JAMs are nonetheless useful to estimate approximate M/L ratios for ETGs. However, relative best-fit comparisons between JAM models in different potentials to infer dark matter profiles or IMF variations may be unreliable and need to be verified by dynamical models with unconstrained VEs.

Table 2.3: Table of different characteristic parameters of the models of NGC 4660. The columns are: (1) If the A_{lm} is fitted for this model, (2) if ATLAS^{3D} kinematics are fitted for this model, (3) if the cross term is fitted for this model, (4) which initial model is used in this model, (5) the total χ^2 of the model with the ATLAS^{3D} kinematics, (6) the χ^2 of the velocity v of the model with the ATLAS^{3D} v , (7) the χ^2 of the velocity dispersion σ of the model with the ATLAS^{3D} σ , (8) the χ^2 of the h_3 moment of the model with the ATLAS^{3D} h_3 , (9) the χ^2 of the h_4 moment of the model with the ATLAS^{3D} h_4 , (10) the χ^2 of the density of the model with the density from the deprojected MGE photometry, (11) the cross $c_{(R,z)}$ parameter, (12) the standard deviation on the cross $c_{(R,z)}$ parameter, (13) the Mass-to-Light Ratio in $M_\odot/L_{\odot,r}$ fitted within NMAGIC, (14) the relative data strength $\gamma_{\text{Kin}}/\gamma_{\text{Total}}$, (15) inclination in degrees.

A_{lm}	ATLAS ^{3D} Kinematics	Cross Term	Initial Model	ATLAS ^{3D} χ^2	$v \chi^2$	$\sigma \chi^2$	$h_3 \chi^2$	$h_4 \chi^2$	A_{lm} χ^2	$c_{(R,z)}$ param	$c_{(R,z)}$ param σ	M/L	$\gamma_{\text{Kin}}/\gamma_{\text{Total}}$	i
Yes	Yes	No	ICA	1.68	1.57	1.62	2.21	1.30	0.64	0.235	0.044	4.77	1	68
Yes	Yes	No	ICB	1.70	1.61	1.64	2.20	1.35	0.78	0.210	0.035	4.77	1	68
Yes	Yes	No	ICC	1.74	1.64	1.71	2.28	1.33	0.53	0.357	0.052	4.74	1	68
Yes	Yes	No	ICD	1.69	1.59	1.58	2.26	1.34	0.53	0.234	0.045	4.76	1	68
Yes	No	Yes	ICA	11.36	26.42	12.86	3.84	2.30	0.084	0.039	0.042	-	0	68
Yes	No	Yes	ICB	10.182	21.58	13.28	3.49	2.38	0.069	0.043	0.042	-	0	68
Yes	No	Yes	ICC	12.63	27.48	15.77	3.73	3.51	0.15	0.048	0.042	-	0	68
Yes	No	Yes	ICD	10.98	24.76	12.78	3.94	2.43	0.051	0.052	0.067	-	0	68
Yes	Yes	Yes	ICA	1.95	1.73	2.16	2.41	1.49	0.109	0.060	0.032	4.82	0.91	68
Yes	Yes	Yes	ICB	1.96	1.74	2.13	2.48	1.48	0.0935	0.063	0.031	4.82	0.91	68
Yes	Yes	Yes	ICC	2.00	1.84	2.21	2.45	1.49	0.265	0.080	0.052	4.80	0.91	68
Yes	Yes	Yes	ICD	1.96	1.77	2.10	2.47	1.48	0.168	0.066	0.040	4.81	0.91	68
Yes	Yes	Yes	ICA	3.68	3.78	4.34	3.87	2.75	0.329	0.037	0.046	4.75	0.09	68
Yes	Yes	Yes	ICB	3.53	3.49	4.34	3.70	2.61	0.298	0.040	0.044	4.76	0.09	68
Yes	Yes	Yes	ICC	3.50	3.57	4.47	3.40	2.59	0.557	0.058	0.055	4.79	0.09	68
Yes	Yes	Yes	ICD	3.61	3.63	4.38	3.77	2.67	0.903	0.051	0.058	4.76	0.09	68
Yes	Yes	Yes	ICB	3.17	3.04	3.99	3.41	2.25	0.100	0.052	0.033	4.82	0.5	68
Yes	Yes	Yes	ICB	2.56	2.40	2.97	3.04	1.82	0.074	0.0611	0.055	4.76	0.25	68
Yes	Yes	No	ICB	1.44	1.40	1.36	1.85	1.16	0.896	0.179	0.033	4.81	1	70
Yes	No	Yes	ICB	7.06	8.74	14.29	2.51	2.71	0.664	0.0491	0.069	-	0	70
Yes	Yes	Yes	ICB	1.60	1.51	1.60	2.03	1.26	0.0296	0.0486	0.0385	4.82	0.91	70
Yes	Yes	Yes	ICB	2.54	2.41	2.90	3.01	1.85	0.135	0.0272	0.0308	4.77	0.09	70
Yes	Yes	Yes	ICB	2.46	2.32	2.75	2.93	1.84	0.0207	0.0365	0.0565	4.79	0.5	70
Yes	Yes	Yes	ICB	2.06	1.98	2.13	2.56	1.59	0.0233	0.0399	0.0257	4.79	0.2	70

Table 2.4: JAM fit parameters to the ATLAS^{3D} data of NGC 4660 and NGC 4697. Column (1) is the galaxy ID, (2) the anisotropy parameter β_z , kept constant for the whole galaxy, (3) M/L in the SDSS r -band fitted by the JAM method, (3) the rotation parameter κ , defined in Cappellari (2008), (4) the reduced χ^2 of the model with respect to the ATLAS^{3D} v_{rms} data, (5) the reduced χ^2 of the model with respect to the ATLAS^{3D} v_{mean} , (6) the reduced χ^2 of the model with respect to the ATLAS^{3D} velocity. This quantity is not minimised in the fit, instead the projected angular momentum of the model and data are kept as close as possible Cappellari (2008). (7) is the reduced χ^2 of the mean σ of the model with ATLAS^{3D} and (8) is the inclination in degrees.

Galaxy	β_z	M/L	κ	χ^2/DOF			i [deg.]
				v_{rms}	v_{mean}	σ_{mean}	
NGC 4660	0	4.82	0.714	6.73	5.23	9.99	68
NGC 4660	0.05	4.84	7.44	6.14	5.10	8.68	68
NGC 4660	0.1	4.87	0.790	5.58	5.10	7.07	68
NGC 4660	1.4	4.89	0.850	5.16	5.71	5.51	68
NGC 4660	0.15	4.89	0.865	5.06	5.88	5.18	68
NGC 4660	0.2	4.92	0.926	4.63	7.01	4.34	68
NGC 4660	0.23	4.94	0.955	4.43	8.10	4.22	68
NGC 4660	0.25	4.95	0.972	4.32	9.09	4.24	68
NGC 4660	0.3	4.99	1.01	4.21	1.30	4.63	68
NGC 4660	0.35	5.02	1.05	4.39	18.4	5.52	68
NGC 4660	0.4	5.06	1.09	5.01	2.46	6.91	68
NGC 4660	0	5.13	0.728	3.41	8.98	6.70	74
NGC 4660	0.05	5.16	0.759	3.22	8.85	6.00	74
NGC 4660	0.1	5.19	0.801	3.17	8.76	5.39	74
NGC 4660	0.14	5.20	0.849	3.25	8.71	5.00	74
NGC 4660	0.15	5.21	0.864	3.30	8.65	4.91	74
NGC 4660	0.20	5.25	0.961	3.68	10.2	5.14	74
NGC 4660	0.23	5.27	1.03	4.07	14.2	6.10	74
NGC 4660	0.25	5.28	1.08	4.42	19.4	7.21	74
NGC 4660	0.30	5.31	1.24	5.65	39.7	12.3	74

Table 2.5: Table of different characteristic parameters of the models of NGC 4697. The columns are: (1) If the A_{lm} is fitted for this model, (2) if ATLAS^{3D} kinematics are fitted for this model, (3) if the SLUGGS kinematics are fitted to this model, (4) if the cross term is fitted for this model, (5) the initial model used, (6) the total χ^2 of the model with the ATLAS^{3D} kinematics, (7) the χ^2 of the velocity v of the model with the ATLAS^{3D} v , (8) the χ^2 of the velocity dispersion σ of the model with the ATLAS^{3D} σ , (9) the χ^2 of the h_3 moment of the model with the ATLAS^{3D} h_3 , (10) the χ^2 of the h_4 moment of the model with the ATLAS^{3D} h_4 , (11) the χ^2 of the model with the SLUGGS mean velocity, (12) the χ^2 of the velocity dispersion σ of the model with the SLUGGS σ , (13) the χ^2 of the h_3 moment of the model with the SLUGGS h_3 , (14) the χ^2 of the h_4 moment of the model with the SLUGGS h_4 , (15) the χ^2 of the density of the model with the density from the deprojected MGE photometry, (16) the cross $c_{(R,z)}$ parameter (17) the standard deviation on the cross $c_{(R,z)}$ parameter (18) the Mass-to-Light Ratio in $M_{\odot}/L_{\odot,r}$ fitted within NMAGIC, (19) the halo model name, (20) the relative data strength $\gamma_{\text{Kin}}/\gamma_{\text{Total}}$, (21) inclination in degrees.

A_{lm}	ATLAS ^{3D} Kinematics	SLUGGS Kinematics	Cross Term	Initial Model	ATLAS ^{3D} χ^2	v χ^2	σ χ^2	h_3 χ^2	h_4 χ^2	v χ^2	σ χ^2	h_3 χ^2	h_4 χ^2	A_{lm} χ^2	$c_{(R,z)}$ param	$c_{(R,z)}$ param σ	M/L	Halo	γ_{Kin} γ_{Total}	i
Yes	Yes	No	No	ICA	0.411	0.531	0.388	0.353	0.371	-	-	-	-	0.00144	0.119	0.027	4.95	A	1	80
Yes	Yes	No	No	ICB	0.380	0.532	0.333	0.318	0.338	-	-	-	-	0.000528	0.164	0.050	4.97	A	1	80
Yes	Yes	No	No	ICC	0.377	0.539	0.323	0.312	0.332	-	-	-	-	0.000601	0.218	0.0379	4.87	A	1	80
Yes	Yes	No	No	ICD	0.375	0.520	0.325	0.318	0.339	-	-	-	-	0.000574	0.152	0.033	5.01	A	1	80
Yes	No	No	Yes	ICA	9.79	16.95	18.19	0.853	3.184	-	-	-	-	2.01	0.0216	0.0397	-	A	0	80
Yes	No	No	Yes	ICB	10.32	22.64	15.22	0.812	2.596	-	-	-	-	0.412	0.0158	0.0135	-	A	0	80
Yes	No	No	Yes	ICC	10.19	24.81	12.75	1.050	2.167	-	-	-	-	0.946	0.0199	0.0242	-	A	0	80
Yes	No	No	Yes	ICD	9.93	21.38	14.82	0.787	2.741	-	-	-	-	0.569	0.0178	0.0247	-	A	0	80
Yes	Yes	No	Yes	ICB	0.912	0.793	1.493	0.547	-	-	-	-	-	0.000800	0.0178	0.0145	5.20	A	0.01	80
Yes	Yes	No	Yes	ICB	0.498	0.546	0.608	0.363	-	-	-	-	-	0.000770	0.0222	0.0126	5.34	A	0.1	80
Yes	Yes	No	Yes	ICB	0.422	0.528	0.425	0.341	-	-	-	-	-	0.000601	0.0469	0.0167	5.19	A	0.5	80
Yes	Yes	No	Yes	ICB	0.388	0.532	0.346	0.322	-	-	-	-	-	0.000561	0.0951	0.0151	5.03	A	0.91	
Yes	Yes	No	No	ICB	0.449	0.606	0.465	0.347	0.379	-	-	-	-	0.0538	0.182	0.0625	4.95	A	1	70
Yes	No	No	Yes	ICB	4.11	7.25	4.99	2.16	2.04	-	-	-	-	0.0337	0.0229	0.0146	5.18	A	0	70
Yes	Yes	No	Yes	ICB	7.57	17.39	7.52	1.82	3.55	-	-	-	-	0.167	0.0250	0.0151	5.35	A	0.01	70
Yes	Yes	No	Yes	ICB	0.650	0.657	0.939	0.418	0.589	-	-	-	-	0.0545	0.0259	0.0155	5.39	A	0.1	70
Yes	Yes	No	Yes	ICB	0.522	0.615	0.650	0.371	0.452	-	-	-	-	0.0761	0.0688	0.0270	5.24	A	0.5	70
Yes	Yes	No	Yes	ICB	0.464	0.611	0.503	0.344	0.398	-	-	-	-	0.0226	0.136	0.0513	5.02	A	0.9	70
Yes	Yes	Yes	No	ICB2	0.479	0.602	0.476	0.418	0.417	0.391	0.929	0.276	1.849	0.00121	0.167	0.042	4.97	A	1	80
Yes	Yes	Yes	No	ICB2	0.475	0.603	0.469	0.414	0.414	0.382	0.762	0.275	1.702	0.00128	0.229	0.094	4.94	B	1	80
Yes	Yes	Yes	No	ICB2	0.464	0.597	0.439	0.404	0.415	0.366	0.624	0.266	1.68	0.00151	0.303	0.142	4.89	C	1	80
Yes	Yes	Yes	No	ICB2	0.438	0.589	0.381	0.380	0.404	0.331	0.384	0.258	1.67	0.00162	0.404	0.173	4.77	D	1	80
Yes	Yes	Yes	No	ICB2	0.434	0.584	0.378	0.371	0.403	0.327	0.376	0.265	1.75	0.00177	0.371	0.155	4.77	D q=0.9	1	80
Yes	Yes	Yes	No	ICB2	0.412	0.579	0.333	0.349	0.385	0.310	0.480	0.285	1.91	0.00226	0.497	0.183	4.64	F	1	80
Yes	Yes	Yes	No	ICB2	0.413	0.579	0.337	0.346	0.390	0.319	0.528	0.275	1.73	0.00206	0.439	0.166	4.64	F q=0.9	1	80
Yes	Yes	Yes	No	ICB2	0.406	0.594	0.331	0.337	0.362	0.314	1.022	0.281	1.83	0.00138	0.488	0.168	4.53	J q=0.9	1	80
Yes	Yes	Yes	No	ICB2	0.442	0.619	0.494	0.325	0.330	0.330	3.10	0.331	2.24	0.00328	0.376	0.146	4.32	K	1	80
Yes	No	No	Yes	ICB2	7.16	24.52	2.09	1.11	0.928	5.42	1.64	6.28	34.13	0.00113	0.0177	0.01340	-	A	0	80
Yes	No	No	Yes	ICB2	7.21	24.80	1.98	1.15	0.917	5.57	1.46	6.21	33.95	0.000893	0.0198	0.0148	-	B	0	80
Yes	No	No	Yes	ICB2	7.07	23.62	2.72	0.970	0.958	5.43	1.52	5.27	28.70	0.000628	0.0192	0.0119	-	C	0	80
Yes	No	No	Yes	ICB2	7.35	25.55	1.69	1.23	0.930	6.33	2.47	5.33	30.08	0.00719	0.0274	0.0225	-	D	0	80
Yes	No	No	Yes	ICB2	7.07	23.84	2.49	0.98	0.977	5.62	1.51	4.13	23.31	0.00709	0.0259	0.0363	-	D q=0.9	0	80
Yes	No	No	Yes	ICB2	7.61	26.52	1.69	1.33	0.918	6.96	6.00	4.32	27.05	0.00272	0.0457	0.0384	-	F	0	80
Yes	No	No	Yes	ICB2	7.07	24.07	2.25	0.972	0.99	5.88	2.38	3.03	18.80	0.0163	0.0356	0.0295	-	F q=0.9	0	80
Yes	No	No	Yes	ICB2	7.10	24.36	2.08	0.972	1.00	5.86	3.66	2.23	22.24	0.0265	0.0549	0.0472	-	J q=0.9	0	80
Yes	No	No	Yes	ICB2	9.00	29.02	4.57	1.50	0.90	6.81	30.94	1.85	46.76	0.0411	0.0586	0.0536	-	K	0	80
Yes	Yes	Yes	Yes	ICB2	0.586	0.607	0.663	0.450	0.624	0.562	0.715	0.629	2.031	0.00225	0.0307	0.0147	5.09	A		80
Yes	Yes	Yes	Yes	ICB2	0.583	0.602	0.654	0.451	0.626	0.581	0.707	0.592	2.026	0.00171	0.0320	0.0162	5.08	B		80
Yes	Yes	Yes	Yes	ICB2	0.589	0.600	0.662	0.449	0.645	0.604	0.757	0.574	2.003	0.00246	0.0337	0.0152	5.06	C		80
Yes	Yes	Yes	Yes	ICB2	0.575	0.595	0.611	0.436	0.656	0.674	1.151	0.529	2.055	0.00510	0.0393	0.0194	4.99	D		80
Yes	Yes	Yes	Yes	ICB2	0.584	0.599	0.623	0.437	0.676	0.652	1.205	0.502	1.957	0.00707	0.0407	0.0220	4.99	D q=0.9		80
Yes	Yes	Yes	Yes	ICB2	0.568	0.591	0.592	0.414	0.675	0.753	2.014	0.469	2.254	0.0170	0.0542	0.0334	4.92	F		80
Yes	Yes	Yes	Yes	ICB2	0.560	0.586	0.585	0.405	0.666	0.710	2.134	0.458	2.175	0.0287	0.0527	0.0342	4.92	F q=0.9		80
Yes	Yes	Yes	Yes	ICB2	0.559	0.598	0.567	0.392	0.679	0.763	3.409	0.414	2.351	0.0282	0.0601	0.0328	4.85	J q=0.9		80
Yes	Yes	Yes	Yes	ICB2	0.525	0.584	0.578	0.349	0.588	0.738	6.851	0.352	2.725	0.0272	0.0720	0.0650	4.65	K		80

Appendices

2.A Photometry Appendix

Photometric data of the galaxy is used in the making an NMAGIC model in two separate aspects. Photometry can be used to create a spherical initial particle model from a distribution function calculated from the photometry deprojected into the 1D density. The photometry deprojected in 3D is also used in order to constrain the density of the galaxy in the NMAGIC modelling process to create an oblate, prolate or triaxial galaxy.

The goal of our modelling process is to produce a model with a density that is consistent with the photometric and kinematic data available. In order to make a model consistent with a set of kinematic observables using NMAGIC, the density constraint needs to extend to radii several times larger the radial extent of the kinematic data, as some orbits which can alter the kinematics at the centre can extend to large radii. Therefore the initial particle model calculated must extend to these large radii for the particle to be still bound by the potential at them. For NGC 4697, whose photometric data and its use in NMAGIC is described in De Lorenzi et al. (2008), the 3D density extends to 5 times the furthest kinematic data used our models. For NGC 4660, however, the Multi Gaussian Expansion (MGE) data available from Scott et al. (2013) only extends to radii approximately 2.5 times larger than the kinematic data radial extend. We therefore use extrapolation in order to create an initial model of sufficient radial extent, as well as constrain the model to larger radii, described in this appendix.

2.A.1 MGE Data

The photometry used for NGC 4660 is represented using the MGE method (Cappellari, 2002), with the MGE fitting parameters given in Scott et al. (2013). The MGE fitting method (Cappellari, 2002) combines Gaussians with different axis ratio, dispersions, and amplitude to fit 2D photometric data. These Gaussians are used to analytically describe the surface brightness, and can be deprojected into a 3D density.

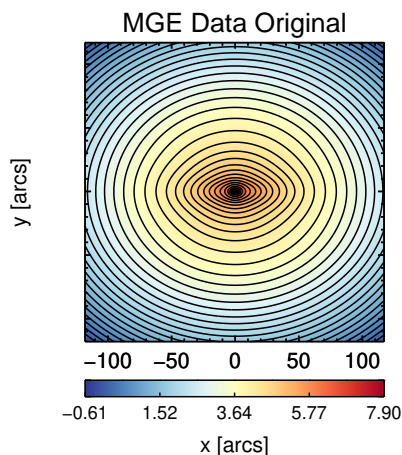


Figure 2.A.1: The MGE photometric data of NGC 4660 from Scott et al. (2013). The colour scale is in units of $\log_{10} L_{\odot,r}$ in each pixel. The contours are in steps of $0.5 \text{ mag/arcseconds}^2$. A zoomed in view of Figure 2.2, showing the more central structure.

NGC 4660

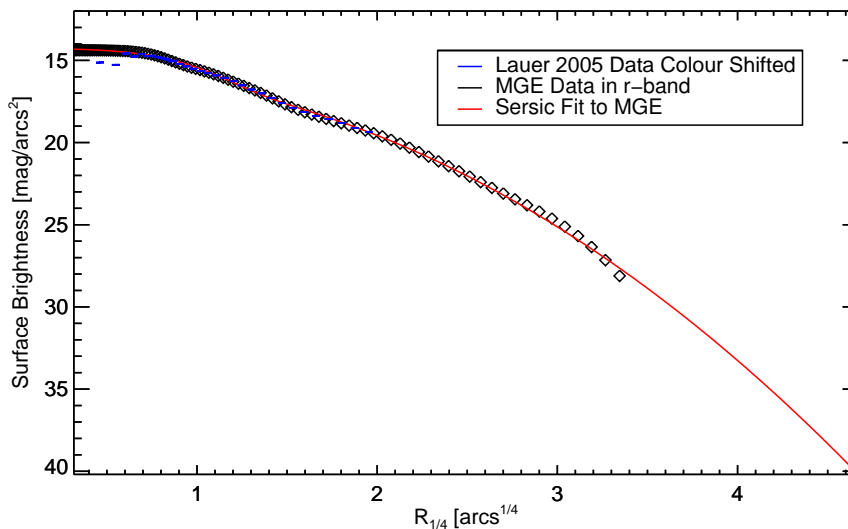


Figure 2.A.2: The major axis surface brightness profile of NGC 4660 in units of magnitudes/arcseconds² against projected radius $R^{1/4}$ in units of arcseconds. Blue is the data from Lauer et al. (2005), black is the MGE Data of NGC 4660, red is the double Sersic fit with parameters in Table 2.A.1.

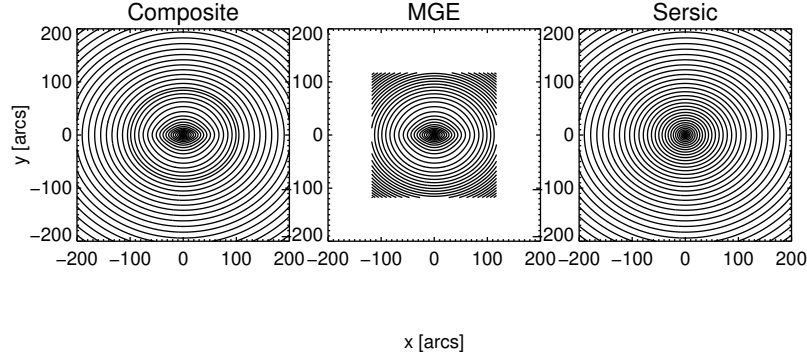


Figure 2.A.3: Contours of the Photometry of NGC 4660. Left to Right: Contours of the Composite Image of MGE photometry image used within an elliptical radius of $3q\sigma_{max}$ where $\sigma_{max} = 39.3''$, the contours of the MGE data within a square of extent of $3\sigma_{max}$, the contours of a Sérsic fit to major axis of MGE with axis ratio $q = 0.85$. The contours are in steps of $0.5 \text{ mag/arcseconds}^2$.

The parameterisation of MGE is expanded onto a grid using the axisymmetric equation:

$$\Sigma(x, y) = \sum_{j=1}^N I'_j \exp\left(-\frac{1}{2\sigma'_j}\left(x'^2 + \frac{y'^2}{q'_j}\right)\right), \quad (2.21)$$

where the model is composed by N Gaussian components of dispersion σ'_j , observed axial ratio q'_j , and peak intensity I'_j . The photometry of NGC 4660 from Scott et al. (2013) is shown on Figure 2.2 in SDSS r-band.

The distance used by ATLAS^{3D} is 15 Mpc (Scott et al., 2013). The inclination of NGC 4660 used is 67° (Cappellari, 2008) for NGC 4660. Scott et al. (2013) gives an inclination of 74° , so we repeat our analysis in Section 2.4.5 to show the robustness of our results against the inclination degeneracy. In order to extrapolate the MGE photometry a flattened 2D Sérsic fit is used.

2.A.2 Sérsic Fit

The first step is to make a 1D fit to the major axis profile of the MGE photometry, and then expand this into 2D using a flattening axis ratio. A double-component Sérsic profile parametrisation from Hopkins et al. (2009), allowing more complex profile, is fitted to the

major-axis photometry of the NGC 4660 MGE data (Equation 1.3 and 1.4). The parameters n'_s and n_s are fixed to $n'_s = 1.0$ and $n_s = 1.88$, given by Hopkins et al. (2009), while the effective radii and normalisation are fitted. The n parameters are fixed, since according to Hopkins et al. (2009) leaving this parameter free does not result in an improvement in the fits. The parameter κ is computed using Equation 1.4 from Ciotti (1991). This equation is solved using the ZBRENT IDL routine which is based on the routine in Press et al. (1992). The result of the fits is shown on Figure 2.A.2.

2.A.3 Comparison to other Photometry

In addition to the MGE data from Scott et al. (2013), there exists major axis photometric data and an ellipticity profile for NGC 4660 from Lauer et al. (2005). It is shown on Figure 2.A.2, colour shifted to match the MGE data. The range of the Lauer et al. (2005) is $0.227''$ to $14.594''$ along the major axis of the galaxy. The surface brightness is consistent with the Scott et al. (2013) data, outside of a radius of $0.1''$. [The distance used in Lauer et al. (2005) is 17.9 Mpc.]

2.A.4 Composite Image

NGC 4660 has elliptical isophotes in its outskirts. In order to make a 2D representation, therefore, the double-component Sérsic fit to the major axis must be flattened by an axis ratio consistent with the ellipticity of the galaxy in its outskirts. The axis ratio of the largest Gaussian in the MGE data is therefore chosen as the ellipticity of the 2D Sérsic profile with $q = 0.85$. The 2D Sérsic photometry is shown on panel 3 of Figure 2.A.3.

Having obtained a 2D representation of the outskirts of the galaxy the exact transition point between the original data and the extended data must be chosen. This is done by finding where the original photometry stops being a good representation of the galaxy needs to be estimated. The photometry is accurate to the point where the Gaussians start falling off more rapidly than the real photometry. The largest Gaussian of the NGC 4660 parametrisation has a dispersion of $39''$, and the fall off point of a Gaussian is approximately between $2 - 3\sigma$, so therefore estimated to be $78 - 117''$ for NGC 4660. The magnitude contours become increasingly dense at the edge of the image on Figure 2.2 that the profile falls off very rapidly there as the largest Gaussian falls off, shown in 1D along the major axis on Figure 2.A.4, showing the transition radius of $3\sigma q = 100''$ in green. The point of fall off is on an ellipse that is flattened as the largest Gaussian so the transition is chosen to be an ellipse. A contour of the composite image is shown on panel 1 of Figure 2.A.3, with Panel 2 and 3 showing the MGE data and Sérsic fit it is comprised of respectively. This shows that the composite image has some discontinuity at the transition radius. This discontinuity is, however, smoothed over by an MGE fit to the now extended composite

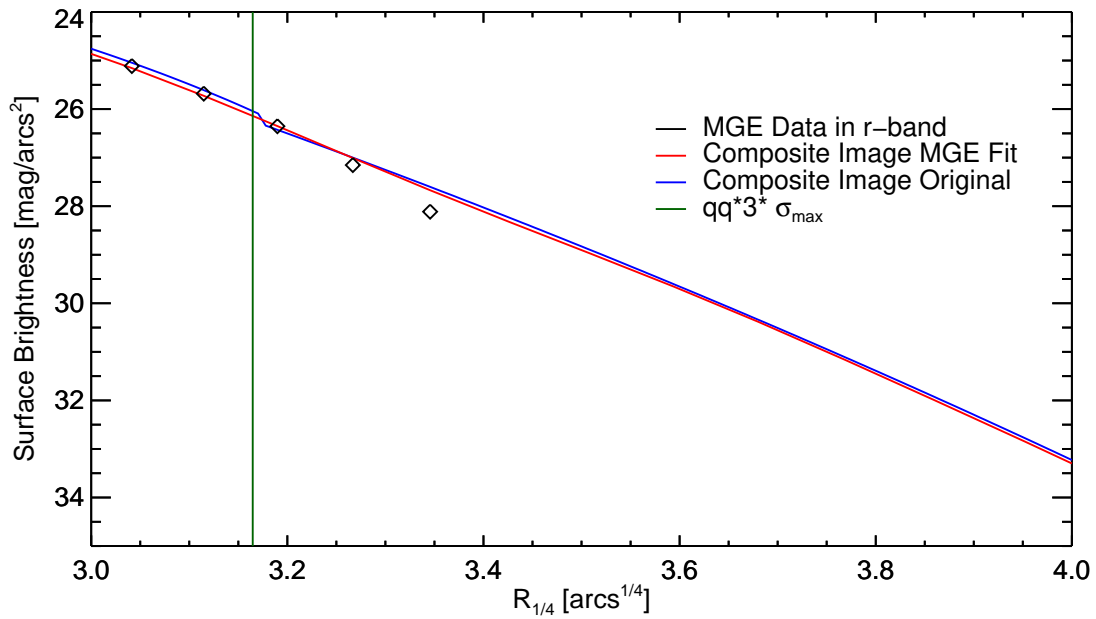


Figure 2.A.4: The major axis surface brightness profile of NGC 4660 in units of magnitudes/arcseconds² against projected radius $R^{1/4}$ in units of arcseconds in the transition region between the MGE data and the Sérsic extrapolation. The black points are the original data to $3\sigma_{max}$, the blue line is the Composite image, the red line is the MGE fit to the Composite image. The green line shows $qq * 3 * \sigma_{max}$, the semi-major axis of the ellipse beyond which the Sérsic fit is used.

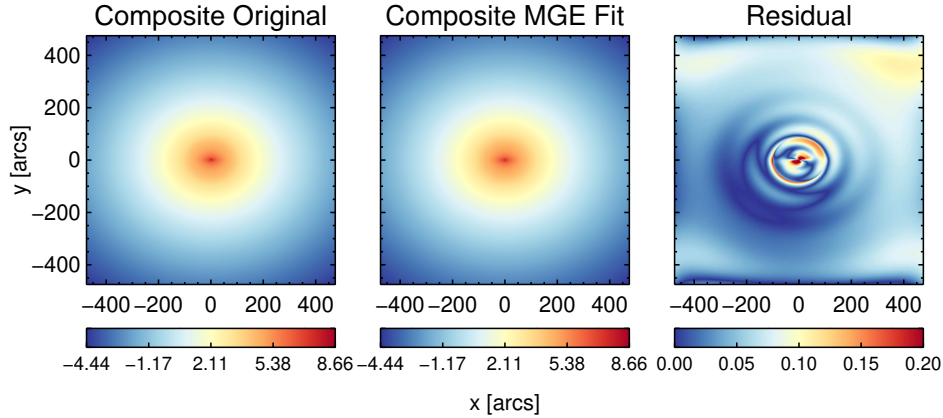


Figure 2.A.5: NGC 4660 Left to Right: The original composite image in log units of $L_{\odot,r}$, the MGE fit to the composite image in log units of $L_{\odot,r}$ with parameters shown in Table 2.A.2, the absolute value of the residual between the two images normalised by the original composite image. The residual value is always positive because it is the absolute value.

image. The MGE fit to the composite image results in a $\chi^2 = 1.17$.

A residual between the original composite image and its MGE fit is shown on Figure 2.A.5, and shows the main residual exists where the transition radius discontinuity of the original image is smoothed over by the MGE. The next section gives more details on the MGE fitting routine, using the software from Cappellari (2002), and how it has been implemented.

2.A.5 MGE Fitting Routine

Testing

The first step is to calculate profile in units of solar luminosity from MGE expansion from Scott et al. (2013). The purpose of this is to show that the method of making an image of the luminosity using the MGE expansion from Scott et al. (2013) and applying an MGE fit recovers MGE image and expansion with similar parameters.

The routine FIND GALAXY is used to find the overall ellipticity and centre of the

galaxy. SECTORS PHOTOMETRY is then used to divide the image into 37 profiles of width equally spaced by 2.5° from 0 to 90° . This, therefore, makes the assumption of axis-symmetry. MGE FIT SECTORS uses the sectors to calculate an MGE fit using the linear regime with 1600 Gaussians as input. These routines are software provided by Michele Cappellari (Cappellari, 2002).

In order to test that our implementation of this method is working correctly, the MGE fit is reapplied to the MGE output from Equation 2.21 and the Scott et al. (2013) parameterisation. The fitting reproduces the original MGE image shown on Figures 2.2. The values of the χ^2 of NGC 4660 fits are shown in Table 2.A.2.

MGE Fit to the Composite Image

The same method is applied to the composite images of NGC 4660. The magnitude contours of the fits are shown on Figure 2.A.3, and the χ^2 and other parameters are shown in Table 2.A.2. The fit to NGC 4660 is good with a χ^2 of 1.17, and Figure 2.A.5 shows that the majority of the residual is below 20% when normalised by the original image. On Figure 2.A.6 the original MGE data from the Scott et al. (2013) parameterisation is shown out to 3σ along the major axis and compared to the MGE fit to the composite image along the major axis.

2.A.6 Photometry used in NMAGIC

Having extrapolated the photometry, it is deprojected into 3D density using the MGE method, and used to create the initial particle model. In addition, the photometry ranging to $180''$, or 6 times the extent of the kinematic data, is used as an observable in NMAGIC. For use in NMAGIC it is expanded on spherical harmonics.

2.A.7 Spherical Harmonics

The axisymmetric oblate luminosity density ν can be deprojected using the following equation from Cappellari (2008):

$$\nu(R, z) = \sum_{j=1}^N \frac{L_j}{(\sqrt{2\pi}\sigma_j)^3 q_j} \exp\left(-\frac{1}{2\sigma_j'}\left(R^2 + \frac{z^2}{q_j^2}\right)\right), \quad (2.22)$$

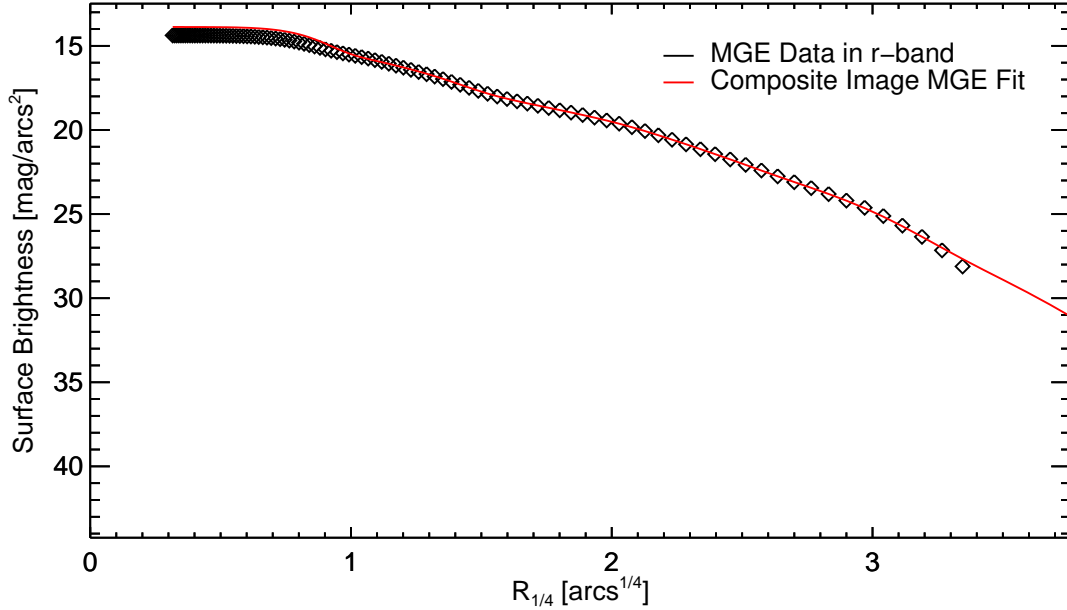


Figure 2.A.6: The major axis surface brightness profile of NGC 4660 in units of magnitudes/arcseconds² against projected radius $R^{1/4}$ in units of arcseconds. Black is the MGE Data of NGC 4660, red is the MGE fit to the Composite Image. The radius range (with $R_{\max} = 200''$) shown is the extent used for the density observable for NMAGIC.

where the model is composed by N Gaussian components of dispersion σ_j , where L_j is the total sec-sphersec-spher of the Gaussians, and q_j is the intrinsic axial ratio defined as:

$$q_j = \frac{\sqrt{q_j'^2 - \cos^2(i)}}{\sin^2(i)}, \quad (2.23)$$

where q_j' is the observed axis ratio as used in 2.21 and i is the inclination, with $i = 90^\circ$ being edge-on.

This luminosity density is then expanded onto spherical harmonics, which are used as a fitted observable in NMAGIC. The A_{00}, A_{20} , and A_{40} terms of the original MGE data, the composite profile, and the Sérsic profile are shown Figure 2.A.7. All the profiles are normalised with the same mass, that of the Sérsic profile.

The total luminosity within $180''$ is calculated from the spherical harmonics for the total profile of NGC 4660 is $0.6649 \times 10^{10} L_{\odot,r}$, which is consistent with the Scott et al. (2013) total luminosity value of $0.6471 \times 10^{10} L_{\odot,r}$.

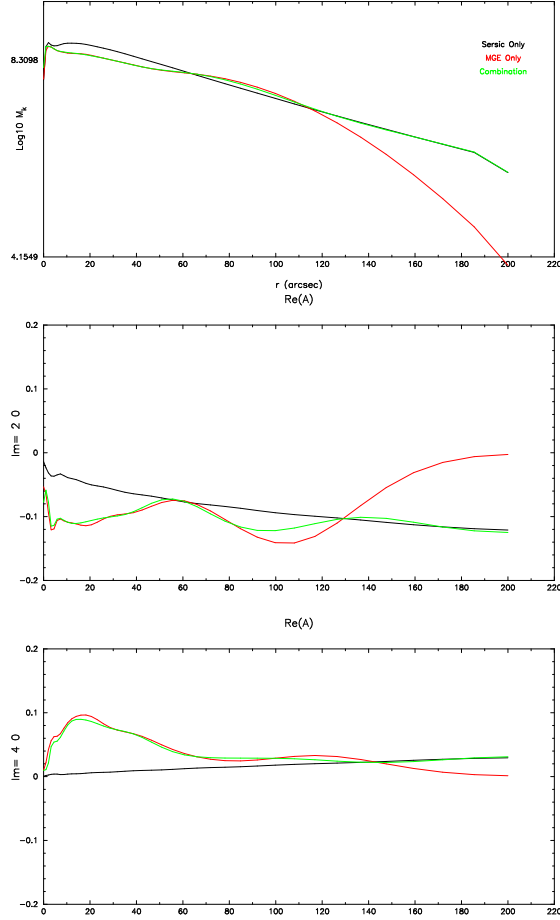


Figure 2.A.7: Spherical harmonics of the NGC 4660 photometry as described in Section 2.A.7. From top to bottom: $\log_{10} A_{00}$ normalised by total luminosity of the Sérsic profile, A_{20} normalised by A_{00} , A_{40} normalised by A_{00} . The Sérsic profile with an axis ratio $q = 0.65$ is in black, the original MGE parameterisation from Scott et al. (2013) extrapolated in red, and the Composite profile in green.

Table 2.A.1: Sérsic parameters. Parameters fixed in the fit are shown in bold.

Galaxy	I'	$R_{\text{extra}}('')$	n_s'	I_0	q	Fit to
NGC 4660	1100	1.89	1.00	408	17.3	1.88 0.7 Major

Table 2.A.2: Table of MGE fit parameters. Column (1) is the ID of the galaxy, Column (2) is the χ^2 of the MGE fit to the image, Column (3) is the number of Gaussians used by the MGE parameterisation, Column (4) is the number of sectors of the image used by the MGE fit, Column (5) is the global ellipticity found by the MGE code, Column (6) is the largest dispersion of the MGE fit Gaussians, Column (7) is the axis ratio q used in case of photometric extrapolation.

	Galaxy	Cut	χ^2	Number of Gaussians	Sectors	Eps	Max Gaussian σ (")	q
MGE Test	NGC 4660	3σ	0.597	19	37	0.347	39.3	
Composite	NGC 4660	3σ	1.17	22	37	0.214	184.7	0.85

2.B Kinematics Appendix

The steps to process the ATLAS^{3D} and SLUGGS data sets as input observables for NMAGIC models are described in the following section.

2.B.1 4-fold symmetrising ATLAS^{3D} data of NGC 4697

In this section we describe the process of symmetrising the ATLAS 3D data of NGC 4697 available from Cappellari et al. (2011). The ATLAS^{3D} data is used to scale the SLUGGS data, which would carry asymmetries in the ATLAS^{3D} data forward into the scaled field, which would not be a good representation of the galaxy.

The first step of the process of symmetrising the ATLAS^{3D} data is to adjust the systemic velocity and centre point of the kinematic field. We rotate the velocity field by the PA=67.2° (Krajinović et al., 2011) such that the major axis is aligned to the x-axis of our Cartesian reference frame. Using a series of slits parallel to the major axis we determine that $v - v_{sys} = 0$ is not at $(x, y) = (0, 0)$ as it should be in an anti-symmetric rotating field. Therefore we recenter the x central coordinate by $x'_c = x_c + 0.2''$. As shown on Figure 2.B.1a even after the recentering, there is an offset between the velocities measured along the positive and negative major axis. The red line denotes the mean velocities along the negative major axis from $-5''$ to $-30''$, being $\bar{v}_- = -95 \text{ km s}^{-1}$. Analogously, the black line denotes the mean velocity along the positive major axis measured from $5''$ to $30''$, being $\bar{v}_+ = 105 \text{ km s}^{-1}$. The offset of 10 km s^{-1} between the two can be even more clearly seen on Figure 2.B.1b, where the absolute value of the negative velocities along the minor axis are overplotted onto measurements along the positive major axis. In order to correct this global rotational asymmetry, we globally subtracted 5 km s^{-1} from the velocity field, resulting in $\bar{v}_+ = 100 \text{ km s}^{-1}$ and $\bar{v}_- = 100 \text{ km s}^{-1}$ and thus a symmetric field.

The impact of these changes on the entire kinematic field can be seen by comparing Fig-

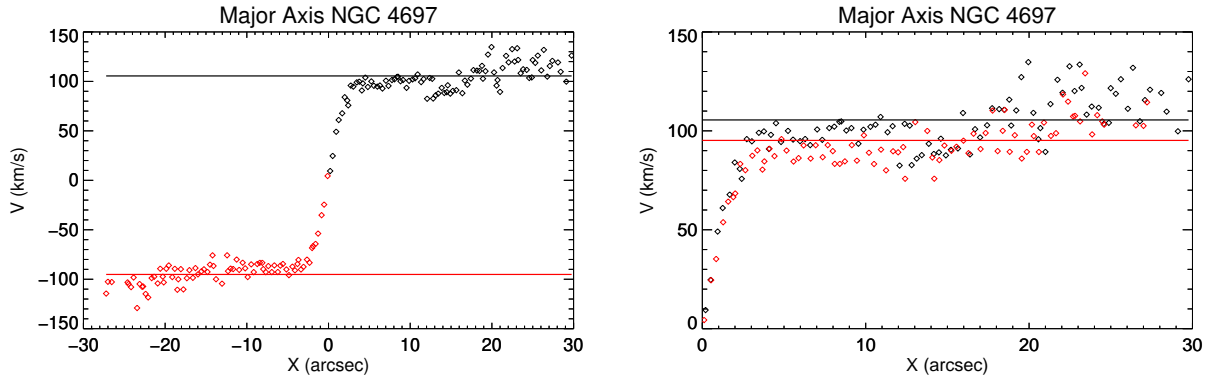


Figure 2.B.1: Velocity of the NGC 4697 ATLAS^{3D} data in kms^{-1} vs Radius as the points, with $-1'' < y < 1''$ of the ATLAS 3D data, where $y = 0''$ is the major axis. The black points have $x > 0''$ and the red points $x < 0''$. The line is the mean between $5''$ and $30''$ for $x > 0''$ and $-5''$ and $-30''$ for $x < 0''$. The left plot shows the true anti-symmetric values of the field and right plot shows the same as the left with absolute values taken for x and v for comparison.

ure 2.B.3, showing the original data and the diagonal residual, and Figure 2.B.4, showing the data after the recentering and systematic velocity shifting. The diagonal residual is calculating the deviation from symmetry of the kinematic field by either adding (or subtracting) in the anti-symmetric v and h_3 (symmetric σ and h_4) the diagonally opposite value, shown diagrammatically on Figure 2.B.2. The diagonally opposite value is defined in polar coordinates for (r, θ) as $(r, \theta + 180^\circ)$.

On Figure 2.B.3 the diagonal residual of v is overall positive, with a large positive area in the centre. The overall positive residual is driven by the velocity offset between the positive and negative major axis also shown on Figure 2.B.1, and the very large positive residual in the centre is due to the centring offset. As shown on Figure 2.B.4, the recentering and velocity shifting lead to a mix of positive and negatives values, suggesting no general trend.

After the shifting and recentering of the kinematics, they are 4-fold symmetrised using the method from Cappellari (2008). The resulting 4-fold symmetrised field is shown on Figure 2.B.5, where the diagonal residual is globally ~ 0 for all the kinematic fields, showing the symmetry.

2.B.2 The SLUGGS data

A circularised radial profile of fitted velocity, dispersion, h_3 , h_4 and kinematic position angle PA_{kin} of NGC 4697 is available from Foster et al. (2016), ranging out to $\approx 150''$,

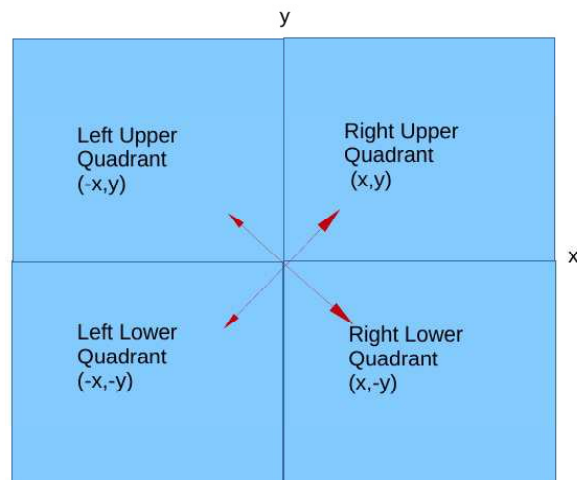


Figure 2.B.2: Diagram of a kinematic field where the major axis is aligned with the x -axis in Cartesian coordinates. The field is broken up into 4 quadrants. The residual of two diagonal quadrants is found, shown by the arrows.

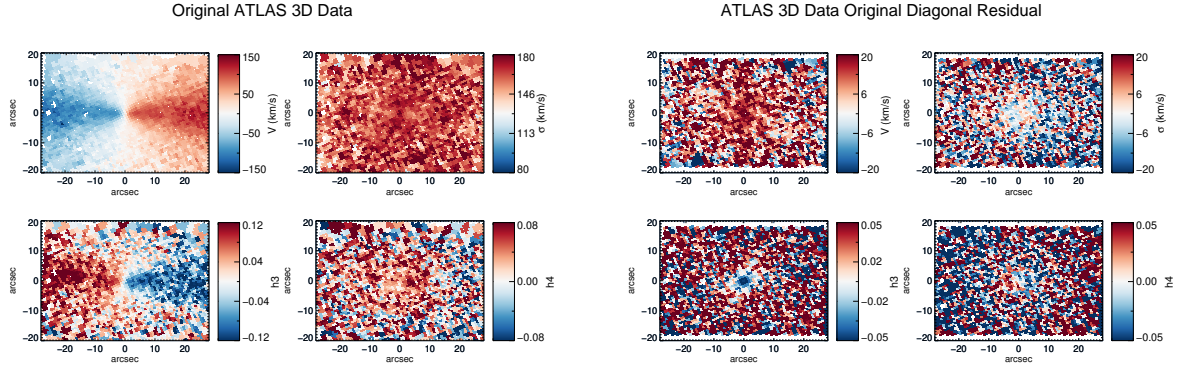
Original ATLAS^{3D} Data

Figure 2.B.3: For velocity, σ , h_3 and h_4 the original (left) ATLAS^{3D} data of NGC 4697 and its diagonally symmetric residual (right).

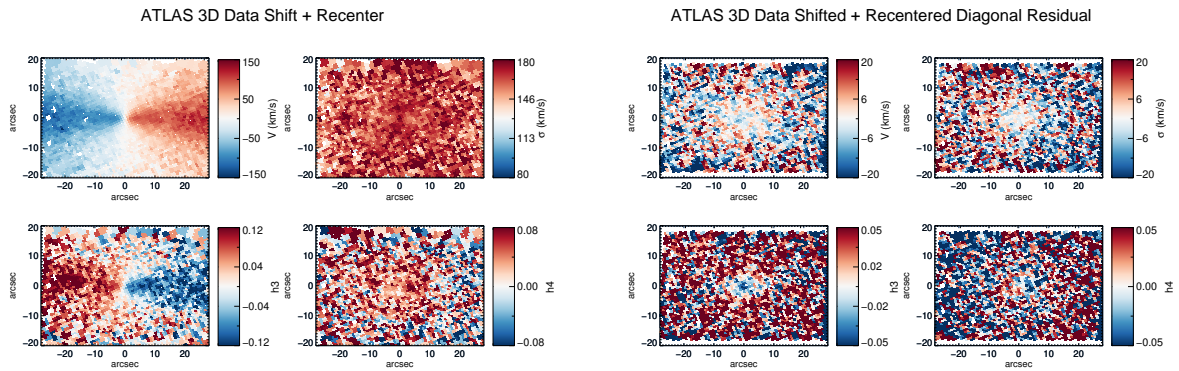
Shifted and Recentered ATLAS^{3D} Data

Figure 2.B.4: For velocity, σ , h_3 and h_4 the ATLAS^{3D} data (left) of NGC 4697 which has had its centre shifted by $x'_c = x_c + 0.2''$, and a global reduction in the velocity of 5 km s^{-1} and its diagonally symmetric residual (right).

4-fold Symmetrised ATLAS^{3D} Data

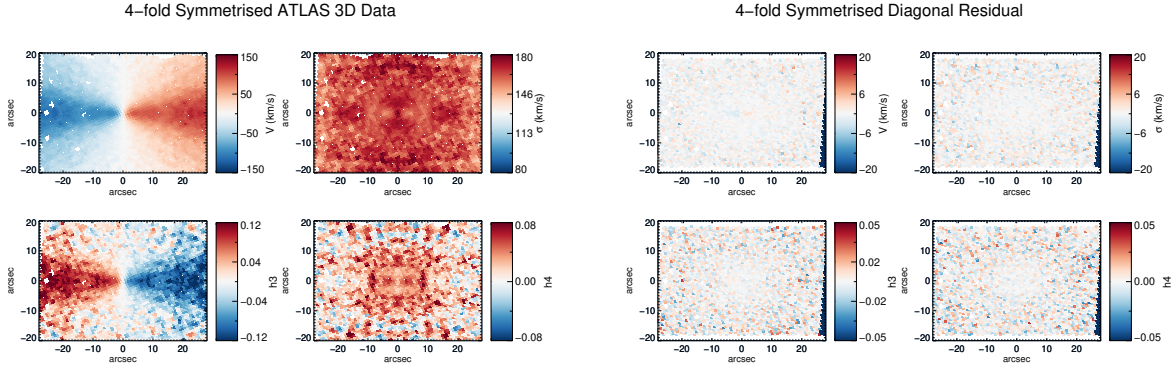


Figure 2.B.5: For velocity, σ , h_3 and h_4 the ATLAS^{3D} data (left) of NGC 4697 which has had its centre shifted by $x'_c = x_c + 0.2''$, and a global reduction in the velocity of 5kms^{-1} as shown on Figure 2.B.4 and subsequently been 4-fold symmetrised and its diagonally symmetric residual (right).

or $\approx 2.5R_e$. This circular radial profile can be analytically converted into a 2D kinematic field, using equations from Foster et al. (2016).

Our NMAGIC models to NGC 4697 are smooth and axisymmetric, so any kinematics modelled by NMAGIC will also be smooth and axisymmetric. To calculate a smooth field we first fit a least-squares regression to the radial profile. These fits are linear for v , h_3 and h_4 . The dispersion is too complex for linear fit to be a good representation, so a fourth-order polynomial was used within $60''$, and a linear fit at $> 60''$, shown on Figure 2.B.6. These fits are then extrapolated along elliptical annuli, with the ellipticity of the galaxy $\epsilon = 0.32$, given by Foster et al. (2016), in order to construct a 2D kinematic fields. While the symmetric terms such as velocity dispersion and h_4 do not vary azimuthally in the elliptical bins, the azimuthal variation of the anti-symmetric kinematics velocity and h_3 do. Analytic formulas are provided by Foster et al. (2016) allowing them to vary azimuthally with angle ϕ can be described by:

$$v_{2D} = v \cos\phi, \quad (2.24)$$

$$h_{3,2D} = h_3 \cos\phi. \quad (2.25)$$

The resulting 2D velocity fields are shown on Figure 2.B.7.

2.B.3 Comparison of the different kinematic data sets

In addition to the ATLAS^{3D} data out to $1/3R_e$ and the SLUGGS data to $\approx 2.5R_e$, we also use VIMOS data from Spiniello et al. (2015) ranging out to $\approx 60''$, or $\approx 1R_e$ along the major axis. Additionally, De Lorenzi et al. (2008) presents long-slit data along the major

SLUGGS Kinemetry Profiles

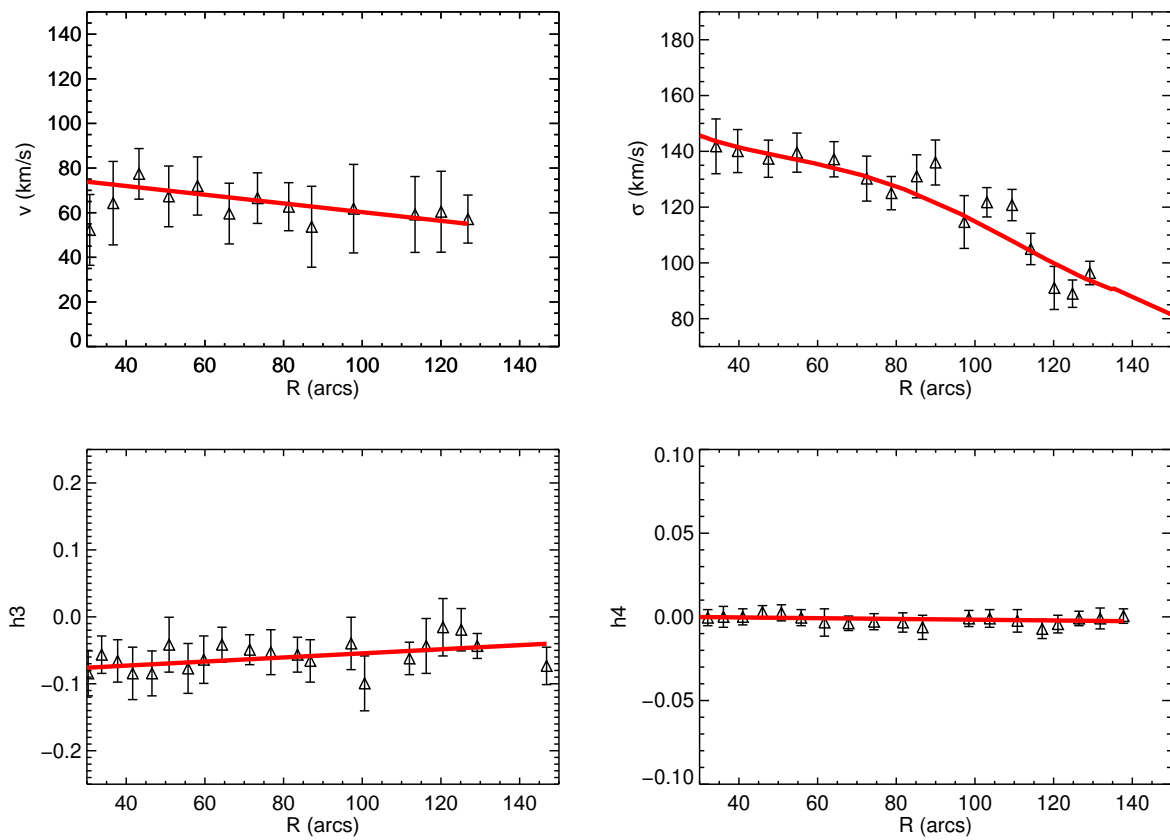


Figure 2.B.6: The SLUGGS kinematic data, velocity, σ , h_3 and h_4 on a circularised radius from Foster et al. (2016) with the least-squares fits used to calculate the 2D fields overlotted with red lines.

SLUGGS 2D Kinematics unscaled

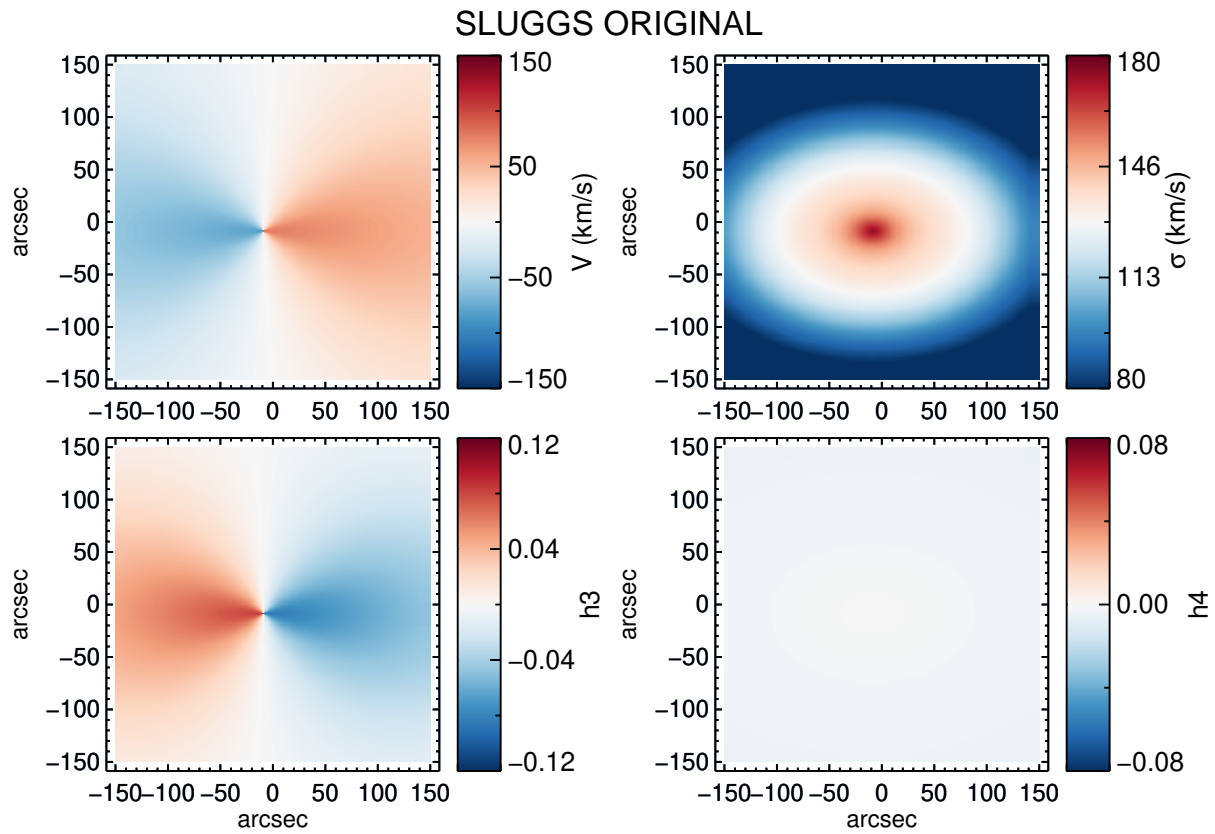


Figure 2.B.7: The 2D SLUGGS kinematic data, velocity, σ , h_3 and h_4 , calculated from the 1D circularised profile from Foster et al. (2016) and analytic functions described in the text with no scaling from the ATLAS^{3D} data applied.

(to $\approx 100''$) and minor axis (to $\approx 50''$). Performing dynamical modelling simultaneously on different data sets requires them to be approximately consistent within errors. We find that the VIMOS data, ATLAS^{3D} data, and the long-slit data are consistent with one another in v , σ , h_3 and h_4 , as described in Spiniello et al. (2015).

There is, however, an offset between SLUGGS and both ATLAS^{3D} and VIMOS in v and h_3 . The velocity v is lower in the SLUGGS data set than in ATLAS^{3D} and VIMOS. The offset between the ATLAS^{3D} data sets and the SLUGGS in general has already been discussed in previous publications (e.g. Spiniello et al., 2015; Cappellari et al., 2015; Foster et al., 2016). In Cappellari et al. (2015) JAM models are fitted to the combined SLUGGS and ATLAS^{3D} data sets, and the offset between the two is compensated by scaling up the v_{rms} of the SLUGGS data using a single scaling factor to match the v_{rms} of the ATLAS^{3D} data. Our motivation for following this prescription is twofold: i) Foster et al. (2016) states the offset issue is present throughout the whole SLUGGS sample, and ii) Spiniello et al. (2015) independently confirms the ATLAS^{3D} kinematics for NGC 4697 with their VIMOS measurements.

2.B.4 Scaling the SLUGGS data

Due to the inconsistencies in v and h_3 between the SLUGGS and ATLAS^{3D} data sets, we scale the SLUGGS data such that it is consistent with the ATLAS^{3D} in the regions of overlap. The offset between the two 2D velocity and h_3 fields varies between the major, minor and intermediate axis of the field. Therefore any attempt to scale the SLUGGS velocity field by a single global factor for the whole field would therefore lead to a mismatch along either the major or minor axis.

The SLUGGS v and h_3 fields are generated with a cosine expansion (see equation 2.25). The ATLAS^{3D} fields deviate from a single cosine significantly. It is better represented by a Fourier series of finite harmonics:

$$v(R, \theta) = a_0(R) + \sum_{n=1}^N a_n(R) \cos(n\theta) + \sum_{n=1}^N b_n(R) \sin(n\theta), \quad (2.26)$$

where R is the radius, θ is the position angle, and N is taken to be a finite number of terms.

In order to find a function to scale the entire field, we fit a function to the ratio of v_{SLUGGS}/v_{SAURON} and $h_{3SLUGGS}/h_{3SAURON}$, calculated between $15''$ and $29''$, which is the outer edge of the ATLAS^{3D} field. The outer edge of the ATLAS^{3D} field is used for the two reasons that we are trying to scale the entire SLUGGS field out to $150''$ so we want to use the outermost radial extent, and that SLUGGS is most accurate outside of the centre of the galaxy. The ratios v_{SLUGGS}/v_{SAURON} and $h_{3SLUGGS}/h_{3SAURON}$ are shown on Figure 2.B.8.

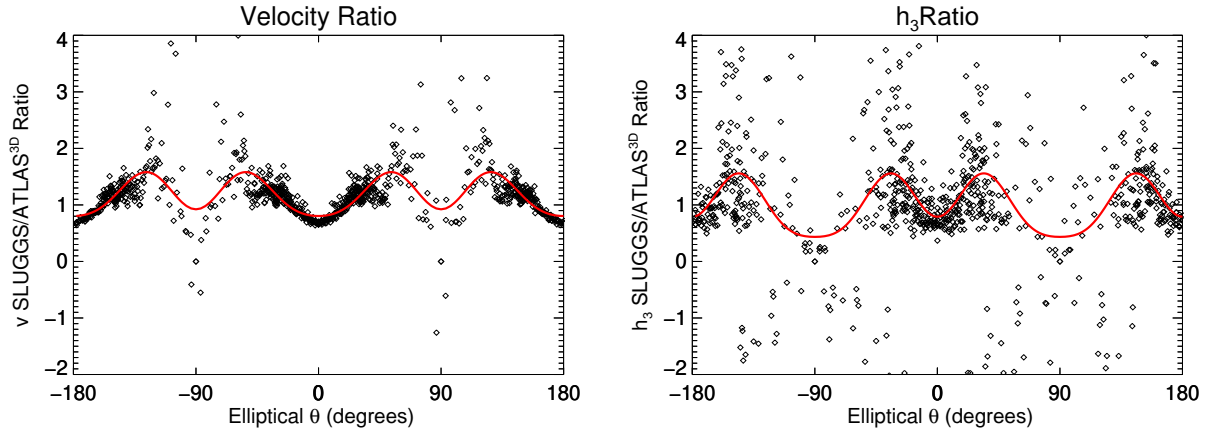
Velocity Ratio of SLUGGS and ATLAS^{3D}

Figure 2.B.8: The ratio between the original (unscaled) SLUGGS 2D velocity (left) and h_3 (right) data and the ATLAS^{3D} velocity data (regridded) for NGC 4697 inside an ellipse with $q = 0.68$ and a semi-major axis of between $15 - 29''$ are the black points. The red line is a positive cosine fit to the black points, which is used to scale the entire velocity field. $\theta = 0$ corresponds to the major axis.

The elliptical angle is calculated using the $\text{atan}(y/x)$, therefore 0° , and $\pm 180^\circ$ representing the major axis, and $\pm 90^\circ$ representing the minor axis.

The ratio between the SLUGGS and ATLAS^{3D} data can also be fitted well using a Fourier Series. Since NMAGIC creates an axisymmetric galaxy, we use a symmetric Fourier series in order to scale the SLUGGS velocity field, as not to introduce any asymmetries:

$$v(R, \theta) = a_0(R) + \sum_{n=1}^N a_n(R) \cos(n\theta) \quad (2.27)$$

The function fitted to this residual is used to scale the SLUGGS velocity field at every (R, θ) , where n is a series of even numbers, in order to obtain a symmetric function. The resulting fits are shown in as a red line on Figures 2.B.8.

The entire SLUGGS v and h_3 data set at every radius is then scaled up by the functions shown on Figure 2.B.8 the resulting scaled 2D kinematics are shown on Figure 2.B.9. Lastly, we confirm the transition region. The transition between the two data sets is shown on Figures 2.B.10 and 2.B.11, for the original SLUGGS data and the rescaled version, showing that the rescaled version is much more consistent with the ATLAS^{3D} data set, as well as the long-slit data.

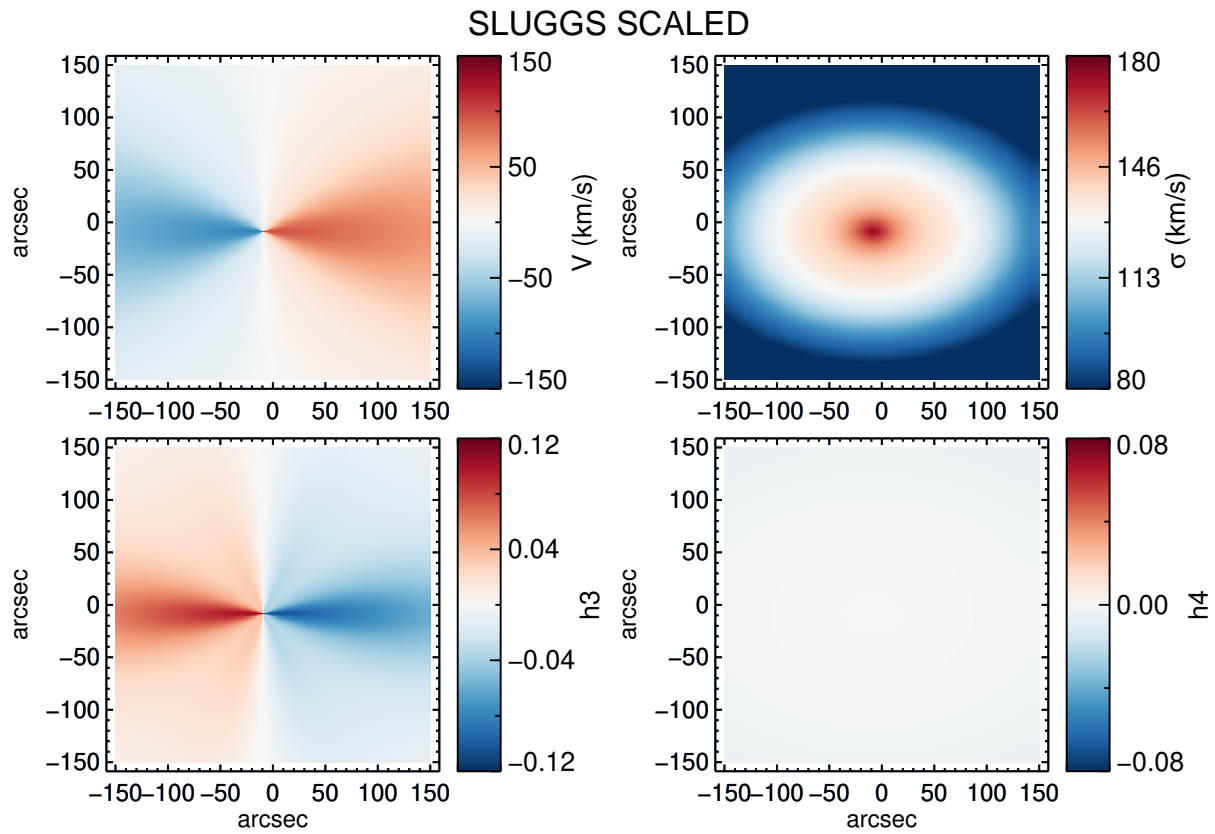


Figure 2.B.9: The 2D SLUGGS kinematic data, velocity, velocity dispersion, h_3 and h_4 , calculated from the 1D circularised profile from Foster et al. (2016) and analytic functions described in the text with the scaling for v and h_3 from Figure 2.B.8 applied to every point. These are the SLUGGS kinematics used for NMAGIC modelling.

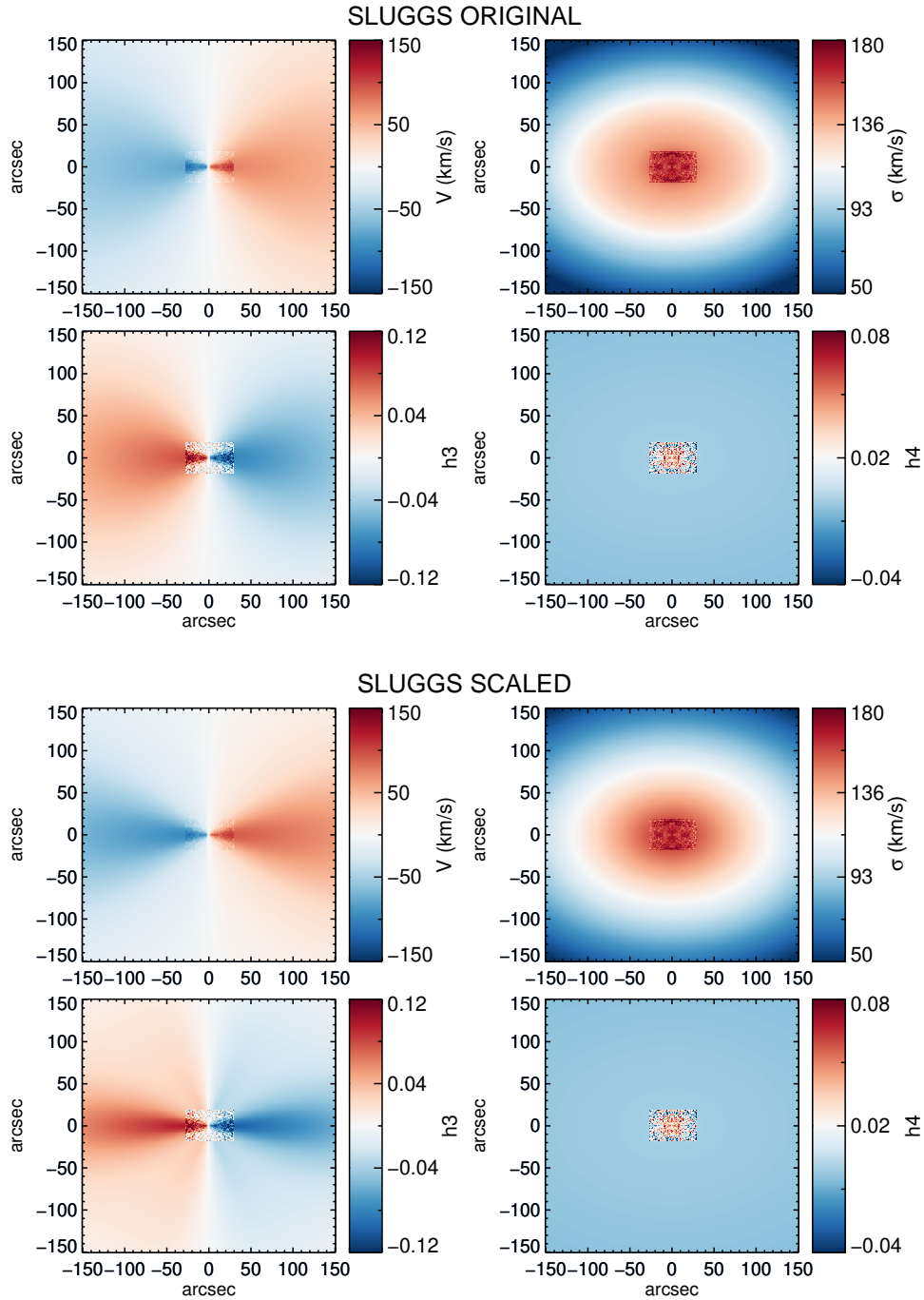
Transition between ATLAS^{3D} and SLUGGS

Figure 2.B.10: The ATLAS^{3D} data of NGC 4697 in the centre, and around it the SLUGGS data unscaled (top) and scaled (bottom) using function from Figure 2.B.8.

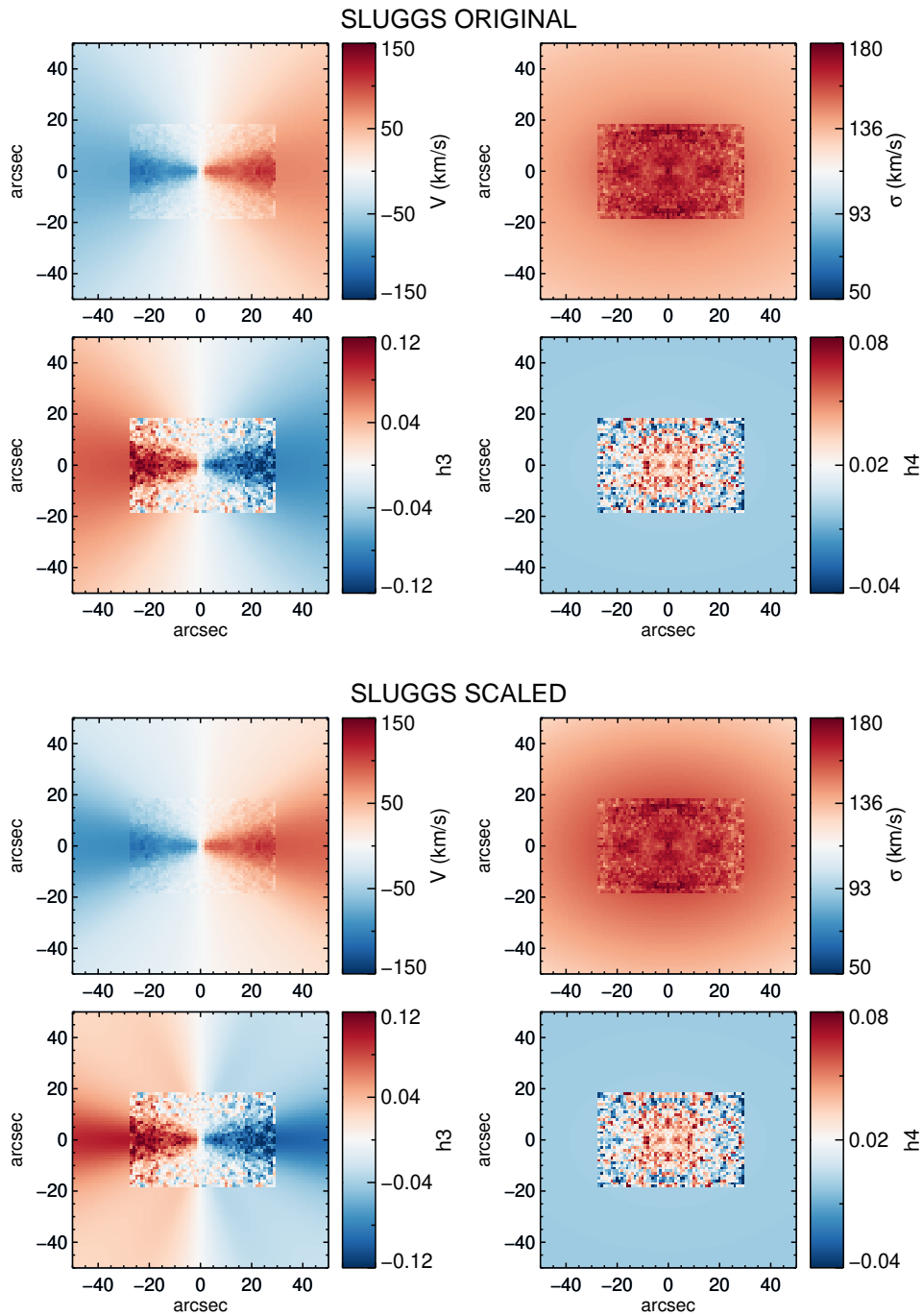
Transition between ATLAS^{3D} and SLUGGS

Figure 2.B.11: The ATLAS^{3D} data of NGC 4697 in the centre, and around it the SLUGGS data unscaled (top) and scaled (bottom) using function from Figure 2.B.8, zoomed in for a more detailed look at the transition region.

Gaussian Noise

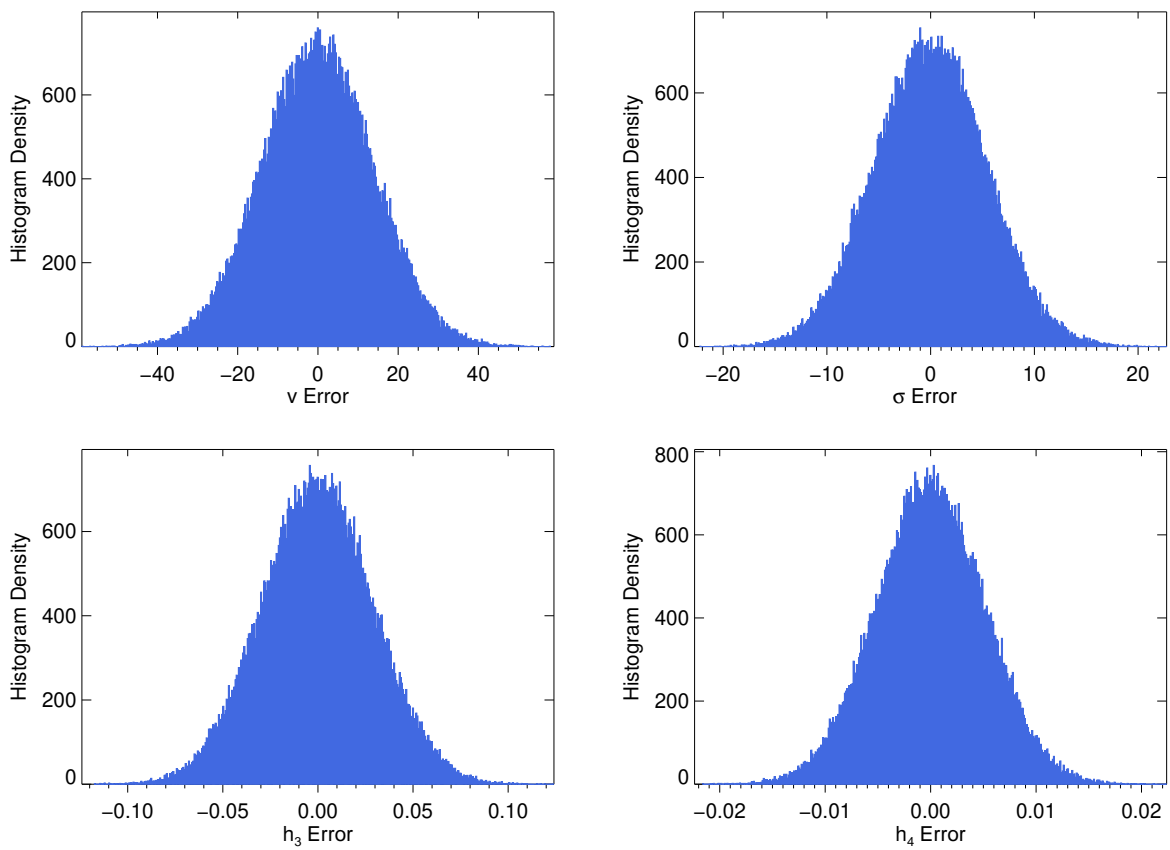


Figure 2.B.12: Histograms of a randomly sampled Gaussian, where the σ_G is the mean error of the kinematic property, velocity, σ , h_3 , and h_4 . Values drawn from these distributions are used to create noise in the 2D SLUGGS kinematics.

2.B.5 Estimating errors for the 2D SLUGGS Kinematics

NMAGIC uses χ^2 in order to minimise the difference between the model and the data. Since the 2D SLUGGS data was derived analytically, the measurement error of each point in the grid is not known. For the purposes of making a model in NMAGIC, we use a constant error for each data point. This constant error is chosen to have a magnitude similar to the error given for the 1D radial data from Foster et al. (2016). We then adjust the relative data scaling γ and μ within NMAGIC to converge to the best model.

This still leaves us with the issue of how to quantify the quality of our results once the final models are complete, as we have no true measurement errors available to calculate the χ^2 from. Once again, we use a constant error for the entire kinematic field. This allows us to compare the quality of different models with respect to the data. We chose the constant error to be a mean of the error given for the 1D radial data from Foster et al. (2016), which we calculate to be for the velocity field $\Delta_v = 14 \text{ kms}^{-1}$, for the dispersion $\Delta_\sigma = 7.2 \text{ kms}^{-1}$, and for h_3 , $\Delta_{h_3} = 0.029$, and h_4 , $\Delta_{h_4} = 0.015$.

2.B.6 Resolution and NMAGIC Calibration

Since the SLUGGS 2D kinematics are produced using analytic functions, the grid on which they are evaluated and used as an NMAGIC observable can be varied. The resolution of the grid chosen seeks to maximise the resolution of the data given the particle resolution of the model. We made models to data at a resolution of 50×50 pixels and 100×100 pixels and found no significant differences between the models. A resolution larger than 100×100 was determined to have too large particle noise at large radii. We therefore chose a 100×100 pixel resolution for the SLUGGS data input into NMAGIC.

Since the NMAGIC method uses χ^2 we add Gaussian noise, using a pseudo-random sampling IDL routine which implements the method from Box & Muller (1958). The dispersion of the Gaussian, σ_G , is scaled using $\Delta_v, \Delta_\sigma, \Delta_{h_3}$ and Δ_{h_4} , keeping the noise reasonable in comparison to the error. Example histograms of the noise added are shown on Figure 2.B.12.

2.C NMAGIC Method Details

2.C.1 Pseudo-SAURON velocity fields

The Pseudo-SAURON method is used to observe the Gauss-Hermite moments of the NMAGIC particle model without requiring kinematic data input, as done in the method

from De Lorenzi et al. (2008). De Lorenzi et al. (2008) use the v and σ of the input kinematic data to calculate the Gauss-Hermite series. When $h_1 = h_2 = 0$, the v and σ of the data are equal to the best fitting Gaussian to the line-of-sight velocity distribution (LOSVD) of the model. Therefore in the modelling process, the model weights are changed such that h_1 and h_2 become close to 0, and the underlying model LOSVD is close to the LOSVD of the data. To find the underlying LOSVD of the model, the parameters h_1 and h_2 are therefore used in equations (van der Marel & Franx, 1993; Rix et al., 1997):

$$v_{\text{model}} = v_{\text{data}} + \sqrt{2}\sigma h_1, \quad (2.28)$$

$$\sigma_{\text{model}} = \sigma_{\text{data}} + \sqrt{2}\sigma h_2. \quad (2.29)$$

In the case where v_{data} and σ_{data} are not known, these have to be estimated from the model directly. The model v and σ are therefore calculated by binning the particles, iterating until h_1 and h_2 are close to 0. This iteration depends on a time-step condition to ensure that the true value is used during temporal smoothing. The time-step must be larger than the temporal smoothing timescale of the model.

2.D JAM models of different dark matter halos

Using NMAGIC we found that there are no JAM models with real distributions. Nevertheless, making JAM models using the JAM method gives “characteristics” of the model such as z -anisotropy and M/L . Having found good models to the kinematic data using dark matter halos using the NMAGIC method, we make models to the same set of dark matter halos using the JAM method. NGC 4697 is chosen, as having its inclination known due to the nuclear dust lane enables us to fix this parameter, which is often left free in JAM model analysis such as in Cappellari et al. (2013a). We leave the z -anisotropy and M/L as free parameters in our analysis.

2.D.1 Adapting Observables to the JAM method

The NMAGIC and JAM methods require differently formatted observables, such as photometry, dark matter parameterisation, and kinematic data. To facilitate comparison we try to keep the observables, as consistent as possible between the NMAGIC and JAM methods.

Photometry

Elliptical NMAGIC models use spherical harmonics as their density constraint, while the JAM method uses the MGE formalism for its density and potential. For NGC 4697 we

therefore use the Magorrian (1999) representation from De Lorenzi et al. (2008) of the photometry to make an image of NGC 4697. We then fit an MGE to the image. The resultant image compared to the original from the Magorrian (1999) method is shown on Figure 2.D.1, with residual shown to be less than 5 % globally.

Dark Matter Profiles

A dark matter density profile is calculated from the logarithmic potentials A-K. A 1D MGE fit is made to these, and parameterised in 2D using the axis ratio q of the potential for each Gaussian in order to create an MGE dark matter potential.

Kinematics

The JAM method uses the mean (Gaussian) velocity and dispersion, while NMAGIC makes use of the fitted velocity, dispersions and higher Gauss-Hermite moments. The ATLAS^{3D} survey has both the mean and fitted kinematics available for NGC 4697, which we use as input for our JAM models. The SLUGGS data has only the fitted kinematics available. Therefore we use the correction from van der Marel & Franx (1993) to calculate the mean velocity and dispersions:

$$v_G = v_{GH} + \sqrt{3}\sigma_{GH}h_3\sigma_G = \sigma_{GH}(1.0 + \sqrt{6}h_4) \quad (2.30)$$

2.D.2 Model without dark matter

The JAM model code when used without dark matter can scale the optimal M/L when fitting the v_{rms} , equivalent to scaling the v_{rms} of the model by $\sqrt{M/L}$. This is not possible for models with dark matter, which is why we search the M/L parameter space. It does allow us, however, to test our parameter search method. For a range of β_z we find the optimal M/L using the JAM scaling technique, and compare it to the optimal M/L found by our parameter space search technique.

On Figure 2.D.2 we show the probability contours of the v_{rms} in M/L and β_z parameter space, with the best fitting M/L for each β_z using the JAM optimisation technique over-plotted with diamonds. The figure shows that the best $M/L - \beta_z$ pairs intersect with the contours of maximum probability in the parameter space. Both techniques therefore find the same best M/L for each β_z .

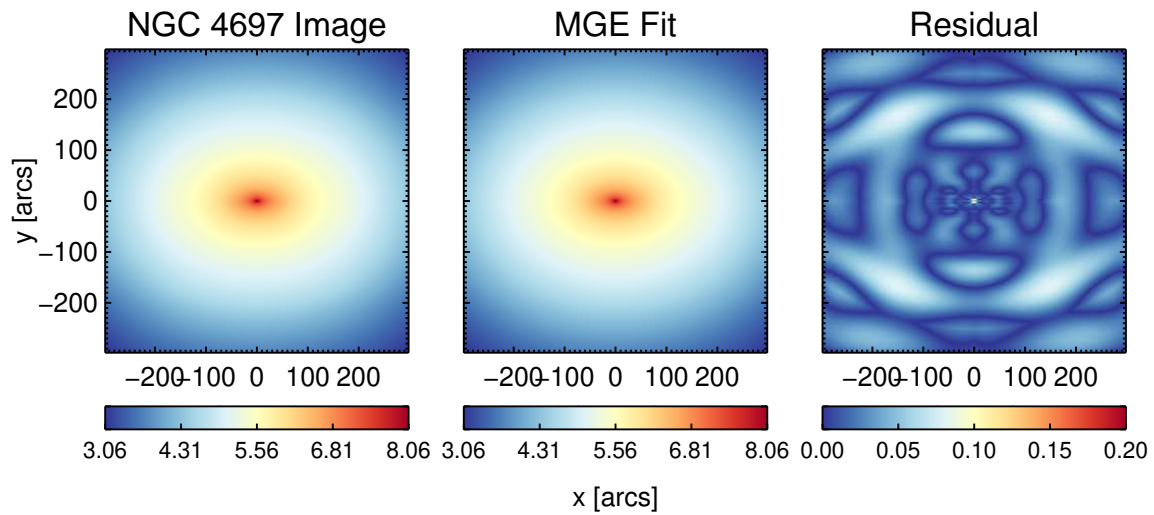


Figure 2.D.1: The De Lorenzi et al. (2008) photometry (left), the MGE fit to the De Lorenzi et al. (2008) photometry (middle) and the absolute value of the residual between them (right).

2.D.3 JAM Model Dark Matter Halos

We compare these models to those made by NMAGIC for the same dark matter halos, especially in terms of the M/L , β_z and dark matter halo favoured by the models. In Section 2.5.2 we compare our non-JAM NMAGIC model to the one where we attempt to force the JAM condition and fit the kinematics and find that the Mass-to-Light Ratio of the “Kin + Cross” models are higher than the “Kin Only” models by an average of 5%. This effect is even stronger for the true JAM models, with their M/L an average of 10% larger than those for the “Kin Only” models.

The “Kin Only” NMAGIC models prefer an intermediate dark matter halo D, while the “Kin + Cross” models prefer a stellar matter only model. The true JAM models also prefer a stellar matter only model when considering the χ^2 of the v_{rms} .

2.E Modelling Appendix

Here we include plots of models not included in the main text of the chapter.

2.E.1 NGC 4660

2.E.2 NGC 4697

Dark Matter

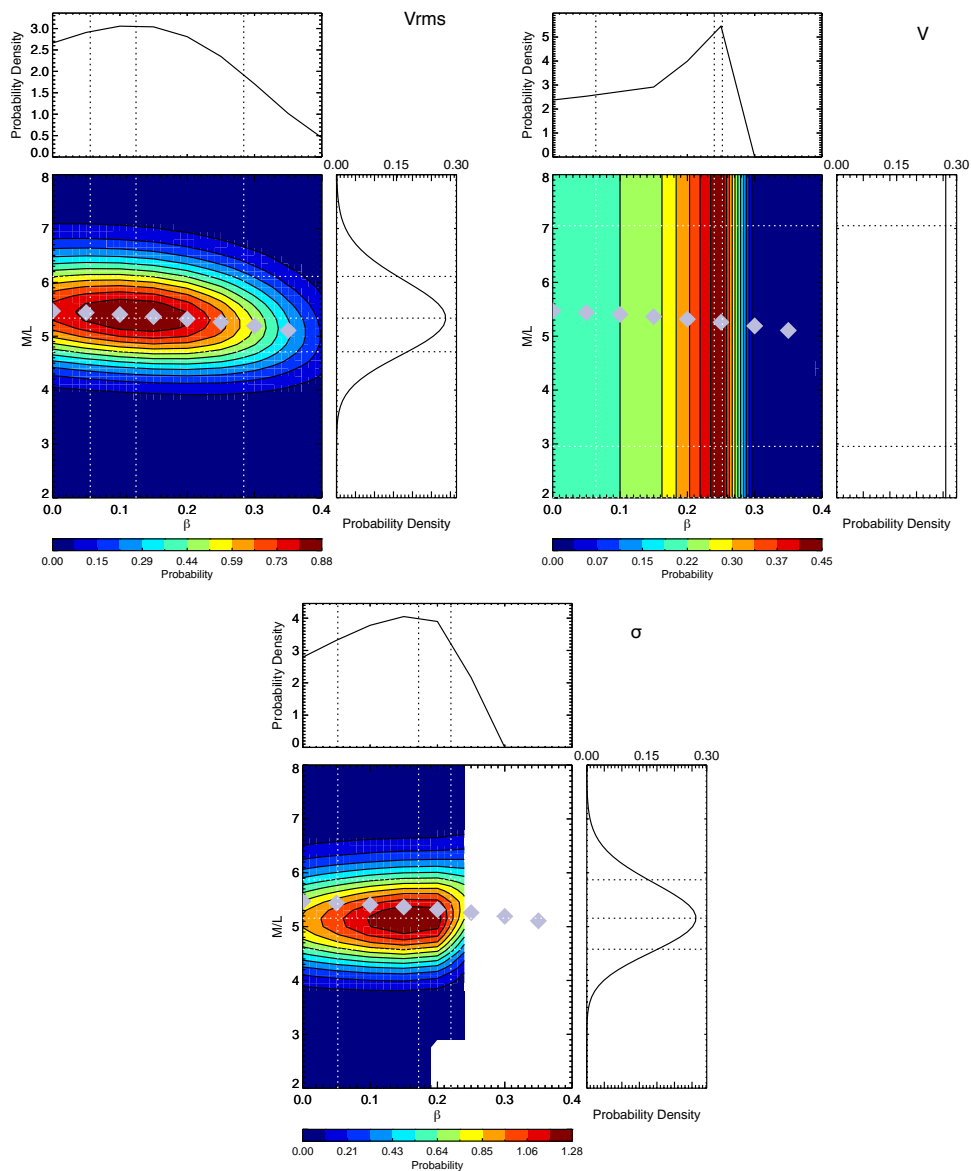


Figure 2.D.2: The 2D probability (central plot) of the parameters M/L and z anisotropy to reproduce the v_{rms} (top, left), v (top, right), and σ (bottom) of the combined ATLAS^{3D} and SLUGGS kinematic data for a model of NGC 4697 with only stellar matter. The overplotted diamonds show the best M/L for each anisotropy as derived by the JAM internal routine. The marginalised 1D probability of the parameters β_z (top) and M/L (right) for the v_{rms} .

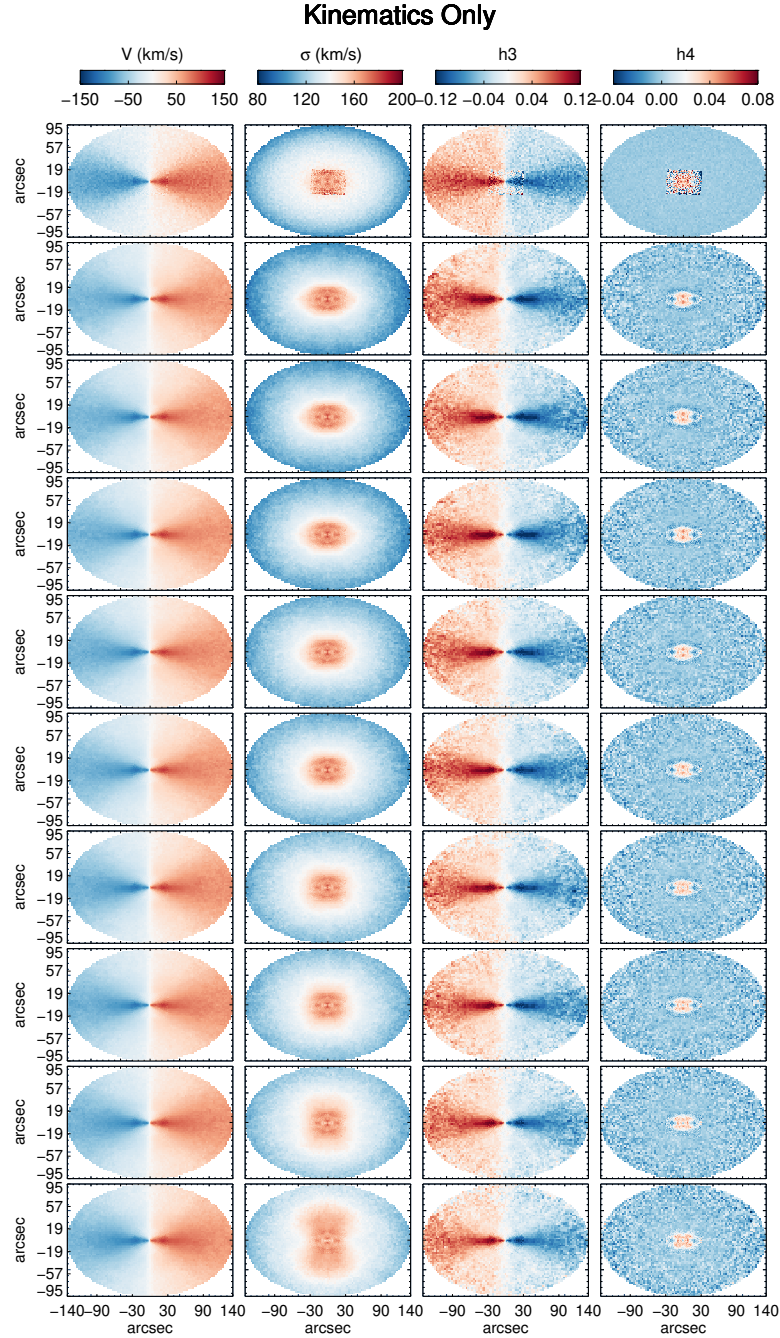


Figure 2.E.1: The v , σ , h_3 and h_4 of the 2D SLUGGS field data compared to that of models with different halos, A-K, ordered in increasing dark matter content for data driven models which fit the ATLAS^{3D} and SLUGGS kinematics only.

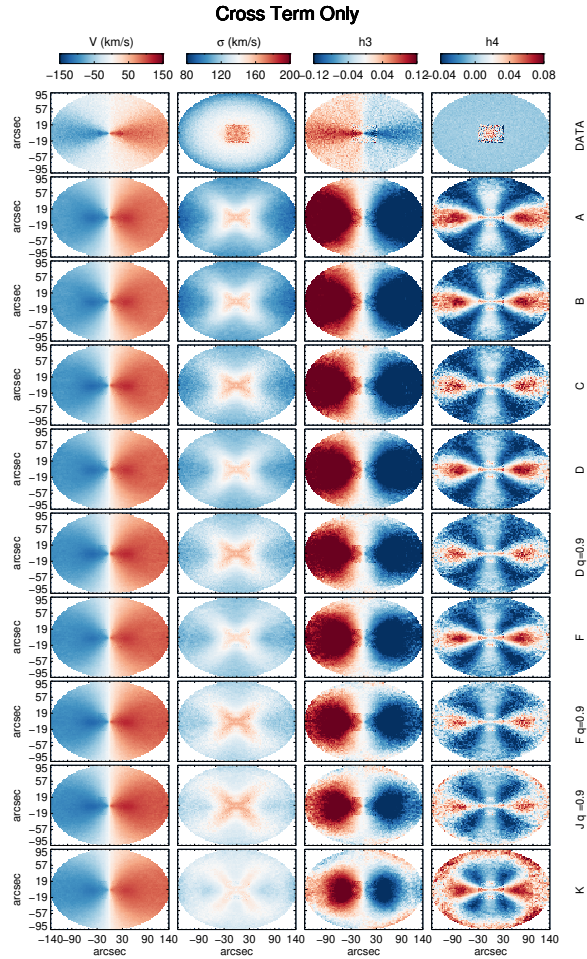


Figure 2.E.2: The v , σ , h_3 and h_4 of the 2D SLUGGS field data compared to that of models with different halos, A-K, ordered in increasing dark matter content, for models which enforce the JAM condition only.

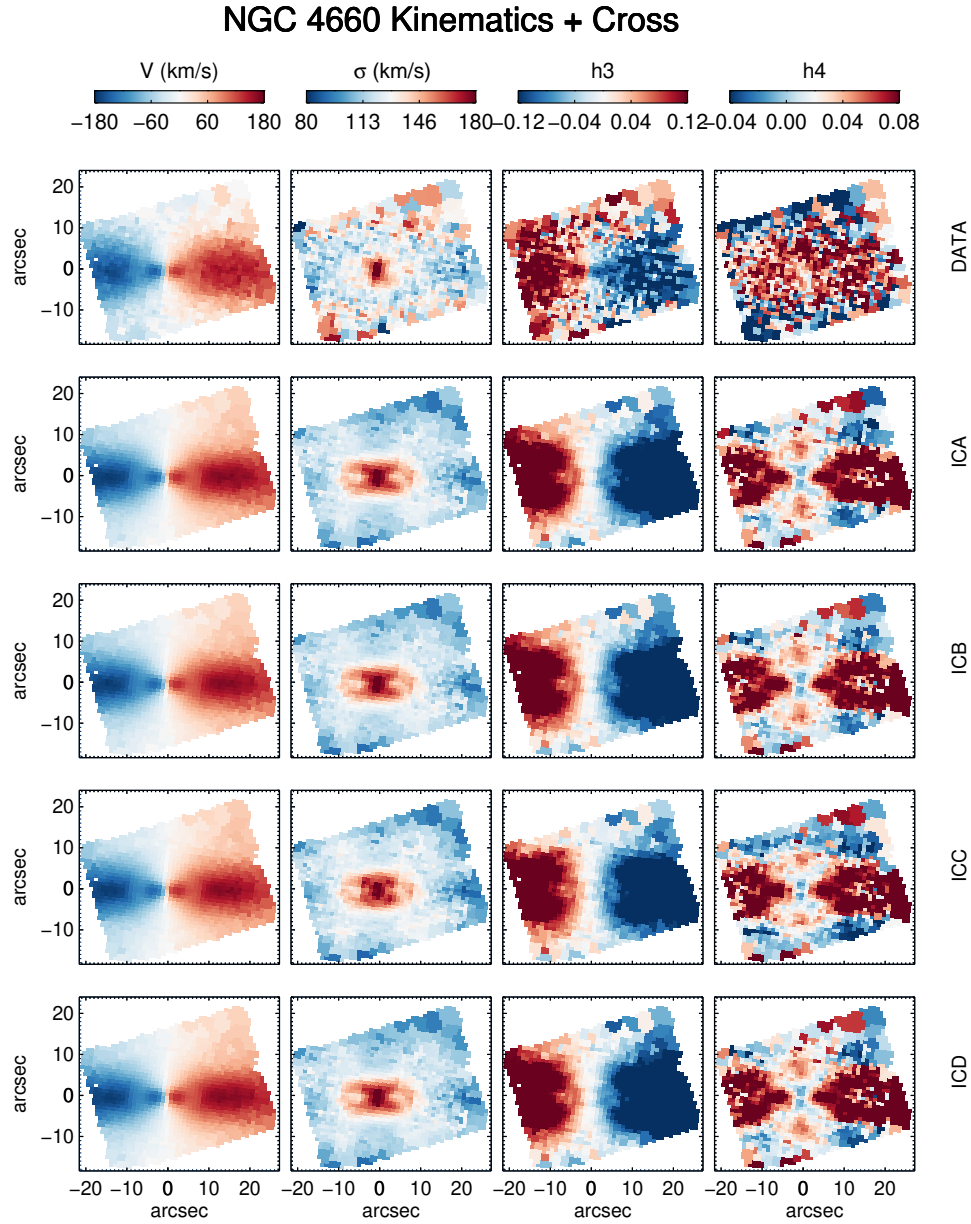


Figure 2.E.3: The first row shows the ATLAS^{3D} kinematic data, v , σ , and the h_3 and h_4 moments of NGC 4660. Subsequent rows show the projected kinematics of NMAGIC models which use the photometry and kinematics as an observable, in addition to the JAM assumption. The models differ which initial model is used, from top to bottom: Isotropic ICA, Mildly Anisotropic ICB, Strongly Anisotropic ICC, and “JAM-like” ICD. These models have a relative data strength of 0.09.

Circular Velocity

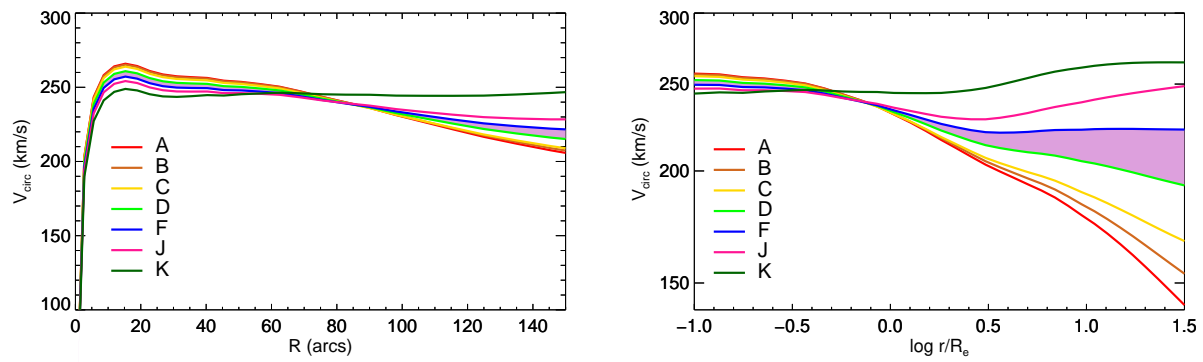


Figure 2.E.4: The circular velocity of the total matter (dark plus stellar) of models A-K used for modelling NGC 4697.

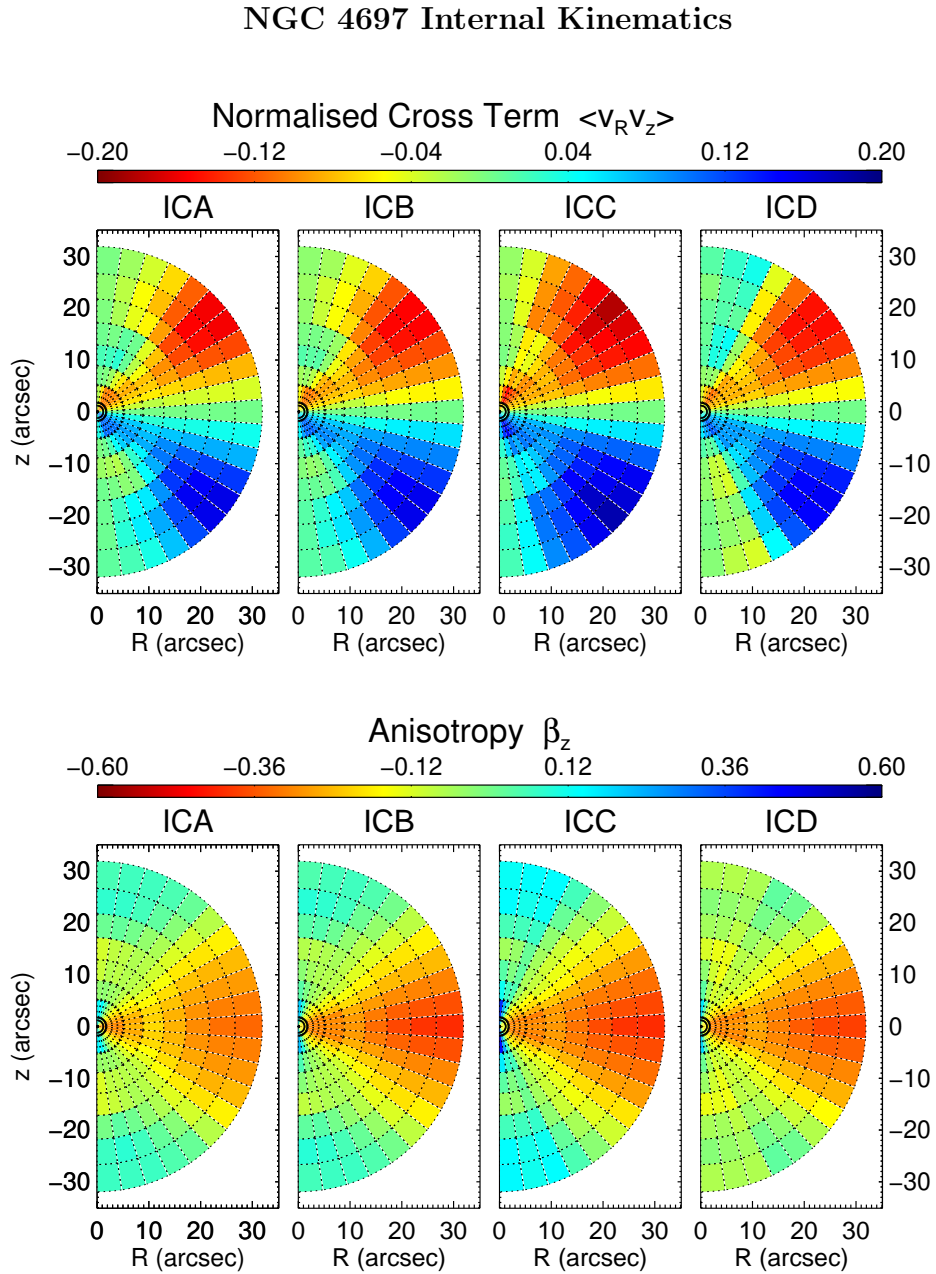


Figure 2.E.5: The cross term correlation $c_{(R,z)}$ (top row) and the z -anisotropy (bottom row) of kinematics driven models of NGC 4697, with initial models used from left to right: the “isotropic” model ICA, the “mildly-anisotropic” model ICB, “the strongly anisotropic” model ICC, and the “JAM-like” model ICD.

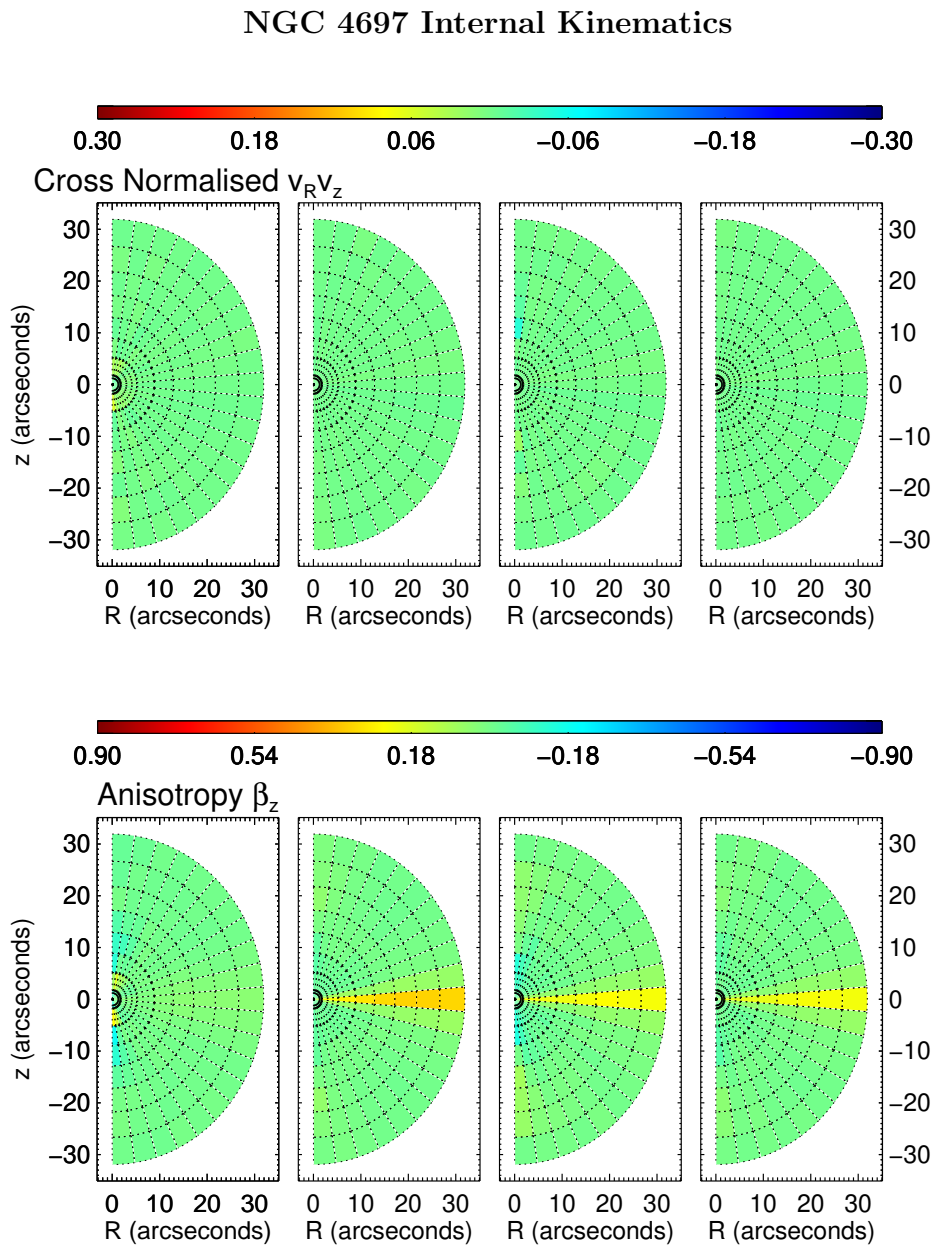


Figure 2.E.6: Same as Figure 2.E.5 with the JAM assumption and photometry, without kinematics, used as observables instead.

NGC 4697 Internal Kinematics Tension

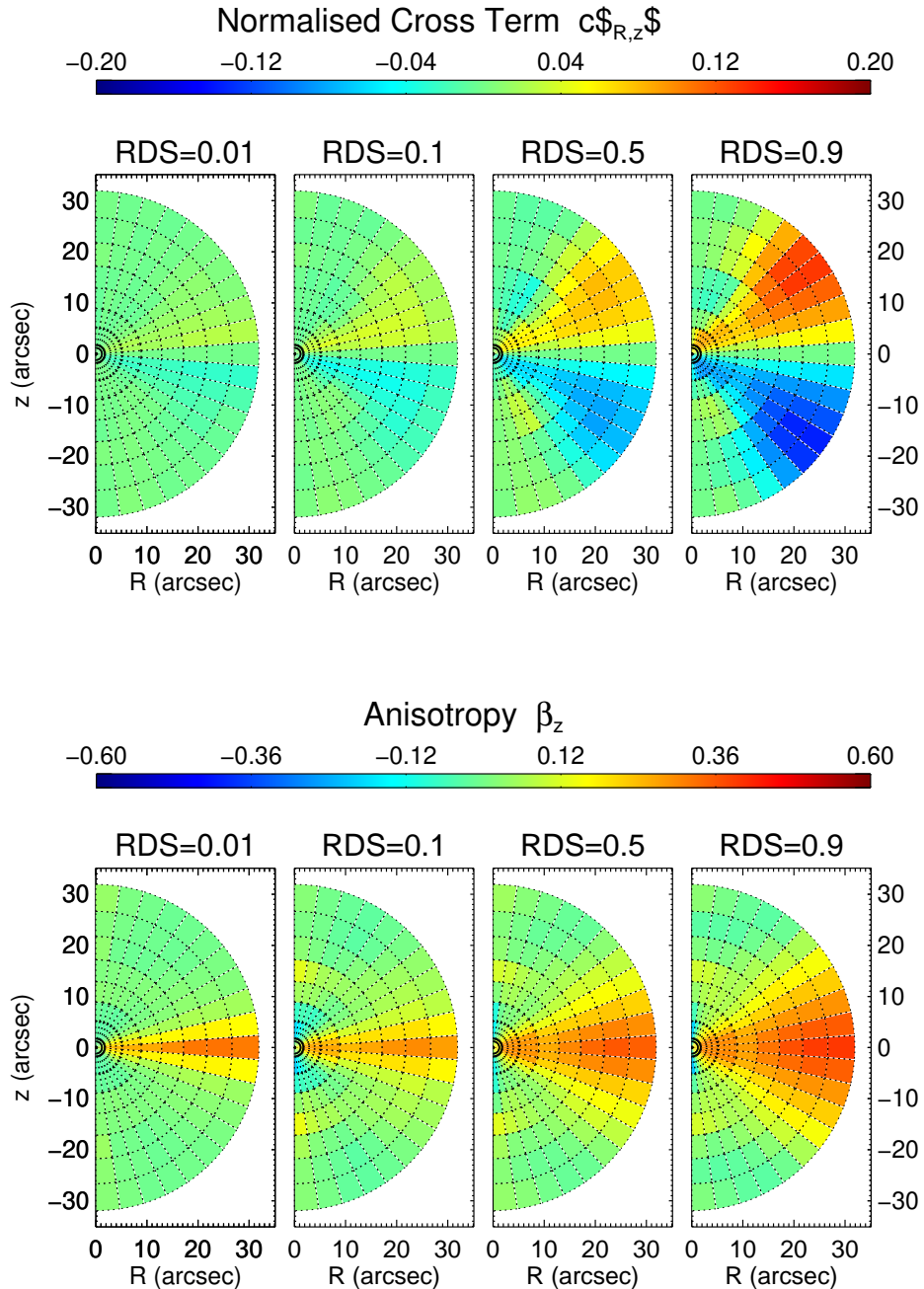


Figure 2.E.7: The cross term correlation $c_{R,z}$ (top row) and the z -anisotropy (bottom row) in the meridional plane of NGC 4697 within $30''$, fitted to the kinematics, photometry, and JAM condition with different relative data strengths (RDS)

NGC 4697 Internal Kinematics Tension

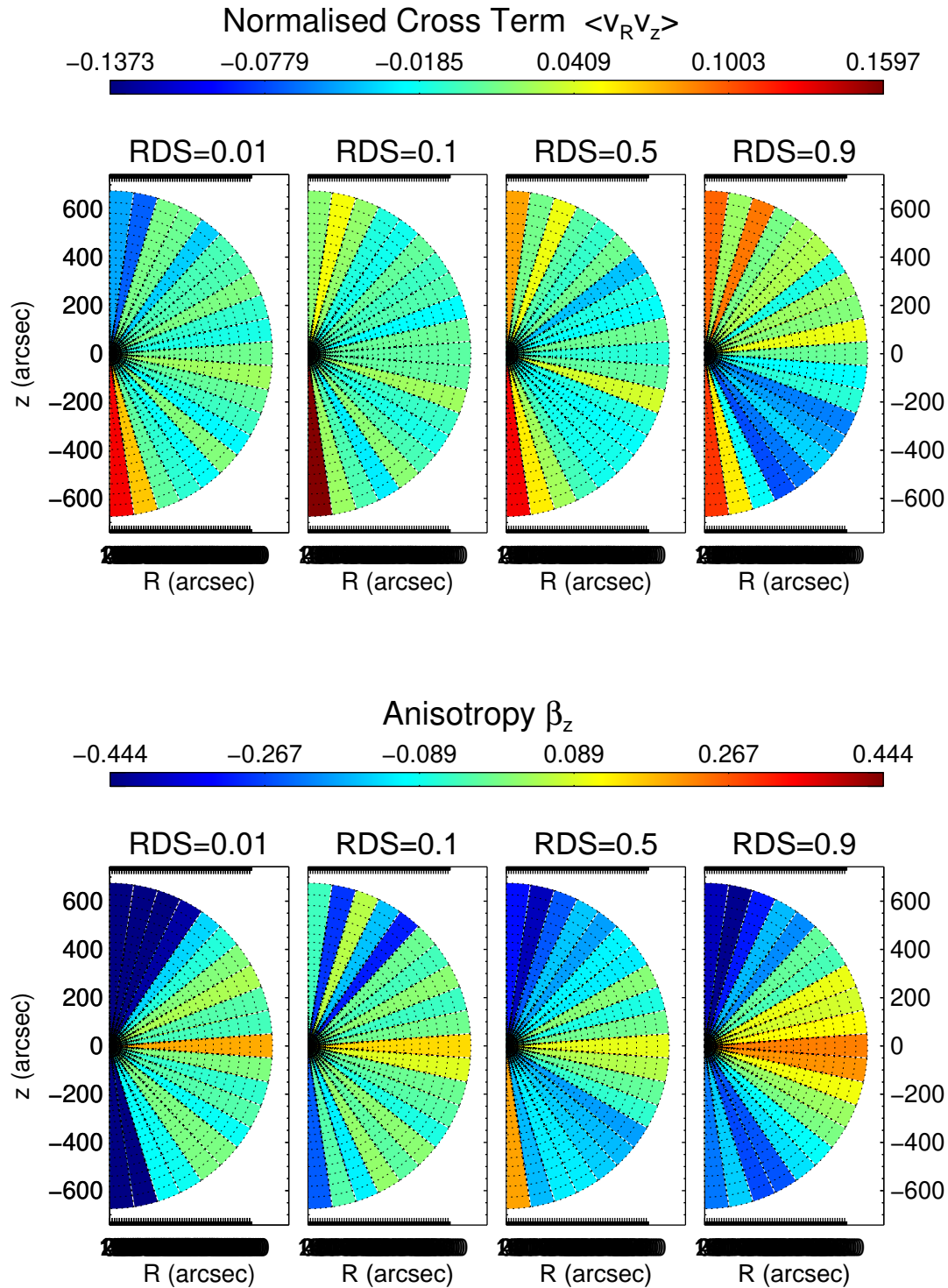


Figure 2.E.8: Same as Figure 2.E.7 with a differently weighted γ parameter, enforcing the JAM condition stronger than the models on Figure 2.E.7.

Comparison to 1D SLUGGS data Kinematics Only

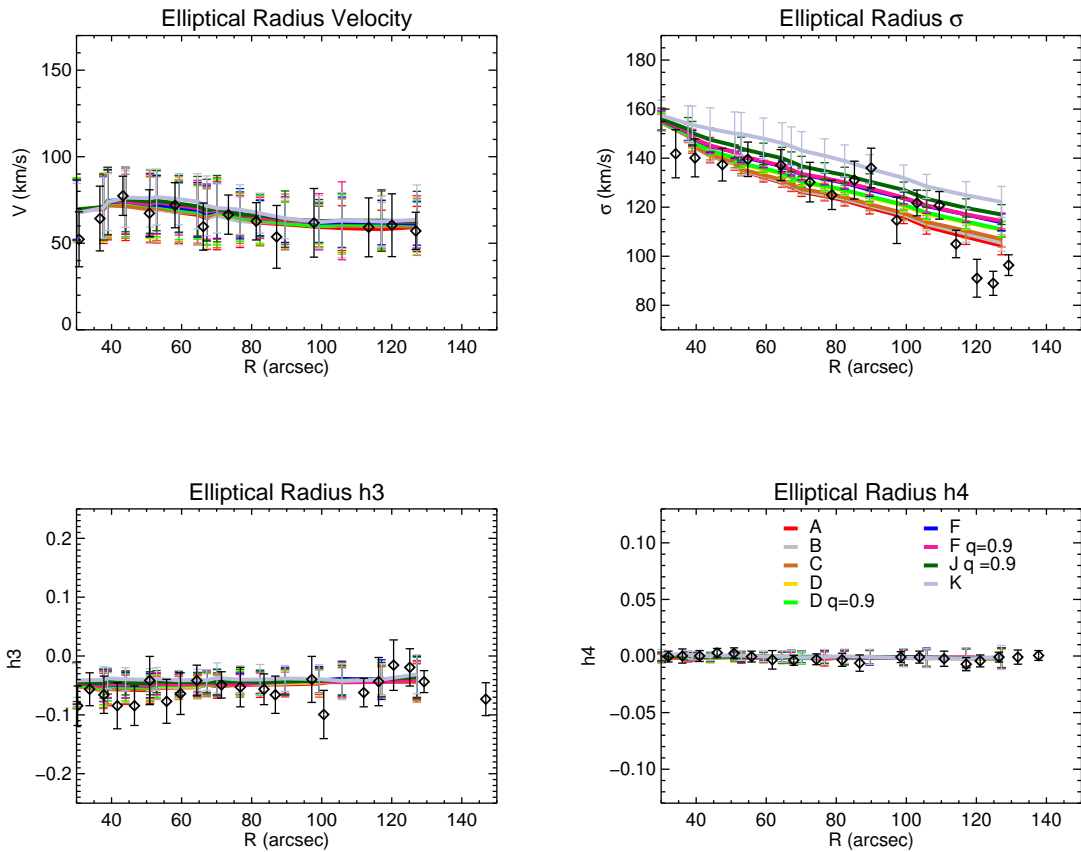


Figure 2.E.9: SLUGGS kinematic data as shown in Foster et al. (2016) on elliptical radii, compared to elliptically binned models with different dark matter halos which fit kinematic data (SLUGGS and ATLAS^{3D}) only, whose parameters are given in Table 2.2. The velocity and h_3 data have the ATLAS^{3D}-SLUGGS scaling described in Section 2.2.3 reversed.

Comparison to 1D SLUGGS data Cross Only

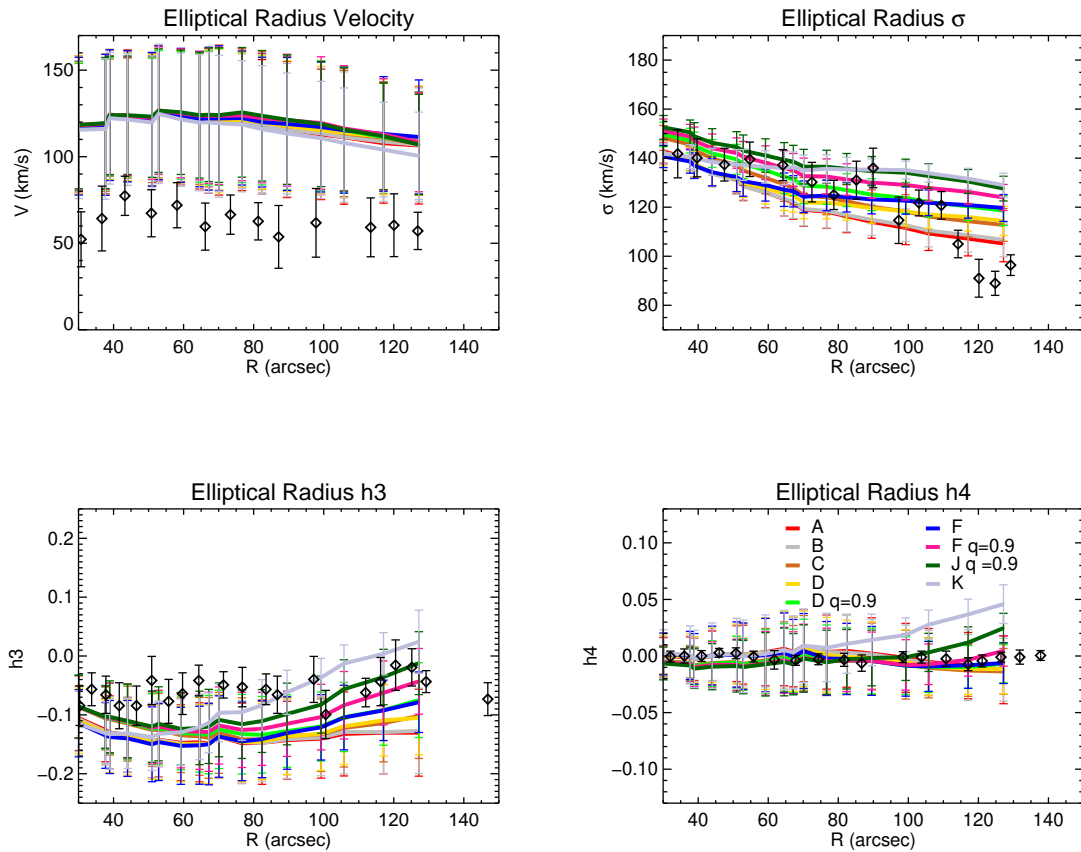


Figure 2.E.10: SLUGGS kinematic data as shown in Foster et al. (2016) on elliptical radii, compared to elliptically binned models with different dark matter halos which enforce the JAM condition, whose parameters are given in Table 2.2. The velocity and h_3 data have the ATLAS^{3D}-SLUGGS scaling described in Section 2.2.3 reversed.

Comparison to 1D SLUGGS data Kinematics + Cross

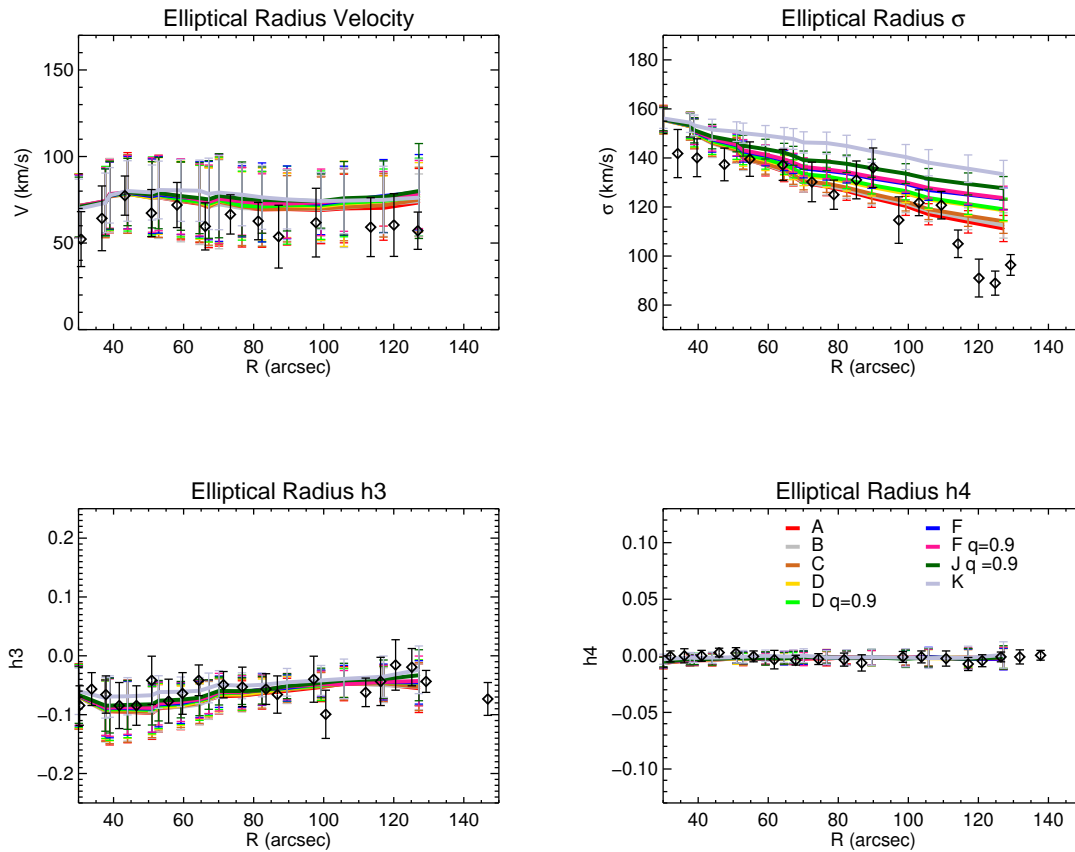


Figure 2.E.11: SLUGGS kinematic data as shown in Foster et al. (2016) on elliptical radii, compared to elliptically binned models with different dark matter halos which enforce the JAM condition and use the kinematic data as an observable, whose parameters are given in Table 2.2. The velocity and h_3 data have the ATLAS^{3D}-SLUGGS scaling described in Section 2.2.3 reversed.

Chapter 3

Triaxial Models

The only definitively known integral of triaxial galaxies is that of energy E . Observationally, twists in the kinematic axis and photometric axis, as well as their misalignment with respect to each other point to triaxiality. Slow rotators are more likely to be triaxial than faster rotators (Cappellari et al., 2007; Weijmans et al., 2014; Foster et al., 2017).

Galaxy surveys such as Emsellem et al. (2007), Cappellari et al. (2007) and Pulsoni et al. (2017) include a significant fraction of galaxies thought to be triaxial, depending on the survey selection. Much modelling such as Jeans modelling, JAM modelling and some Schwarzschild modelling has previously been spherical or axisymmetric. There are unique challenges to triaxial modelling, as there is no analytic way to make the models, and in general, there are no integrals other than energy. It is therefore difficult to specify the velocity at a given position of a particle (Dehnen, 2009).

Assuming an incorrect symmetry for the galaxy has been shown to have consequences for estimating scientifically important quantities, such as stellar and dark matter mass in Thomas et al. (2007) using Schwarzschild modelling and in Li et al. (2016) using the Illustris simulation. van den Bosch & de Zeeuw (2010) constructs triaxial Schwarzschild models of M32 and NGC 3379, finding that the best fitting triaxial model has approximately twice the black hole mass of the best axisymmetric model of NGC 3379. This has the implication that assuming axisymmetry could result in black hole masses being wrongly estimated. An efficient method for making triaxial models that accurately recovers galaxy properties is therefore important.

3.1 Triaxial N-Body Models using Made-to-Measure Method

The N-Body Model

The first step in creating the triaxial model given a density distribution is to use the method from Debattista & Sellwood (2000), adapted in De Lorenzi (2007). The differential density distribution is given in terms of the energy E and the angular momentum L by Binney & Tremaine (2008), as shown in Equation 2.14. The density distribution is calculated using Equation 2.14 as described in Section 2.3.4. This method creates a non-rotating spherical particle model, with model (x, y, z) and its velocities (v_x, v_y, v_z) in equilibrium. Each particle has equal weight in the internal units of this model, $w_p = 1/N$ and the total particle weight $w_{tot} = 1$. In order to achieve a particle model that has a triaxial density the particle model the shape of model is modified to be triaxial using the coordinate transform:

$$x' = x \tag{3.1}$$

$$y' = qy \tag{3.2}$$

$$z' = pz \tag{3.3}$$

with q and p as the axial ratios:

$$T = \frac{1 - p^2}{1 - q^2} \tag{3.4}$$

However, although this modifies the shape of the particle model to be flattened, the velocities (v_x, v_y, v_z) are no longer in equilibrium for this system. In order to place the model into equilibrium, it is evolved in NMAGIC towards the triaxial target density. The x, y, z shape of the model is already at the desired point. Therefore the target density of the model is calculated directly from the model itself on spherical harmonic shells. The radial range of the target density is reduced to $r < 122.4$ kpc, since when evolving a particle model in NMAGIC, the target density always has to have a smaller radial range than the particle model due to noise at large radii and to allow large ranging orbits. The uncertainty on the target density is taken to be the particle noise, calculated from randomly rotating the spherical model fifty times and finding a spread of the three-dimensional densities calculated from the different angles. The flattened model is then evolved in NMAGIC in a self-consistent potential towards the target density, with additional steps after the evolution to test equilibrium.

Since NMAGIC works by modifying the weights of particles to get the desired distribution, the weight of the particles in the final triaxial model are now unequal, but still adding up to the total mass in internal units of the mass of the particles $w_{tot} = 1$. Scaled to physical units, the model is given a total mass of $10^{10} M_{\odot}$, with a $M/L = 1$. The

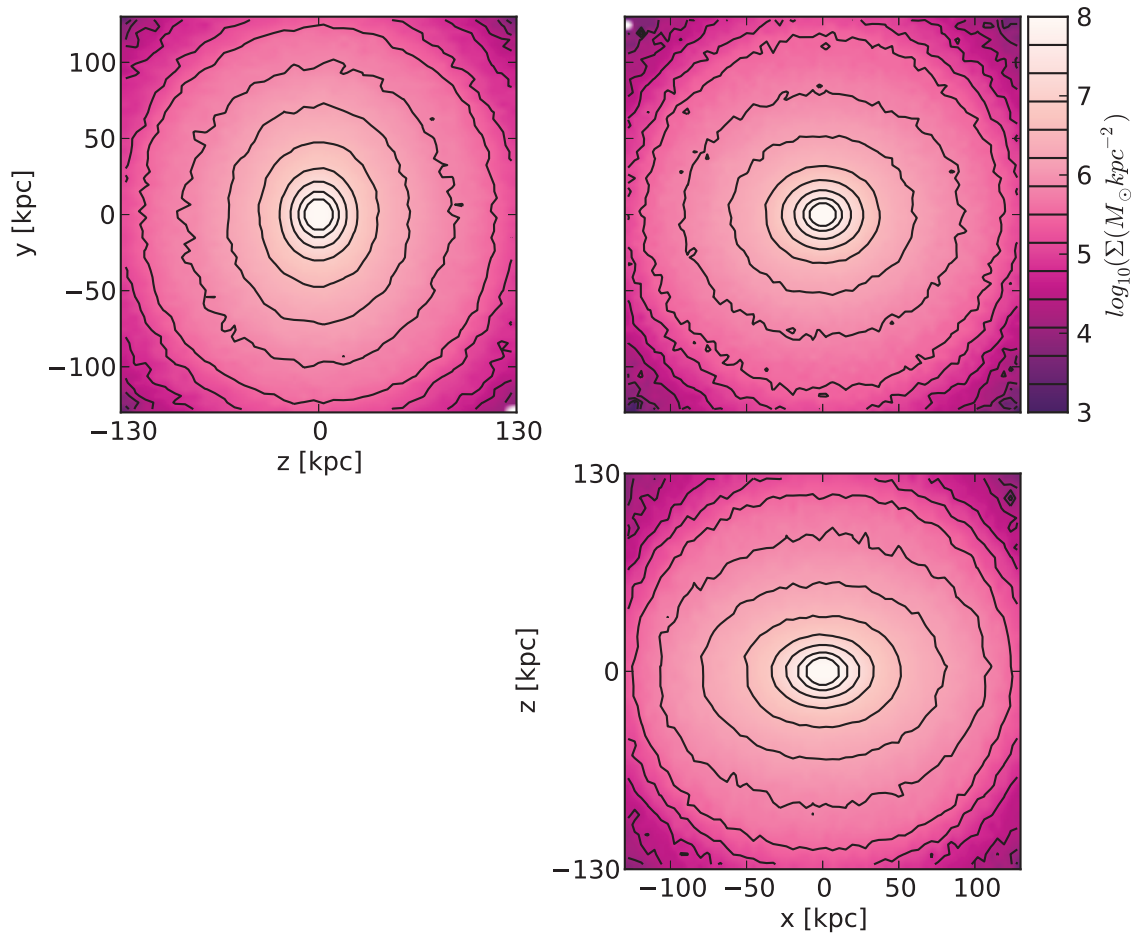


Figure 1: The x , z , and y projection of the density of the 4 million particle triaxial model in equilibrium after NMAGIC evolution.

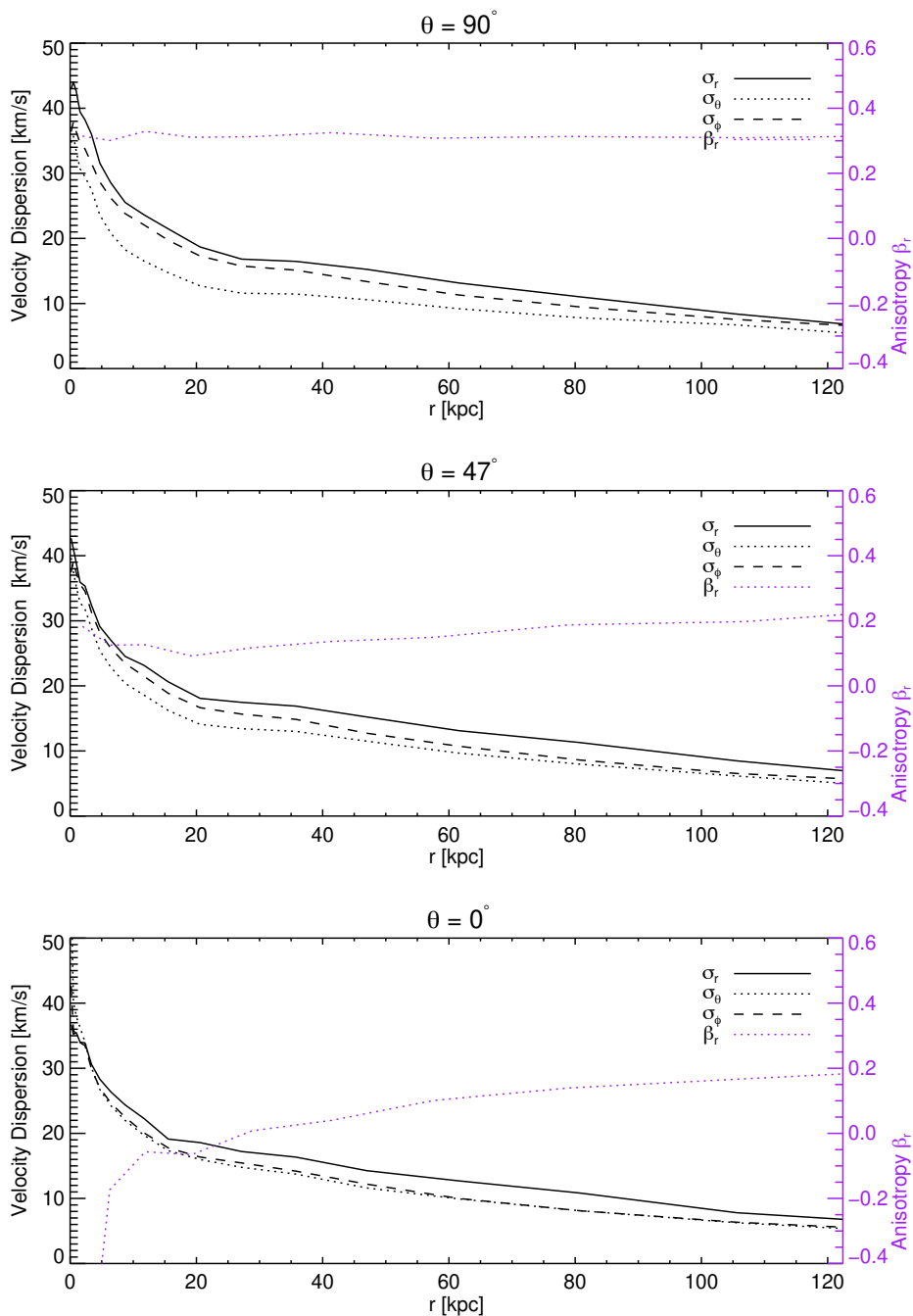


Figure 2: The internal velocity dispersions σ_r , σ_θ , and σ_ϕ with radius r in spherical coordinates of the 4 million triaxial particle model in equilibrium after NMAGIC evolution. From top to bottom: Along the major axis $\theta = 0^\circ$, along an intermediate axis $\theta = 47^\circ$, and along the minor axis $\theta = 90^\circ$. For all profiles $\phi=0^\circ$.

ratio M/L is one of the parameters which the Schwarzschild modelling tries to recover by making a Schwarzschild model to the NMAGIC particle model. Views of the particle model are shown on Figure 1.

Anisotropy of the N-body Model

As well as the model's shape, its anisotropy has to also be initialised and considered. For constructing the initial spherical model from the distribution function, the circularity equation from Gerhard (1991) is used:

$$f(E, L) = g(E)h(c) \quad (3.5)$$

The function $h(c)$ shifts stars on surfaces of constant energy, while $g(E)$ expresses how the stars are distributed on these surfaces, covering all of (E, L) space. Regarding $h(c)$, c depends on E and L through $c = L/(L_0 + L_c(E))$. The parameter $L_c(E)$ is the angular momentum of a circular orbit at energy E , and L_0 is the angular momentum constant.

There are several different analytic forms that $h(c)$ can take to create tangential or radial anisotropy profiles. In this particular case we take the radial parameterisation presented in Gerhard (1991):

$$h(c) = h_\alpha(c) = (1 - c^2)^\alpha, \quad (3.6)$$

where the parameter α controls the level of anisotropy $\beta_r = 1 - (\sigma_\phi^2 + \sigma_\theta^2)/2\sigma_r^2$. In our case we use $\alpha = 1$ to model a galaxy with mildly radial anisotropy. When the spherical model is squashed and subsequently fitted to equilibrium in NMAGIC, this profile is altered by the fitting process, but the scale of the initial anisotropy can still have some effect on the final model. The anisotropy β_r and velocity dispersions along three directions (r, θ, ϕ) of the triaxial equilibrium NMAGIC model are shown in Figure 2.

3.2 Applications of Triaxial Modelling

3.2.1 Testing a Schwarzschild Model

A triaxial model was evolved in NMAGIC to test the triaxial Schwarzschild code known as SCHERPA (**SCH**warzschild **mE**thod for **tR**iaxial early-ty**Pe** **gA**laxies) developed by Fabrizio Finozzi, presented in detail in Finozzi (2018).

The target density of this method is a density from photometry of NGC 4649. This is a massive elliptical galaxy, deprojected in Das et al. (2011), using the method from Magorrian (1999). A self-consistent gravitational potential was chosen. To achieve sufficient resolution for the Schwarzschild model to be tested, a model of 4 million particles

was created with $n_E = 400$, $n_L = 250$, and $n_{LE} = 40$. The number of radial divisions of the density represented as spherical harmonics as in equation 1.33 is chosen to be $n_r = 60$, and $l = m = 8$. The radial interval for the particles is chosen to be $0.3 - 201.0$ kpc. The distance of the galaxy is taken to be NGC 4649's (16.83 Mpc), taken from Tonry et al. (2001).

The values of the triaxiality parameters were chosen in Finozzi (2018) as $q = 0.7$ and $p = 0.85$ to yield $T = 0.55$. The values are chosen to obtain for q in the realistic range of $q \approx 0.6 - 0.8$ according to Binney & de Vaucouleurs (1981) and Tremblay & Merritt (1996) and following Vincent & Ryden (2005) to keep $T = 0.4 - 0.8$, which is consistent with bright elliptical galaxies. The model is evolved for 115,000 time steps, with 20,000 additional steps to test equilibrium. The errors of the target density are calculated using the method from De Lorenzi et al. (2007), in which randomly rotated particle realization of the target density are produced in order to estimate an error. In our instance we rotated a particle model of 4 million particles 50 times. Using these errors a reduced χ^2 with the NMAGIC model was calculated. The reduced χ^2 is 0.35666 before the equilibrium testing. Additionally, equilibrium testing was performed, after testing stability. The density of the model did not significantly alter during stability and equilibrium testing. The model is therefore thought to be stable and in equilibrium.

The density of the final model in three projections is shown in Figure 1, which shows its triaxiality. Another check of the triaxiality of the model is performed by calculating the inertia tensor using the method from De Lorenzi (2007), which gave a result of $q = 0.702$ and $p = 0.852$ within a distance of 122.4 kpc for the model.

Here we present a summary of the results of the tests using the triaxial N-body model performed by Finozzi (2018). A set of tests is performed by projecting the N-body model along the principal axis, x, y, z , and by binning the particles to calculate smooth density, intrinsic and projected kinematics profiles. To test the Schwarzschild method the characteristics (eg. internal kinematics, M/L) recovered by the method were compared to the same characteristics of the NMAGIC-produced particle model. Projecting the model in (x, y, z) , the ratio M/L of the triaxial N-body model is recovered within 2% of the true value. The intrinsic kinematics are recovered within 4.5%. When the model is projected in the line-of-sight ($\theta = 45^\circ, \psi = 45^\circ, \phi = 112^\circ$) the internal kinematics are recovered within 3.7% of the true value. The same result is recovered when an MGE re-and-deprojection is used on an image made of the particle model. In addition, the viewing angle is recovered within 7°, and the intrinsic shape (q, p) is recovered within 6%. Compared to the triaxial separable Abel models of van den Bosch & van de Ven (2009) the intrinsic shape is better recovered by SCHERPA. Having a method of accurately determining important intrinsic quantities of triaxial galaxies is important, making Schwarzschild modeling a versatile tool for many different scientific problems.

3.3 Modelling M87

M87 is a giant elliptical galaxy in the Virgo cluster, close to the centre of sub-cluster A, the dynamical center (Binggeli et al., 1987). It is thought to have a history of galaxy mergers (De Lucia & Blaizot, 2007), and is thought to not be entirely in equilibrium due to the presence of extended tidal features (Mihos et al., 2005; Janowiecki et al., 2010). This, along with its triaxiality, makes it an interesting target for dynamical modelling.

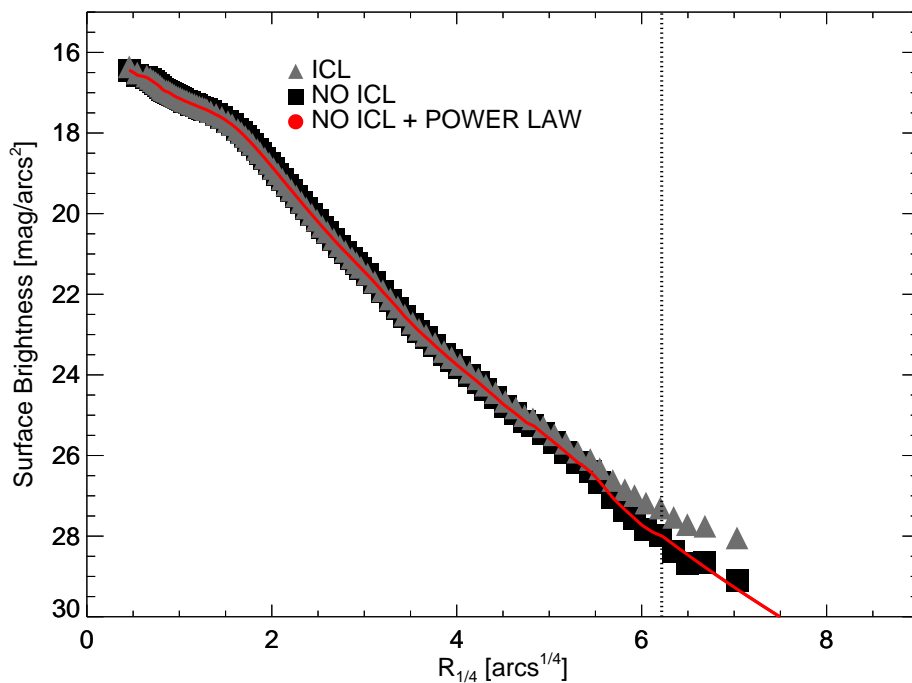


Figure 3: Surface brightness in V -band magnitude of M87 from Kormendy et al. (2009). The black squares is the photometry without the ICL component Longobardi et al. (2015b), the red line is the interpolation and power-law extrapolation used for the NMAGIC models, and the grey triangles are the surface brightness with the ICL component.

3.3.1 Photometry

We use the photometry of M87 from Kormendy et al. (2009), with the ICL component subtracted (Longobardi et al., 2018). The photometry of M87 has an intracluster light (ICL) component, shown on Figure 3. Since the ICL is thought not to be in a relaxed state (Longobardi et al., 2018), we use the surface brightness without the ICL component for the

density. The 1D profile is interpolated, and beyond $1494''$ interpolated and extrapolated using a power law. A 2D photometric field is then constructed along elliptical radii, using ellipticity $\epsilon = 0.4$. We use a distance for M87 throughout of 14.53 Mpc (Ciardullo et al., 2002; Longobardi et al., 2015c). Then, using the same method as for NGC 4660 in Section 2.A, an MGE is fitted to the 2D field.

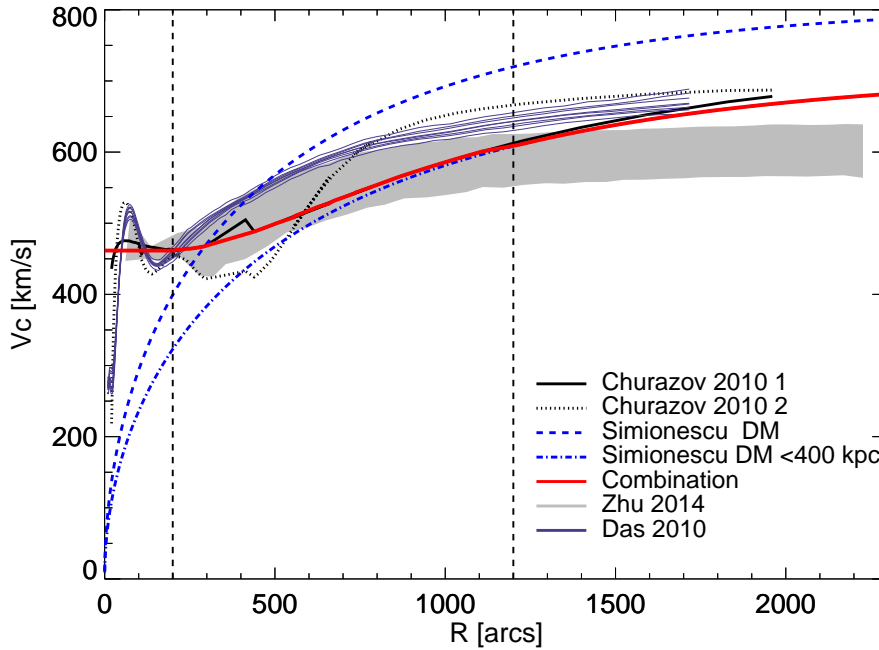


Figure 4: Circular velocity curves of M87 from different literature, and the combined (Churazov et al. (2010) 1 and Simionescu et al. (2017) < 400 kpc) profile used for our NMAGIC models in red. The two smoothed X-ray profiles from Churazov et al. (2010) are in black (labelled Churazov 2010 1 and Churazov 2010 2), the two NFW dark matter profiles from Simionescu et al. (2017) in blue, the Zhu et al. (2014) profile and confidence intervals as the grey area, and the Das et al. (2010) profiles from their analysis in dark blue.

Triaxial Density

The MGE fit to the photometry is axisymmetric, with one axis ratio (q) of every Gaussian. However, we require a triaxial luminosity density for M87. We therefore use a version of the MGE density equation, from van den Bosch et al. (2008), which allows another axis

ratio (p) for every parameter, allowing the introduction of triaxiality:

$$j(x, y, z) = \sum_{j=1}^N \frac{L_j}{(\sigma_j \sqrt{2\pi})^3 p_j q_j} \times \exp \left[-\frac{1}{2\sigma_j^2} \left(x^2 + \frac{y^2}{p_j^2} + \frac{z^2}{q_j^2} \right) \right], \quad (3.7)$$

where j is the luminosity density in Cartesian (x, y, z) coordinates, σ is the x -axis dispersion of the Gaussians, p and q are the axial ratios, N is the total number of Gaussians required, and j is the individual Gaussian. This parameterisation allows for q and p to vary with radius, as it can be set as different values for individual Gaussians. For the target density of M87, p and q are chosen to be similar values in the center, with p becoming larger than q in the outer parts of the galaxy. The inclination angle θ used is 90° , and ϕ is also 90° .

3.3.2 Potential

The circular velocity is a combination of a flat profile out to $200''$ (~ 15 kpc) from Churazov et al. (2010), a deprojected curve from the X-ray potential from Churazov et al. (2010) between $200''$ and $1200''$. We use the NFW model to M87 from Simionescu et al. (2017) for $r > 1200''$ (~ 88 kpc).

The Churazov et al. (2010) X-ray potential Φ is given in units of μm_p keV, where μ is the mean atomic weight of the gas, assumed to be $\mu = 0.61$ in Churazov et al. (2010) and m_p is the proton mass. We calculate the circular velocity from the potential using:

$$v_{\text{circ}}^2(r) = r \frac{d\Phi}{dr} \quad (3.8)$$

and convert the units to kms^{-1} . We use the smoothed X-ray potential.

$$(3.9)$$

The NFW circular velocity used to calculate the profile from the parameters given by Simionescu et al. (2017):

$$g(c) = \frac{1}{\ln(1+c) - c/(1+c)} \quad (3.10)$$

$$\frac{v_{\text{circ}}^2(r)}{v_{\text{vir}}^2} = \frac{g(c)r_v}{r} \left(\log\left(1.0 + c \frac{r}{r_v}\right) - \frac{c r/r_v}{1.0 + (c r/r_v)} \right) \quad (3.11)$$

where G is the gravitational constant, c is the concentration parameter, r_v is the virial radius, v_{vir} is the virial circular velocity, which is calculated using the virial mass $M_{\text{vir}, v_{\text{circ}}}$ is the circular velocity, and r is the radius. We compare our circular velocity to Zhu et al. (2014) and Das et al. (2010), shown in Figure 4.

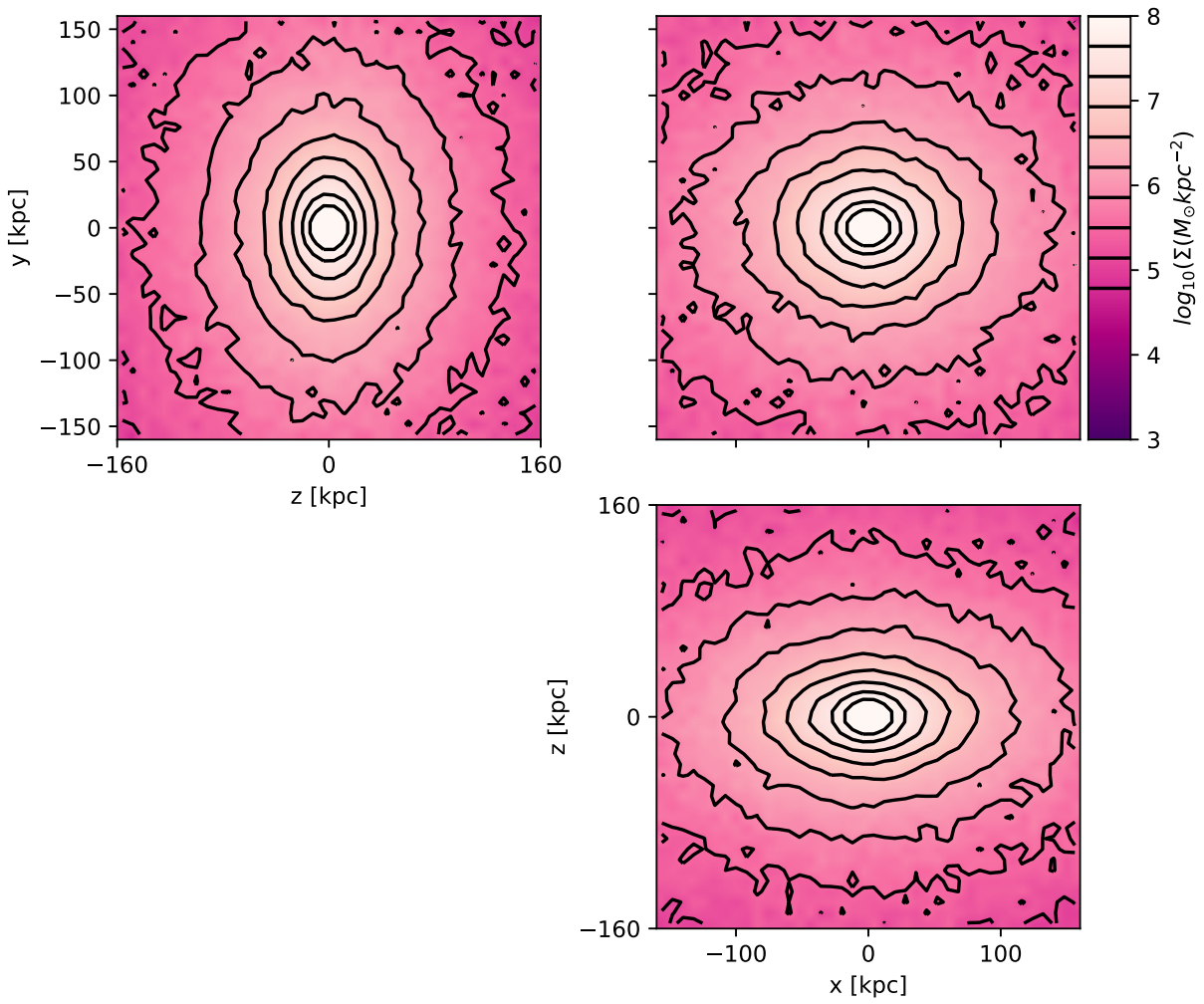


Figure 5: The x , z , and y views of the surface density of the anisotropic M87 model.

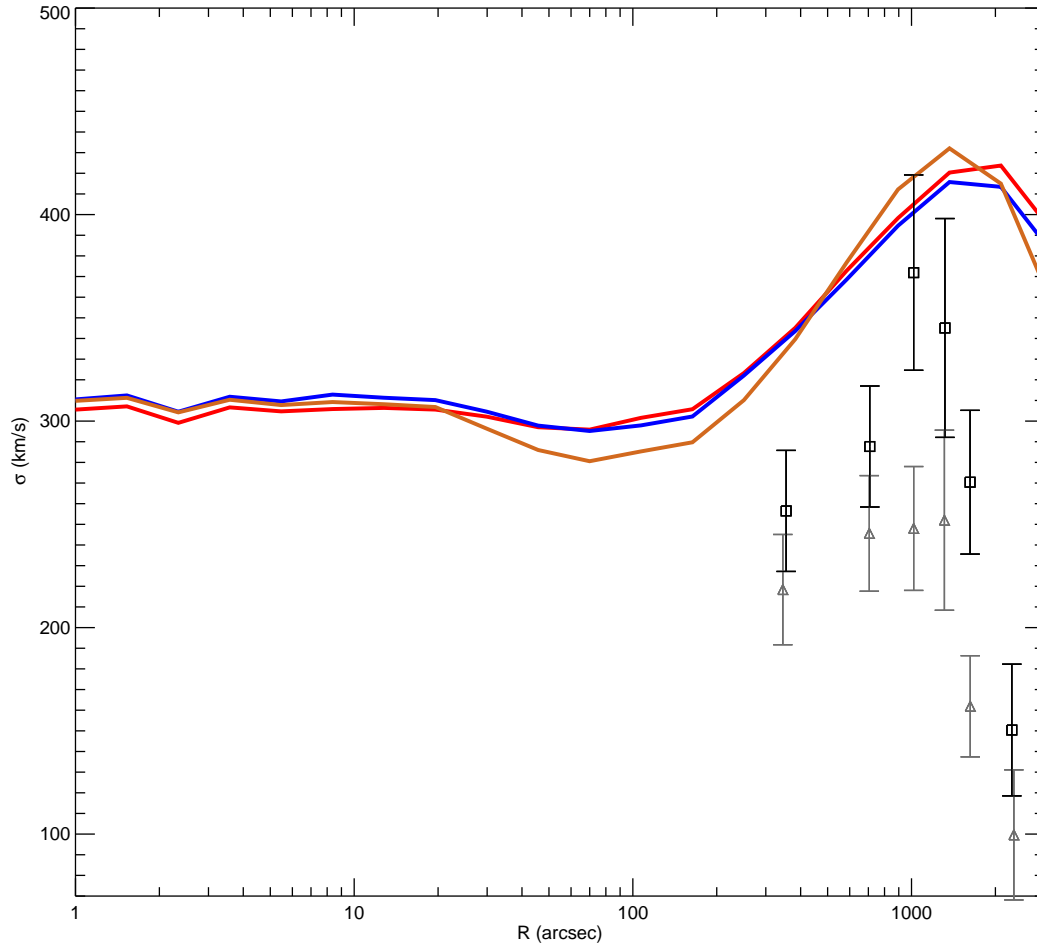


Figure 6: The lines are the velocity dispersion of three different (see Figure 7 for profiles) NMAGIC models with different anisotropies corresponding to the same colour in Figure 7, with the brown model being nearly isotropic, the red an intermediate anisotropic model, and the blue being the most strongly anisotropic model of the three. The points are the PNe dispersions from Longobardi et al. (2018), with the black squares giving the root-mean-square dispersion (likely overestimation) and the grey triangles the robust sigma (likely underestimation).

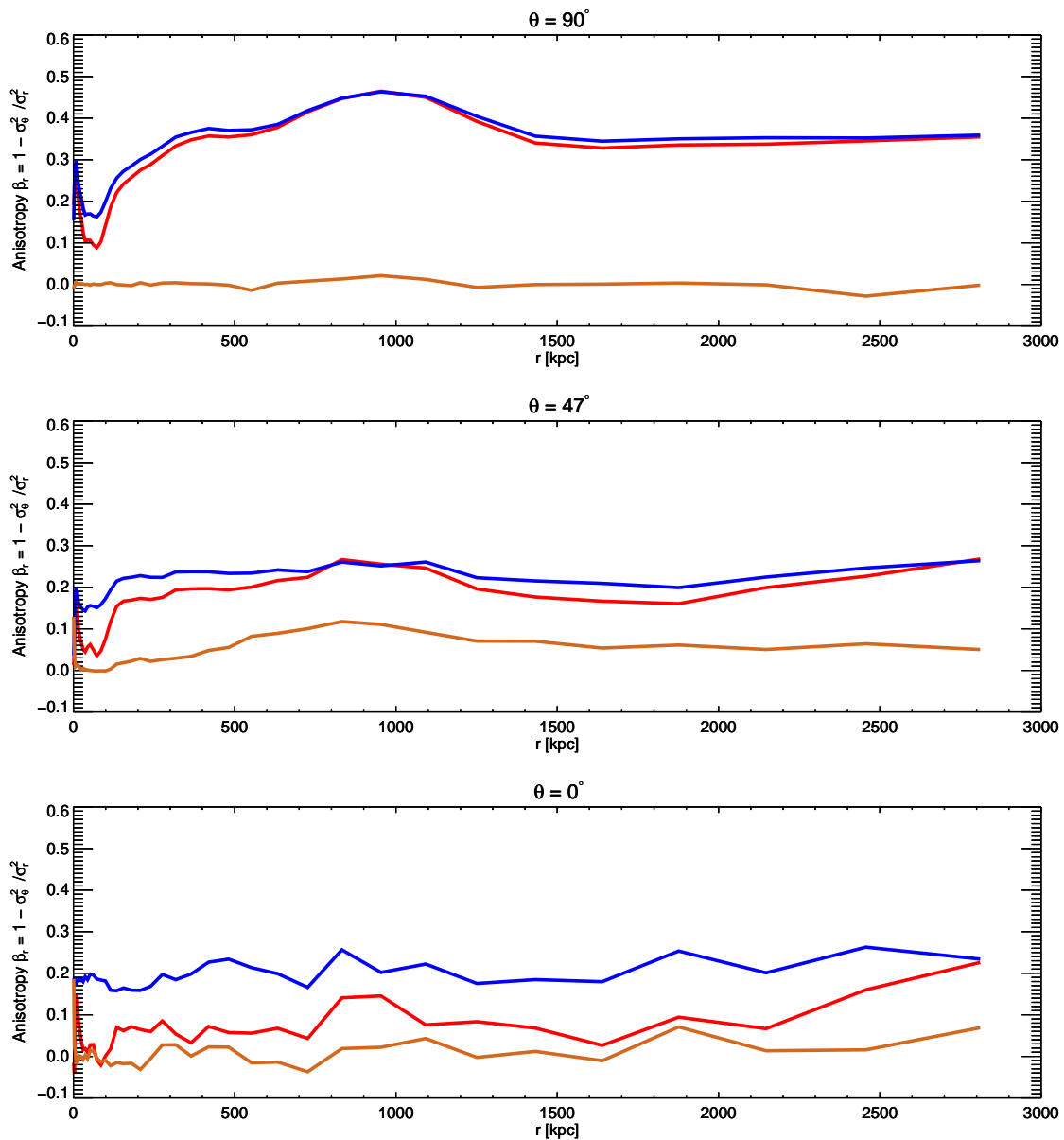


Figure 7: The r -anisotropy of three different NMAGIC models to see (Figure 6 for σ profiles in same colours) M87 along the major (0°), minor (90°), and intermediate (47°) internal axis of the model. The brown line is a nearly isotropic model, the red line an intermediate radial anisotropic model, and the blue line a more strongly radially anisotropic model.

3.3.3 M87 NMAGIC Models

Using the circular velocity as an external potential, along with the stellar density as described above, we make an NMAGIC model to M87, successfully creating a triaxial model shown in Figure 5. We use several different anisotropies using β fitting as implemented in Chapter 2. These β_r anisotropies are shown in Figure 7, with their corresponding elliptically averaged projected mean σ profiles shown in Figure 6.

The model is compared to the PNe data profiles from Longobardi et al. (2018), which gives an overestimate and underestimate of the σ profile using a root-mean-square and robust techniques detailed in Longobardi et al. (2018). The NMAGIC σ profile overestimates the PNe data, although it has a similar shape of a sharp rise and decline.

In addition, there is σ data for the centre of M87 from IFU data from Emsellem et al. (2014) and absorption line data from van der Marel (1994). Our models overestimate the σ in the centre compared to these data as well, but match its shape. Varying the anisotropy alters the shape, but not the overall normalisation sufficiently to match the data. This is likely caused by an overestimate of the circular velocity profile. Churazov et al. (2010) estimates a circular velocity 20 kms^{-1} lower than we use of 440 kms^{-1} .

3.4 Conclusions

We set out to make a self-consistent triaxial model using NMAGIC, which was successfully completed with a flattening of $q = 0.702$ and $p = 0.852$. Similar techniques are then applied to make a triaxial model of the galaxy M87 using an external circular velocity curve derived from a combination of X-ray data from Churazov et al. (2010) and an NFW model from Simionescu et al. (2017). This results in an overestimate of the σ profile when compared to data from Emsellem et al. (2014) and van der Marel (1994) and PNe data from Longobardi et al. (2018). This is thought to be an overestimation of the circular velocity. A future extension of project could be the use of kinematic fitting to fit the IFU data from Emsellem et al. (2014) in the centre and scale to the PNe in the outer part of the galaxy in order to produce a more accurate σ profile. This procedure could help to discern the range of anisotropy structures that might be viable for M87.

Chapter 4

Spherical Jeans models of stars and gas kinematics in NGC 4278

This chapter is based on contributions to Arnaboldi et al. (2018), in prep.

The outskirts of galaxies are dynamically interesting regions, where dark matter dominates and evidence of mergers and accretion events can be found (Coccatto et al., 2013). NGC 4278 in particular is interesting because it is different from other intermediate angular momentum ellipticals, suggesting a higher dark matter fraction. The use of kinematic tracers such as planetary nebulae (PNe) and globular clusters (GC), for which magnitude is radially independent, enables us to gain line-of-sight velocity information out to several effective radii of the galaxy (e.g. Arnaboldi et al., 1998, 1996, 1994; Coccatto et al., 2013). Planetary nebulae are excellent kinematic tracers, as they are found to be in good agreement with the light and kinematics of the stellar population (Cortesi et al., 2013; Coccatto et al., 2009).

Planetary nebulae and globular clusters have been used to obtain information about the dark matter halo (Romanowsky et al., 2003; De Lorenzi et al., 2008; Napolitano et al., 2011; Deason et al., 2012) and kinematics. They have been used to identify stellar streams from gravitational interactions between galaxies (Spiniello et al., 2018), identify stellar-kinematic substructures (Hartke et al., 2018), and find accretion events (Longobardi et al., 2015a).

NGC 4278, a low luminosity elliptical galaxy ($L_B = 1.17 \times 10^{10} L_\odot$) in the Coma I group, has an uncharacteristic flat v_{rms} profile that is more typical of high mass ellipticals. Intermediate luminosity ETGs seem to show systematic trends for the fraction of dark matter, i.e., within $5R_e$ they appear to have the lowest values (Alabi et al., 2016). Hence, the current extended v_{rms} profile for NGC 4278 is interesting because it is difficult to look at dark-matter fraction at the outermost radii measured by the kinematic tracers, i.e.,

within $10R_e$.

To investigate this effect, the potential and anisotropy of NGC 4278 are modelled using spherical Jeans equations. Kinematics data from SAURON for the inner region ($< 0.5R_e$) and PNe data for the outer region of the galaxy (up to $10R_e$) are used to discriminate between different models. The PNe of NGC 4278 and its satellite galaxy NGC 4283 were detected and their line-of-sight velocities measured using the Planetary Nebulae Spectrograph (PN.S). The PN.S uses counter-dispersed slitless spectroscopy, for which more details can be found in Douglas et al. (2002).

This work was done in collaboration with Chaitra Narayan, who was supervised by Magda Arnaboldi and reduced the PNe data, and Lodovico Coccato who fitted the Sérsic profile and removed outliers from the PNe sample using sigma-clipping. This work is described in Section 4.1.

A sub-structure was also found that might have been tidally stripped from the companion galaxy NGC 4283. The sub-structure contains both PNe and globular clusters from Usher et al. (2013). The PNe ascribed to this substructure are excluded from our v_{rms} calculation.

4.1 Data

The main characteristics of NGC 4278 and NGC 4283 are shown in Table 1. Several steps are taken before the PNe data can be used for analysis of these galaxies. This process is detailed in Arnaboldi et al. (2018) and summarised here. The association of the PNe to NGC 4278 and to NGC 4283 needs to be identified in order to separate their kinematic properties.

Following the method of McNeil et al. (2010) and McNeil-Moylan et al. (2012), the individual PN is assigned a probability of belonging to either galaxy dependent on surface brightness of galaxy at the PN position and PN velocity. There is no PN with ambiguous galaxy association, mostly likely as a consequence of the large systemic velocity separation between the two galaxies. The separation of the PN velocities is shown in Figure 2. NGC 4278 has 77 PN associated to it, and NGC 4283 has 12. Figure 2 shows a two Gaussian fit obtained by bootstrapping over 10000 iterations, finding the peak of the NGC 4278 velocities to be (622 ± 21) kms^{-1} . This is consistent with the Cappellari et al. (2011) value of (620 ± 5) kms^{-1} and the Pulsoni et al. (2017) value of (605 ± 17) kms^{-1} . We find a peak value of (1050 ± 21) kms^{-1} for NGC 4283, which is consistent with the Cappellari et al. (2011) value of (1056 ± 5) kms^{-1} .

Figure 2 shows 8 PN outliers, which are removed from the main kinematic sample.

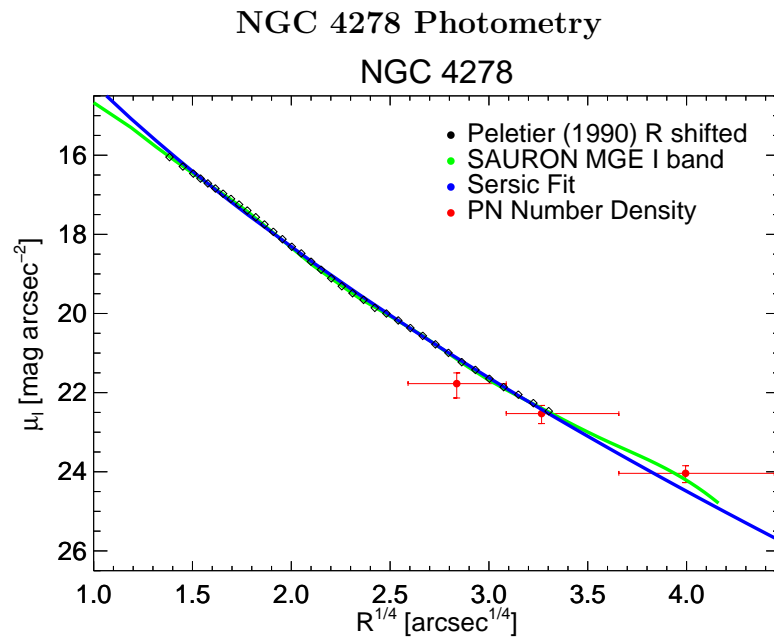


Figure 1: The colour-shifted Peletier et al. (1990) surface brightness profile as black diamonds, the PNe number density as the red points, the SAURON MGE I -band as the green line, and the Sérsic I -band fit to the Peletier et al. (1990) data in blue.

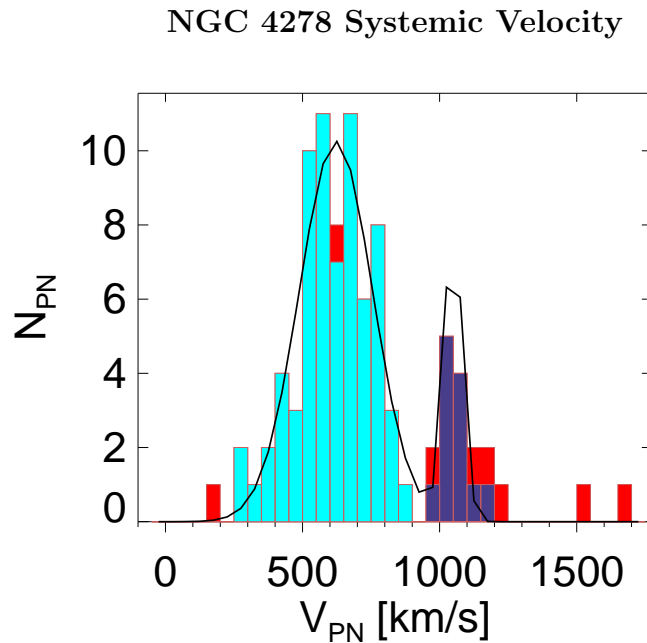


Figure 2: Velocity distribution of the sigma-clipped sample of the PNe with a bin size of 50 km s^{-1} . The black line represents a fit of a sum of two Gaussians to the distribution. The red bars show the sigma-clipped PNe, done by Lodovico Coccato. The blue and dark blue bars are PNe assigned as belonging to NGC 4278 and NGC 4283, respectively.

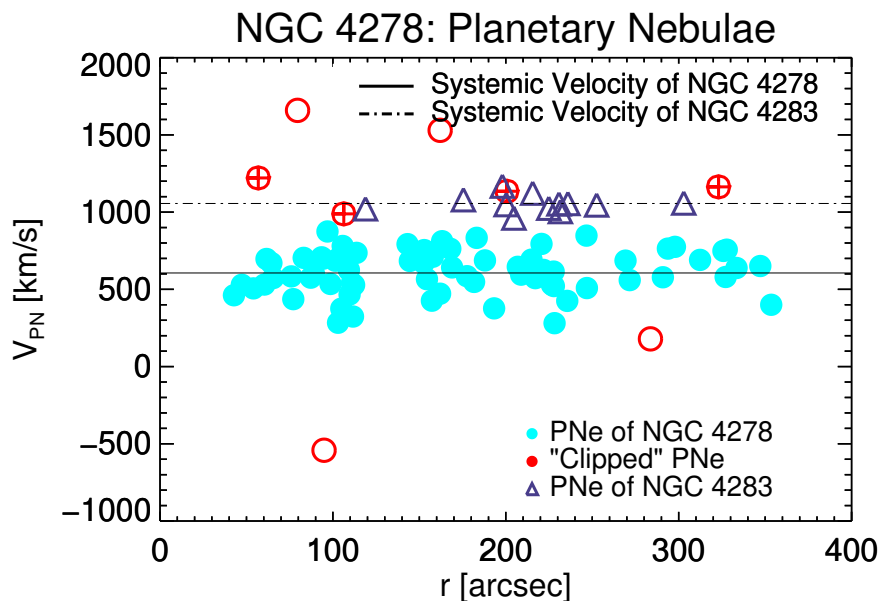


Figure 3: Line-of-sight velocities of the PNe of NGC 4278 against projected distance from the center (radius). The dark blue triangles belong to NGC 4283 and the light blue dots to NGC 4278. The red circles represent the clipped PNe. The red circles with crosses inside are thought to belong to a substructure discussed in Section 4.4.

These are selected by being more than 2.5σ from the mean velocity of their neighbours, in a method described in more detail in Arnaboldi et al., in prep., as shown in the phase space diagram of Figure 3. Comparing the kinematics and the HI disk from Morganti et al. (2006) show are misaligned, with the misalignment varying with radius.

4.2 Data for use in JAM modelling

4.2.1 Photometry

In order to make a spherical Jeans model of NGC 4278, we require extended photometry $> 350''$, beyond the point where the PNe kinematics extend. For the inner $100''$, R -band data are available from Peletier et al. (1990). The PNe number density ranges from $65''$ to $255''$. A Sérsic profile is fitted to the Peletier et al. (1990) data and PNe number density with parameters $\mu_{R,e} = 21.24$ mag arcsec $^{-2}$, $R_{R,e} = 34.60''$, and $n = 6.87$. PNe number density is obtained from all PNe down to a completeness magnitude $m=27.7$ mag. This was determined by detecting simulated objects on artificial images with the same properties such as noise, point spread function and instrumental magnitude as the science images in Arnaboldi et al., in prep. The number density profile was corrected for spatial incompleteness inside $80''$; at larger radii the sample is $> 90\%$ complete. The completeness was determined by detecting simulated sources added to observed images, as describe in Arnaboldi et al., in prep. An *HST*/F814W I -band MGE profile of NGC 4278 is available from Cappellari et al. (2006a), with the largest Gaussian having a σ of $152''$. The profile is accurate to within approximately a factor of 2 of the largest Gaussian in radius, spanning a range of $r = 0.01 - 304.1''$. It has a $R_{I,e} = 32''$. These data are shown in Figure 1. The Peletier et al. (1990) data and the Sérsic fit is colour shifted to be consistent with the Cappellari et al. (2006a) data. Figure 1 shows that the colour-shifted Peletier et al. (1990) data and Sérsic profile from Cappellari et al. (2006a), and the PNe number density are all consistent with one another, except within $< 2''$. There is a large peak in the Sérsic profile that is not found in the Cappellari et al. (2006a) data. Since the Cappellari et al. (2006a) data extend further into the centre and are more accurate, they are used for the Jeans modelling at the central radii, with the Sérsic fit used for the remaining radial range.

4.2.2 Root-mean-square velocity (v_{rms})

The root-mean-square (RMS) velocity $v_{rms} = \sqrt{\sigma^2 + v^2}$, where v is the rotational velocity, is used instead of the velocity dispersion σ . The RMS velocity v_{rms} is a measure of the kinetic energy. The PN data are used for large radii, while the azimuthally averaged SAURON data are used at smaller radii (see Figure 4).

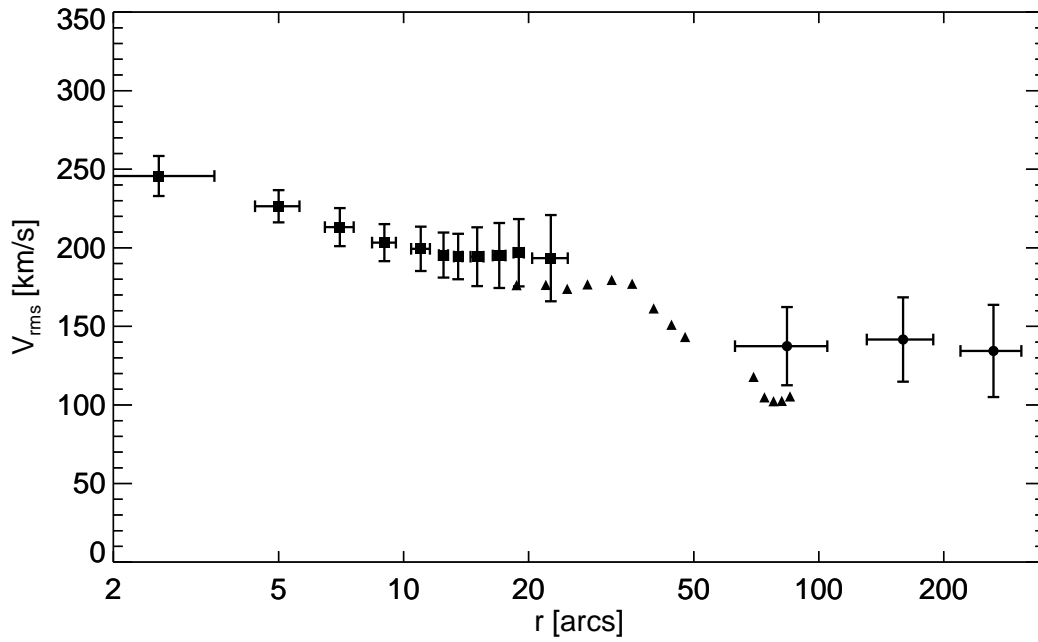


Figure 4: Azimuthally averaged v_{rms} data as a function of radius in arcseconds on a logarithmic scale. SAURON data are indicated by squares, SLUGGS data are indicated by triangles, and the PNe data are indicated by circles. The PNe and SAURON data have error bars showing standard deviations from the azimuthal averaging.

4.2.3 HI Data

The potential can be constrained using measurements of the circular velocity from the HI disk presented in Morganti et al. (2006). Their data, shown in Figure 5, are de-projected using a linear fit to the axis ratio of the disk as a function of radius. The errors are calculated by propagating the standard error of the fit and the measurement errors. Since the disk is face-on at the centre, the central region within a radius of $R < 100''$ is not used.

Large deviations from a flat disk occur at $R > 300''$ due to the two tails of the HI disk. HI velocity data are therefore used in the radial range $100'' < R < 300''$ only. We compare our circular velocity values with the recent measurements published by Serra et al. (2016) and find that the two values are consistent within the uncertainties.

Table 1: Properties of the galaxies NGC 4278 and NGC 4283 used in this chapter and their source. Row (1) & (2) are the RA and DEC of the center of the galaxies, row (3) is the systemic velocities, and row (4) is the adopted distance.

	NGC 4278	NGC 4283	Source of data
RA (J2000)	185.02832	185.086609	Cappellari et al. (2011)
Dec (J2000)	29.280619	29.310898	Cappellari et al. (2011)
Systemic velocity (kms^{-1})	606/620	1056	Pulsoni et al. (2017)/ Cappellari et al. (2011)
Distance (Mpc)	15.6	15.3	Cappellari et al. (2011)

4.3 Jeans Modelling

In the current analysis, the galaxy is assumed to be spherically symmetric, with no rotation. Under these assumptions, the components of the velocity dispersion tensor are $\sigma_r^2 = \bar{v}_r^2$, $\sigma_\theta^2 = \bar{v}_\theta^2$, and $\sigma_\phi^2 = \bar{v}_\phi^2$, leading to the Jeans equation of the form:

$$\frac{d}{dr}(j\sigma_r^2) + \frac{2\beta}{r}j\sigma_r^2 = -j\frac{d\Phi}{dr}, \quad (4.1)$$

where $j(r)$ is the stellar density and $\Phi(r)$ is the total gravitational potential. The anisotropy parameter is $\beta = 1 - \sigma_\theta^2/\sigma_r^2$ which becomes $\beta = 0$ for an isotropic system. The total gravitational potential $\Phi(r)$ can be decomposed into contributions from stellar matter and dark matter, $\Phi(r) = \Phi_{\text{stellar}}(r) + \Phi_{\text{DM}}(r)$ (Binney & Mamon, 1982).

Using $j(r)$, $\Phi(r)$ and $\beta(r)$, the Jeans equations are solved to find the radial velocity dispersion σ_r . The radial velocity dispersion is then projected along the LOS in order to

provide the LOS velocity dispersion σ_{LOS} , which can then be compared to the velocity dispersion data shown in Figure 4. Parameterisations of $j(r)$ and $\Phi(r)$ and $\beta(r)$ are therefore required, according to the analytical formulas described in the following:

Density

For the inner part of the galaxy the density profile is obtained by surface brightness de-projection using Abel Integrals. For the outer part the Lima Neto et al. (1999) Sérsic parametrisation of the density profile is used.

Potential

There are six different potential parameterisations used in this paper:

- i) **“Constant”**: This model does not separate dark mass and stellar mass. A constant fit to the circular velocity is used to model the total potential.
- ii) **“Power Law”**: A power law is used to model the total potential, without separating dark and stellar mass.
- iii) **“Stellar Only”**: Only the stellar matter from the density is used to model the potential.
- iv) **“NFW”**: This model uses the stellar potential combined with a Navarro-Frenk-White (NFW) profile to model the dark matter to give the total potential.
- v) **“Quasi-Isothermal”**: This uses the stellar potential and a quasi-isothermal potential for modelling the dark matter.
- vi) **“NFW Combination”**: In addition to the stellar potential, it combines an NFW at the center and a constant circular velocity at large radii to create the dark matter potential.

Since there is a constraint on the circular velocity v_c , the dark matter halo is parameterised in terms of v_c and converted to a mass profile $M(r)$ using the relation

$$v_{\text{circ}}^2(r) = G \cdot \frac{M(r)}{r}. \quad (4.2)$$

Spherical symmetry is assumed for the stellar mass model. The surface brightness is de-projected to find the luminosity density using Abel integrals. The density is calculated from the luminosity density using a Mass-to-Light Ratio (M/L), which is varied as a parameter. The density is then integrated to find the mass.

The three dark matter models (NFW, Quasi-Isothermal, NFW Combination) are parameterised as follows:

Quasi-Isothermal The quasi-isothermal model is parameterised in v_{circ}

$$v_{\text{circ}}^2(r) = \frac{v_0^2 r^2}{r_c^2 + r^2}, \quad (4.3)$$

where v_0 is the value of the circular velocity at large radii and r_c is the change radius.

NFW For comparison, a Navarro-Frenk-White (NFW) model is also used to parameterise the potential due to the dark matter halo. The density of the NFW dark matter halo is given by Navarro et al. (1996) and Lokas & Mamon (2001):

$$\rho = \frac{\rho_c^0 \delta_{\text{char}}}{(r/r_s)(1 + r/r_s)^2}, \quad (4.4)$$

where ρ_c^0 is the critical density of the universe, $r_s = r_v/c$, with r_v being the virial radius and c the concentration, and

$$\delta_{\text{char}} = \frac{vc^3 g(c)}{3} \quad (4.5)$$

with

$$g(c) = \frac{1}{\ln(1+c) - c/(1+c)}. \quad (4.6)$$

Therefore, the circular velocity is given by:

$$\frac{v_{\text{circ}}^2(r)}{v_{\text{vir}}^2} = \frac{g(c)r_v}{r} \left(\log\left(1.0 + c \frac{r}{r_v}\right) - \frac{c r/r_v}{1.0 + (c r/r_v)} \right) \quad (4.7)$$

where G is the gravitational constant and v_{vir} is the virial circular velocity, which is calculated using the virial mass M_{vir} . After estimating the total stellar mass using photometry data, we use the virial mass M_{vir} found using the abundance matching method from Behroozi et al. (2010).

The concentration parameter c is constrained using the relation between M_{vir} and c from Planck (Dutton & Macciò, 2014):

$$c_{\text{vir}}(M_{\text{vir}}) = 10^{a-b \log_{10}(M_{\text{vir}})h/10^{12}}, \quad (4.8)$$

where $a = 1.025$, $b = 0.097$, and $h = 0.671$. The virial radius is also calculated from the halo mass.

NFW Combination The modified NFW model, the ‘‘NFW Combination’’, is parameterised as an NFW below a radius of $100''$, and as a flat circular velocity curve above $100''$.

Anisotropy and projecting the radial dispersion

The r -anisotropy parameter β_r can be analytically parameterised with radial dependence, as done in Churazov et al. (2010):

$$\beta_r(r) = \frac{\beta_2 r^{c_\beta} + \beta_1 r_a^{c_\beta}}{r^{c_\beta} + r_a^{c_\beta}}, \quad (4.9)$$

where β_1 and β_2 are the anisotropy parameters at $r = 0$ and $r \rightarrow \infty$ respectively, r_a is the anisotropy radius, and exponent c_β controls the sharpness of the transition. The radial velocity dispersion is then given by:

$$\sigma_r^2(r) = \frac{v_c^2}{j(r)W(r)} \int_r^\infty \frac{j(x)W(x)}{x} dx, \quad (4.10)$$

where

$$W(x) = x^{2\beta_1} (x^{c_\beta} + r_a^{c_\beta})^{2(\beta_2 - \beta_1)/c_\beta}, \quad (4.11)$$

see Churazov et al. (2010) for further details.

The radial velocity dispersion is then convolved with the projected density to give the LOS velocity dispersion (Binney & Mamon, 1982):

$$\sigma_{\text{LOS}}^2(R) = \frac{2}{I(R)} \int_R^\infty \left(1 - \beta_r \frac{R^2}{r^2}\right) \frac{\rho(r)\sigma_r^2 r}{\sqrt{r^2 - R^2}} dr. \quad (4.12)$$

where $I(R)$ is the projected density and R is the projected radius. The projected density is given by:

$$I(R) = 2 \int_R^\infty \rho(r) r / (r^2 - R^2)^{\frac{1}{2}} dr. \quad (4.13)$$

4.3.1 v_{rms} predictions from spherically symmetric Jeans models

We present the results of the different potential models, with the velocity dispersion shown in Figure 5.

Constant v_{circ} Model (i) and Power Law (ii)

An isotropic model corresponding to a constant circular velocity of 300 kms^{-1} is used, on the basis of the HI rotation curve. This model slightly overestimates the velocity dispersion data at radii $R > 180''$, and underestimates the velocity dispersion data at radii $R < 25.5''$. It fits the model around $100''$, which is shown on Figure 5.

A power law is used to model the total mass of the galaxy, corresponding to a slope of $\gamma = 2.1$ in the density $\rho_{total} \approx r^{-\gamma}$. The power law mass, with a radial dependence of $r^{0.9}$, is normalized at $100''$ to correspond to a circular velocity of 300 kms^{-1} at that radius, as seen on Figure 5.

Stellar Mass Model (iii)

In calculating the stellar potential, the Mass-to-Light Ratio (M/L) is the only independent variable considered. Cappellari et al. (2006b) calculate the stellar population mass-to-light ratio and two dynamical M/L from a two-integral Jeans model and a Schwarzschild model. The stellar population model uses the Salpeter initial mass function (IMF) mass-to-light Ratio, with an old stellar population and an uncertainty of 10%. It is consistent with the Kroupa IMF if reduced by a factor of 30% (Cappellari et al., 2006b). The best fit M/L is slightly higher than the error range of the Salpeter IMF.

Figure 5 shows that the velocity dispersion at extended radii cannot be described by the best fit model using stellar mass only. Either dark matter or anisotropy is needed to match the velocity dispersion at large radii. The addition of dark matter and anisotropy for this purpose is discussed in the subsequent sections. The circular velocity curve of the best fit model compared to the HI data shows that there is not enough mass at extended radii to match the HI data.

Dark Matter Models (iv - vi)

When compared to the HI data, the isotropic quasi-isothermal, NFW, and NFW Combination halos all fit within the error bars of the data. In order to determine the characteristic shape of the circular velocity at large radii the velocity dispersion data is therefore used.

The quasi-isothermal profile, which is not plotted on Figure 5, does not fit the velocity dispersion data at the outermost radii of the SAURON data as well as the NFW. The NFW is therefore the best fit for the centre. However, at the radii constrained by the PNe data, a flat velocity curve such as the quasi-isothermal profile fits the data better, which leads to the use of the NFW Combination halo, which has a flat circular velocity curve at large radii.

Massive early-type galaxies usually have more quasi-isothermal total mass profiles and flat circular velocity curves, while low-mass ETGs have more slowly rising dark matter profiles, and falling velocity curves (Romanowsky et al., 2003; Morganti et al., 2013; Wu et al., 2014). NGC 4278 has a flat velocity curve, despite being an intermediate luminosity elliptical.

All three models are applied using both the stellar-population M/L and a best fit M/L . Just as with the stellar-only model, a slightly higher mass-to-light ratio than for the stellar population only fits the data best in the centre. Cappellari et al. (2013b) conclude that more massive elliptical galaxies have a Salpeter IMF, while disk galaxies and lighter ellipticals have lighter IMFs such as Kroupa. In the case of NGC 4278, a M/L slightly higher than the Salpeter IMF fits the data best, with and without dark matter. In this respect NGC 4278 is therefore more similar to a massive elliptical than an intermediate luminosity ETG.

For the NFW models we derive the values of c and r_{vir} using the PLANCK cosmological parameters and the Behroozi et al. (2010) relation to stellar mass. We, however, still conduct an investigation into varying these affects the v_{rms} . Varying the virial radius, shown on Figure 6 shows that although the v_{rms} in the area of the PNe could be improved by a larger virial radius, the outer SAURON points would be less well fitted. In addition, the HI data would also be fitted more poorly. Varying the concentration parameter shows that a very high value of $c = 10$ could fit the v_{rms} better than the PLANCK value of $c=8.62$, but this fits the HI circular velocity data much more poorly. In addition all models still increase beyond the last radial point of the v_{rms} . We have not done a throughout parameter search of every value of c and r_{vir} possible, however, this exercise shows us that the techniques from Behroozi et al. (2010) and Dutton & Macciò (2014) give reasonable results in the available parameter space.

The reason why the NFW is concluded to be a less good model than the “NFW Combination” is because the model velocity dispersion increases after the largest radii of the data as shown on Figure , even though from looking at the 2D velocity field (Arnaboldi et al. in prep) this doesn’t seem to be what the data is indicating will happen.

Constraints on Anisotropy

The PNe and HI data are not sufficient to precisely constrain the anisotropy. Models reproducing the “Constant v_c ” potential, but with a radially varying anisotropy profile as in Churazov et al. (2010) were created, with the best fitting model shown in Figure 8. The parameters of the analytic anisotropy profile are, $\beta_1 = 0$, $\beta_2 = 0.7$, $r_a = 0.001R_e$, and $c_\beta = 2$. Even in the case of the profile with a very short transition radius, the anisotropy in the centre is not sufficient to increase the inner velocity dispersion profile to the point where it matches the data in the centre. The conclusion is therefore that one needs a more concentrated mass than what the constant circular velocity profile provides, in order to match the central velocity dispersion data, such as in the stellar matter only models.

A similar analysis is performed on the stellar matter only models. A radially varying anisotropy profile is applied to the stellar matter only model to see the effect on the inner radii, and extended where more velocity dispersion is needed to fit the data. Applying

a tangentially varying anisotropy profile decreases the velocity dispersion in the centre, moving the dispersion further from the data and does not increase the dispersion a large radii significantly. A radial anisotropy profile applied to the stellar model fits the velocity dispersion in the centre very well, and decreases the dispersion at large radii. Therefore radial anisotropy can be used to explain the dispersion in the centre without dark matter, but dark matter is needed to explain the dispersion at large radii.

Figure 8 shows NFW models with several different anisotropies. This confirms what is found for the stellar only models, in the centre anisotropy can improve the fit. At large radii where the PNe data is present it can also improve the fit. However, as shown in the previous section varying concentration parameter and virial radius can also alter the outskirts in a similar way. Normally, the mass-anisotropy degeneracy would prevent us from distinguishing between the effect of changing the potential and anisotropy, however, since the HI limits how greatly we can vary the potential we can constrain that some radial anisotropy is likely in this galaxy.

Gerhard et al. (2001) find some radial anisotropy in their profile within the central region of $R < 20''$ of the galaxy. In this analysis, a constant anisotropy profile of $\beta = 0.3$ is applied to the galaxy, using the quasi-isothermal dark matter halo and the best fit mass-to-light ratio. This improves the fit in the centre of the galaxy by increasing the velocity dispersion. It also improves the fit to the velocity dispersion at large radii by decreasing it.

Constraints on Dark Matter Fraction

For the isotropic quasi-isothermal stellar population and best fit mass-to-light ratio models, we find dark matter fractions for two different effective radii of $R_e = 1$ and $R_e = 5$. The values are given in Table 2. The dark matter fractions increase by approximately a factor of two between $R_e = 1$ and $R_e = 5$. Wu et al. (2014) find dark matter fractions of $(15 - 30)\%$ at $R_e = 1$ and $(40 - 65)\%$ at $R_e = 5$. Table 2 shows that our dark matter fractions are consistent with this at $R_e = 1$, but larger than this at $R_e = 5$. Larger and more massive galaxies have larger dark matter fractions, and the models of NGC 4278 predict values at the high end of these ranges at $R_e = 5$. This again points to characteristics more typical of a more massive elliptical galaxy.

Cappellari et al. (2013a), using the r -band photometry, give a dark matter fraction of 26% at $R_e = 1$ for NGC 4278 (model within $r < 30''$). Differences between this model and the one presented can be attributed to a combination of less extended data and different modelling assumptions.

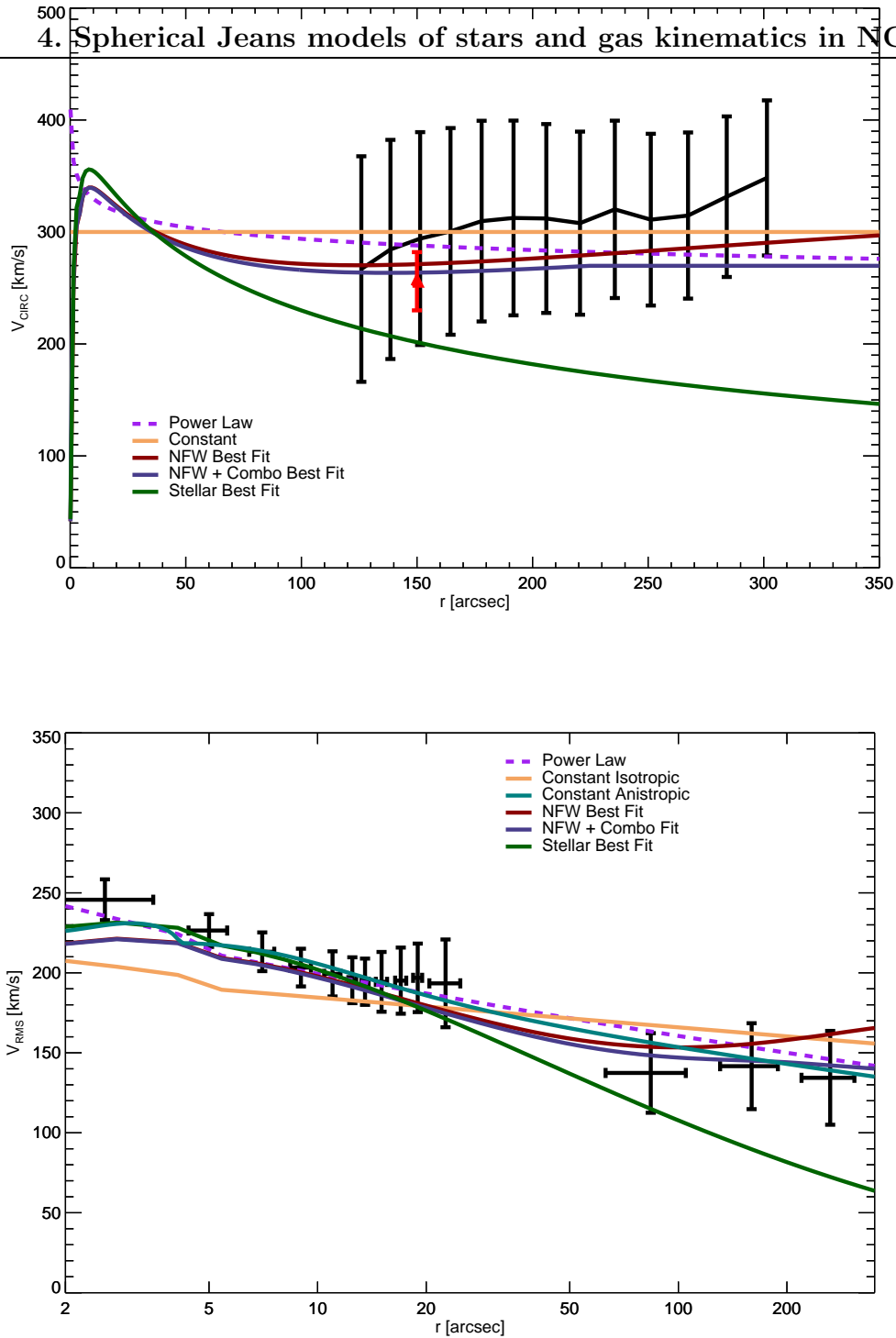


Figure 5: HI circular velocity data (top) from Morganti et al. (2006) in black. The red point corresponds to the value from Serra et al. (2016). Coloured lines show models of varying potentials. v_{rms} profiles (bottom) from SAURON and PNe data. Their corresponding circular velocities are shown on top with the same colours. All these models are isotropic.

Table 2: Dark matter fractions of the models. $R_e = 1$ Sérsic is $47.8''$, derived from the Sérsic fit. $R_e = 1$ ATLAS^{3D} is $32''$ Cappellari et al. (2011). The ATLAS^{3D} R_e is used for comparison to Alabi et al. (2016).

DM Halo	M/L Ratio $M_{\odot}/L_{\odot,I}$	M/L Ratio (Type)	$R_e = 1$ Sérsic	$R_e = 5$ Sérsic	$R_e = 1$ ATLAS ^{3D}	$R_e = 5$ ATLAS ^{3D}
NFW	3.05	Salpeter	0.16	0.67	0.10	0.52
NFW	3.3	Best Fit	0.14	0.63	0.083	0.48
NFW Combination Model	3.05	Salpeter	0.16	0.67	0.10	0.52
NFW Combination Model	3.3	Best Fit	0.15	0.65	0.090	0.50

Table 3: Parameters used to create Jeans Models of NGC 4278. Column (1) is the name of the model, column (2) is the colour used in Figure 5 for the model, column(3) is the best fitting M/L , column (4) is the anisotropy of the model, column (5) is the virial radius of the NFW if applicable, column (6) is the concentration parameter c of the NFW if applicable, column (7) is the constant circular velocity beyond $100''$ if applicable, column (8) is the constant velocity of the total profile if applicable, column (9) is the index α of the total density power law used for the total potential if applicable.

Name	Colour	M/L Ratio $M_{\odot}/L_{\odot,I}$	β	r_{vir}	c_{NFW}	$v_{100''}$	v_{constant}	α
Constant	Orange	—	—	—	—	—	300 km s^{-1}	—
Power Law	Purple	—	—	—	—	—	—	-2.1
NFW	Red	3.3	0.0	586 kpc	8.03	—	—	—
NFW Combination	Blue	3.3	0.0	—	—	270 km s^{-1}	—	—
Stellar	Green	3.3	0.0	—	—	—	—	—

Table 4: The dark matter fraction f_{DM} of NGC 4278 for our models compared to those of Alabi et al. (2016). Our stellar mass is derived from an I -band luminosity of $3.20 \times 10^{10} L_{\odot}$ and M/L of 3.3 in I -band.

Models	Stellar Mass M_{\odot}	Total Mass at $5R_e$ M_{\odot}	f_{DM} at $5R_e$
Alabi et al. (2016) $M/L_K = 1, \beta = 0$ NFW Combo	7.59×10^{10}	$2.8 \pm 0.4 \times 10^{11}$	0.75 ± 0.06
$M/L_I = 3.3, \beta = 0$	1.06×10^{10}	1.96×10^{11}	0.50

Density

Remus et al. (2013) state that mergers with a high gas fraction produce a steeper inner density slope than mergers with a low gas fraction. The inner density slope of NGC 4278 is steep, and NGC 4278 also contains a substantial HI disk of mass $(6.9 \times 10^8) M_{\odot}$ (Morganti et al., 2006). This further supports the hypothesis that there has been a history of mergers.

4.4 The galaxy NGC 4283: a satellite being disrupted while orbiting in the NGC 4278 halo

The galaxy NGC 4283, also traced by the PNe, has a significantly different systemic velocity of $\sim 1050 \text{ km s}^{-1}$ compared to NGC 4278, shown in Figure 2, and are well separated in the phase space. There are several PNe, however, which are spatially associated to NGC 4278, but have a too high velocity to be associated to it (3σ away), as shown in red on the phase space diagram in Figure 9. When these clipped PNe are shown spatially in Figure 10, a stream across the centre of NGC 4278 can be observed.

The globular cluster data from Foster et al. (2016), which also cover both galaxies, have much fewer than expected globular clusters associated to NGC 4283. We tag globular clusters associated to NGC 4278 which are within 1σ of the systemic velocity of NGC 4283, shown in Figure 9. These tagged globular clusters are shown in red in Figure 10. They follow the same stream structure across the centre of NGC 4278 as the PNe. This, in conjunction with the few globular clusters associated to NGC 4283, supports the picture that we are tracing a stream stripped from NGC 4283 by the halo of NGC 4278 which it is orbiting. The final structure is shown in Figure 11.

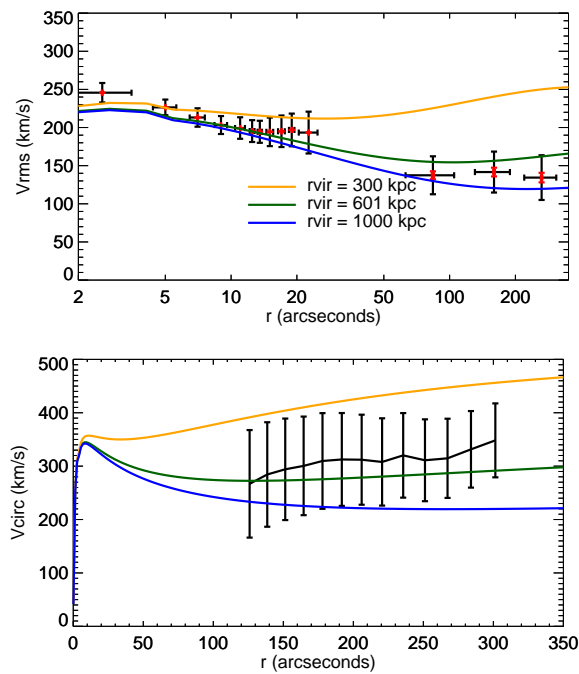


Figure 6: The v_{rms} (top) and v_c (bottom) of Jeans models to NGC 4278 with NFW dark matter profiles with different virial radii $r_{vir} = 300$ kpc, 601 kpc, and 1000 kpc.

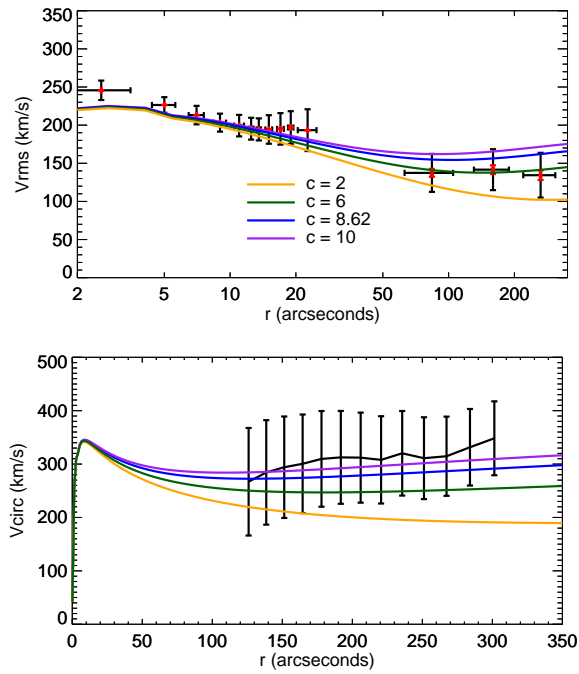


Figure 7: The v_{rms} (top) and v_c (bottom) of Jeans models to NGC 4278 with NFW dark matter profiles with different NFW concentration parameters $c = 2, 6, 8.62,$ and 10 .

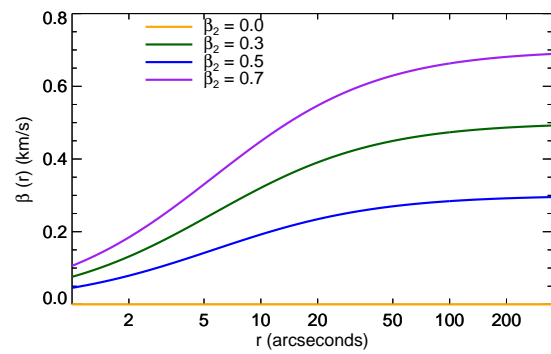
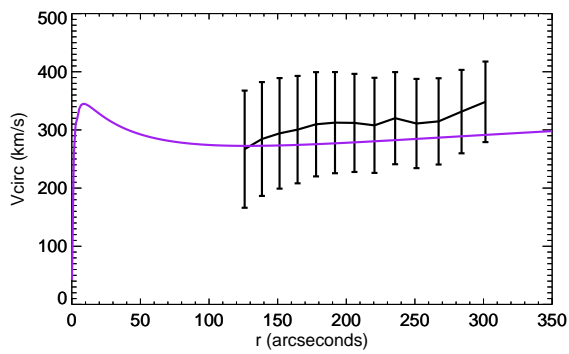
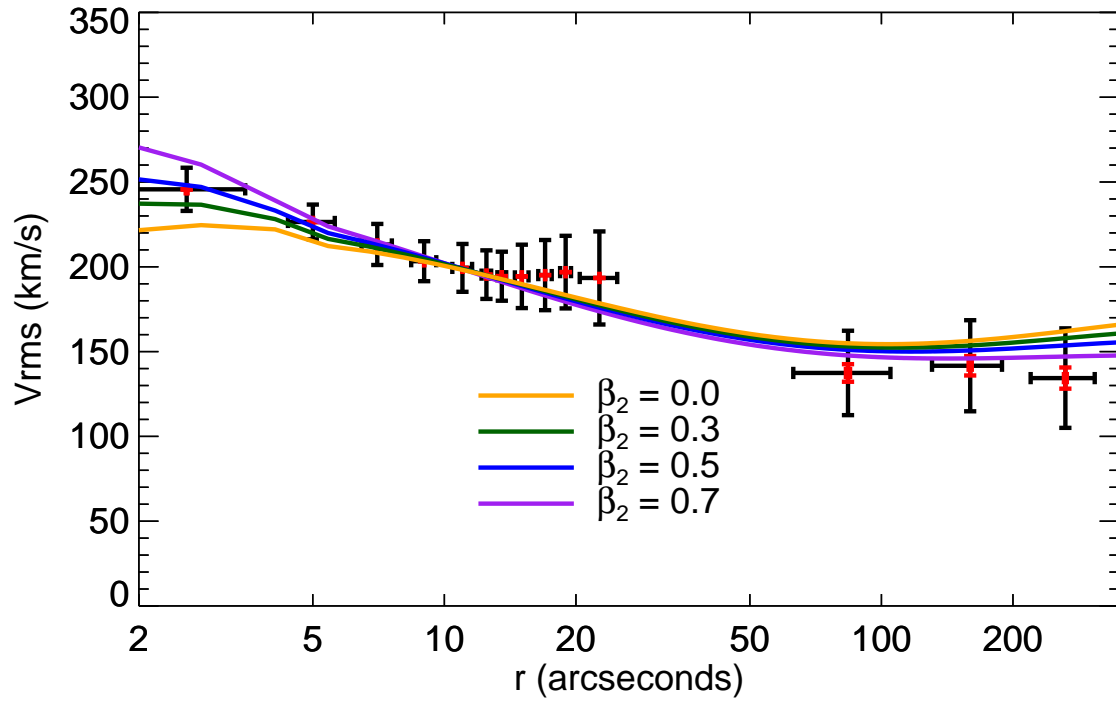


Figure 8: The v_{rms} (top) of Jeans models to NGC 4278 with NFW dark matter profiles and different anisotropies profiles, with different β_2 (see Equation 4.11).

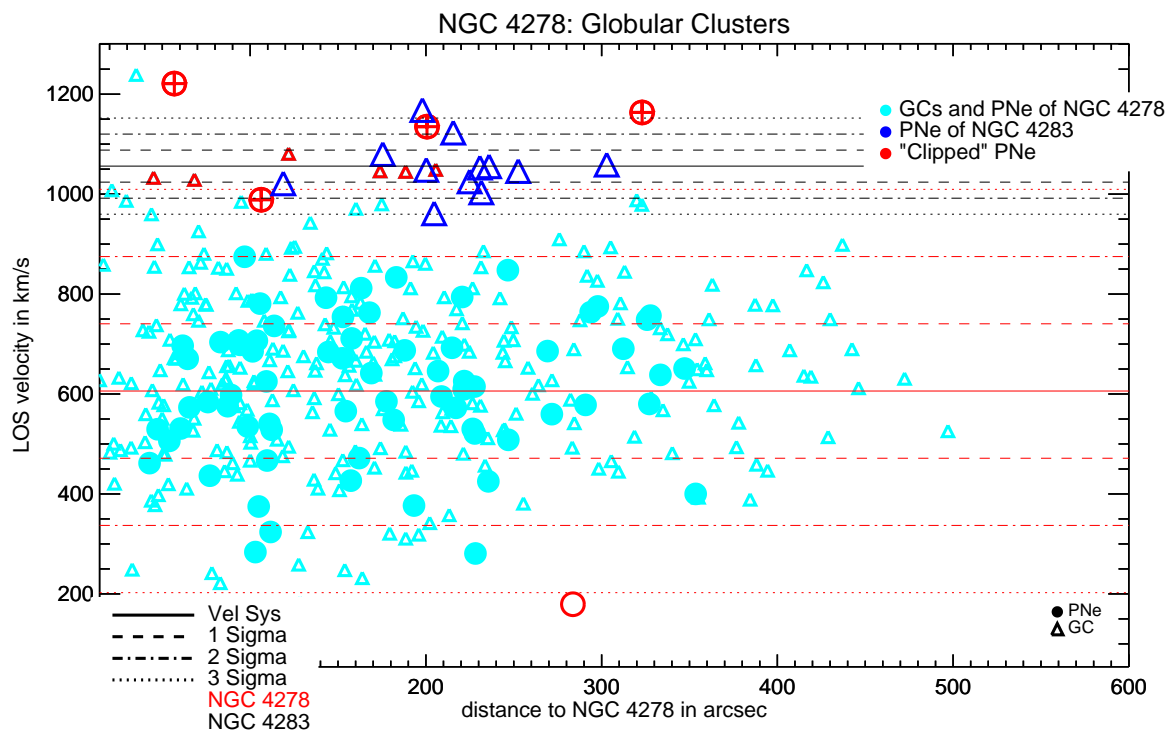


Figure 9: Phase space diagram of GCs (triangles) and PNe (circles) in a 100 arcmin² field around NGC 4278. The objects associated to NGC 4278 are shown in light blue and to NGC 428 3 are dark blue. We identify a subset of GCs and “clipped” PNe at the systemic velocity of NGC 4283 (dash-dotted line). There are 6 additional GCs at the systemic velocity of NGC 4283, shown as the red triangles. Figure 10 shows those that could also spatially belong to a structure..

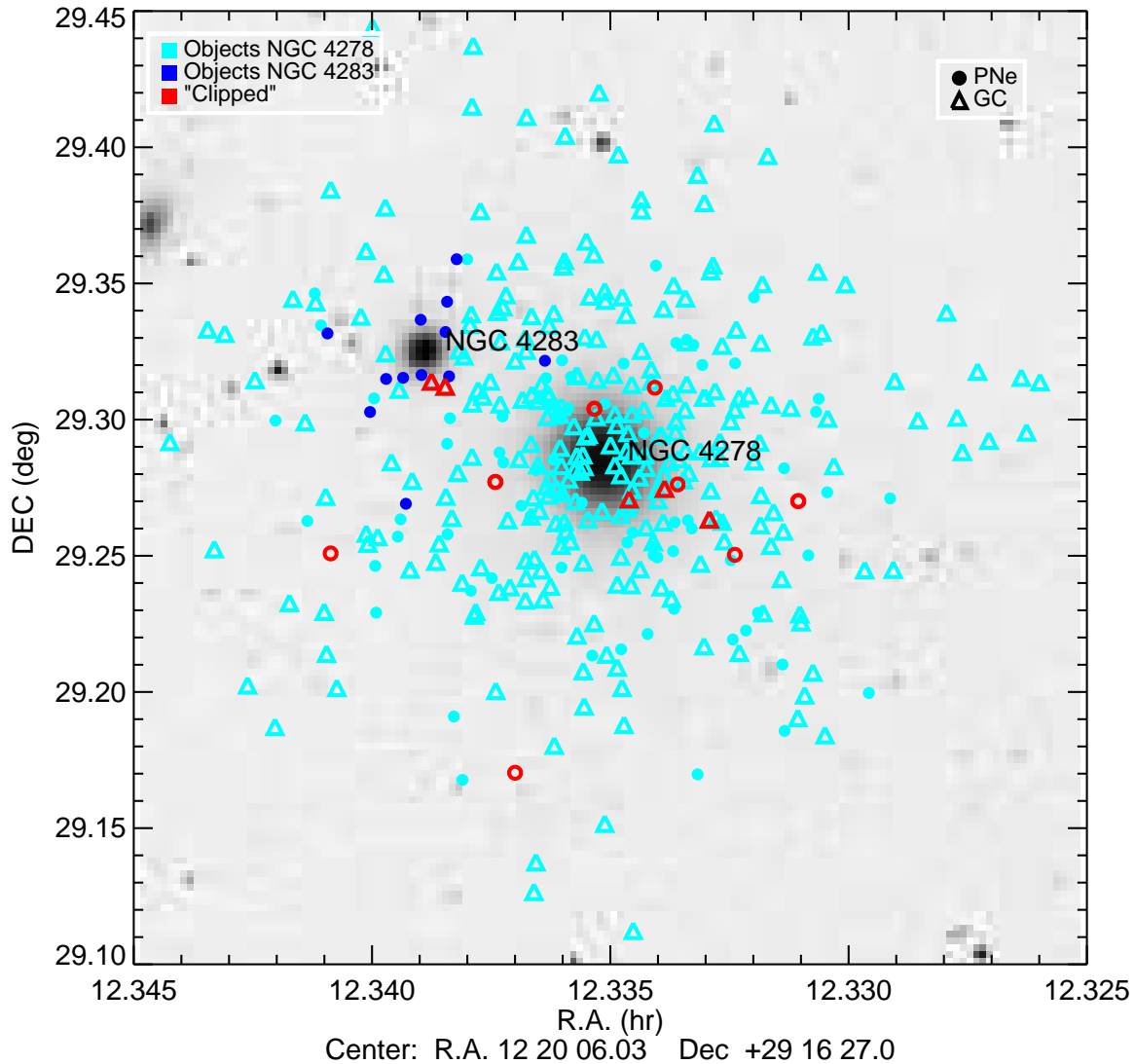


Figure 10: Spatial distribution of PNe (circles) and GCs (triangles) in a 100 arcmin² field centred on NGC 4278. The objects associated to NGC 4278 are light blue, and to NGC 4283 are dark blue. The clipped PNe, those associated with NGC 4273 and the GCs at the NGC 4283 velocity are red. Their spatial distribution is suggestive of a broad structure, approximately aligned with the NGC 4278/NGC 4283 centres, stretching across the host halo.

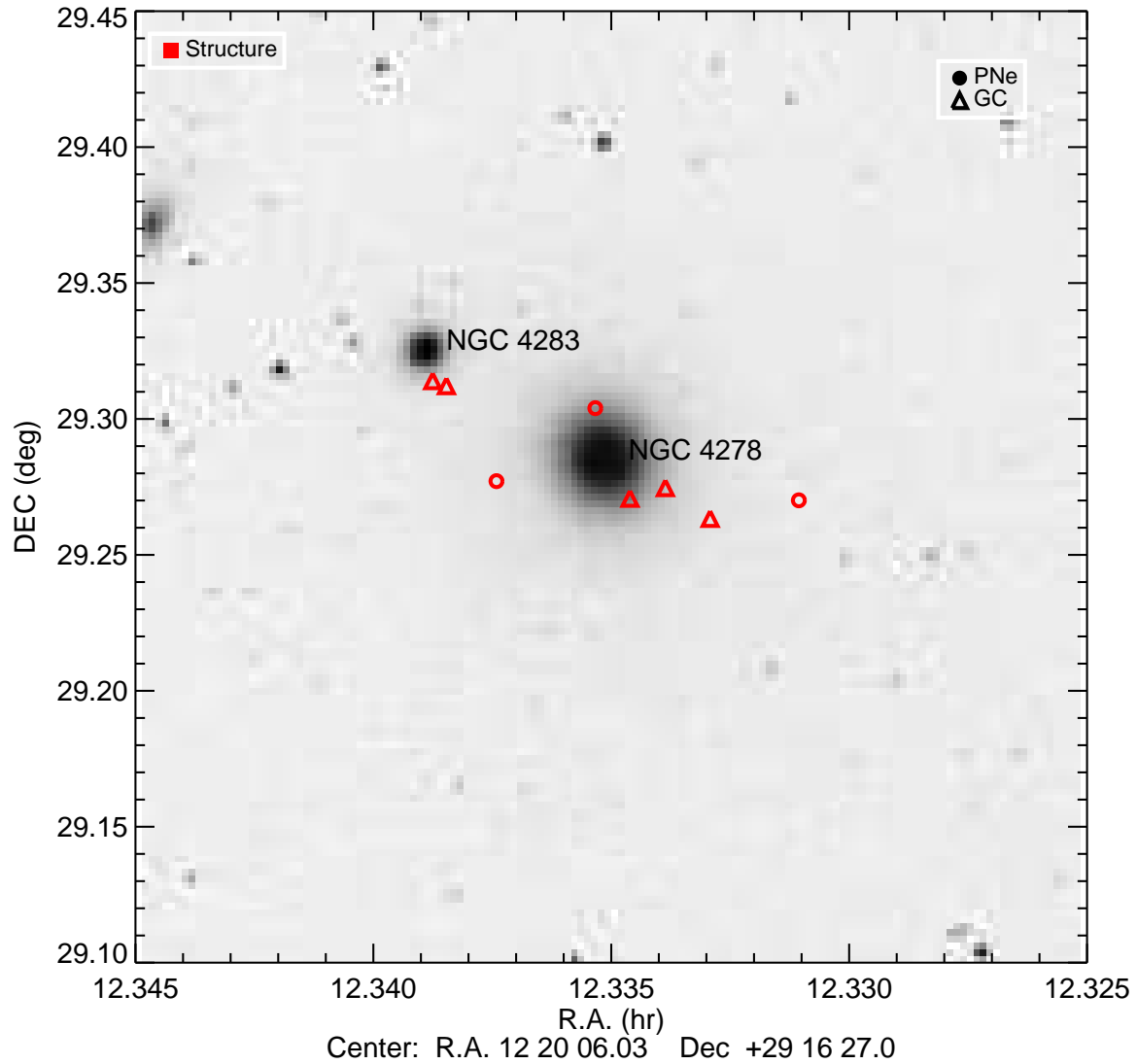


Figure 11: Same as Figure 10, only the GCs and PNe associated to the substructure of NGC 4278 is shown. The triangles are globular clusters and the circles are PNe.

4.4.1 Conclusion

The kinematics of the galaxy NGC 4278 and its satellite galaxy NGC 4283 are probed using the kinematics of its PNe and GC, as well as the rotation velocity of its HI gas. Finding the azimuthally averaged v_{rms} of NGC 4278 using the PNe kinematics out to $10 R_e$ yielded a flat v_{rms} curve at large radii more typical of a massive elliptical than an intermediate mass elliptical galaxy such as NGC 4278.

Using a power law for total mass of the model yields a model with a $\gamma = -2.1$ density profile best fitting to the data. An isothermal density profile points to a history of mergers, more typical of high mass galaxies, according to Remus et al. (2013), with each merger moving the density profile closer to a quasi-isothermal profile.

The PNe of NGC 4278 and NGC 4283 are found to be kinematically well separated with a systemic velocity difference of 400 km s^{-1} . Analysis of the PNe kinematic phase space of NGC 4278 and NGC 4283 shows several PNe with a velocity close to that of NGC 4283, but spatially in a stream across NGC 4283. The same behaviour is found in Globular cluster data, supporting the presence of a substructure stripped from NGC 4283 by the halo of NGC 4278.

The kinematic misalignment between the gas and stellar kinematics (Morganti et al., 2006), the lack of equilibrium in the HI data at large radii (Morganti et al., 2006), the isothermal density profile, and the substructure point to a history of several independent accretion events which occurred to NGC 4278.

Jeans modelling using a potential with only stellar matter finds that this assumption alone is unable to match the flat v_{rms} profile observed in the outskirts of the galaxy. Using dark matter in the potential additionally makes models which are consistent with the v_{rms} of the galaxy, leading to the conclusion that NGC 4278 contains dark matter.

Chapter 5

Summary and Conclusions

In this thesis dynamical modelling techniques were applied to elliptical galaxies.

In Chapter 2 we tested whether the assumptions for the velocity ellipsoids used in JAM modelling lead to physical distribution functions, and the effect of the assumptions on galaxy characteristics such as M/L , anisotropy and dark matter content. We use the elliptical galaxies NGC 4660 and NGC 4697, and ATLAS^{3D} and SLUGGS kinematics. The galaxy NGC 4660 is very well constrained by the ATLAS^{3D} kinematics, reaching up to an effective radius of $3 R_e$. NGC 4697 in contrast is constrained by the ATLAS^{3D} kinematics only up to $1/3 R_e$. SLUGGS kinematics are therefore used to extend the range constrained range of this galaxy. We first make a series of models using only stellar matter and the ATLAS^{3D} kinematics. We made Jeans JAM models to NGC 4660 and NGC 4697 and found that the root-mean-square velocity v_{rms} is reproduced well by these models.

We then use NMAGIC to make kinematic-driven models to the kinematics and photometry without assumptions on the velocity ellipsoid to find the unconstrained dynamical structure of the galaxy. If the galaxy is not well constrained, there would be a large dependence on initial particle model used in the model. We therefore employ four very kinematically different initial models, and find that for NGC 4660 they are unique for their inclination. The final fitted models are independent of and insensitive to the initial model. The kinematic-driven models for both NGC 4660 and NGC 4697 we arrive at are anisotropic, with a significant non-zero cross term.

To probe the effect of cylindrical alignment of velocity ellipsoids on the models, we evolve the $\langle v_R v_z \rangle$ term towards $\langle v_R v_z \rangle = 0$ by using it as an observable in NMAGIC. Although we are able to find models with almost cylindrically aligned velocity ellipsoids, these are all nearly meridionally isotropic, with the exception of the major axis where the spherical and cylindrical alignment regimes are consistent with each other. These models differ most strongly from the kinematic data in their σ and h_4 . This is found for both NGC 4660 and

NGC 4697. When attempting to fit a constant β_z over the whole meridional plane, another assumption often implemented in JAM Jeans modelling, we find for both galaxies that, unless deviations from a constant β_z occur in the intermediate axis, the density cannot be modelled.

To probe whether a reasonable compromise is possible between cylindrical alignment and the kinematic data, we make a set of models that use both the kinematics and the JAM constraint as an observable. We study a series of models exploring the tension between the kinematics and the JAM condition by weighting them differently with respect to one another in NMAGIC. The resulting models for both NGC 4660 and NGC 4697 fit neither the JAM condition nor the kinematics as well as the applicable previous models.

For NGC 4660 no model is found for which the cross term is nearly zero and the kinematics are fitted well, suggesting no dynamically self-consistent JAM model exists, i.e., the JAM models have no underlying physical distribution function. Furthermore, we find an increase in anisotropy for the tension models with stronger relative kinematic data strength, suggesting a zero cross term is incompatible with anisotropy. For NGC 4697 the same effect is found, however with one of the compromise models presenting a more reasonable compromise than for NGC 4660. This achieves a higher but still reasonable kinematic χ^2 and a cross term only double that of the JAM-driven only models. For NGC 4697 it is also found that a higher cross term correlates with higher anisotropy in the models. We therefore conclude that how well a galaxy is represented by a JAM model is related to how close its ideal internal structure is to an isotropic rotator. We perform this analysis for two inclinations for each of the galaxies and derive the same conclusions for both inclinations.

Having confirmed similar behaviour for both galaxies in stellar-only potentials, we add dark matter in the form of logarithmic potentials to NGC 4697, using the SLUGGS data to extend the kinematically constrained range. We make the same set of JAM Jeans and NMAGIC models described above to the ATLAS^{3D} and SLUGGS kinematics using a range of low to high mass dark matter halos.

In the kinematically driven models, we find that the velocity dispersion is the best discriminator between models and that an intermediate halo with an axis ratio of $q = 0.9$ (“D09”) fits the total kinematic data best, with a total χ^2 of 1.1. All halo models are found to have a significant non-zero cross term, with the lowest cross term present in the stellar-matter-only model.

For the JAM condition driven models, we find again that the result of models with a nearly cylindrical cross term have an almost meridionally isotropic structure. The models significantly deviate from the kinematically driven models in v , σ , h_3 and h_4 , with a very different shape of σ observed.

The series of dark matter halo models that fit both the kinematics and JAM are both less well fitted, with the compromise found most strongly in the σ , as the JAM-driven and

kinematic-driven models differ strongly in σ shape. Models with a cylindrically aligned velocity ellipsoid are not able to well reproduce and discern between different dark matter halos.

The results described in this chapter suggest that the only JAM models with physical distribution functions are nearly meridionally isotropic, and that JAM models with constant $\beta_z \neq 0$ are unphysical. JAMs are nonetheless useful to estimate approximate M/L ratios for elliptical galaxies. However, relative best-fit comparisons between JAM models in different potentials to infer dark matter profiles or IMF variations may be unreliable and need to be verified by dynamical models with unconstrained velocity ellipsoids.

The results of Chapter 2 will be submitted for publication.

In Chapter 3 we produce a self-consistent triaxial model using NMAGIC. We make a model of M87 using the photometry with the inter-cluster light removed (Longobardi et al., 2018) and a circular velocity curve X-ray Churazov et al. (2010) and an NFW model from Simionescu et al. (2017). We over-estimate the IFU (Emsellem et al., 2014) and PNe data (Longobardi et al., 2018), likely due to an overestimation of the circular velocity and therefore the potential.

Using planetary nebulae and globular clusters as kinematic tracers, as well as a HI gas rotation curve, we investigate the intermediate mass elliptical galaxy NGC 4278 and its companion NGC 4283 in Chapter 4. PNe allow us to trace the v_{rms} of NGC 4278 to large radii of $10 R_e$. NGC 4278 noteworthy flat v_{rms} was modelled using spherical Jeans modelling and a power law potential, and best fitted by an isothermal potential derived from a total density profile of $\rho(r) = r^\gamma$ with $\gamma = -2.1$. This points to a merger history more typical of high mass galaxies (Remus et al., 2013).

Bibliography

- Ade P. A. R., et al., 2016, A&A, 594, A13
- Alabi A. B., et al., 2016, MNRAS, 460, 3838
- Arnaboldi M., Freeman K. C., Hui X., Capaccioli M., Ford H., 1994, The Messenger, 76, 40
- Arnaboldi M., et al., 1996, ApJ, 472, 145
- Arnaboldi M., Freeman K. C., Gerhard O., Matthias M., Kudritzki R. P., Méndez R. H., Capaccioli M., Ford H., 1998, ApJ, 507, 759
- Arnaboldi M., Söldner-Rembold I., Narayan C. A., Coccato L., Gerhard O., Pulsoni C., Napolitano N., team P., 2018
- Babcock H. W., 1939, Lick Observatory Bulletin, 19, 41
- Behroozi P. S., Conroy C., Wechsler R. H., 2010, ApJ, 717, 379
- Bender R., Saglia R. P., Gerhard O. E., 1994, MNRAS, 269, 785
- Bennett C. L., et al., 2013, ApJS, 208, 20
- Binggeli B., Tammann G. A., Sandage A., 1987, AJ, 94, 251
- Binney J., 2012, MNRAS, 426, 1328
- Binney J., 2014, MNRAS, 440, 787
- Binney J., Mamon G. A., 1982, MNRAS, 200, 361
- Binney J., Merrifield M., 1997, Galactic Astronomy: James Binney and Michael Merrifield. Princeton series in astrophysics, Princeton University Press, <https://books.google.de/books?id=zw4fnwEACAAJ>
- Binney J., Tremaine S., 2008, Galactic Dynamics: Second Edition. Princeton University Press
- Binney J., de Vaucouleurs G., 1981, MNRAS, 194, 679

- Binney J. J., Davies R. L., Illingworth G. D., 1990, *ApJ*, 361, 78
- Binney J., et al., 2014, *MNRAS*, 439, 1231
- Blaña Díaz M., et al., 2018, *MNRAS*, 481, 3210
- Bond N. A., et al., 2010, *ApJ*, 716, 1
- Box G. E. P., Muller M. E., 1958, *Ann. Math. Statist.*, 29, 610
- Büdenbender A., van de Ven G., Watkins L. L., 2015, *MNRAS*, 452, 956
- Cappellari M., 2002, *MNRAS*, 333, 400
- Cappellari M., 2008, *MNRAS*, 390, 71
- Cappellari M., 2016, *AR&A*, 54, 597
- Cappellari M., et al., 2006a, *MNRAS*, 366, 1126
- Cappellari M., et al., 2006b, *MNRAS*, 366, 1126
- Cappellari M., et al., 2007, *MNRAS*, 379, 418
- Cappellari M., Neumayer N., Reunanen J., van der Werf P. P., de Zeeuw P. T., Rix H.-W., 2009, *MNRAS*, 394, 660
- Cappellari M., et al., 2011, *MNRAS*, 413, 813
- Cappellari M., et al., 2012, *Nature*, 484, 485
- Cappellari M., et al., 2013a, *MNRAS*, 432, 1709
- Cappellari M., et al., 2013b, *MNRAS*, 432, 1862
- Cappellari M., et al., 2015, *ApJL*, 804, L21
- Chandrasekhar S., 1939, *ApJ*, 90, 1
- Churazov E., et al., 2010, *MNRAS*, 404, 1165
- Ciardullo R., Feldmeier J. J., Jacoby G. H., Kuzio de Naray R., Laychak M. B., Durrell P. R., 2002, *ApJ*, 577, 31
- Ciotti L., 1991, *A&A*, 249, 99
- Coccatto L., et al., 2009, *MNRAS*, 394, 1249
- Coccatto L., Arnaboldi M., Gerhard O., 2013, *MNRAS*, 436, 1322
- Cortesi A., et al., 2013, *A&A*, 549, A115

- Das P., Gerhard O., Churazov E., Zhuravleva I., 2010, MNRAS, 409, 1362
- Das P., Gerhard O., Mendez R. H., Teodorescu A. M., de Lorenzi F., 2011, MNRAS, 415, 1244
- De Lorenzi F., 2007, PhD thesis, University of Basel, Faculty of Science
- De Lorenzi F., Debattista V. P., Gerhard O., Sambhus N., 2007, MNRAS, 376, 71
- De Lorenzi F., Gerhard O., Saglia R. P., Sambhus N., Debattista V. P., Pannella M., Méndez R. H., 2008, MNRAS, 385, 1729
- De Lorenzi F., et al., 2009, MNRAS, 395, 76
- De Lucia G., Blaizot J., 2007, MNRAS, 375, 2
- Deason A. J., et al., 2012, MNRAS, 425, 2840
- Debattista V. P., Sellwood J. A., 2000, ApJ, 543, 704
- Dehnen W., 2009, MNRAS, 395, 1079
- Dehnen W., Gerhard O. E., 1993, MNRAS, 261, 311
- Dejonghe H., de Zeeuw T., 1988, ApJ, 333, 90
- Dejonghe H., de Bruyne V., Vauterin P., Zeilinger W. W., 1996, A&A, 306, 363
- Douglas N. G., et al., 2002, PASP, 114, 1234
- Dutton A. A., Macciò A. V., 2014, MNRAS, 441, 3359
- Eddington A. S., 1915, MNRAS, 76, 37
- Einasto J., Kaasik A., Saar E., 1974, Tartu Astrofüüs. Obs. Preprint, Nr. 1, 8 p., 1
- El-Badry K., Wetzel A. R., Geha M., Quataert E., Hopkins P. F., Kereš D., Chan T. K., Faucher-Giguère C.-A., 2017, ApJ, 835, 193
- Emsellem E., et al., 2007, MNRAS, 379, 401
- Emsellem E., Krajnović D., Sarzi M., 2014, MNRAS, 445, L79
- Evans N. W., Sanders J. L., Williams A. A., An J., Lynden-Bell D., Dehnen W., 2016, MNRAS, 456, 4506
- Finozzi F., 2018, PhD thesis, Ludwig-Maximilians-Universität
- Foster C., et al., 2016, MNRAS, 457, 147

- Foster C., et al., 2017, MNRAS, 472, 966
- Gerhard O. E., 1991, MNRAS, 250, 812
- Gerhard O. E., 1993, MNRAS, 265, 213
- Gerhard ., 1994, Galactic Dynamics and N-Body Simulations, 433, 191
- Gerhard O., Kronawitter A., Saglia R. P., Bender R., 2001, AJ, 121, 1936
- Guth A. H., 1981, Phys. Rev. D, 23, 347
- Hartke J., et al., 2018, preprint, ([arXiv:1805.03092](https://arxiv.org/abs/1805.03092))
- Hermite C., 1864, Sur un nouveau developpement en serie de fonctions. Vol. 58, Comptes Rendus de l'Academie des Sciences
- Hopkins P. F., Cox T. J., Dutta S. N., Hernquist L., Kormendy J., Lauer T. R., 2009, ApJS, 181, 135
- Hubble E., 1929, Contributions from the Mount Wilson Observatory, vol. 3, pp.23-28, 3, 23
- Janowiecki S., Mihos J. C., Harding P., Feldmeier J. J., Rudick C., Morrison H., 2010, ApJ, 715, 972
- Kalnajs A. J., 1977, ApJ, 212, 637
- Komatsu E., 2003, New Astronomy Review, 47, 797
- Kormendy J., Fisher D. B., Cornell M. E., Bender R., 2009, ApJS, 182, 216
- Kovac J. M., Leitch E. M., Pryke C., Carlstrom J. E., Halverson N. W., Holzappel W. L., 2002, Nature, 420, 772
- Krajnović D., et al., 2011, MNRAS, 414, 2923
- Krajnović D., et al., 2013, MNRAS, 432, 1768
- Lablanche P.-Y., et al., 2012, MNRAS, 424, 1495
- Lauer T. R., et al., 2005, AJ, 129, 2138
- Levison H. F., Richstone D. O., 1985a, ApJ, 295, 340
- Levison H. F., Richstone D. O., 1985b, ApJ, 295, 349
- Li H., Li R., Mao S., Xu D., Long R. J., Emsellem E., 2016, MNRAS, 455, 3680
- Li H., et al., 2018, MNRAS, 476, 1765

- Lima Neto G. B., Gerbal D., Márquez I., 1999, MNRAS, 309, 481
- Liu J., Chen X., Ji X., 2017, Nature Physics, 13, 212
- Lokas E. L., Mamon G. A., 2001, MNRAS, 321, 155
- Long R. J., Mao S., 2010, MNRAS, 405, 301
- Longobardi A., Arnaboldi M., Gerhard O., Mihos J. C., 2015a, A&A, 579, L3
- Longobardi A., Arnaboldi M., Gerhard O., Hanuschik R., 2015b, Astronomy & Astrophysics, 579, A135
- Longobardi A., Arnaboldi M., Gerhard O., Hanuschik R., 2015c, A&A, 579, A135
- Longobardi A., Arnaboldi M., Gerhard O., Pulsoni C., Söldner-Rembold I., 2018, A&A
- Lynden-Bell D., 1962, MNRAS, 124, 95
- Magorrian J., 1999, MNRAS, 302, 530
- Masi S., 2002, Progress in Particle and Nuclear Physics, 48, 243
- McNeil-Moylan E. K., Freeman K. C., Arnaboldi M., Gerhard O. E., 2012, A&A, 539, A11
- McNeil E. K., Arnaboldi M., Freeman K. C., Gerhard O. E., Coccato L., Das P., 2010, A&A, 518, A44
- Merritt D., 1993, ApJ, 413, 79
- Mihos J. C., Harding P., Feldmeier J., Morrison H., 2005, ApJ, 631, L41
- Morganti R., et al., 2006, MNRAS, 371, 157
- Morganti L., Gerhard O., Coccato L., Martinez-Valpuesta I., Arnaboldi M., 2013, MNRAS, 431, 3570
- Napolitano N. R., et al., 2011, MNRAS, 411, 2035
- Natarajan P., et al., 2017, Monthly Notices of the Royal Astronomical Society, 468, 1962
- Navarro J. F., Frenk C. S., White S. D. M., 1996, ApJ, 462, 563
- Neumayer N., Cappellari M., Reunanen J., Rix H.-W., van der Werf P. P., de Zeeuw P. T., Davies R. I., 2007, ApJ, 671, 1329
- Oort J. H., 1932, Bulletin Astronomical Inst. Netherlands, 6, 249
- Opitsch M., 2016, PhD thesis, Ludwig-Maximilians-Universität

- Opitsch M., Fabricius M. H., Saglia R. P., Bender R., Blaña M., Gerhard O., 2017, preprint, (arXiv:1707.06652)
- Ostriker J. P., Peebles P. J. E., Yahil A., 1974, ApJL, 193, L1
- Peacock J. A., 1999, Cosmological Physics
- Peletier R. F., Davies R. L., Illingworth G. D., Davis L. E., Cawson M., 1990, AJ, 100, 1091
- Penzias A. A., Wilson R. W., 1965, ApJ, 142, 419
- Pérez-Villegas A., Portail M., Wegg C., Gerhard O., 2017, ApJL, 840, L2
- Portail M., 2016, PhD thesis, Ludwig-Maximilians-Universität
- Portail M., Wegg C., Gerhard O., Martinez-Valpuesta I., 2015a, MNRAS, 448, 713
- Portail M., Wegg C., Gerhard O., 2015b, MNRAS, 450, L66
- Portail M., Gerhard O., Wegg C., Ness M., 2017a, MNRAS, 465, 1621
- Portail M., Wegg C., Gerhard O., Ness M., 2017b, MNRAS, 470, 1233
- Press W., Teukolsky S., Vetterling W., Flannery B., 1992, Numerical Recipes in C. Cambridge University Press, Cambridge
- Pulsoni C., et al., 2017, preprint, (arXiv:1712.05833)
- Remus R.-S., Burkert A., Dolag K., Johansson P. H., Naab T., Oser L., Thomas J., 2013, ApJ, 766, 71
- Rix H.-W., de Zeeuw P. T., Cretton N., van der Marel R. P., Carollo C. M., 1997, ApJ, 488, 702
- Romanowsky A. J., Douglas N. G., Arnaboldi M., Kuijken K., Merrifield M. R., Napolitano N. R., Capaccioli M., Freeman K. C., 2003, Science, 301, 1696
- Rubin V. C., Ford Jr. W. K., Thonnard N., 1978, ApJL, 225, L107
- Saglia R. P., Bender R., Gerhard O. E., Jeske G., 1997, in Persic M., Salucci P., eds, Astronomical Society of the Pacific Conference Series Vol. 117, Dark and Visible Matter in Galaxies and Cosmological Implications. p. 113
- Sato C., 1980, PASJ, 32, 41
- Schwarzschild M., 1979, ApJ, 232, 236
- Schwarzschild M., 1982, ApJ, 263, 599
- Scott N., et al., 2013, MNRAS, 432, 1894

- Scott N., et al., 2015, MNRAS, 451, 2723
- Serra P., Oosterloo T., Cappellari M., den Heijer M., Józsa G. I. G., 2016, MNRAS, 460, 1382
- Sersic J. L., 1968, Atlas de galaxias australes
- Simionescu A., Werner N., Mantz A., Allen S. W., Urban O., 2017, MNRAS, 469, 1476
- Smith M. C., Wyn Evans N., An J. H., 2009, ApJ, 698, 1110
- Smoot G. F., et al., 1992, ApJL, 396, L1
- Söldner-Rembold I., Gerhard O., 2018
- Spiniello C., Napolitano N. R., Coccato L., Pota V., Romanowsky A. J., Tortora C., Covone G., Capaccioli M., 2015, MNRAS, 452, 99
- Spiniello C., et al., 2018, MNRAS, 477, 1880
- Springel V., et al., 2005, Nature, 435, 629
- Syer D., Tremaine S., 1996, MNRAS, 282, 223
- Thomas J., Saglia R. P., Bender R., Thomas D., Gebhardt K., Magorrian J., Corsini E. M., Wegner G., 2007, MNRAS, 382, 657
- Thomas J., et al., 2009, MNRAS, 393, 641
- Tonry J. L., Dressler A., Blakeslee J. P., Ajhar E. A., Fletcher A. B., Luppino G. A., Metzger M. R., Moore C. B., 2001, ApJ, 546, 681
- Tremblay B., Merritt D., 1996, AJ, 111, 2243
- Trimble V., 1987, Annual Review of Astronomy and Astrophysics, 25, 425
- Usher C., Forbes D. A., Spitler L. R., Brodie J. P., Romanowsky A. J., Strader J., Woodley K. A., 2013, MNRAS, 436, 1172
- Vincent R. A., Ryden B. S., 2005, ApJ, 623, 137
- Weijmans A.-M., et al., 2014, MNRAS, 444, 3340
- Wu X.-P., Chiueh T., Fang L.-Z., Xue Y.-J., 1998, MNRAS, 301, 861
- Wu X., Gerhard O., Naab T., Oser L., Martinez-Valpuesta I., Hilz M., Churazov E., Lyskova N., 2014, MNRAS, 438, 2701
- Zhu L., et al., 2014, ApJ, 792, 59

Zhu L., et al., 2018, MNRAS, 473, 3000

Zwicky F., 1933, Helvetica Physica Acta, 6, 110

de Zeeuw T., Peletier R., Franx M., 1986, MNRAS, 221, 1001

van den Bosch R. C. E., de Zeeuw P. T., 2010, MNRAS, 401, 1770

van den Bosch R. C. E., van de Ven G., 2009, MNRAS, 398, 1117

van den Bosch R. C. E., van de Ven G., Verolme E. K., Cappellari M., de Zeeuw P. T., 2008, MNRAS, 385, 647

van der Marel R. P., 1994, MNRAS, 270, 271

van der Marel R. P., Franx M., 1993, ApJ, 407, 525

Acknowledgements

Firstly, I would like to thank my supervisor Ortwin Gerhard for giving me the opportunity to work on this exciting research project, and for all the scientific support and discussions over the years. I also express my gratitude to Magda Arnaboldi for her guidance and support, in particular regarding the work on NGC 4278.

My thanks goes to Alessia Longobardi for her advice in the early years of my PhD and the her collaboration on the work on M87. I gratefully acknowledge the useful discussions I had with Chiara Spiniello regarding the kinematics of NGC 4697.

I would like to thank Sotiris Chatzopoulos, Maria de los Angeles Perez Villegas, Matias Blaña Díaz, and Mathieu Portail for many useful discussion regarding the theory and technicalities of dynamical modelling. My gratitude also out goes to Claudia Pulsoni for our discussions regarding in particular the extended kinematics of NGC 4697, and Fabrizio Finozzi for his part in the collaboration on triaxial models. I thank Johanna Hartke for her support and for proof-reading parts of this thesis.

My thanks goes out to my fellow group members and officemates over the years Surangkhan Rukdee, Anna Brucalassi, Claudia Pulsoni, Alessia Longobardi and Maria Jose Bustamante Rossell for making my day-to-day work environment pleasant. I also thank Shola Maria Wylie and Jonathan Clarke for brightning up the last year of my thesis. I thank my friends Dijana Vrbanec, Haakon Andresen, Suryashree Aniyani, and David Dodsworth for their emotional and technical support all these years. All my gratitude to my aunt Andrea Hestermann and her partner Christoff Geiger for taking me under their wing during my time in Munich. All my thanks to my friend Lu An, far-away, but still giving me so much time and support.

I would like to thank my father Stefan Söldner-Rembold for all his encouragement and practical advice. Thank you to my mum Ana Söldner-Rembold and my sister Daniela Q. Söldner-Rembold for supporting me with all their love and humour in my thesis time. And finally to my husband, Jeffrey Chi Chung Chan, for being my foundation and for taking care of me throughout the entire PhD time.